Subduction cycling and its controls on hyperactive volcanism in the Taupo Volcanic Zone, New Zealand

A thesis presented in partial fulfilment of the requirements for the degree of

Doctor of Philosophy

in

Earth Science

at Massey University

Palmerston North, New Zealand

Carlos Rodolfo Corella Santa Cruz

2023

MASSEY UNIVERSITY
TE KUNENGA KI PŪREHUROA
UNIVERSITY OF NEW ZEALAND

Abstract

The origin and magmatic evolution of arc magmas are strongly influenced by transcrustal and source processes. Transcrustal processes are often employed to explain the geochemical diversity seen in arc magmas, from mafic to the most felsic endmembers. Source processes are usually used to explain the diversity seen particularly in mafic magmas. Yet, the relative contributions of both processes are highly controversial and difficult to identify. The southernmost volcanic expression of the Tonga-Kermadec-Hikurangi subduction system, the Pleistocene to Holocene Taupo Volcanic Zone (TVZ), is a suitable volcanic area to assess these ideas. Here, the subduction of the unusually thick Hikurangi Plateau has strong effects on tectonic erosion.

The TVZ is dominated by rhyolites, which is unusual given the thin (~16 km) basement comprised mostly of the Permian to Early Jurassic Torlesse metasedimentary terrane. In comparison, the southern TVZ, dominated by andesitic volcanism, is located on a thicker (~30 km) crust. The general view of the magmatic evolution of the TVZ corresponds to mafic magmas coming from the mantle, ponding at the base of the crust, where they assimilate crustal material and start to ascend through the crust where more transcrustal processes occur. In this thesis, the impact of assimilation-fractional crystallisation (AFC) on rock composition was assessed by using major and trace element concentrations, Sr-Pb isotope systematics and the Magma Chamber Simulator (MCS), yielding thermodynamically constrained results. It was found that i) variations seen in mafic magmas cannot be reproduced by transcrustal processes alone, ii) some intermediate samples can be explained by AFC and mixing, but others cannot, and iii) large volumes of crustal assimilation (50%) and fractionation (90%) are required to reproduce the signatures of the most felsic endmembers.

In Pb isotope space, a broadly linear correlation of the magmas is seen, consistent with the mixing of two endmembers: the mantle and a ‘crustal material’. One possibility would be mixing these two endmembers in the source before the transcrustal ascent of magmas. This idea was examined by analysing samples from the Hikurangi margin provided by the IODP Expedition 375. Through the calculation of the bulk chemical and Sr-Pb-Nd-Hf isotopic compositions of the subducting material, it was found that there is no geochemical correlation between this material and the TVZ. This material is too variable and too radiogenic to generate the broadly linear relation seen in Pb isotopic space, and it is also inconsistent in all other isotopic systems (Sr-Nd-Hf). The material located in the accretionary prism and above the décollement zone is homogenous and strongly correlates in the Sr-Pb-Nd isotopic systems. This material would be subducted if affected by tectonic erosion. Once this material is tectonically eroded, it can contribute to the source from

where the magmas are being generated. The isotopic correlations are seen in fluid-mobile and fluid-immobile elements. Thus, the recycled material contributed by releasing fluids and melts or solid material derived from the subducting slab. Whether these interactions occur at the slab-mantle interface and/or during a diapiric ascent remains uncertain. Thus, the isotopic diversity of the TVZ may be controlled by crustal recycling of tectonically eroded material, with subsequent transcrustal processing adding to the diversity generated already in the source. This process would not only limit the amounts of crustal assimilation needed to generate the isotopic signatures of the most felsic endmembers but would also explain the isotopic diversity seen in the most mafic endmembers and the presence of andesites with primitive isotopic signatures. Ultimately, the impacts of crustal recycling in subduction zones can help elucidate the processes of magmatic differentiation, crustal growth, crustal recycling and crustal loss.

Acknowledgements

First, I thank CONACYT for providing funding for my living expenses and university fees (Número de apoyo 739571), and Catalyst Seeding Grant (CSG-MAU1901) for providing funding for the analytical expenses of this project. I am extremely grateful to every member of my supervisory committee. Particularly, I thank my main supervisor, Georg Zellmer, not only for allowing me to work on this project, but also for waiting for me to get a scholarship. I am grateful for all the discussions we had, with his guidance and with his enthusiasm in these particularly difficult years globally. This opportunity helped me to improve not only professionally, but also as a person. Although it was very frustrating to be interrupted several times by the pandemic, possibly the highlight of this project was the laboratory work done with the supervision of Claudine Stirling. I really enjoyed learning and developing the laboratory procedures, and having access to the analytical part of it was really amazing. I am very grateful for her guidance during these years. On the same page, I am really grateful to everyone who helped me during the laboratory and analytical work: Malcolm Reid, David Barr, Candace Martin and Sophie Gangl. Many thanks to the guidance and the great ideas provided by co-supervisor Susanne Straub, who really made me question many aspects of the geologic consensus I was taught. Many thanks for the guidance, always great feedback and samples provided by co-supervisors Marco Brenna and Karoly Nemeth.

I thank James Day for editorial handling, and Tyrone Rooney, Jussi Heinonen, Sarah Mazza and an anonymous reviewer for constructive reviews that significantly improved the manuscript presented in Chapter 4. I thank Jon Woodhead and Masumi Mikoshiba for providing standards JMC-475 and JNdi-1, respectively. I also thank all scientists involved in the IODP Expedition 372B/375 for all the information publicly available and for providing the samples for this project. Many thanks to the thesis examiners Tyrone Rooney, Tod Waight and Jon Procter for their constructive feedback that will help me to improve my future work. Special thanks to my friends Daniel Coulthard, Szabolcs Kosik, Nessa D'Mello, Sophie Gangl, and William Preston for their help during field and laboratory work. I am also thankful for the friends made along the way, particularly Joan, Merce, Charline, Robyn, Rupsa, Silvia(x2), Romana, Ling, Caio, James, Gabe, Rayen, Ceci, et al. Also, many thanks to Brylie, Adam, Sylvie, and Kari for their friendship, company and their amazing food.

Quiero agradecer a toda mi familia por siempre estar conmigo, aunque a distancia, especialmente a mi sacrosanta madre Graciela y mis hermanos Iliana, Jesús, Graciela y Carolina, quienes desde niño me apoyaron en seguir y luchar por mis sueños, por más particulares que fueran. Agradezco mucho también a mis amigos Francis, Cristal, Heidy, Karla, Ari, Lilián, Yedid, Bárbara, Rocío,

entre muchos otros, que siempre me han apoyado en todo. También tengo un gran agradecimiento para todos mis profesores de Geología, pero particularmente estoy agradecido con Diana Meza y Jesús Vidal por ser grandes inspiraciones para mí y por sus grandes enseñanzas. Un gran agradecimiento muy especial para Francisco Paz, quien me enseñó muchísimas cosas sobre geología y sobre la vida, una gran inspiración para mí y un gran amigo que me tuvo muchísima paciencia y gracias a quien he logrado conseguir muchos de mis sueños. Я премного благодарен Алексею Иванову, Елене Демонтеровой и Марине Филенко, без вашей помощи я бы никогда не смог этого сделать.

Table of contents

List of figures

List of tables

List of acronyms

AD – Above the *décollement*

AFC – Assimilation-fractional crystallisation

AP – Accretionary Prism

BD – Below the *décollement*

Cfz – Cook fracture zone

CRC – Collision/reaction cells

DEM – Digital Elevation Model

DSN – Desolvating nebuliser

EB – Emerald Basin

EC-AFC – Energy-constrained assimilation fractional crystallisation

EC – Tectonically erodible material

ESA – Electrostatic analyser

FA – Forearc

GERM – Geochemical Earth Reference Model

GLOSS – Global Subducting Sediments

GLOSS-II – Global Subducting Sediments 2

GSJ – Geological Survey of Japan

HAB – High Alumina Basalts

HCit – Citric acid

HDPE – High-density polyethylene

HFSE – High Field Strength Elements

HP – Hikurangi Plateau

HPS – High Purity Standard

HREE – Heavy Rare Earth Elements

HS – Hikurangi sediments

HT – Havre Trough

ICP – Inductively coupled plasma

ICP-MS – Inductively coupled plasma mass spectrometer

IODP – International Ocean Discovery Program

LB – Lau Basin

LILE – Large Ion Lithophile Elements

LINZ – Land Information New Zealand

LIP – Large Igneous Province

LLD – Liquid line of descent

LOI – Loss of Ignition

LOD – Limits of detection

LREE – Light Rare Earth Elements

MC-ICP-MS – Multiple-collector inductively coupled plasma mass spectrometer

MCS – Magma Chamber Simulator

MCS-AFC – Magma chamber simulator assimilation fractional crystallisation

MS – Mass spectrometer

MQ – Milli-Q H_2O

NFoB – Norfolk Basin

NHT – New Hebrides Trench

NIFS – North Island Fault System

NIST – National Institute of Standards and Technology

NLB – North Loyalty Basin

ODP – Ocean Drilling Program

OVC – Okataina Volcanic Centre

PuT – Puysegur Trench

Q-ICP-MS – Quadruple inductively coupled plasma mass spectrometer

REE – Rare Earth Elements

TAS – Total alkali versus silica

TMVB – Trans-Mexican Volcanic Belt

TVZ – Taupo Volcanic Zone

USGS – United States Geological Survey

VB – Volcanic cone

VE – Vertical Exaggeration

VMfz – Vening Meinesz fracture zone

WD-XRF – Wavelength dispersive X-ray fluorescence

XRF – X-ray fluorescence

Chapter 1- Introduction

1.1 Magma generation and differentiation processes in subduction zone systems

Subduction zones are found at convergent plate margins and are associated with the sinking of lithospheric plates. They are considered as the largest recycling systems on Earth, delivering materials such as oceanic and continental lithosphere, sediments and seawater back into the mantle (Stern, 2002). It is well documented that the release of fluids from the slab lowers the mantle solidus and causes the generation of magmas in subduction zones around the globe (*e.g.*, Bacon, 1990, De Astis et al., 2000, Kushiro, 2007, Stern, 2002). Fluids released by the slab do not only contain volatile elements such as C, Cl and S, but also a range of elements that depend on the subducting material, the thermal structure of the subducting plate, and the releasing pressure (*e.g.*, Li & Ni, 2020, Ribeiro et al., 2022). The subducting slab, from top to bottom, is comprised of layers of sediments, oceanic crust and subducting lithospheric mantle with varying thicknesses in different subduction zones.

The thickness and composition of the sediments present in the subducting slab have large variations in different trenches but are similar along the same trench (Plank, 2014, Plank & Langmuir, 1998). The thickness of the sediment layer varies from a few meters (*e.g.*, Tonga) to several kilometres (*e.g.*, Makran. Gulf of Oman and Andes) of different lithologies such as turbidites, clay, chert, carbonates and volcaniclastics. For example, Andaman (Java), and Makran (Gulf of Oman) sediment layers are comprised mainly of turbidites, while Hikurangi (Kermadec-New Zealand) sediments are comprised mainly of carbonates and volcaniclastics and Kamchatka (Russia) sediments are dominated by clay and chert (Plank, 2014). The oceanic crust, located below the sedimentary cover, has a

mafic to ultramafic composition, and typically constitutes of ~1 km of extrusive rocks, ~1 km of sheeted dykes and ~5 km of gabbro and ultramafic rocks, *i.e.*, a typical thickness of ~7 km (Staudigel, 2003). The oceanic crust is altered by seawater and hydrothermal fluids, with highly enriched alkali elements (*e.g.*, Li and Cs) and U as well as Ca, Pb, Si and Fe contents (Kelley et al., 2003). The enrichment of these elements is important to note because fluids and melts released from the subducted slab play a key role in magma generation processes at subduction zones (Bacon, 1990, De Astis et al., 2000, Kushiro, 2007, Spandler & Pirard, 2013, Stern, 2002). Slab fluid composition depends on the proportions and compositions of the different dehydrating layers. The increase of pressure cause increasingly more siliceous supercritical fluids to return to the mantle not only fluid-mobile elements, such as Rb, Ba, Li, Sr, Pb, U and large ion lithophile elements (LILE), but also more immobile high field strength elements (HFSE), such as Nb, Ta, Hf, Th, and the rare earth elements (REE) (Gamal El Dien et al., 2019, Keppler, 1996, Kessel et al., 2005a, Kessel et al., 2005b, Mibe et al., 2011). A representation of LILE, HFSE and other elements showing their ionic charge and radius is shown in **Figure 1.1**.

Figure 1.1: Ionic radius versus ionic charge for trace elements (in black) from Rollinson and Pease (2021), major elements (in red) indicate where substitutions occur.

Magma production in subduction environments is responsible for generating approximately 80% of the continental crust, which on average has an andesitic composition, making it the main process responsible for crustal growth on Earth at present (*e.g.*, Barth et al., 2000, Plank & Langmuir, 1998, Stern, 2002, Taylor, 1967). Although mafic magma generation by slab fluid addition and partial melting of the hydrated mantle in subduction zones is well accepted, the processes generating evolved magmas, such as andesites, dacites and rhyolites are much more varied and contested. A variety of processes can generate silica-rich melts in subduction zones, and they are broadly divided into two: (i) Transcrustal processes such as fractional crystallisation and crustal assimilation (AFC), causing mantle mafic magmas to become more felsic in the crust, and (ii) slab additions to the mantle source that can be in the form of slab melts, slab fluids and other slab materials, leading to subcrustal generation of both mafic and intermediate magmas.

1.1.1 Transcrustal processes: the role of AFC in the generation of evolved magmas

The generation of intermediate to evolved magmas is strongly affected by the thickness of the overriding crust. Mafic mantle melts become more silicic with the increasing crustal thickness due to the crust acting as a density filter, causing longer fractionation, longer cooling times, and allowing extensive magma-crust interactions (*e.g.*, Farner & Lee, 2017, Leeman, 1983, Plank & Langmuir, 1988). The compositional diversity found in magmas have been traditionally understood as a result of different degrees and conditions of assimilation and fractional crystallisation. Fractional crystallisation occurs while the magma is cooling or degassing, and crystals start to form and separate from the liquid. An important factor controlling the composition of the evolving liquid is the mineral assembly and their respective partition coefficients (commonly denoted as D or K), as fractionation will increase or decrease the concentrations of given elements in the residual liquid depending on the partition coefficients of the minerals fractionating from the liquid (DePaolo, 1981b).

Likewise, concurring crustal assimilation, a process in which material from the wall rock is incorporated into the magma, controls the composition of the evolving liquid. Assimilation depends on a range of variables such as the temperature of both the magma and the wall rock, the cooling rate, the heat of crystallisation, the pressure as well as the composition and relative masses of both the magma and the assimilant (Gribble, 1990). When the wall rock melt is assimilated by the magma, it often causes a change in the chemical and in the isotopic composition of the magma due to the different isotopic composition of the assimilated material, unlike fractional crystallization alone. Some limitations arise for AFC to generate felsic magmas from mafic precursor magmas because it requires large volumes of crustal assimilation and extensive fractionation,

which in turn produce large quantities of ultramafic-mafic residues. These residues are often absent in arcs and are typically interpreted as a result of lower crustal delamination (Hawkesworth & Kemp, 2006, Magni & Király, 2020).

1.1.2 Subcrustal processes: the role of mantle – slab interactions in magma generation

Sub-arc source mantle processes are also important factors that control the composition of arc magmas, and in some cases, they have a more substantial input than transcrustal processes (Kelemen, 1995, Plank & Langmuir, 1988, Turner & Langmuir, 2015a, Turner & Langmuir, 2015b). Together with the release of slab fluids, crustal recycling is a major process influencing magma generation that is not limited to subduction zones, but also affects intraplate volcanism (*e.g.*, Armstrong, 1981, Johnson & Plank, 2000, Patchett & Bridgwater, 1984, Tollstrup & Gill, 2005, Weaver, 1991, White & Patchett, 1984). Crustal recycling affects the dynamic evolution of the Earth by bringing back material into the mantle via crustal delamination or subduction and hence not only destroying crust, but also contributing to crustal growth (Patchett & Samson, 2003). Thus, subduction zones are responsible for the creation of new crust by magma generation and its destruction by both subaerial and tectonic erosion, making them an essential piece of the crustal recycling process (*e.g.*, Armstrong, 1981, Straub et al., 2020, von Huene & Scholl, 1993).

1.1.2.1 Tectonic erosion and crustal recycling

Tectonic erosion is the breakup, wearing away and removal of rocks of the overriding plate by subduction (Straub et al., 2020, von Huene et al., 2004, von Huene & Scholl, 1991). This process is a key part of crustal recycling by returning parts of the overriding crust into the mantle, some of which will be recycled through arc magmatism (Stern,

2011). When the subducting oceanic crust bends downwards into the trench, it releases stress by normal faulting which generates a graben that can accommodate material from the overriding plate (von Huene et al., 2004). Furthermore, upward fluid drainage from the lower plate increases the material strength below the plate interface and weakens the overlying material by hydrofracturing (Stern, 2011, von Huene et al., 2004). The morphology of the subducting plate is an important factor affecting tectonic erosion. Subducting ridges, seamounts, oceanic plateaus or any irregularity in the subducting plate, cause uplift and subsequent drop of the overriding forearc, which in turn causes a more significant fracturing and higher efficiency in the transport of trench sediments and debris (Cande & Leslie, 1986, Laursen et al., 2002, Stern, 2011, von Huene et al., 2004, von Huene & Scholl, 1991). All these factors cause the overlying plate to progressively lose coherence and increase the rate of tectonic erosion (**Figure 1.2**). Tectonic erosion can occur in either the front of the forearc or along the subcrustal underside of the forearc, named ‘frontal’ or ‘basal’ erosion respectively (Stern, 2011, von Huene & Scholl, 1991).

Figure 1.2: Cross-section after Stern (2011). The subduction channel is filled with oceanic sediments and debris eroded from the forearc wedge. Basal erosion results in mass transfer from the bottom of the forearc wedge to the lower plate as fragments are dragged into the subduction channel, while frontal erosion results in mass transfer from the frontal prism into the subduction channel.

Subducted and tectonically eroded material may be recycled back to the overriding crust by mixing with the mantle and incorporating it into arc magmas (Stern, 2011). Due to these processes, the geochemical signature of the overriding plate may be detected in arc lavas together with that of the subducted sediments, but can be misinterpreted as crustal assimilation or contamination during magma ascent (von Huene et al., 2004). However, ascending magmas do not necessarily assimilate the crustal basement of the overriding crust (Stern, 2011, Straub et al., 2015). Crustal recycling in subduction zones is a complex process that is sometimes difficult to identify, and it is important to differentiate between the various endmembers: subducting sediments, tectonically eroded crust, subducted oceanic crust and the overlying crustal basement which may be assimilated. All of these

components may have similar or different compositions depending on the subduction zone in question.

Recycling of tectonically eroded material has been reported in some subduction-related volcanic zones. Magmatism in the Central Andes has been linked to the recycling of continental material introduced by tectonic erosion, causing a geochemically enriched mantle (Kay et al., 2005, Risse et al., 2013). Furthermore, in the Southern Andes, the input of variable tectonically eroded crustal compositions has been linked to the generation of mantle heterogeneities (Holm et al., 2014). Magmas in Costa Rica and Panama, Central America, link to the incorporation of ophiolitic forearc crust into the mantle by forearc subduction based on Pb isotopic ratios (Goss & Kay, 2006). Another example of input of tectonically eroded material into subduction-related magmatism is found in the Trans-Mexican Volcanic Belt. Here, tectonically eroded material is thought to be interacting with the mantle generating pyroxenitization and subsequent melting (Straub et al., 2011, Straub et al., 2008) or by undergoing a diapiric ascent and subsequently melting, thereby contributing to arc magma generation (Parolari et al., 2018, Parolari et al., 2021, Straub et al., 2015). In fact, crustal recycling of tectonically eroded material may be a globally important process in magma generation at subduction zones (Straub et al., 2020).

1.1.2.2 Impacts of crustal recycling in the magma generation processes

The recycled crust is not restricted to the subducting oceanic crust and its sedimentary cover but can also include frontal or basal tectonically eroded material, or any mixture of such materials. Recycled material can consist of eroded crust, sediments, oceanic crust and silica-rich slab fluids, and contribute to the compositional diversity found in global

arcs, consistent with experimental data (*e.g.*, Drummond et al., 1996, Förster & Selway, 2021, Hauff et al., 2003, Johnson & Plank, 2000, Martin et al., 2005, Schiano et al., 1995, Shimoda et al., 1998, Skora & Blundy, 2010, Tatsumi, 2001, Tatsumi & Hanyu, 2003, Yogodzinski et al., 1995). Processes in which crustal material is recycled into the mantle and subsequently participates to magma generation in volcanic arcs, can be grouped into: (i) melting of the subducting slab in either the basalt-gabbro section or its sediment section, generating magnesian andesites and/or adakites (*e.g.*, Defant & Drummond, 1990, Drummond et al., 1996, Martin et al., 2005, Shimoda et al., 1998, Tatsumi, 2001, Yogodzinski et al., 1995); (ii) reaction of these melts with the surrounding mantle causing pyroxenitization and subsequent pyroxenite melting, which can result in high-Mg# basalts, magnesian andesites and dacites (*e.g.*, Straub et al., 2011, Straub et al., 2008, Tatsumi, 2001); and (iii) detachment of material from the slab through a diapiric ascent followed by partial melting in the hot core of the mantle wedge, generating diverse melts with chemical variation from basaltic to dacitic (Behn et al., 2011, Castro et al., 2010, Castro & Gerya, 2008, Currie et al., 2007, Kelemen & Behn, 2016, Marschall & Schumacher, 2012, Nielsen & Marschall, 2017, Parolari et al., 2018, Parolari et al., 2021, Straub et al., 2015).

1.2 Radiogenic isotope systems: tools to unravel the complex magma generation and evolution processes

Different radiogenic isotope systems are crucial tools for gaining a better understanding of the processes operating in subduction zones, and the components involved in the genesis of arc magmatism. Isotopic composition is usually expressed as one or more isotope ratios, where the radiogenic isotope is compared to another isotope of the same element that is neither radiogenic nor radioactive, and is used to normalize its abundance (DePaolo, 1981a). For example, by convention, the $^{87}Sr/^{86}Sr$ ratio is used to monitor the

systematics of the radiogenic Sr isotope system. Specifically, ^{87}Sr is the product of the radioactive decay of ^{87}Rb which has a half-life of 48.8 Byr (**Figure 1.3**), while the normalizing isotope, ^{86}Sr, is neither radiogenic nor radioactive and therefore, the $^{87}Sr/^{86}Sr$ isotopic ratio reflects the time-integrated difference in the Rb/Sr elemental ratios of the source. The same principle applies to the Nd isotope system, whereby ^{147}Sm decays to ^{143}Nd with a half-life of 106 Byr (**Figure 1.3**). The abundance of radiogenic ^{143}Nd normalised to stable ^{144}Nd to give the $^{143}Nd/^{144}Nd$ isotopic ratio, reflecting the time-integrated difference in the Sm/Nd elemental ratios of the source (Allègre, 1987). Rubidium and strontium are both incompatible trace elements. In addition, Rb has a large ionic radius, which means that it is excluded from many minerals. As a result of this incompatibility, it is highly concentrated in the crust and depleted in the mantle due to consecutive extractions of partial melts. On the other hand, Sr has a slightly smaller ionic radius than Rb and as a result, Sr is also concentrated in the crust and depleted in the mantle, but not to the same extent as Rb.

These characteristics are then translated to an enrichment of Rb over Sr in the crust and a depletion of Rb over Sr in the mantle. Thus, the decay over time of Rb causes $^{87}Sr/^{86}Sr$ ratios to be higher in the crust and lower in the mantle. However, both Rb and Sr are LILE and thus quite soluble in fluids, potentially impacting their use as robust tracers. Tracers employing less mobile isotopes of the HFSE may thus be preferable. For example, a similar process occurs with Sm and Nd, where Nd is depleted in the mantle relative to Sm, thus making $^{143}Nd/^{144}Nd$ ratios higher in the mantle than in the crust. In a similar fashion to Sm and Nd, Lu and Hf (where ^{176}Lu decays to ^{176}Hf with a half-life of 37.12 Byr) are good indicatives of petrogenetic processes. Both Sm and Lu, that decay to Nd and Hf isotopes, are more compatible in garnet and thus they are enriched in the mantle

residue atter melting which in turn increases both ^{176}Hf and ^{143}Nd radiogenic isotopes in the mantle and have lower isotopic ratios in the crust (Blichert-Toft & Albarède, 1997, Vervoort et al., 1999).

Finally, Pb has four isotopes: ^{204}Pb, ^{206}Pb, ^{207}Pb and ^{208}Pb, with ^{204}Pb being the only non-radiogenic isotope, while ^{206}Pb, ^{207}Pb and ^{208}Pb are all products of radioactive decay. Specifically, ^{206}Pb and ^{207}Pb are the end products of ^{238}U and ^{235}U decay, respectively, while ^{208}Pb is the end product of ^{232}Th decay (**Figure 1.3**). As Th is slightly more incompatible than U, and the latter is more incompatible than Pb, the crust is enriched in these radiogenic isotopes, giving rise to lower $^{206}Pb/^{204}Pb$, $^{207}Pb/^{204}Pb$, $^{208}Pb/^{204}Pb$ in the mantle relative to the crust, in a similar manner as for $^{87}Sr/^{86}Sr$ and conversely to $^{142}Nd/^{144}Nd$ and $^{176}Hf/^{177}Hf$, which have higher ratios in the mantle relative to the crust. Thus, any crust-mantle interaction can be easily detected through these isotopic systems.

However, it may be necessary to resolve subtle variations in crustal isotopic compositions when trying to differentiate if this interaction occurred in the source following forearc crustal recycling, or as transcrustal assimilation. Deconvolving the processes at work becomes even more complicated if there is a need to differentiate between different crustal components such as between the upper crust, sediments and lower crust, especially because of the similarity between the first two crustal components and the lack of information for the latter component. To this end, $^{176}Hf/^{177}Hf$ can prove very useful in differentiating between different types of sediments in the source, together with associated differences in the Nd/Hf ratios, as pelagic sediments show more radiogenic isotope signatures than terrigenous sediments (Marini et al., 2005, Straub et al., 2015). The $^{176}Hf/^{177}Hf$ isotopic ratios, alongside $^{206}Pb/^{204}Pb$, $^{207}Pb/^{204}Pb$ and $^{208}Pb/^{204}Pb$

systematics, have been used to prove that crustal recycling occurs in different arc lavas, such as in Mexico, and the Aleutian and Izu-Bonin arcs (*e.g.*, Jicha et al., 2004, Straub et al., 2010, Straub et al., 2015).

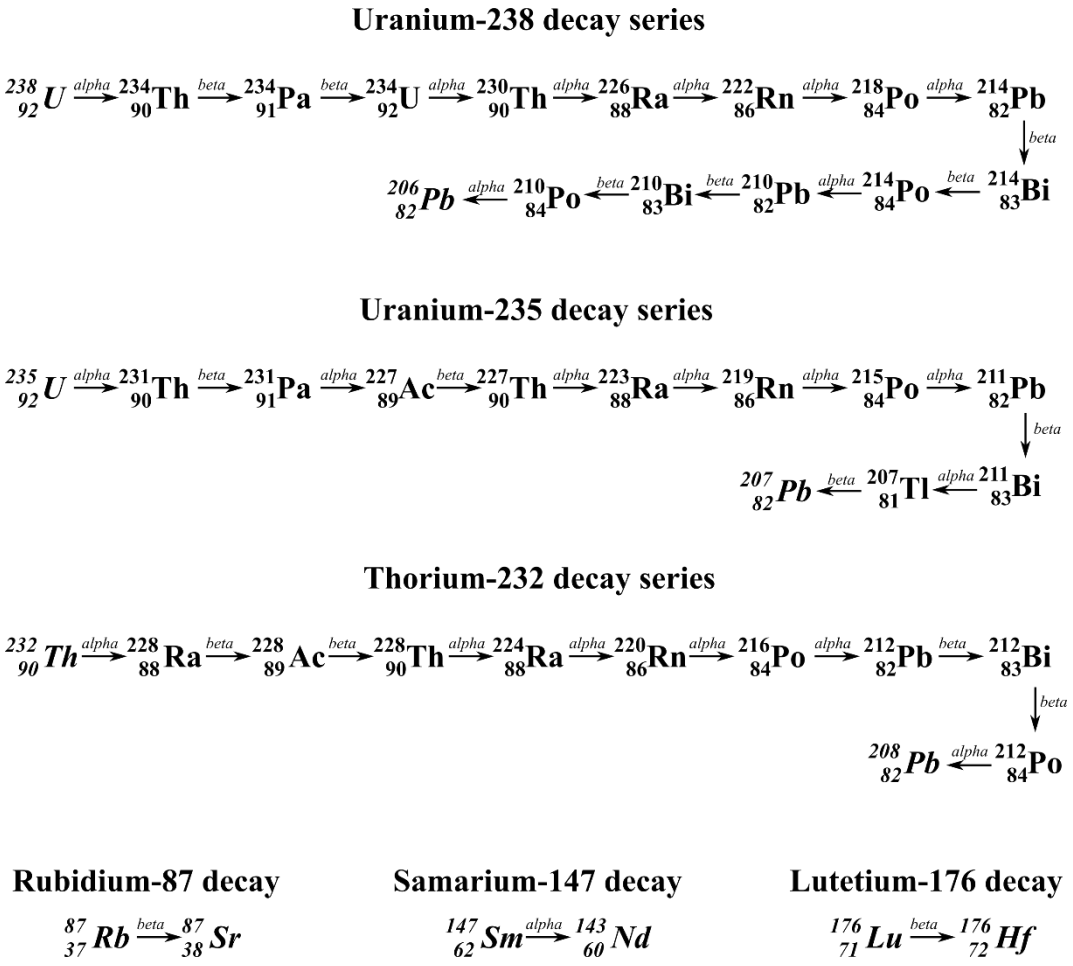

Figure 1.3: Diagram showing the different decay series for the Pb isotope end-products as well as the type of radiogenic decay in Rb-Sr, Sm-Nd and Lu-Hf isotope systems. Starting and ending isotopes are in italics.

Radiogenic isotopic systems may facilitate a better understanding of the origin of volcanism within the Taupo Volcanic Zone (TVZ), which is the topic of this thesis. Volcanism in the TVZ is triggered by the subduction of the Pacific plate below the Australian plate, where an oceanic plateau, the 'Hikurangi Plateau', has been subducted since about 25 – 30 Ma (Nicol et al., 2007, Seebeck et al., 2013). Using Sr-, Nd and Pb- isotope datasets, Timm et al. (2014) suggested that the subduction of this plateau has a strong effect on tectonic erosion and implications for the petrogenesis of arc volcanoes

of the Kermadec arc, north of the TVZ. To date, however, no studies have been carried out to identify a potential role for crustal recycling by tectonic erosion within the TVZ.

1.3 Objectives

This thesis aims to provide a better understanding of the petrogenetic processes involved in TVZ volcanism, focusing on its chemical and isotopic characteristics. Mafic, intermediate and felsic volcanic samples are considered, together with sediments from the subducting slab and accretionary prism. The following objectives have been designed to determine the genetic relationships between these materials:

1. Determine the chemical (major and trace element concentrations) and Sr-Pb isotopic characteristics of the TVZ from samples taken from mafic, intermediate, and felsic eruptions covering the whole compositional and temporal spectrum. Based on these results, thermodynamic forward modelling through the Magma Chamber Simulator is applied to consider crustal assimilants that have previously been chemically and isotopically characterized, together with pressure, temperature and water contents. This aims to test if crustal assimilation is a plausible process for generating the geochemical and isotopic diversity of the TVZ using a thermodynamically robust framework, as previous studies have suggested AFC may be a dominant process in the generation of felsic melts in the TVZ. The results of this investigation are presented in **Chapter 4**.
2. Determine the chemical and Sr-Pb isotopic characteristics of the trench sediments using selected samples from the International Ocean Discovery Program (IODP) Expedition 375 from sites U1520C, U1520D, U1518E and U1518F for each relevant lithostratigraphic unit. For this, a selected suite of samples representative of each unit is used to determine major element compositions, and 10 representative samples are used for the quantification of trace element concentrations, and Sr and Pb isotopic

compositions. These datasets are used to estimate the bulk major and trace concentrations and isotopic composition of the sediments entering the Hikurangi trench as well as the signatures of those being accreted and subsequently eroded, based on the relative proportions of different lithologies in the subducting sediment pile. The results of this study are presented in **Chapter 5**.

3. Compare the chemical and isotopic signatures of TVZ volcanism with those of the subducting sediments to determine to which extent the subducting sediments, or conversely, the tectonically eroded accretionary prism, may be involved in the genesis of arc magmas. This objective will be achieved using the datasets acquired and discussed in the previous chapters, as well as additional Nd-Hf isotopic data for both arc magmas and sediments. These additional isotopic systematics may allow the subducted sediments and eroded material contributions to the mantle source to be distinguished, and thus their role in crustal recycling and crustal growth processes to be elucidated. The results of this investigation are presented in **Chapter 6**.

1.4 Thesis outline

This thesis is divided as follows into eight chapters which, due to the publication nature of this dissertation, may contain some repetitive sections:

Chapter 1: Introduction. This chapter offers a broad introduction to the magma generation and evolution processes in subduction zone-related magmatism, including crustal recycling processes and their general input in these genetic processes. It also summarises the use of different isotopic ratios to identify different processes occurring during magma generation and evolution. It concludes with the main objectives (see above) and outline of the thesis.

Chapter 2: Geological background. This chapter is divided into three sections starting with the general geology of the TVZ including that of its basement. Then, the second section discusses the petrogenetic models that have been proposed for TVZ magmatism over time, including assimilation-fractional crystallisation, crustal anatexis, source heterogeneities and sedimentary addition. Finally, a general discussion follows the tectonic framework of the TVZ, with an emphasis on the Hikurangi margin and the subduction of the Hikurangi Plateau causing tectonic erosion.

Chapter 3: Methodology. This chapter explains the methodology used in this thesis from sample selection to sample preparation, laboratory procedures and analytical procedures for determining major and trace element concentrations as well as Sr-Pb-Nd-Hf isotopic compositions. Furthermore, data processing methods such as the Magma Chamber Simulator and the bulk sediment composition calculations employed in the following chapters are also detailed in this chapter.

Chapter 4: Transcrustal versus source processes leading to magma differentiation in subduction zones: a case study from the Taupo Volcanic Zone, New Zealand. This chapter focuses on energy-constrained thermodynamical AFC modelling based on the Magma Chamber Simulator software to test the generally accepted dominance of transcrustal processes in the generation of evolved magmas of the TVZ. Using Pb isotopic data, it is also proposed that the input of tectonically eroded material (Torlesse terrane) as well as subducting sediments (GLOSS-II) into the mantle can reproduce the broadly linear Pb-isotope trend of the TVZ, and that transcrustal processes may be subordinate. This paper has been published on *Geochimica et Cosmochimica Acta*.

Chapter 5: Geochemical characterisation of forearc and subducting sediments in the Hikurangi Margin from IODP Expedition 375 drills U1518 and U1520. This chapter reports major and trace element concentration data as well as Sr-Pb isotope ratios for the subducting and accretionary prism materials in the Hikurangi margin, east of the North Island, New Zealand. These materials are further divided into subducting material (below the *décollement*) and accreted/forearc material (above the *décollement* and accretionary prism). The bulk elemental and isotopic compositions of these subdivisions are then calculated. This paper has been submitted to the *New Zealand Journal of Geology and Geophysics*.

Chapter 6: Crustal recycling of tectonically eroded forearc sediments and its impact on magma generation of the Taupo Volcanic Zone, New Zealand. This chapter reports Nd-Hf isotope ratios for the TVZ and IODP samples to compare, together with previously published Sr-Pb data for the same sample suite, the interactions between the TVZ and the subducting and eroding material. With these data, it was found that in these isotopic systems (Sr-Pb-Nd), a clear input of tectonically eroded material to the mantle source of the TVZ can explain its isotopic diversity. Furthermore, subducting material does not correlate with the TVZ signature in any of the isotopic systems (Sr-Pb-Nd-Hf). Thus, these findings indicate that crustal recycling in the source of the TVZ magmas is the main process dominating the Sr-Pb-Nd-Hf isotopic compositions of this volcanic zone and that crustal assimilation is not as significant as previously thought, and instead is of limited importance. This paper will be submitted as a Letter to the *Journal of Petrology*.

Chapter 7: Synthesis. This chapter compiles the findings of Chapters 4, 5 and 6, and discusses how they contribute to our global understanding of magma generation processes in subduction zones and the impact of crustal recycling by sediment subduction and tectonic erosion.

Chapter 8: Conclusions and outlook. This final chapter presents a summary of the results, their implications, and future directions of research in the TVZ and beyond.

Chapter 2 - Geological background

2.1 Tectonic setting

The Tonga-Kermadec-Hikurangi subduction zone extends for 2,700 km from Samoa to the North Island, New Zealand, with NNE-SSW orientation (**Figure 2.1**). Here, convergence between the Pacific and Australian plates occurs with one of the highest rates of back-arc extension on Earth, with the Lau basin opening up at the rate of 160 mm/yr (Bevis et al., 1995). The north and central portions, referred to as Tonga and Kermadec respectively, correspond to intra-oceanic arcs, while the southern portion, referred to as Hikurangi, corresponds to a continental arc: the Taupo Volcanic Zone (TVZ) (Turner et al., 1997). Along the Hikurangi trench, east of New Zealand, the convergence rate decreases from 57 mm/yr in the north to 27 mm/yr in the south (Clark et al., 2019). In the Hikurangi portion, the subduction of an over-thickened oceanic crust occurs by the subduction of the ~15 km thick Hikurangi Plateau, unlike the Tonga and Kermadec portions, where the subducting crust has an average oceanic crustal thickness (King, 2000, Mortimer & Parkinson, 1996). This plateau is a fragment of the Cretaceous Ontong Java-Manihiki-Hikurangi Large Igneous Province (LIP) (Davy & Wood, 1994, Taylor, 2006). Extended information about the Hikurangi Plateau and its sedimentary cover is presented in **section 2.4**.

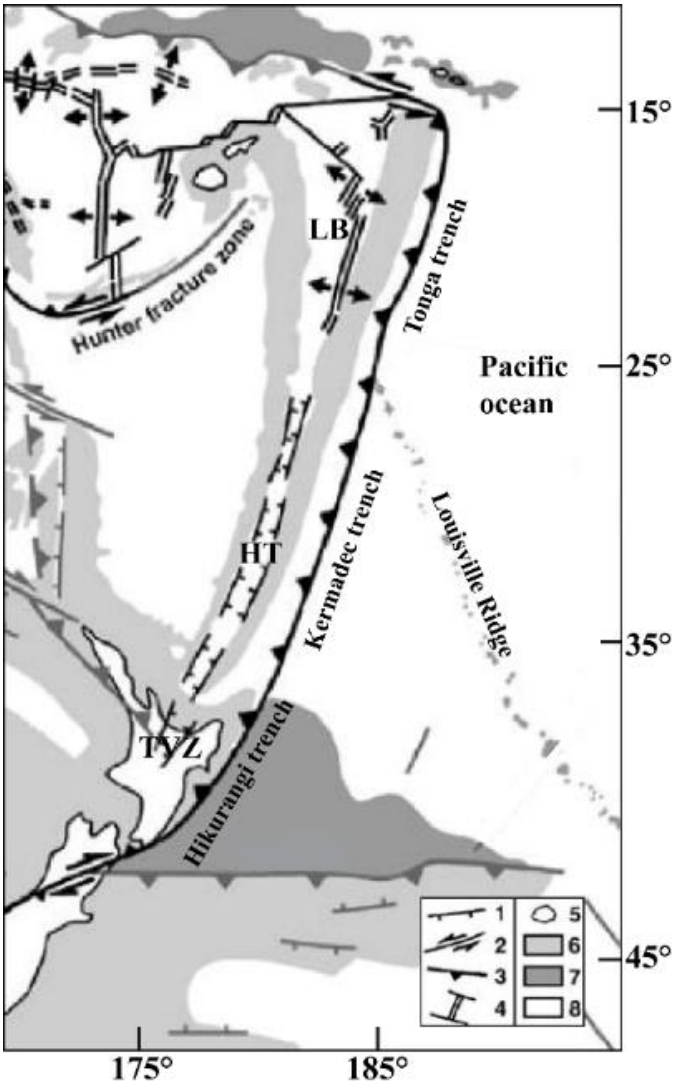

Figure 2.1: Tonga-Kermadec-Hikurangi Trench, modified after Schellart et al. (2006). 1, normal fault; 2, strike-slip fault; 3, subduction zone; 4, spreading ridge and transform faults; 5, land; 6–8, sea, with 6, continental or arc crust; 7, oceanic plateau; 8, basin/ocean floor; TVZ, Taupo Volcanic Zone; HT, Havre Trough; and LB, Lau Basin. Structures in light grey indicate that they are tectonically inactive.

Subduction of the Hikurangi Plateau started beneath the eastern Gondwana margin along the Chatham Rise in the Late Cretaceous, and caused the end of the subduction in this section (Davy, 2014, Davy et al., 2008, Reyners, 2013, Worthington et al., 2006). Subduction recommenced at about 24-30 Ma after re-adjustment of the regional tectonics, but this time beneath the east coast of North Island, New Zealand (Nicol et al., 2007, Seebeck et al., 2013). From ~2 Ma, volcanic activity related to the Hikurangi subduction zone has occurred within the TVZ (Price et al., 2005, Wilson et al., 1995). As discussed in **Chapter 1**, any irregularity in the subducting plate, like the presence of ridges, oceanic

plateaus and seamounts, increase the rate of tectonic erosion (Cande & Leslie, 1986, Laursen et al., 2002, Stern, 2011, von Huene et al., 2004, von Huene & Scholl, 1991). Strike-slip and compressional faulting from seamount and scarp collisions, followed by subsequent extensional faulting and collapse of the upper plate, have been reported as a control on effective tectonic erosion in the Northern Hikurangi and Southern Kermadec margins (Barker et al., 2009, Collot & Davy, 1998, Collot et al., 1996, Lewis et al., 1998, Pedley et al., 2010).

2.2 Volcanism in the Tonga-Kermadec subduction zones

The Tonga and Kermadec oceanic arcs are limited to the west by extensional back-arc basins: the Lau Basin and the Havre Trough, respectively (**Figure 2.1**). Tonga volcanism is dominated by low-K basaltic andesites with local andesites and dacites, while Kermadec volcanism is dominated by low-K tholeiites with subordinate medium-K series, basaltic andesites, dacites and rhyolites (Ewart et al., 1977, Ewart & Hawkesworth, 1987). An important difference between the volcanism in these subduction zones is the source input of different materials. Kermadec Pb isotopic compositions indicate the presence of western Pacific sediments in the source, while at Tonga high U/Th and high $^{230}Th/^{232}Th$ ratios reflect a derivation from the altered oceanic crust (Ewart et al., 1998, Regelous et al., 1997). Turner et al. (1997) proposed a small input of subducted sediment melts into the arc lavas.

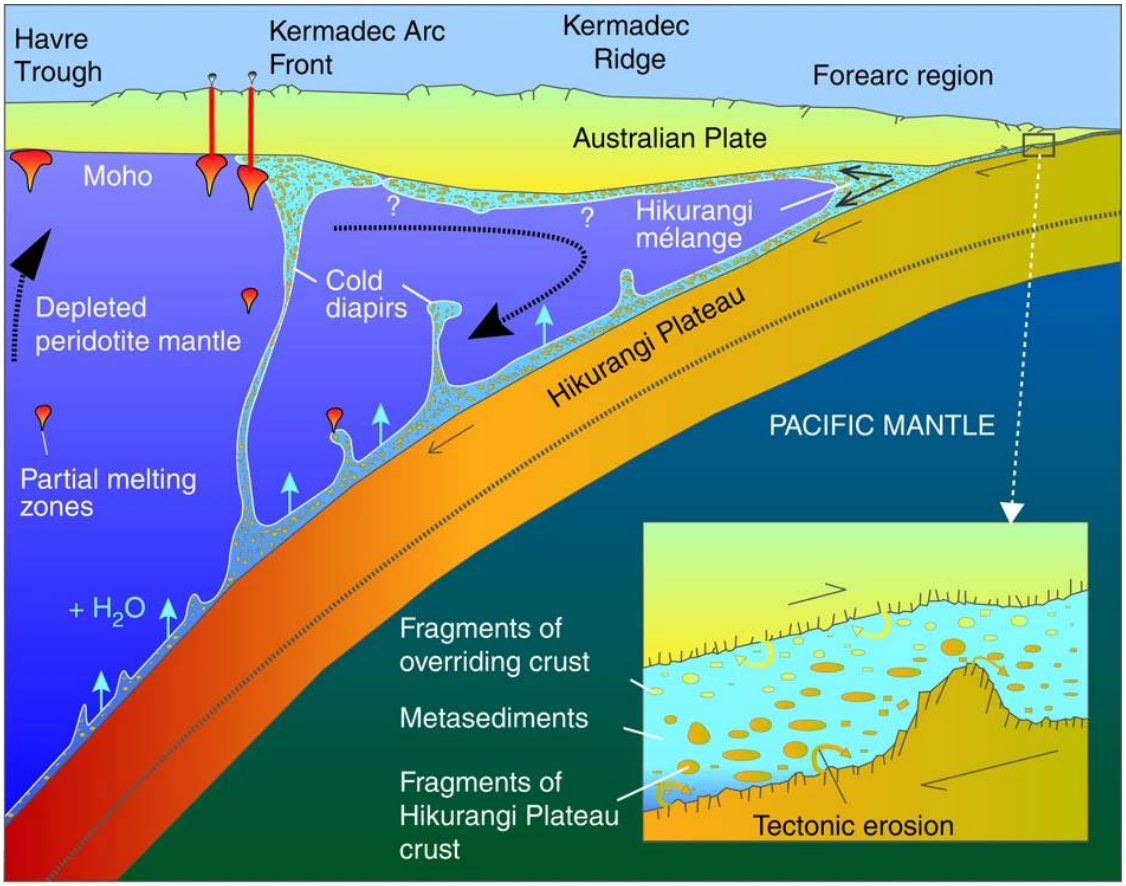

Figure 2.2: Schematic section of the Southern Kermadec Arc from Timm et al. (2014). This illustrates the effect of the Hikurangi Plateau on tectonic erosion and processes in the mantle beneath the Kermadec Arc. Tectonic erosion forms a *mélange* layer containing fragments of the overriding forearc crust and the Hikurangi Plateau itself. This *mélange* is subducted, forms cold diapirs and affects the composition of the Kermadec Arc volcanism.

The southernmost portion of the Kermadec arc is located in the Hikurangi portion of this subduction system. Here, Timm et al. (2014) reported the presence of a subduction *mélange* influencing the chemistry of the Southern Kermadec arc (**Figure 2.2**). Based on a systematic enrichment in Sr-Pb and depletion in Nd isotopic ratios, these authors indicated that this mixture contains fragments from the subducting metasediments, the Hikurangi Plateau and tectonically eroded crust from the overriding plate. The North Island of New Zealand is located to the south of the Southern Kermadec arc, also being part of the Hikurangi portion of the Tonga-Kermadec-Hikurangi subduction zone. Unlike the Tonga and Kermadec oceanic arcs, the TVZ represents a continental arc.

2.3 Crustal basement of the North Island, New Zealand

The basement of the central North Island, New Zealand, consists of the non-crystalline Waipapa and Torlesse composite terranes (**Figure 2.3**). These Permian-Cretaceous terranes are fossil accretionary prisms lithologically tectonized assemblages of weakly metamorphosed greywacke (Adams et al., 2002, Adams et al., 2007, Roser & Korsch, 1999). Specifically, the Torlesse terrane is comprised of successions of quartzose, turbidite-dominated greywackes and is divided into the Early Jurassic Kaweka subterrane and the Early Cretaceous Pahau subterrane (Adams et al., 2007, Adams et al., 2009, Andrews et al., 1976, Mortimer et al., 2014, Speden, 1976). These sediments are derived from continental igneous rocks with a quartzo-feldespathic granitoid composition (Mackinnon, 1983, Price et al., 2012).

On the other hand, the Waipapa terrane has a Permian-Jurassic age and is a monotonous medium-grained greywacke-siltstone succession, with a higher proportion of volcanic and volcaniclastic felsic-intermediate igneous sources compared to the Torlesse terrane (Adams et al., 2007, Black, 1994). The location of the exact boundaries between the Waipapa and Torlesse terranes is unclear, as they are covered by the TVZ. However, Price et al. (2015) proposed that the base of the crust beneath the TVZ corresponds to the Torlesse composite terrane, while the Waipapa composite terrane is only located in the uppermost portion of the crust (**Figure 2.3**).

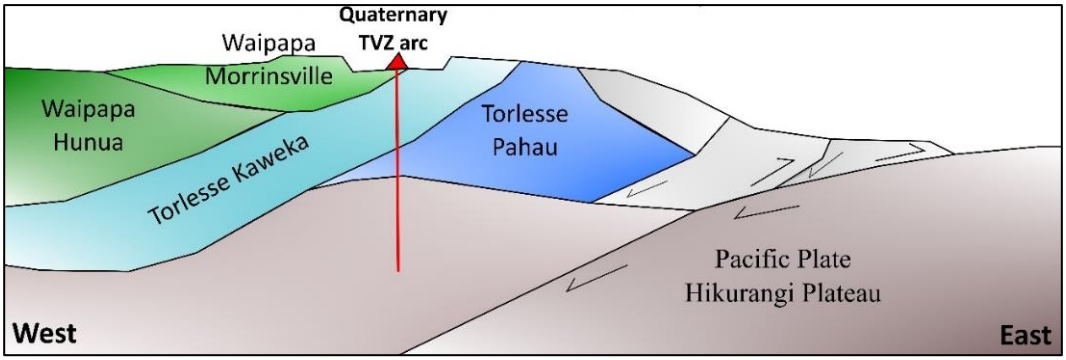

Figure 2.3: Schematic cross-section showing the relationship between central North Island composite terranes and the TVZ, after Price et al. (2015).

While the Torlesse and Waipapa composite terranes are the dominant lithologies in the crustal basement underneath the TVZ, the crustal structure is variable. Tectonic extension in the Taupo Rift, central North Island accommodates normal faults generating, in some cases, well-defined grabens with extension ranging from 2-6 mm/yr in the northern and southern portions, to 9 mm/yr in the central portion (Darby et al., 2000, Villamor & Berryman, 2001, Villamor & Berryman, 2006). Due to this extension, crustal thickness varies from ~16 km in the northern and central portions of the TVZ (Stratford & Stern, 2004) to ~30 km in the southern portion (Salmon et al., 2011).

2.4 Taupo Volcanic Zone (TVZ)

The TVZ is the southernmost portion of the Tonga-Kermadec-Hikurangi subduction zone, resulting from the subduction of the Pacific plate below the North Island, New Zealand (**Figure 2.1**). This volcanic zone can be divided in different ways. Wilson et al. (1995) proposed two main groups: the old TVZ, ranging from the onset of volcanic activity at *c*. 2 Ma up to the Whakamaru Group eruptions at *c*. 0.34 Ma, and the young TVZ from the Whakamaru Group eruptions at *c*. 0.34 Ma to the present (**Figure 2.4**). Deering et al. (2011) proposed two different periods: 2 – 0.7 Ma, dominated by andesite volcanism, and 0.7 – present, dominated by rhyolitic volcanism within the central TVZ. Houghton et al. (1995) divided the central TVZ into three different periods: Period I, from

1.68 – 1.53 Ma, characterized by rhyolitic ignimbrites erupted from the Mangakino Volcanic Centre. Period IIA, from 1.21 – 0.89 Ma, was characterised by an intense episode of volcanism with the two largest ignimbrites in central Taupo, and a product of the Mangakino and Kapenga volcanic centres; Period IIB, from 0.77 – 0.68 Ma, represented by ignimbrites from the Kapenga Volcanic Centre. Period IIIA, from 0.34 – 0.32 Ma represented by ignimbrites from the Whakamaru Group; Period IIIB (0.28 – 0.15 Ma) characterized by ignimbrite eruptions from six caldera centres (Kapenga, Maroa, Okataina, Reporoa, Rotorua and Taupo), and period IIIC (0.065 Ma – Present) covering eruptions from the two centres at the northern and southern ends of the central TVZ.

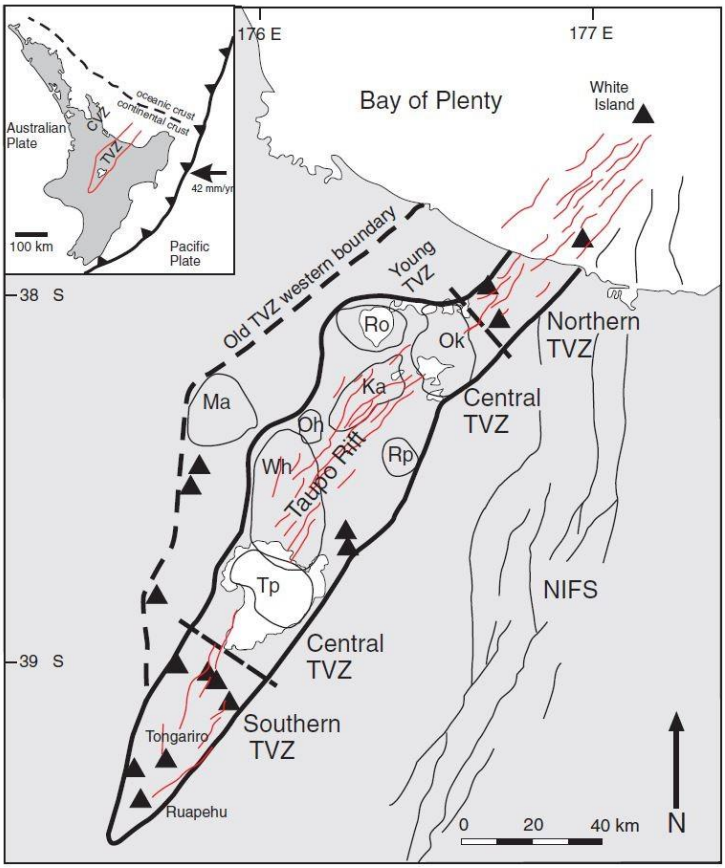

Figure 2.4: Regional map of the TVZ from Deering et al. (2011), insert showing its location in the North Island and the relationship to the subduction of the Pacific plate beneath the Australian plate. Regional map showing Old and Young TVZ from Wilson et al. (1995) and the present-day compositional divisions between the more andesitic southern and northern TVZ and the rhyolitic Central TVZ. Ma, Mangakino; Ka, Kapenga; Ro, Rotorua; Rp, Reporoa; Tp, Taupo; Wh, Whakamaru; Ok, Okataina; Oh, Ohakuri. CVZ, Coromandel Volcanic Zone; NIFS, North Island Fault System. Andesitic composite cones are shown as black triangles.

Geographically, the TVZ is divided into northern, central and southern segments (**Figure 2.4**), where the northern and southern segments are dominated by andesitic volcanism, and the central segment by rhyolitic volcanism (Wilson et al., 1995, Wilson et al., 1984). Volumetrically, the continental TVZ is dominantly felsic, with rhyolitic volcanism accounting for >95% of the total volume, dacitic volcanism <0.1%, and andesitic volcanism <3 %. In comparison, mafic volcanism represents only <0.1% (Cole, 1979, Gamble et al., 1990, Wilson et al., 1984).

2.4.1 Rhyolitic volcanism

Rhyolitic eruptions have been extensively studied in the TVZ due to their overwhelming volume when compared to dacitic, andesitic and basaltic eruptions. The Mangakino caldera, located in the western boundary and corresponding to the old TVZ period (**Figure 2.4**), includes andesitic and rhyolitic eruptions with ages of *c*. 1.6 Ma. The main eruption around this time corresponds to the Ngaroma Ignimbrite, which is partially welded, altered, fine-grained and has small plagioclase crystals (Briggs et al., 1993, Briggs et al., 2005, Houghton et al., 1995, Martin, 1961). This caldera became active again at *c*. 1.22 Ma with one of the biggest eruptions in the TVZ (**Figure 2.5**), producing the >300 km^3 pumice-rich, crystal-rich (feldspar, minor quartz and mafic crystals), non-welded Ongatiti Ignimbrite (Briggs et al., 1993, Houghton et al., 1995, Martin, 1961). Activity continued at *c*. 1.18 Ma with the formation of the welded Ahuroa Ignimbrite with 3 mm long plagioclase and minor hypersthene and magnetite crystals (Briggs et al., 1993, Martin, 1961). The last three eruptions of the Mangakino Volcanic Centre correspond to the hornblende crystal-rich pumice-rich Rocky Hill, the biotite pumice-rich Kidnappers and the Marshal eruptions with sparse plagioclase and hypersthene crystal fragments, with >300 km^3 of erupted material for the first, 1200 km^3 for the second and >50 km^3 for

the third event, being some of the biggest eruptions in the TVZ (Briggs et al., 1993, Cooper et al., 2016, Martin, 1961).

The Kapenga Volcanic Centre (**Figure 2.5**) became active at *c*. 0.9 Ma with the eruption of the andesitic and rhyolitic Tikorangi Ignimbrite (Hildyard et al., 2000). Activity continued with the Matahana, Rahopeka and Waiotapu ignimbrites, with plagioclase and pyroxene crystal fragments and traces of quartz and biotite, followed by a period of quiescence from *c*. 0.7 Ma to 0.25 Ma (Houghton et al., 1995, Martin, 1961). During this period of quiescence in the Kapenga Volcanic Centre, the Whakamaru Volcanic Centre became volcanically active between 0.34 and 0.33 Ma. The Whakamaru Group ignimbrites are lithic and plagioclase-quartz-rich with minor hypersthene, sanidine, magnetite, biotite and hornblende, and have a collective volume of >1000 km^3 (Brown et al., 1998, Houghton et al., 1995). After this activity, the Kapenga Volcanic Centre reactivated with the eruption of the Pokai and Ohakuri ignimbrites (Houghton et al., 1995), coeval to the activity of the Okataina Volcanic Centre with the eruption of the Matahina ignimbrite which contains quartz and hornblende (Cole et al., 2010, Martin, 1961).

The Reporoa caldera had its only major scale eruption at 0.23 Ma forming the Kaingaroa ignimbrite, in the east flank of the central TVZ, which has very sparse and small plagioclase fragments (Beresford & Cole, 2000, Martin, 1961). The Rotorua caldera was formed between 0.23 and 0.22 Ma by the eruption of the Mamaku Ignimbrite with high silica rhyolitic, rhyolitic and dacitic composition (Milner et al., 2003). According to Leonard (2003), the Maroa Volcanic Centre is also coeval with this activity, having the Korotai ignimbrite (0.28 Ma), Putauaki and Orokonui ignimbrites (0.27 and 0.25 Ma,

respectively) and the Atiamuri ignimbrite (0.23 Ma), with plagioclase, quartz, magnetite and hypersthene (Martin, 1961). Lastly, the early history of the Taupo Volcanic Centre (**Figure 2.4**, **Figure 2.5**), from 320 to 65 ka, is mainly represented by domes and two welded ignimbrites (Rangatira Point and Kawakawa Bay). The 320 km^3 non-welded Oranui ignimbrite, with quartz, plagioclase, orthopyroxene and hornblende, the world's largest 'wet' eruption, at *c*. 26.5 ka, marks a major change in the development of the system and formation of the modern Lake Taupo (Smith et al., 2005, Wilson, 2001). The post-Oranui activity comprises a sequence of 28 eruptions, 27 of them being represented by pyroclastic deposits and one being represented by lava extrusion beneath the lake (Sutton et al., 1995).

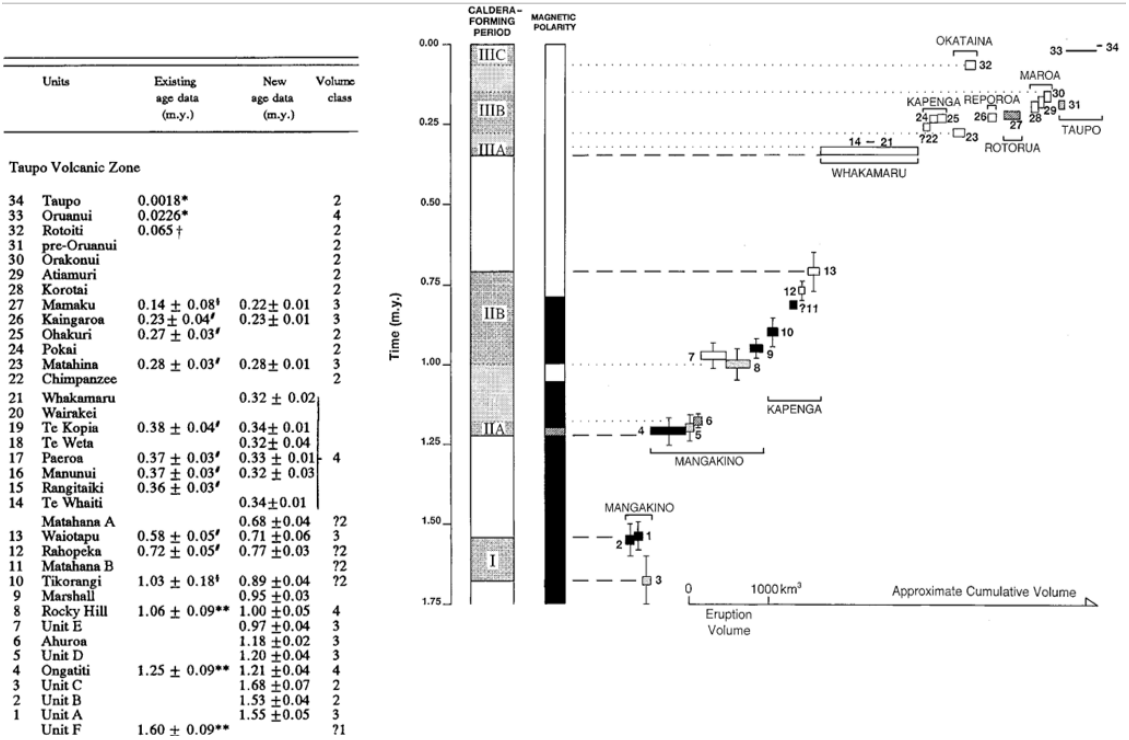

	Units	Existing age data (m.y.)	New age data (m.y.)	Volume class
	Taupo Volcanic Zone			
34	Taupo	0.0018*		2
33	Oruanui	0.0226*		4
32	Rotoiti	0.065†		2
31	pre-Oruanui			2
30	Orakonui			2
29	Atiamuri			2
28	Korotai			2
27	Mamaku	0.14 ± 0.08‡	0.22 ± 0.01	3
26	Kaingaroa	0.23 ± 0.04‡	0.23 ± 0.01	3
25	Ohakuri	0.27 ± 0.03‡		2
24	Pokai			2
23	Matahina	0.28 ± 0.03‡	0.28 ± 0.01	3
22	Chimpanzee			2
21	Whakamaru		0.32 ± 0.02	
20	Wairakei			
19	Te Kopia	0.38 ± 0.04‡	0.34 ± 0.01	
18	Te Weta		0.32 ± 0.04	
17	Paeroa	0.37 ± 0.03‡	0.33 ± 0.01	4
16	Manunui	0.37 ± 0.03‡	0.32 ± 0.03	
15	Rangitaiki	0.36 ± 0.03‡		
14	Te Whaiti		0.34 ± 0.01	
	Matahana A		0.68 ± 0.04	?2
13	Waiotapu	0.58 ± 0.05‡	0.71 ± 0.06	3
12	Rahopeka	0.72 ± 0.05‡	0.77 ± 0.03	?2
11	Matahana B			?2
10	Tikorangi	1.03 ± 0.18‡	0.89 ± 0.04	?2
9	Marshall		0.95 ± 0.03	
8	Rocky Hill	1.06 ± 0.09**	1.00 ± 0.05	4
7	Unit E		0.97 ± 0.04	3
6	Ahuroa		1.18 ± 0.02	3
5	Unit D		1.20 ± 0.04	3
4	Ongatiti	1.25 ± 0.09**	1.21 ± 0.04	4
3	Unit C		1.68 ± 0.07	2
2	Unit B		1.53 ± 0.04	2
1	Unit A		1.55 ± 0.05	3
	Unit F	1.60 ± 0.09**		?1

Figure 2.5: Summary diagram of the time-volume-source of major ignimbrites in the central TVZ from Houghton et al. (1995).

2.4.2 Dacitic and andesitic volcanism

Dacitic and andesitic volcanism is more spatially constrained than rhyolitic volcanism in the TVZ. The Edgecumbe volcano, in the northern portion of the TVZ, northeast of the Okataina Volcanic Centre, is a main cone surrounded by a series of flows and small domes with dacitic-andesitic compositions formed between 8530 and 1850 years BP (Carroll et al., 1997, Cole, 1979, Cole et al., 2001). These lavas are porphyritic with phenocrysts of plagioclase, orthopyroxene, clinopyroxene, titanomagnetite, quartz, biotite and amphibole (Carroll et al., 1997, Cole et al., 2001). Between Rotorua and Taupo, the hydrothermally altered Maungakakaramea (Rainbow Mountain) is formed by dacitic domes (Beresford & Cole, 2000). Between the Maroa and Taupo Volcanic centres, the Tauhara Volcanic Complex covers an area of more than 17 km and consists mainly of dacitic domes dated at *c*. 31 ka (Stipp, 1968). These domes show a coarsely porphyritic texture with plagioclase, orthopyroxene, clinopyroxene, hornblende and quartz phenocrysts with accessory olivine, biotite, apatite, titanomagnetite and ilmenite (Graham & Worthington, 1988). According to Thompson (1964), the Maunganamu or Mosquito Hill, south of Lake Taupo, is another dacitic dome.

Andesitic volcanism is currently restricted to the northern and southern portions of the TVZ (Wilson et al., 1995). However, at *c*. 1.9 Ma, Titiraupenga volcano was formed 20 km northwest of Lake Taupo, in the western margin of the old TVZ (Stipp, 1968). This volcano is comprised of low-Si strongly porphyritic andesites containing phenocrysts of augite, orthopyroxene, plagioclase and scarce olivine (Froude & Cole, 1985). Further southwards to Titiraupenga, the closely related Pureora andesite volcano has low-Si porphyritic andesites with plagioclase, augite and hypersthene as phenocrysts (Cole & Teoh, 1975). On the eastern side of the TVZ, Rolles Peak is an andesite with minor

plagioclase and clinopyroxene, rare orthopyroxene and hornblende phenocrysts (Graham & Worthington, 1988) with a K-Ar age of 712 ka (Tanaka et al., 1996). In the northern portion of the TVZ, the main andesitic volcanoes are Edgecumbe (see above) and White Island, the latter being New Zealand's most active volcano (Cole et al., 2000, Graham & Cole, 1991). In the southern portion of the TVZ lies the Tongariro Volcanic Centre which has four major andesitic massifs: Kakaramea, Pihanga, Tongariro and Ruapehu, and smaller cones and flows of Maungakatote, Pukeonake, Hauhungatahi and Ohakune (Cole, 1978). The Tongariro Volcanic Centre corresponds to the youngest and southernmost volcanic expression of the TVZ, with the Kakaramea, Ruapehu and Tongariro massifs having been active from *c.* 0.23 Ma to the present (Cole, 1978, Nairn et al., 1998, Stipp, 1968).

2.4.3 Basaltic volcanism

The occurrence of the typically monogenetic basaltic volcanism is mainly associated with faulting, close to the intersections with calderas and concentrated especially in the central portion of the TVZ (Gamble et al., 1993, Hiess et al., 2007). Phreatomagmatic eruptions are particularly important eruptive styles in the basaltic occurrences of the TVZ (Hiess et al., 2007, Kósik et al., 2016, Kósik et al., 2017). Mineralogy of the TVZ basalts can vary from having plagioclase, olivine, clinopyroxene, orthopyroxene in Pukeonake (Beier et al., 2017), olivine, clinopyroxene and orthopyroxene in Ohakune (Kósik et al., 2016), plagioclase, clinopyroxene and olivine in Te Hukui (Kósik et al., 2017), only olivine and plagioclase in Kakuki (Gamble et al., 1990), and even aphyric in Tarawera (Cole, 1970). Disequilibrium textures are also common in the mafic magmas of the TVZ in the form of corona-textured reaction rims or pyroxene overgrowth in olivines, and plagioclases with resorption surface textures (*e.g.*, Coote et al., 2018, Kósik et al., 2016, Law et al., 2021).

2.4.4 Petrogenesis and magma evolution - transcrustal models

Mafic volcanism, corresponding to high-alumina basalts, is thought to originate from a peridotitic mantle and in some cases interact with crustal rocks and melts (*e.g.,* Cole, 1973, Graham et al., 1995, Hiess et al., 2007). It has been proposed that these mafic magmas melt and assimilate the greywacke crust, producing rhyolitic magmas (**Figure 2.6**). This idea has been widely accepted to generate the magma evolution processes of the TVZ, where mafic magmatism interacts with crustal material and undergoes assimilation and fractional crystallisation to generate more evolved magmas, including andesites and basaltic andesites (*e.g.,* Gamble et al., 1990, Graham & Hackett, 1987). Thus, although making up <1% of the total erupted volume, mafic volcanism is thought to play a key role in the magma generation and evolution of the whole geochemical variation of the TVZ.

Early research in the trace element concentrations of dacites and rhyolites pointed to crustal anatexis and further fractionation, without mixing or evolving from a basaltic precursor (Reid, 1983, Reid & Cole, 1983). This idea became obsolete with the study of Nd-Sr isotopic ratios: Gamble et al. (1993) proposed that mafic magmas from the mantle undergo assimilation of the Torlesse Composite terrane, with improbable involvement of the Waipapa Composite terrane. This observation is consistent with the crustal structure underneath the TVZ where the Waipapa Composite terrane only covers the upper section of the crust, making assimilation unlikely (Price et al., 2015).

Figure 2.6: Schematic view of the TVZ from Hiess et al. (2007), showing the role of transcrustal processes in the magmatic generation and evolution.

Following this idea, McCulloch et al. (1994) proposed, based on Sr-Nd-Pb-O isotopes, that basalts ponding at the base of the TVZ lithosphere assimilate 15 – 25 % of Torlesse roof rock in the upper part of the magma chamber, undergoing independent fractionation from the lower part and generating rhyolitic magmas. This would require the partially contaminated magma to reach up to ~70 % of fractional crystallisation. This idea was also followed by Graham et al. (1995), who dismissed crustal anatexis alone and suggested that rhyolitic magmas can be generated by AFC of basaltic magmas. The concept of an 'extraction window' in crystal mushes has also been considered as a process occurring in the TVZ alongside crustal assimilation (Deering et al., 2011). Here, andesitic melts can be generated from a lower crustal mush in dry basalts by 50 – 80 % crystallisation of pyroxenes, plagioclase and Fe-Ti oxides; dacites can be produced by a similar extent of crystallisation but with hornblende instead. These dacitic melts can then rise into the upper crust and further crystallise by 50 %, forming a mush where large amounts of rhyolitic melts are stored.

Mixing of mafic minerals (olivine and pyroxene) with a felsic intra-crustal mush has also been invoked to generate intermediate samples with a high Mg# in the Tongariro Volcanic Centre, Southern TVZ (Beier et al., 2017, Conway et al., 2020, Svoboda et al., 2021). Magmas from the Okataina Volcanic Centre, Northern TVZ, show $\delta^{18}O$ homogeneity in quartz crystals despite their resorption textures, suggesting that these melts were derived from an isotopically homogeneous source, and indicating a basaltic parent with variable subduction flux and assimilation of >25 % of Torlesse-like metasediments (Sas et al., 2021a). Furthermore, Sr isotopic ratios in plagioclase crystals indicate that they were formed in intermediate melts rather than mafic melts, suggesting ~20 % of crustal contamination, with consistent relative contributions across the lifespan of the system (Sas et al., 2021b).

2.4.5 Slab interactions with the magma source

Magma generation in the TVZ is not restricted to transcrustal processes, but is also related to slab interactions with the mantle underneath the North Island, New Zealand. Gamble et al. (1993) noted an increase of 'subduction components' in the TVZ basalts with respect to the Tonga-Kermadec magmas, suggesting trace element input from the slab, also reflected in the radiogenic isotopic ratios. This input may come from the recycling of subducted sediments, with variations in the volcanoes reflecting variable efficiency of melt transfer in the crust (Gamble et al., 1996). These source variations are also supported by Graham et al. (1995), who observed that AFC does not reproduce the observed characteristics of the high-alumina basalts, indicating variations in the source region instead. A key finding of Gamble et al. (1996) is that the transition from oceanic crust to continental crust in the Kermadec-Hikurangi system does not correlate with a significant increase in trace elements compositions or isotopic ratios sensitive to crustal

contamination (**Figure 2.7**). These authors advocated for the idea that melting beneath the arc would be triggered by a combination of decompression and reactions between the slab and the mantle.

Figure 2.7: Plot of $^{208}Pb/^{204}Pb$ isotope variation versus latitude from Gamble et al. (1996), including basalts from the Kermadec Arc to the TVZ. Sediments and back-arc basalts are shown for comparison, as are the basalts from the back-arc regions. The dashed line marks the boundary between the continental and oceanic crust. Analytical information, such as error bars, is discussed in the source publication.

This model has also been supported by Rooney and Deering (2014), who showed that variable slab melt and fluid additions to the mantle can generate the characteristics found in the TVZ basalts, which would then undergo transcrustal AFC processing to generate the voluminous rhyolitic volcanism. Additionally, Waight et al. (2017) reported that TVZ Nd-Hf isotopic ratios cannot be explained using a single mantle-derived end-member with or without source and transcrustal addition. Thus, they proposed that variable degrees of source addition of bulk sediment or melts as well as variation in the mantle itself, plus 10 – 15 % AFC involving the Torlesse Composite terrane, are required to explain the variations seen in the TVZ.

2.5 Structure of the Hikurangi Plateau and its sedimentary cover

As stated in **section 2.1**, the Hikurangi Plateau (HP) and its sedimentary cover are being subducted beneath the east coast of New Zealand (**Figure 2.8**). In **section 2.3.5**, it was noted that the involvement of the subducting slab has been reported in the magma generation process not only in the TVZ, but along the whole Hikurangi Margin, including the Southern Kermadec arc. Thus, the characteristics of the HP are an important aspect influencing the magmas in this margin.

The HP is part of the *c.* 120 Ma combined Ontong Java/Manihiki/Hikurangi Plateau proposed by Taylor (2006) based on the chemical, physical and age similarities between the three plateaus. The HP and the Manihiki Plateau were separated by the Osbourn spreading centre, which was active between 120 and 86 Ma (Billen & Stock, 2000, Worthington et al., 2006). Subduction of the HP beneath the eastern Gondwana margin along the Chatham Rise started in the Late Cretaceous and caused the subduction to cease along this margin, as its unusual thickness caused coupling with the Gondwana margin (Davy, 2014, Davy et al., 2008, Reyners, 2013, Worthington et al., 2006). After a period of subduction quiescence, subduction of the HP recommenced at about 24-30 Ma, but this time beneath the east coast of the North Island, New Zealand, due to reconfiguration of the regional tectonics (Nicol et al., 2007, Seebeck et al., 2013). During its long history, the HP was covered with ~2 km of sediments from several possible different sources: the HP itself, the Chatham Rise, and the North Island and South Island of New Zealand. Davy et al. (2008) identified six lithological units in the HP using geophysical methods: the basaltic basement, cretaceous volcaniclastic sediments, volcaniclastic sediments with interbedded basalts that may correspond to the last pulses of the HP, Mesozoic laminar sediments, Cretaceous-Oligocene mudstones, and Cenozoic sediments.

Figure 2.8: Schematic view of the subduction of the Hikurangi Plateau from Reyners (2013). Light purple is the currently subducted part, dark purple is yet to be subducted. The fossil trench of subduction under the Gondwana margin is marked with grey. The red line denotes the Alpine Fault, and the blue line the Marlborough fault system. Cfz—Cook fracture zone; EB—Emerald Basin; HT—Havre Trough; LB—Lau Basin; NFoB—Norfolk Basin; NHT—New Hebrides Trench; NLB—North Loyalty Basin; PuT—Puysegur Trench; VMfz—Vening Meinesz fracture zone.

Recently, the International Ocean Drilling Program (IODP) Expedition 372B/375 took place at the Hikurangi Trough (**Figure 2.9**) with the drilling sites U1518, U1519, U1520 and U1526 (Saffer et al., 2019). Sites U1518 and U1519 were drilled in the accretionary wedge, while U1520 and U1526 were drilled in the HP, with the former site being drilled in a zone with a thicker sedimentary cover than the latter. This IODP Expedition identified six lithostratigraphic units from top to base: trench-wedge facies, Ruatoria slide, continued trench-wedge facies, pelagic facies, volcaniclastic facies and mixed lithologies. Description of these units is taken from Barnes et al. (2019), Saffer et al. (2019), Wallace et al. (2019) and presented with higher details relevant to sample selection in **Chapter 3**.

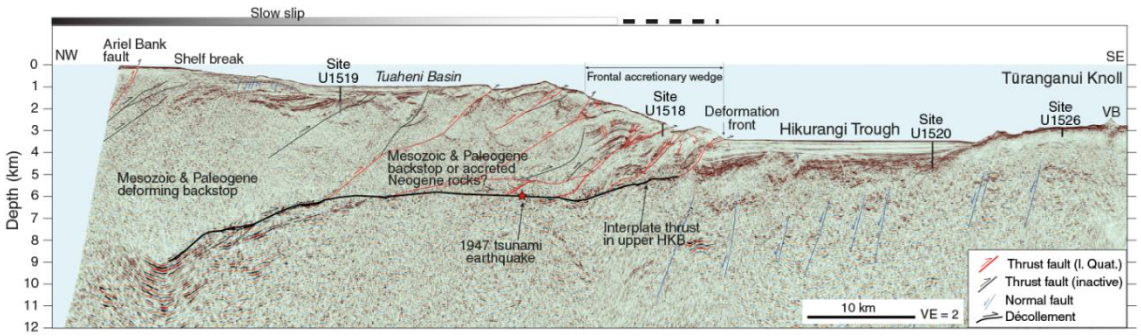

Figure 2.9: Depth-converted seismic profile after Saffer et al. (2019), showing locations and depths of sites drilled during Expedition 375. VB = volcanic cone. VE = vertical exaggeration.

Units I, II and III correspond to hemipelagic settling alternating with turbiditic currents, including material from the Ruatoria debris avalanche. These three units may correspond to the Cenozoic sediments identified by Davy et al. (2008). Unit IV corresponds to pelagic facies with an Early Paleocene – Late Miocene age, while Unit V corresponds to a volcaniclastic sequence with a Late Cretaceous age and Unit VI corresponds to mixed lithologies with an Early Cretaceous age. Unit IV may correspond with sequence Y, and Units V and VI may correspond to the basement and volcaniclastic units from Davy et al. (2008). Recently, Barnes et al. (2020) identified the formation of a *décollement* zone starting at ~800 meters below sea floor (mbsf) in site U1520. This *décollement* zone is of key importance, as all of the material below this depth is being subducted, while the

material above this zone is being accreted to the accretionary prism and may only be subducted by tectonic erosion.

Plank (2014) approximated the bulk composition of the sedimentary cover of the HP using Ocean Drilling Program (ODP) Leg 181 as one component to calculate an approximation to the global sediment input in subduction zones: Global Subducting Sediments II (GLOSS-II). Plank (2014) summarized that the Cenozoic sediment is carbonate-rich, while the Cretaceous sedimentary section has a composition akin to tholeiitic basalts possibly related to the HP. The subducting section and its bulk composition were taken as 50% sediment and 50% Hikurangi volcaniclastics. Newer approximations to the bulk composition of the subducting sediments may yield different elemental concentrations and isotopic ratios, as newer data have become available by employing IODP cores from Expedition 372B/375, which have different unit thicknesses and are located closer to the Hikurangi trench compared to ODP Leg 181.

Chapter 3 - Methodology

This chapter focuses on the methodology employed in this project. It starts with the considerations of sample selection for the Taupo Volcanic Zone (TVZ) eruptives and the accretionary prism and subducting plate sediments. It continues with thin section preparation as well as sample preparation for the analytical procedures, including powder preparation, glass disk preparation for major oxide quantification using X-ray fluorescence (XRF), chemical digestion for trace element concentration analysis by inductively coupled plasma mass spectrometry (ICP-MS), and ion exchange column chromatography in preparation for Pb-Sr-Nd-Hf isotopic analysis by multi-collector inductively coupled plasma mass spectrometry (MC-ICP-MS). Finally, details of the energy-constrained assimilation-fractional crystallization (AFC) modelling employing the Magma Chamber Simulator (MCS), as well as the calculation of bulk compositions of the tectonically eroded and subducting materials, are presented. Due to the organization of this thesis as a series of journal publications, the methods presented herein will be partially repeated in **Chapters 4, 5, and 6**.

3.1 Sample selection

Sampling of the TVZ targeted a diverse suite of volcanic samples concerning their geographical distribution, age, and geochemical characteristics (**Figure 3.1**). Samples were taken from the Northern, Central, and Southern TVZ, from the oldest to the youngest volcanic eruption sequences, and considering geochemical variations ranging from mafic to felsic compositions (**Table 3.1**). The Central and the Northern TVZ are represented by mafic, intermediate, and felsic samples, with different eruptive styles, such as monogenetic phreatomagmatic, volcanic cones, domes, lava flows, and pyroclastic deposits. The Southern TVZ samples are mostly represented by intermediate lava samples

and one felsic (dacitic) dome. Maungatautari at the western edge of the TVZ was also included for sampling as it was part of the subduction-related volcanic front at *c.* 2 Ma (Prentice et al., 2020), contemporary to the onset of TVZ formation. In total, 34 samples were taken comprising 12 mafic, 13 intermediate, and 11 felsic samples. Although the geochemical diversity of the TVZ is considered in this sample suite, the overwhelming volume of felsic eruptions is only represented by a third of the samples. This distribution of samples has the purpose of obtaining a balanced focus on all chemical variations within the TVZ, regardless of their volumetric proportion, to acquire a good overview of the compositional range and take into consideration all possible petrogenetic characteristics that can be determined from all three groups. All 34 samples were analysed for major and trace element compositions, while 29 samples were selected for additional Sr-Pb-Nd-Hf isotopic analysis. A general description of the full suite of volcanic samples is given in **Table 3.1.**

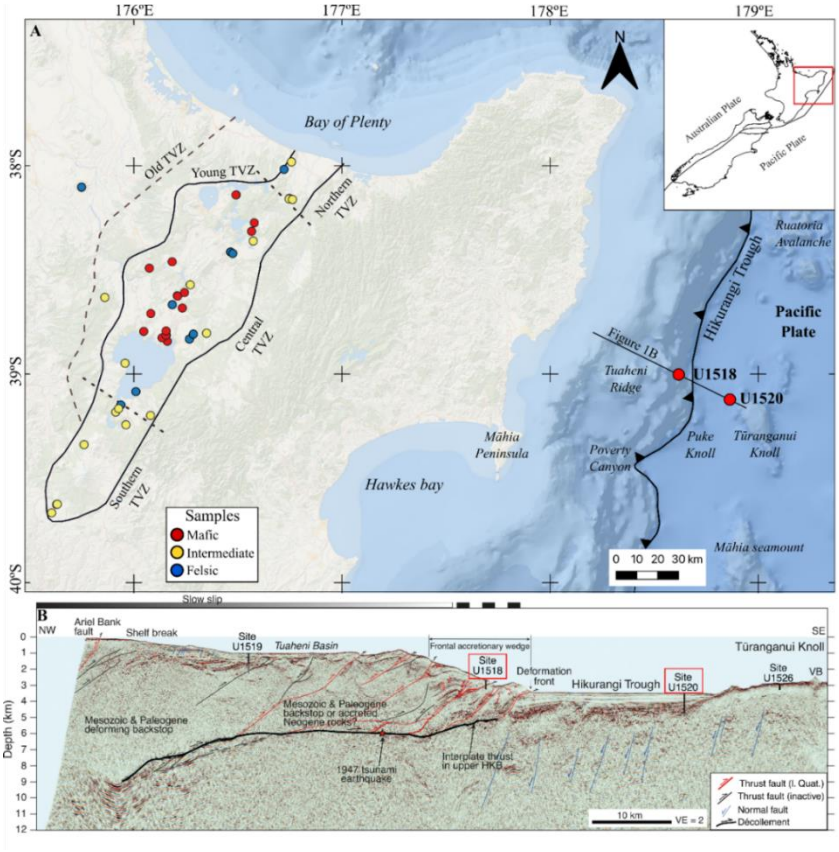

Figure 3.1: (A) Sample locations. Basemap from ESRI Ocean, overview sourced from QMap repository. Young and old TVZ, and southern, central, and northern TVZ after Wilson et al. (1995). Coordinate reference system WGS84/UTM zone 60S. (B) Depth-converted seismic profile 05CM-04 showing locations and depths of sites drilled during Expedition 375 and structural interpretation (Saffer et al., 2019). Red squares highlighting sites U1518 and U1520. VB = volcanic cone. VE = vertical exaggeration.

Table 3.1: Selected samples from the Northern, the Central, and the Southern TVZ. Maungatautari is not part of the TVZ.

Sample	Rock	Age	Comment
		Northern TVZ	
Matahi	Basaltic tephra	*c*. 42 ka	(Pullar & Nairn, 1972)
Manawahe	Dacitic dome	*c*. 0.75 Ma	(Nairn & Beanland, 1989)
Awakaponga	Andesitic flow	*c*. 0.75 Ma	(Nairn & Beanland, 1989)
Edgecumbe	Andesitic flow	*c*. 6 ka	(Carroll et al., 1997)
		Central TVZ	
Kakuki	Scoria	0.221 Ma	(Tanaka et al., 1996)
K-TRIG	Basaltic scoria	0.137 Ma	(Tanaka et al., 1996)
Ongaroto	Basalt	0.086 Ma	(Tanaka et al., 1996)
Acacia Bay	Basaltic tephra	0.1-0.2 Ma	(Wilson & Smith, 1985)
Kinloch	Basaltic lapilli tuff	< 9. 5 Ka	(Matheson, 2010)
Matipan	Basaltic lapilli tuff	-	-
Poihipi	Basaltic scoria	-	-
Tarawera	Basaltic tephra	A.D. 1886	Historic, (Walker et al., 1984)
Kaiapo	Basaltic scoria	-	(Matheson, 2010)
Tatua	Basalt	Late	(Houghton et al., 1987)
Rotokawau	Basaltic lapilli tuff	*c*. 3 ka	(Cole, 1973)
TramRoad	Basaltic lapilli tuff	-	-
Punatekahi	Basaltic scoria cone	45-300 ka	(Matheson, 2010)
Waimarino	Basalt	-	-
Karangahape	Andesite scoria cone	*c*. 290 ka	(Wilson et al., 1984)
Titiraupenga	Andesitic cone	1.89 Ma	(Stipp, 1968)
Rolles Peak	Andesitic cone	0.712 Ma	(Tanaka et al., 1996)
Kaharoa	Lapilli tuff	AD 1305	(Leonard et al., 2002)
Akatarewa	Lapilli tuff	-	-
Hipaua	Dacitic dome	58 ka	(Rosenberg et al., 2020)
Tauhara	Dacitic dome	58 ka	(Rosenberg et al., 2020)
Waikokomuka	Dacitic dome	-	-
Puketerata	Rhyolitic dome	14 ka	(Brooker et al., 1993, Kósik et al.,
Maungakakaramea	Dacitic dome	-	-
Motuoapa Dacite	Dacitic dome	*c*. 35 ka	(Kósik et al., 2021)
Motuoapa Rhyolite	Rhyolitic pyroclastic	*c*. 80 ka	(Kósik et al., 2021)
		Southern TVZ	
Te Ponanga	Andesite	Late	Inferred
Pukeonake	Scoria cone	Late	(Cole, 1978)
Ohakune	Scoria cone	Late	(Kósik et al., 2016)
Ohakune lakes	Andesite	Late	Inferred
Pihanga	Andesite	< 0.2 Ma	(Cole, 1978)
Kakaramea	Andesite	*c*. 0.2 Ma	(Stipp, 1968)
Maungamanu	Dacitic dome	-	-
Maungatautari	Dacite	1.8 Ma	(Robertson, 1983)

A total of 28 additional samples of subducting and accretionary prism sediments were acquired via drill core from cores U1518E and F, and U1520C and D (**Figure 3.1**) accessed through the International Ocean Discovery Program (IODP). Twelve samples were obtained from cores U1518E and F corresponding to the forearc units. Sixteen samples were obtained from cores U1520C and D corresponding to units from the subducting plate and are further differentiated depending on their location with respect to the *décollement* after Barnes et al. (2020). This is an important criterion for this project, as the material above the *décollement* would be accreted to the accretionary prism, while the material below the *décollement* would be subducted. Samples from core U1520D and three samples from core U1520C are located above the *décollement*, while the remaining samples from core U1520C are located below the *décollement* (**Table 3.2**).

Core U1518 unit descriptions are from Saffer et al. (2019). Unit IA has a thickness of 197.7 m (0 - 197.7 meters below the sea floor (mbsf)) and is composed of mud with silty sands as well as an upper ash layer, representing deposition in the presence of frequent turbidity currents alternating with hemipelagic settling. Unit IB has a thickness of 106.83 m (197.7 – 304.53 mbsf) and is composed of mudstone with thin siltstone interbedded with sandy siltstone, indicating less dominant turbidity currents alternating with hemipelagic settling during deposition. Unit II has a thickness of 65.87 m (304.53 – 370.40 mbsf) and is composed of mudstone with sparse siltstone, and represents deposition with hemipelagic settling and tectonic deformation. Unit IIIA has a thickness of 105.30 m (370.40 – 475.70 mbsf) and is composed of mudstone interbedded with sandy siltstone, indicating hemipelagic settling with deformation during deposition. Unit IIIB has a thickness of 16.56 m (475.7 – 492.26 mbsf) and is composed of mudstone interbedded

with sandy siltstone, indicative of deposition in the presence of turbidity currents alternating with hemipelagic settling.

Core U1520 unit descriptions are from Barnes et al. (2019). Unit I, a trench-wedge facies with a Quaternary age (<2.58 Ma), has a thickness of 110.5 m (0 – 110.5 mbsf) and is composed of silty clay to clayey silt interbedded with silt and sand, indicating turbidity current activity and hemipelagic settling during deposition. Unit II, the Ruatoria slide, has a thickness of 109.5 m (110.5 – 120 mbsf) and is composed of silty clay to clayey silt interbedded with silt, deposited at the distal edges of the Ruatoria debris avalanche. Unit III, a trench-wedge facies with a Quaternary – late Miocene age (<11.63 Ma), has a thickness of 289.82 m (220 – 509.82 mbsf) and is composed of mud and mudstone interbedded with silt, indicative of hemipelagic settling and dilute turbidity currents during deposition. Unit IV, a pelagic facies of early Paleocene to late Miocene age (66 - 5.333 Ma), has a thickness of 338.63 m (509.82 – 848.45 mbsf) and is composed of marl, calcareous mudstone and chalk, and represents pelagic sedimentation with airborne ash. Unit V, a volcaniclastic facies with a late Cretaceous age (100.5–66 Ma), has a thickness of 137.79 m (858.45 – 1016.24 mbsf) and is composed of volcaniclastic conglomerate, from the Hikurangi Plateau. Unit VI has mixed lithologies with a Cretaceous age (145 - 66 Ma), a thickness of 29.51 m (1016.24 – 1045.75 mbsf), and is composed of volcaniclastic conglomerate, siltstone, limestone, mudstone and basalt. The base of this unit corresponds with the bottom of the core and does not relate to the actual unit thickness. Units V and VI may correspond to basement and volcaniclastic units identified by Davy et al. (2008), with Unit IV correlating with their sequence Y, and units I, II and III correlating with their Cenozoic sediments.

Table 3.2: Selected samples from IODP cores. Numeric age is based on the fossils present in the samples; the period is present when no approximation is available. Position corresponds to forearc (FA), above *décollement* (AD) and below *décollement* (BD) based on Barnes et al. (2020). Rock description, age, unit and depth interval after Barnes et al. (2019), and Saffer et al. (2019).

Sample	Rock	Age (Ma)	Unit	Position	Depth interval
		U1518E			
26X 6W 69/71	Sandy silt	Quaternary	IA	FA	123 – 133
		U1518F			
5R 1W 12/14	Clayey silt	Quaternary	IB	FA	226 – 236
9R 5W 24/26	Sandy silt	0.63	IB	FA	264 – 274
11R 2W 47/49	Silty clay	Quaternary	IB	FA	284 – 294
12R 2 18/20	Silty clay	0.53 – 2.17	IB	FA	294 – 304
13R 1W 59/61	Clayey silt	Quaternary	II	FA	304 – 313
14R 1W 133/135	Clayey silt	Quaternary	II	FA	313 – 323
16R 4W 24/26	Silty clay	Quaternary	II	FA	332 – 342
19R 3W 33/35	Clayey silt	Quaternary	II	FA	360 – 370
24R 2W 66/68	Silty clay	Quaternary	IIIA	FA	408 – 418
27R 3W 8/10	Sandy silt	Quaternary	IIIA	FA	437 – 447
32R 7 29/31	Silty clay	0.126 – 0.53	IIIB	FA	485 – 495
		U1520D			
2H 7W 67/69	Silty sand	0.011	I	AD	14.15 – 15.15
4H 5W 104/106	Silty sand	0.011 – 0.29	I	AD	30 – 32.5
8H 5W 55/57	Sand	0.011 – 0.53	I	AD	68 – 69
14H 3W 54/56	Silty clay	Quaternary	II	AD	121 – 122
28F 4W 33/35	Sandy silt	Quaternary	III	AD	236.7 – 238
35X 1W 66/68	Silty clay	0.53	III	AD	366.6 – 368
44X 1W 83/85	Silty clay	0.53 – 0.62	III	AD	443.2 – 444.7
		U1520C			
5R 1W 72/74	Marl	10.66	IV	AD	670.4 – 671.9
5R 1W 105/107	Marl	10.66	IV	AD	670.4 – 671.9
13R 2W 51/53	Marl	24.67	IV	AD	748.6 – 750.1
19R 3W 34/36	Muddy chalk	54.4	IV	BD	807.6 – 809
21R 1W 71/73	Chalk	55	IV	BD	823.9 – 825.41
24R 1W 91/93	Silty claystone	< 72	V	BD	852.6 – 853.6
31R 1W 58/60	Coarse	Cretaceous	V	BD	919.7 – 920.6
41R 1W 119/121	Siltstone	100	VI	BD	1015.7 – 1017.2
44R 1W 116/118	Basalt	Cretaceous	VI	BD	1044.5 – 1045.45

Samples were selected to have a complete representation of the units present in the subducting sediments as well as the forearc sediments. All samples were analysed for their major element composition. Ten representative samples for each position (3 from the accretionary prism, 2 from above the *décollement*, and 5 from below the *décollement*) were selected for trace element concentration and Sr-Pb-Nd-Hf isotopic analysis.

3.2 Thin section preparation

Thin sections were made for all of the TVZ samples. The sample was cut to an appropriate size and then ground with grinding powders of 220, 400, 600, and 1000 grit. After grinding, all samples were surface impregnated with epoxy to prevent cracking and the formation of air bubbles. Highly vesicular or fragile samples were also fully impregnated and heated in a 45 ℃ oven overnight, then ground with 80, 120, 220, 400, 600, and 1000 grit grinding powders before surface impregnation. Excess epoxy was removed with 800 and 1200-grit sandpaper and the sample sections were mounted on a glass slide with epoxy, and dried overnight in a 45 ℃ oven. Samples were then ground with a grinding machine until they reached ~70 μm in thickness, or until plagioclase mineral grains yielded a yellowish interference colour. Afterwards, the sample sections were ground using 600 and 100-grit grinding powder until they had the desired thickness of ~30 μm. Each sample was observed using a petrographic microscope to evaluate its mineral and textural compositions.

3.3 Powder preparation

Fresh pieces of each sample were selected, and potentially contaminated outside surfaces, altered zones and xenoliths were removed. The resultant pieces (~600 g) were crushed in a jaw crusher and then dry-sieved to obtain the 2-4 mm particle size fraction. Pyroclastic samples did not require crushing and were directly dry sieved without crushing. Around 30 g of each sample was sub-sampled from the 2-4 mm particle size fraction, removing xenoliths and altered zones by hand-picking while inspecting under a binocular microscope. Samples were cleaned repeatedly with distilled water using an ultrasonic bath over 5 minutes intervals until the water became clear, requiring four to eleven washed, dependent on sample type (**Table 3.3**).

Table 3.3: Times each sample was put into the ultrasonic bath.

Samples	Number of times
Edgecumbe, Pukaterata, Rolles Peak, Andesite dyke, Kakaramea, Hipaua, Motuoapa Dacite	4
Tauhara, Manawahe, Awakaponga, Ohakune lakes	5
Ohakune 2, K-TRIG 1, Matipan, Punatekahi, Tramroad, K-TRIG 2, Kaipio, Titiraupenga, Waikokomuka, Motuoapa Rhyolite	6
Lake Rotokawau, Tatua, Onepu, Pihanga	7
Poihipi, Acacia Bay, Maungakakaramea, Maungamanu mosquito, Te Ponanga	8
Akatarewa, Kinloch, Ohakune 1	9
Tarawera, Maungatautari	11
Matahi	12

After cleaning, volcanic samples were dried overnight in a 60 ℃ oven, then powdered using an agate mortar and pestle, which was cleaned between samples using lab-grade quartz sand and ethanol. Mafic samples were processed first, and felsic samples last to minimize the risk of cross-contamination from different and contrasting compositions. IODP sediment samples were dried for two days in an oven to remove pore water and subsequently powdered using the same procedure as applied to the volcanic samples.

3.4 Whole rock major oxide analysis

Wavelength Dispersive X-ray Fluorescence (WD-XRF) is a technique used for the analysis of bulk specimens, mostly for the quantification of major element (Si, Na, K, Mg, Fe, Ti, Ca, P, and Mn) concentrations represented in oxide form, and some minor element (Rb, Sr, Y, Nb, Zr, Cr, Ni, Cu, Zn, Ga, Ba, Pb, Th, and U) concentrations if their levels are sufficiently high. First, samples are fused into glass discs and then loaded into the XRF instrument. Samples get excited by x-rays generated when the x-ray tube accelerates electrons and bombards them against a metal anode. This radiation causes ionization in the sample, which subsequently rearranges its electron structure and de-excites back to its base state. When this occurs, the irradiated sample emits fluorescence x-rays of energy characteristic of each element, which depends on if the vacancy has to be filled is in the K-, L-, or M- shells (**Figure 3.2**). Each incident photon

creates a current pulse, which is measured by the detector. The current value of a single pulse is proportional to the x-ray energy. The intensity of the fluorescent x-rays depends on the abundance of a given element in the sample. Thus, if the intensity and concentration of a standard sample are known, is possible to calculate the concentration of unknown samples after measuring their intensities and comparing them with the standard samples. This is done by employing a calibration curve based on several samples of known element concentration.

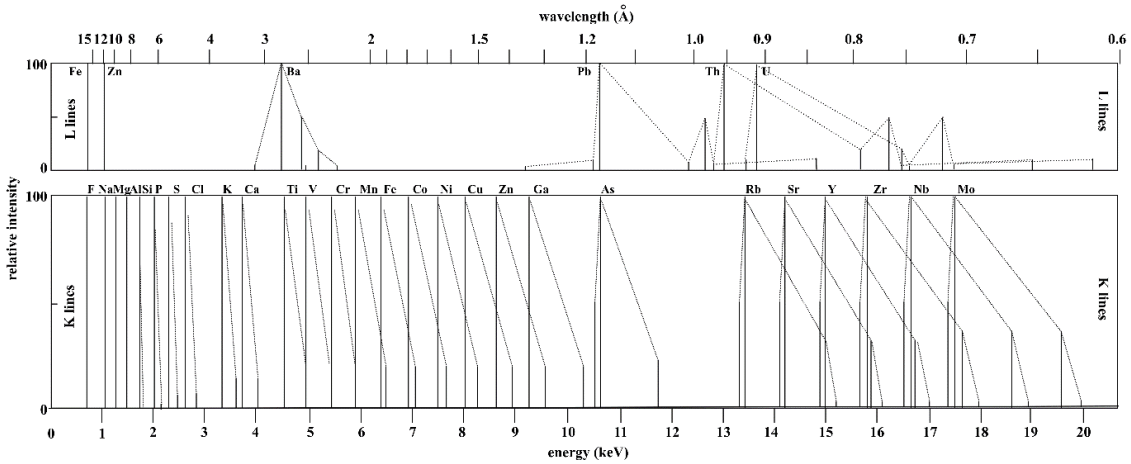

Figure 3.2: Diagram of the x-ray lines found in the spectrum of a rock sample in the region from 0-20 keV used to identify an element within the K- or L- series, after Potts (1987).

In this project, WD-XRF was employed to determine the wt.% of major oxides (SiO_2, Na_2O, K_2O, CaO, $Fe_2O_3^T$, MgO, TiO_2, Al_2O_3, MnO, and P_2O_5) in the samples. First, ~4 g of each sample powder was heated at 110 ℃ for 2.5 h and left in a desiccator overnight to evaporate interstitial moisture (H_2O^-). After this period, ~2 g was taken from each sample and weighed into ceramic crucibles, then heated at 900 ℃ for 3 h to promote oxidation, and re-weighed to obtain the loss of ignition (LOI) according to the following formula:

$LOI = 100\ (\frac{n_2 - n_3}{n_2 - n_1})$, where n_1= empty crucible, n_2= total mass of crucible + sample powder before heating, n_3= total mass of crucible + sample after heating.

After correcting for LOI, ~0.8 g of each oxidised sample was mixed with ~8 g (1:10 ratio) of 12:22 X-Ray flux (35.3 % Lithium Tetraborate and 64.7 % Lithium Metaborate), which facilitates sample melting. This mix was then melted with an XrFuse 2 electric fusion instrument in platinum crucibles (1050 °C, melting time: 3 min, shake time: 10 min, stand time: 10 s, stage 1 cooling time: 2 min, and stage 2 cooling time: 8 min). Crucibles were cleaned between samples with a 20 % citric acid solution for 10 minutes in an ultrasonic bath. Major elements were then analysed with an S8 Tiger 1kW WD-XRF spectrometer (Bruker-AXS, Germany), following routine techniques at Massey University, New Zealand. The internal standards Oreas-24c basalt and Oreas-24b granodiorite (OREAS, Australia) were used to ensure data quality during measurement. The relative uncertainty based on repeat measurements of these standards, reported as 1σ, is typically ±0.5-1 % for major oxides and better than ±3 % for minor oxides, except for P_2O_5 (±5-10 %).

3.5 Sample digestion for trace element concentration and Sr-Pb-Nd-Hf isotopic analysis

All samples were chemically processed within ISO 4 ducted laminar flow workstations housed in an ISO 5 metal-free cleanroom at the Centre for Trace Element Analysis, University of Otago, New Zealand. All reagents used (HF, HNO_3, and HCl) were purified in-house using Teflon and Quartz sub-boiling distillation, and ultra-high purity H_2O was dispensed from a Milli-Q Element water purification system (Millipore, Ltd, USA). Teflon vials (Savillex Ltd, USA) for sample digestion were acid-cleaned before use following standard in-house procedures. Approximately 0.5 g of each sample was weighed into 60 ml Teflon vials and then digested sequentially using 28 M HF, 7M HNO_3, then 6M HCl on a hotplate held at 110 °C, following routine procedures (*e.g.*, Druce et al., 2022, Stirling et al., 2007, Stirling et al., 2005, Stirling et al., 2006). Following acid digestion, the sample digests were weighed and transferred into 30 ml high-density

polyethylene (HDPE) bottles in preparation for further geochemical analyses. The international reference materials BHVO-2 (basalt), BCR-2 (basalt), AGV-2 (andesite), JR-2 (rhyolite), and JG-3 (granodiorite) (USGS, USA and GSJ, Japan) were digested following the same procedure as used for the sample unknowns to ensure data quality, alongside with total procedural replicates.

3.6 Trace element concentration analysis by ICP-MS

Inductively coupled plasma mass spectrometry is capable of quantifying the concentration of nearly every element from Li to U, except for Ar, N, and O which are present in high concentrations in the plasma and the atmosphere, and F and Ne, which cannot be ionized by the argon plasma that supports the instrument. ICP-MS is capable of measuring concentrations from less than 0.1 part per trillion (ppt) to percent levels, the latter with appropriate sample dilution. An ICP-MS consists of two main parts: the ICP, which is at atmospheric pressure, and the MS, which is in a vacuum chamber. At atmospheric pressure, the sample solution goes through a sample introduction system, which pumps it into a nebuliser, and converts it into a fine aerosol that then passes through a spray chamber to remove larger droplets. Fine aerosol droplets are carried by the Ar gas flow into a 10,000 K Ar plasma (ICP) inside a quartz torch, which causes the sample to evaporate and dissociate into individual atoms which are then ionised. The degree of ionisation of each element in the plasma is dependent on its ionization potential and the plasma temperature. Most elements are ionized under ICP conditions, but elements with very high ionization potentials, such as As and Se, remain partially unionised and thus have lower sensitivities and higher limits of detection (LOD). As the ICP is at atmospheric pressure and the MS is in a vacuum chamber, the ions must first pass through the vacuum interface, which consists of sampling cones, followed by a skimmer cone to extract ions

from the plasma and direct them into the high vacuum back end of the instrument. After this, and once inside the vacuum chamber, ion lenses focus the ions into a beam by applying a combination of positive voltage to repel positively charged ions and a negative voltage to attract the ions, which focus the ions into a beam. The beam is also separated from neutral particles and photons from the plasma, as they can cause a high background signal. This is achieved by deflecting the ion beam off the axis with low voltage, while the other uncharged particles continue in a straight line.

Significant spectral overlap in ICP-MS systems occurs when ions of an element of interest have the same mass-to-charge ratio (m/z) as ions of another element or molecular ions. For example, Fe and Ni have isotopes at a mass of 58 amu, causing an isobaric interference. This is addressed by measuring alternative isotopes that do not overlap with isotopes of other elements. In the case of molecular ions, for example, the combination of ^{40}Ar and ^{16}O forms a polyatomic ion with a mass of 56, overlapping with ^{56}Fe, a major isotope of iron. Furthermore, doubly charged elemental ions with the same m/z as the element of interest may also overlap. For example, doubly charged ^{150}Nd interferes with singly charged ^{75}As due to their identical m/z.

Collision/reaction cells (CRC) are often used to address these two cases of spectral overlaps. This consists of an ‘ion guide’, an octupole, in an enclosed chamber pressurised with a gas. The process for removing these interferences depends on the gas added to the chamber. In collision cell mode, the chamber is pressurized with a nonreactive gas, such as helium. As polyatomic ions and doubly charged ions are larger than their singly charged single-atom counterparts, they will collide more often with helium atoms, losing kinetic energy each time. This causes polyatomic ions to exit the chamber with lower

energy than the ions of interest and then are rejected from the ion beam by kinetic energy discrimination. In reaction cell mode, the chamber is pressurized with a reaction gas such as H_2 or O_2, among others. Here, a chemical reaction occurs between the ions and the reaction gas, to form an interference-free species. This, however, can also cause the formation of new species that may overlap with another element of interest. Thus, this mode is only employed when the interferences are predictable.

After limiting the overlapping interferences and thus maximising the accuracy of the measurement, the ions commonly go into a quadruple mass analyser to filter ions by m/z. Here, two pairs of rods with an electric field are configured to determine the mass of the ions that can travel along the axis. Thus, any ions with a different mass than the set mass are ejected from the ion beam. As ions reach the detector, they create a signal that is converted into an electrical current, with intensities given in counts per second (cps) and transformed by the instrument software to a concentration value by comparing the signal intensity to that of a calibration standard of known concentration.

Here, the trace element concentrations were determined using an ICP-MS fitted with a quadrupole mass analyser (Q-ICP-MS) using a 7900 instrument (Agilent Technologies, USA). Given the large concentration range of the quantified elements (0.7 – 1000 µg/g), two dilutions were gravimetrically prepared for each sample. Specifically, a 1:250 dilution was prepared for quantifying major element and higher-level trace element concentrations, while a 1:1000 dilution was prepared for lower-level trace element quantification (Sc, rare earth elements (REE), Hf, Ta, and W). Blanks followed the same procedure in the digestion process. Internal standards containing beryllium (Be), scandium (Sc), germanium (Ge), rhodium (Rh), indium (In), terbium (Tb), and bismuth

(Bi) were added online and used to correct for matrix effects and instrumental drift, as these elements have masses similar to those of the analytes. No collision/reaction gases were used for the measurement of Li and B, while H_2 mode was used for the quantification of ^{56}Fe and ^{78}Se, and He mode was used for the measurement of all other elements. A series of international reference materials comprising BHVO-2, BCR-2, AGV-2 (USGS, United States), JR-2, and JG-3 (GSJ, Japan) were analysed together with the samples to ensure data quality and reproducible results. All results are within 90% of the reported values. Total procedure replicates (3 digestions each for Kinloch, Motuoapa Dacite, and 1520C 24R 1W 91/93) were also used to ensure data quality, with concentrations being within errors. Values for LOD are 10 µg/g for As and Se, 5 µg/g for Ni, Cu, Rb, Sr, Zr, Cd, Sn, Sb, and Ba, 3 µg/g for V and Cr, 2 µg/g for Co, Y, Mo, Nb, 1 µg/g for Li, 0.5 µg/g for Cs, Pb, Th and U, 0.1 µg/g for Be and Ta, 0.06 µg/g for Sc, REE, Hf, Ta, and W.

3.7 Chemical preparation for Sr-Pb-Nd-Hf isotopic analysis

3.7.1 Sr and Pb chemical separation

Sr and Pb were separated from the matrix together using ion exchange chromatographic columns loaded with 250 µl of Sr-spec resin (100-150 µm) (Eichrom Technologies, USA). The procedure is represented in a simplified form in **Table 3.4**. Aliquots of the volcanic sample digests with enough ng of Sr and Pb to run several analyses if required (containing ~2000 ng and ~200 ng, respectively), were dried down and reconstituted with 1 ml of 7N HNO_3. Once loaded onto the column, the matrix elements were eluted using 1 ml of 7N HNO_3. Strontium was initially collected with 2.25 ml of 0.05 HNO_3, and Pb was subsequently collected with 4.25 ml of 8N HCl. A double pass of this procedure was required to extract purified Sr and Pb from the TVZ volcanic samples. The same method

was employed for the IODP sediment samples, but in this case, 3N HNO_3 was used instead of 7N HNO_3, as a triple pass was required to obtain adequate separation and purification of Sr and Pb, due to the higher concentration of K in these samples, which is an important interference of the ion exchange procedure. The Sr and Pb fractions were dried down and redissolved in 1 ml of 2% v/v HNO_3 in preparation for MC-ICP-MS analysis. The international reference materials BHVO-2, BCR-2, AGV-2 (USGS, United States), JR-2, and JG-3 (GSJ, Japan) were employed to ensure data quality, while total procedure replicates (3 digestions each for Kinloch, Motuoapa Dacite, and 1520C 24R 1W 91/93) were used to assess external precision. Total procedural blanks are <60 pg for Sr and <10 pg for Pb, negligible compared to the 300 ng measured for Sr and 10 ng for Pb.

Table 3.4: Simplified procedure of Sr and Pb chromatographic separation, in parenthesis is the alternative procedure for the sediment samples.

Procedure	Eluting reagent	Eluting volume (ml)
Loading sample	7N HNO_3 (3N HNO_3)	1
Rinsing	7N HNO_3 (3N HNO_3)	1
Eluting Sr, collect	0.05N HNO_3	2.25 (0.25 + 2)
Eluting Pb, collect with Sr	8N HCl	4.25 (0.25 + 4)
Dry		
Loading sample	7N HNO_3 (3N HNO_3)	1
Rinsing	7N HNO_3 (3N HNO_3)	1
Eluting Sr, collect	0.05N HNO_3	4.25 (0.25 + 4)
Eluting Pb, collect	8N HCl	4.25 (0.25 + 4)
Dry		
Load Pb elution	7N HNO_3 (3N HNO_3)	1
Rinsing	7N HNO_3 (3N HNO_3)	1
Rinsing	0.05N HNO_3	4.75 (0.25*3 + 4)
Eluting Pb, collect	8N HCl	4.25 (0.25 + 4)

3.7.2 Nd chemical separation

A two-step chemical separation procedure was used to separate Nd from the sample matrix, following a protocol modified from Baker et al. (2002), Pin and Zalduegui (1997), presented in **Table 3.5**. The first step uses a silica glass column filled with 4.5 ml of 100 – 200 µm AG50WX8 resin (Eichrom Technologies, USA). An aliquot of the sample digest equivalent to enough ng to run several analyses if required (containing ~1000 ng of Nd) was evaporated to dryness, redissolved in 2N HCl, and loaded onto the resin. After

loading, 36 ml of 2N HCl followed by 30 ml of 2N HNO_3 was used to respectively elute the major elements and some trace elements (*e.g.*, Rb, Ba, and Sr). The REEs, including Nd, were subsequently collected with 9 ml of 4N HCl and 9 ml of 6N HCl. Both acids are required to maximise the elution of Nd. These elutions are dried down together and reconstituted in 0.2 ml 0.25N HCl in preparation for the second-stage column procedure for purification of the REE fraction.

The second column step employed custom-made Teflon columns loaded with 670 µl of LN spec resin (50 – 100 µm) (Eichrom Technologies, USA). These second-stage columns were made specifically for this project, and thereby required calibration to ensure optimal purification and recovery of Nd. For each column, the calibration procedure involved collecting aliquots every 0.5 ml during the 0.25N HCl elution step to produce elution curves for La, Ce, Pr, and Nd (**Figure 3.3**). The elements Eu and Sm are eluted with 0.75N HCl, however, these elements were not of interest for this study and thus the 0.75N HCl aliquot was not collected. As Sm overlaps in mass with Nd, any residual Sm remaining in the Nd fraction was monitored during the calibration procedure to ensure its concentration was minimal and would not give rise to unwanted isobaric interferences during Nd isotopic measurement.

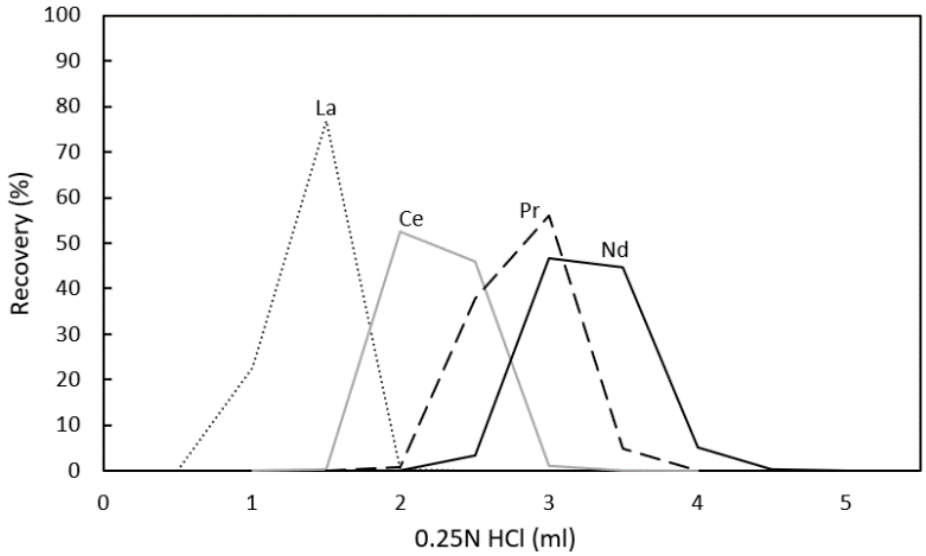

Figure 3.3: Example of the column calibration recoveries for these columns, procedure after Pin and Zalduegui (1997); note that praseodymium and cerium cannot be fully separated from neodymium using this method, however, praseodymium does not cause interference issues and cerium does not interfere with the isotopes of interest.

The REE sample fractions were loaded onto the calibrated and conditioned LN-spec columns using 0.2 ml of 0.25N HCl. The LREE (La, Ce, and Pr) were eluted with 2 or 2.5 ml of 0.25N HCl, depending on the calibration of the column. The Nd fraction, also containing Pr and Ce, was collected using 3.5 ml of 0.25N HCl. The columns were washed with 15 ml of 6N HCl in between uses. As Pr and Ce cannot be quantitatively separated from the Nd fraction, a second pass of the LN-spec columns was required to minimise the proportions of these elements in the final Nd aliquot. The international reference materials BHVO-2, BCR-2, AGV-2 (USGS, United States), JR-2, and JG-3 (GSJ, Japan) were employed to ensure data quality, while total procedure replicates (3 digestions each for Kinloch, Motuoapa Dacite, and 1520C 24R 1W 91/93) were used to assess external precision. Procedural blanks yielded <50 pg, negligible compared to the 30 ng used for the measurement.

Table 3.5: Ion exchange column procedure for Nd, modified after Baker et al. (2002), Pin and Zalduegui (1997). *For the second step (LN spec columns), a few columns had delayed recoveries and thus Nd elution occurred 0.5 ml of 0.25N HCl afterwards.

Procedure	Eluting reagent	Eluting volume (ml)
Column with AG50WX8 resin		
Conditioning resin	2N HCl	16 (1 + 15)
Loading sample	2N HCl	3 (1*3)
Rinsing	2N HCl	3 (1*3)
Removing matrix	2N HCl	33 (18 + 15)
Removing matrix	2N HNO_3	30
Eluting REE, collect	4N HCl	9
Eluting REE, collect	6N HCl	9
Washing resin	~6N HCl	45 (15*3)
Dry		
Change to LN spec column		
Conditioning resin	0.25N HCl	5 (1 + 4)
Load REE elution	0.25N HCl	0.2 (0.1*2)
Rinsing	0.25N HCl	0.3 (0.1*3)
Removing matrix	0.25N HCl	2 or 2.5*
Eluting Nd, collect	0.25N HCl	3.5
Washing resin	~6N HCl	15 (5 + 10)
Repeat LN spec column		

3.7.3 Hf chemical separation

Hafnium was separated and purified from the sample matrix using custom-made Teflon columns loaded with 1 ml of Ln spec resin (100-150 µm) (Eichrom Technologies, USA), following a procedure modified from Münker et al. (2001), and presented in **Table 3.6**. As these columns were made specifically for this project, they had to first be calibrated to ensure optimal recovery and purification of Hf. Column calibration is presented in **Figure 3.5**. An aliquot of each sample digest with enough material to run several analyses if required (containing ~200 ng of Hf), was dried down and reconstituted with 5 ml of 3N HCl admixed with 0.1N ascorbic acid. LN-spec resin is known to preferably absorb Fe^{3+} when in 3N HCl and this can overload the resin and cause the element of interest (Hf) to not be retained on the resin due to a lack of available sites. This is avoided by the addition of ascorbic acid acts to reduce Fe^{3+} to Fe^{2+}, facilitating its elution from the column alongside other matrix elements. The heavy rare earth elements (HREE), and especially Lu and Yb which have isobaric interferences with ^{176}Hf, were then eluted from the column with 3N HCl and 6N HCl, respectively. Titanium creates a non-mass-dependent fractionation that cannot be corrected using the exponential mass

fractionation law during Hf isotope ratio measurement, causing significant shifts in composition towards anomalous values when Ti/Hf is >10 (**Figure 3.4**). Therefore, Ti was subsequently eluted with an aqueous solution of 0.09 citric acid (HCit) - 0.4N HNO_3 - 1 wt% H_2O_2 while retaining Hf on the resin.

Finally, Hf was collected using 6N HCl + 0.4N HF and the columns were washed using 2N HF in preparation for ion exchange processing of the next samples. Due to the matrix of the samples here analysed, up to three ion exchange column passes using the above-described procedure were required to fully elute Ti and minimise the amount of Yb and Lu eluted together with Hf. The international reference materials BHVO-2, BCR-2, AGV-2 (USGS, United States), JR-2, and JG-3 (GSJ, Japan) were employed to ensure data quality, while total procedure replicates (3 digestions each for Kinloch, Motuoapa Dacite, and 1520C 24R 1W 91/93) were used to assess external precision. Procedural blanks yielded <60 pg, negligible compared to the 30 ng used for the measurement.

Figure 3.4: $^{176}Hf/^{177}Hf$ isotopic ratio for a standard solution at different Ti abundances showing that Ti/Hf greater than 10 in the analyte cause a bias of corrected isotope ratios. Figure from Münker et al. (2001).

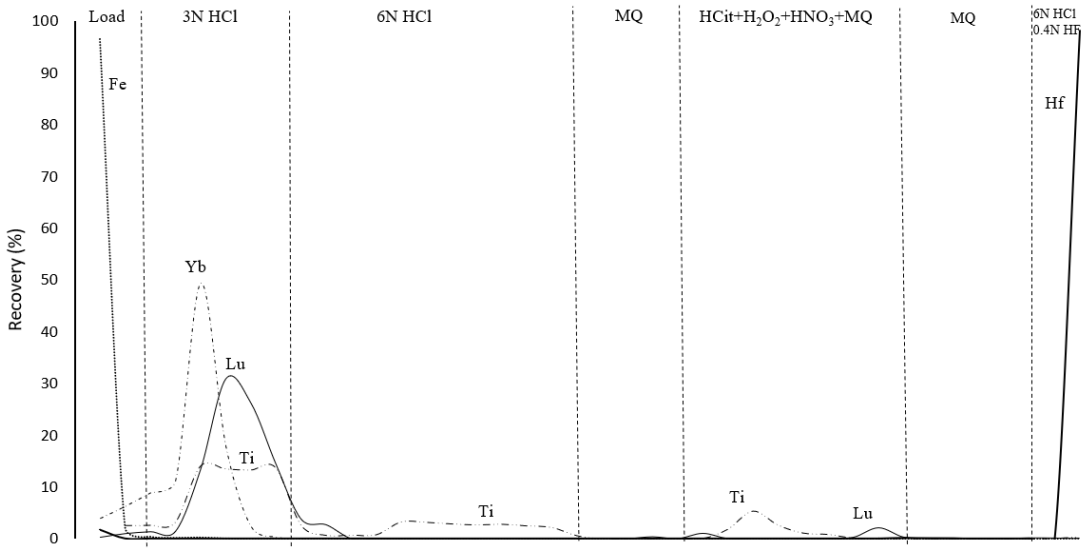

Figure 3.5: Example of an average column calibration recoveries for these columns, procedure is modified after Münker et al. (2001).

Table 3.6: Column chemistry procedure to separate Hf, after Münker et al. (2001).

Procedure	Eluting reagent	Eluting volume (ml)
Conditioning resin	3N HCl	5
Loading sample	3N HCl + 0.1M ascorbic	5
Removing matrix	3N HCl	20 (2*10)
Eluting HREE (Lu – Yb)	6N HCl	40 (4*10)
Rinsing HCl	MQ H_2O	10 (2*5)
Eluting Ti	HCit + conc. HNO_3 + H_2O_2 + MQ H_2O	40 (4*10)
Rinsing H_2O_2+ HNO_3	MQ H_2O	10 (2*5)
Eluting Hf, collect	6N HCl + 0.4N HF	12
Washing resin	2N HF	15 (3*5)
Second & third pass		
Rinsing 2N HF	MQ H_2O	15 (3*5)
Conditioning resin	3N HCl	5
Loading sample	3N HCl	5
Removing matrix	3N HCl	20 (2*10)
Eluting HREE (Lu – Yb)	6N HCl	30 (3*10)
Rinsing HCl	MQ H_2O	10 (2*5)
Eluting Ti	HCit + conc. HNO_3 + H_2O_2 + MQ H_2O	30 (3*10)
Rinsing H_2O_2+ HNO_3	MQ H_2O	10 (2*5)
Eluting Hf, collect	6N HCl + 0.4N HF	12
Washing resin	2N HF	15 (3*5)

3.8 Sr-Pb-Nd-Hf isotopic analysis by MC-ICP-MS

Multiple-collector ICP-MS (MC-ICP-MS) allows for the measurement of the isotopic ratios of the metallic elements with high levels of precision. The process of ionisation is similar to ICP-MS, but the quantification of multiple isotopes at the same time gives rise to very high precision, allowing for measuring interferences at the same time as the isotopes of interest. Samples are diluted accordingly into a low-concentration acid,

typically 2% HNO_3, which is then introduced into the mass spectrometer using a desolvating nebuliser (DSN) to produce a dry aerosol. When the DSN is employed, this results in a 'dry plasma', while when it is not employed it results in a 'wet plasma'. The use of the DSN increases the sensitivity of the instrument, thus it is not necessary when the concentration of the element of interest is high but is useful when the concentration of the element of interest is lower. Once ionised in the 10,000 K argon plasma, ions are extracted from the plasma through the sample and skimmer cones by continuously and homogenously transporting the ions into the high vacuum section of the instrument. Here, isotope mass fractionation occurs due to heavier isotopes preferentially passing through the skimmer cone when compared to lighter isotopes that are easier to deflect off-axis. This fractionation process is mass-dependent and needs to be corrected for by using empirically derived mass fractionation laws. The ion beam is further focused by lenses with differential voltages and accelerated before they enter the electrostatic analyser (ESA), which works as an energy filter that disperses ions with respect to ion energy. Once the ions reach the magnetic sector, they are dispersed based on energy and mass allowing ions with different masses to hit separate Faraday collectors simultaneously. Similar to ICP-MS, when these ions reach the detectors, they create a signal that is converted into an electrical current with an intensity that is proportional to the abundance of each isotope, allowing the measured isotope rations to be obtained.

The measured isotope ratios need to be corrected for instrumental mass fractionation by using the exponential law: $\frac{X_M}{X_T} = \frac{R_M}{R_T}^a$, where X and R are the isotopic ratios of masses m_1/m_2 and m_3/m_4, respectively. M refers to the measured isotope ratio, T refers to the true unfractionated isotope ratio, and $a = \ln(m_3/m_4)/\ln(m_1/m_2)$. Typically, m_1/m_2 corresponds to a naturally stable known isotopic ratio that is used to correct for mass fractionation by

‘internal normalisation’. If the measured element does not have a naturally occurring stable isotopic ratio, another non-interfering element with similar behaviour and with a known stable isotopic ratio needs to be added before measurement to correct by ‘external normalisation’. Furthermore, any spectral interferences need to be corrected for. Although interferences can be minimised in ion exchange column chromatography during chemical preparation, residual interfering elements may remain in the sample analyte. They are monitored during analysis by measurement of a non-interfering isotope of the interfering element, then correcting for their contribution to the isotopes of interest according to their relative abundances. These corrections allow the ‘true’ isotopic ratios to be quantified and normalised to the primary standard if required. The reliability of the results is then verified by comparing the isotope ratios obtained for internationally recognised reference materials and well-characterised secondary standards with their accepted values. Repeat analyses of samples, reference materials, and standards allow for an assessment of external precision in relation to internal precision.

All Sr-Pb-Nd-Hf isotopic analyses were performed by MC-ICP-MS at the Centre for Trace Element Analysis, University of Otago, New Zealand employing a Nu Plasma-HR instrument (Nu Instruments Ltd, UK).

3.8.1 Sr isotopic analysis

After the Sr chemical separation process, samples were further diluted with 2% HNO_3 to contain 300 ng/ml. Samples were analysed in ‘wet plasma mode. The National Institute of Standards and Technology (NIST) 987 primary standard and the in-house High Purity Standard (HPS) secondary standard were measured at the beginning and end of the analytical session, and within-run, between every six analyses of the sample unknowns

and reference materials. All $^{87}Sr/^{86}Sr$ ratios were corrected for instrumental mass fractionation using 'internal normalisation' based on an $^{86}Sr/^{88}Sr$ ratio of 0.1194 and the exponential mass fractionation law (Habfast, 1998, Hart & Zindler, 1989), as well as for potential isobaric interferences from Kr and Rb. All $^{87}Sr/^{86}Sr$ results were normalised to the NIST 987 Sr reference ratio of 0.710248 (McArthur et al., 2001). In-house secondary standards comprising *Tridacna* (sea clam) carbonate and HPS solution were used together with the USGS and GSJ reference materials to monitor analytical performance. Uncertainties are propagated using the external precision of the HPS secondary standard. Reference materials and total procedural replicates are reported in **Appendix A, Figure 3.6** and **Figure 3.7**. Estimates of reproducibility of Sr isotope analyses are based on replicate analyses of standard SRM987 yielding $^{87}Sr/^{86}Sr$ = 0.710247 0±0.000013 (2 SD, n = 18).

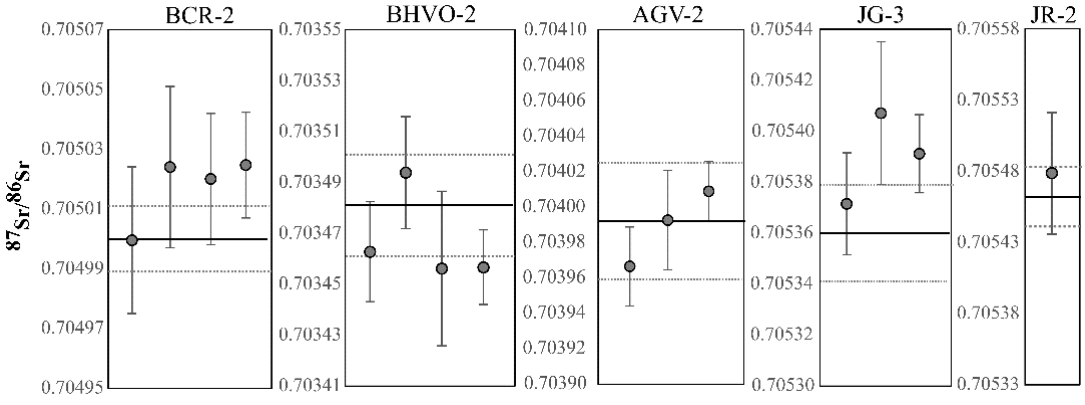

Figure 3.6: Reference materials compared to $^{87}Sr/^{86}Sr$ reported ratios. BCR-2, BHVO-2, and AGV-2 ratios are from Weis et al. (2006), ratios for JG-3 are from Miyazaki and Shuto (1998), and JR-2 ratios are from Li et al. (2012).

3.8.2 Pb isotopic analysis

Unlike Sr, Nd, and Hf, Pb does not have a natural stable isotope ratio, and thus instrumental mass fractionation needs to be corrected for using 'external normalisation' by adding thallium (Tl) into the analyte in a known proportion. Thallium is used for normalisation purposes because it undergoes a similar fractionation as Pb due to their

close masses, and it has a stable isotope ratio, $^{205}Tl/^{203}Tl$. All samples were diluted to give 10 ppb of Pb, and the NIST 997 Tl standard was admixed to the Pb fraction before analysis to give 2 ppb of Tl. Samples were analysed in dry plasma mode. Unknown samples were analysed together with the primary standard NIST 981 Pb and the secondary standard HPS at the beginning and end of each analytical session, and within-run between every four samples and reference materials. The measured $^{206}Pb/^{204}Pb$, $^{207}Pb/^{204}Pb$, and $^{208}Pb/^{204}Pb$ ratios were corrected for instrumental mass fractionation using Tl normalisation adopting a true $^{205}Tl/^{203}Tl$ ratio of 2.3875 for NIST 997 Tl (Belshaw et al., 1998). All ratios were then normalised to the known Pb isotope ratios for NIST 981 known ratios of $^{206}Pb/^{204}Pb$ 16.9406 ± 0.0003, $^{207}Pb/^{204}Pb$ 15.4957 ± 0.0002, and $^{208}Pb/^{204}Pb$ 36.7184 ± 0.0007 after Yuan et al. (2016). Repeat analyses of the in-house HPS secondary standard were used to perform error propagation after normalisation. The international reference materials BHVO-2, BCR-2, AGV-2 (USGS, United States), and JR-2 (GSJ, Japan) were used to monitor the veracity of the analyses, and all gave Pb isotope ratios that overlap with reported values, within error (**Appendix A**, **Figure 3.8**). Total procedural replicates (3 digestions each for Kinloch, Motuoapa Dacite, and 1520C 24R 1W 91/93) were used to assess external precision (**Appendix A**, **Figure 3.7**). The 2SE uncertainties include the analytical uncertainties of the sample and normalising standards.

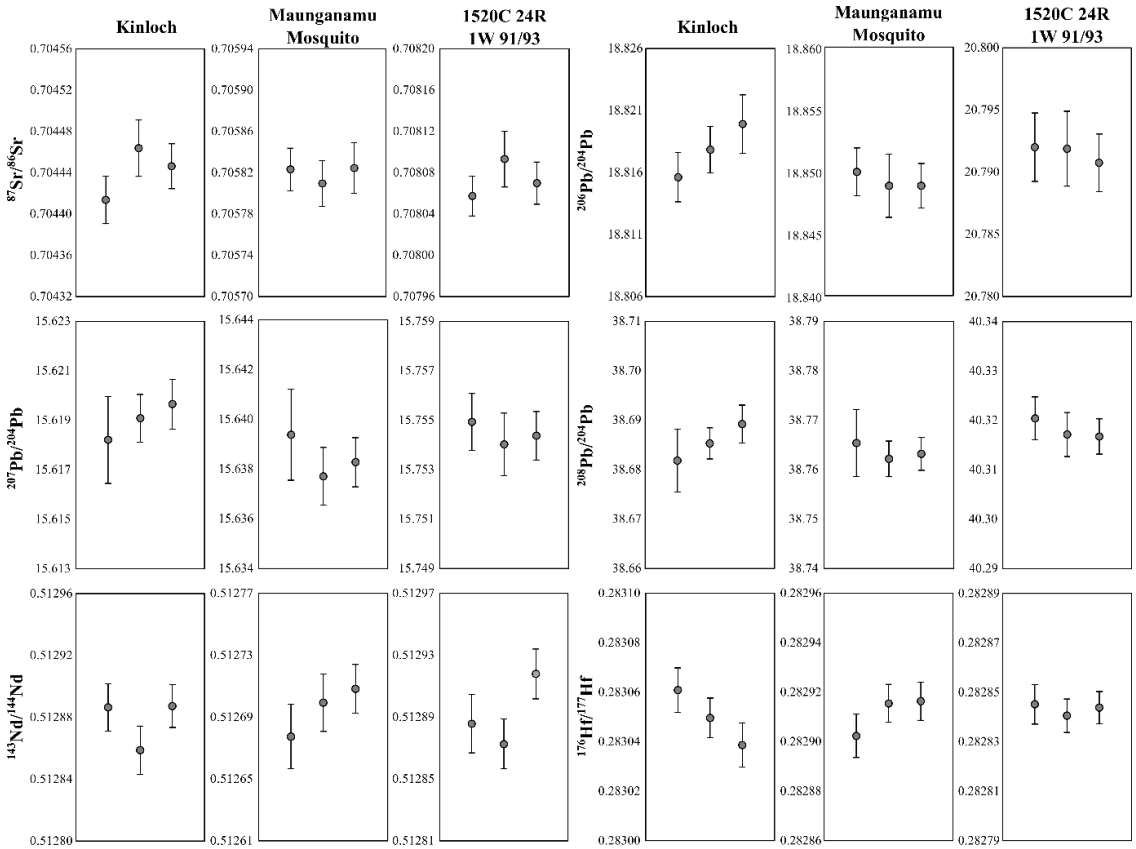

Figure 3.7: Total procedure replicates for Sr-Pb-Nd-Hf analyses using three different digestions of three different samples: One mafic (Kinloch), one intermediate-felsic (Maungamanu mosquito), and one of the IODP samples (1520C 24R 1W 91/93).

In this study, the previously reported Pb isotope ratios for the TVZ from Gamble et al. (1996), Price et al. (2012), Sas et al. (2021b), and Shane et al. (2017) were re-normalised to the NIST 981 Pb standard to allow for direct comparison of the results, including those of the Torlesse subterranes after Price et al. (2015) and Rumble IV after Gamble et al. (1996) (see **Appendix A**). The individual errors reported for the samples are comparable to those of Sas et al. (2021b), while the other studies employed general uncertainty estimates that are larger than the individual errors here presented. Estimates of reproducibility of Pb isotope analyses are based on replicate analyses of standard Pb981 yielding $^{208}Pb/^{204}Pb$ = 36.7184±0.0032, $^{207}Pb/^{204}Pb$ = 15.4957±0.0013, and $^{206}Pb/^{204}Pb$ = 16.9406±0.0012 (2 SD, n=20).

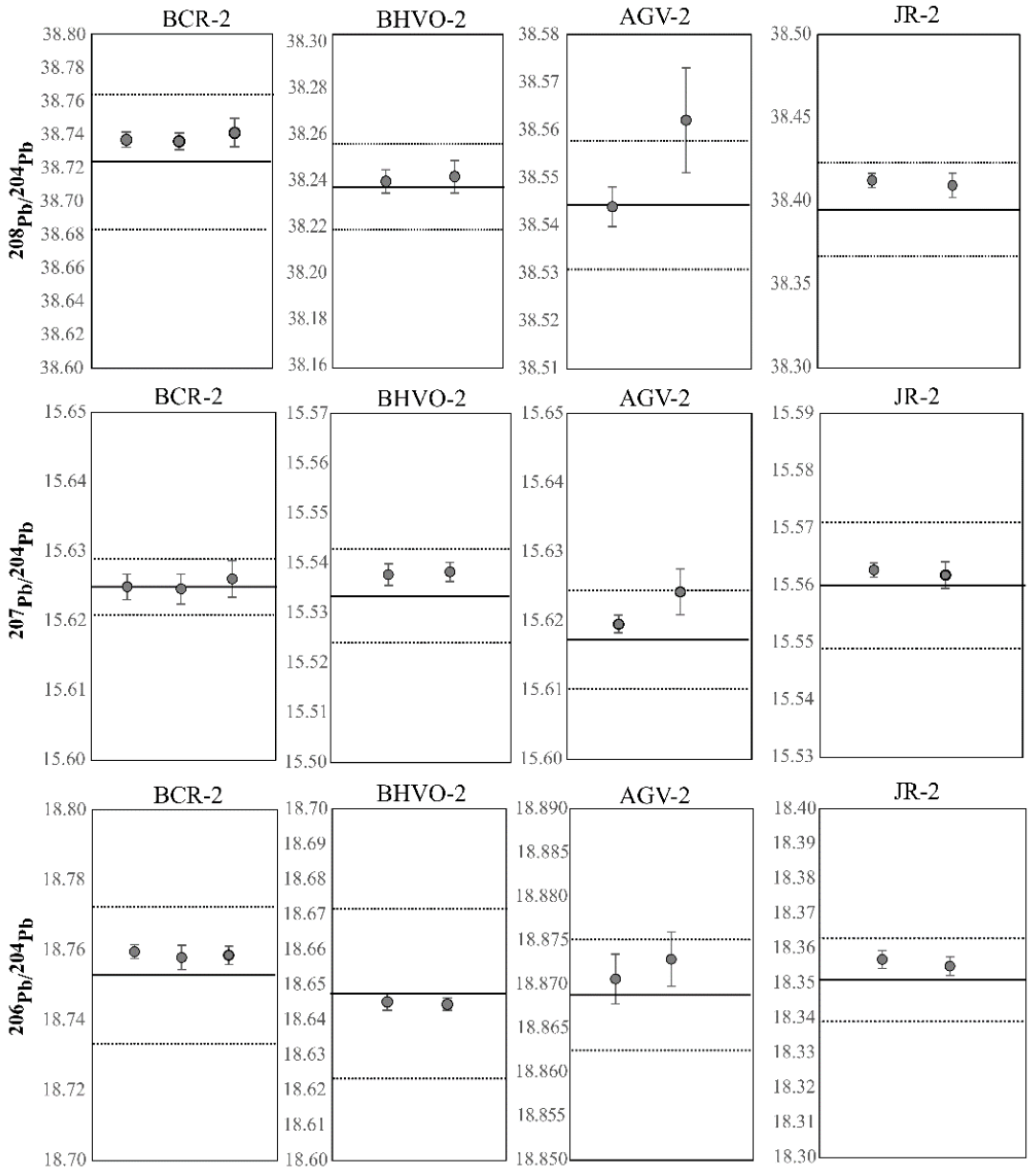

Figure 3.8: Reference materials compared to $^{208}Pb/^{204}Pb$, $^{207}Pb/^{204}Pb$, and $^{206}Pb/^{204}Pb$ reported ratios. BCR-2, BHVO-2, and AGV-2 ratios are from Weis et al. (2006), and JR-2 ratios are from Koide and Nakamura (1990).

3.8.3 Nd isotopic analysis

For Nd isotopic analyses, samples were diluted to give a Nd concentration of 30 ppb and analysed in 'dry plasma' mode. Unknown samples were analysed together with the primary standard JNdi-1 and the secondary standard HPS at the beginning and end of each analytical session, and within-run between every four samples and reference materials. All $^{143}Nd/^{144}Nd$ ratios were corrected for instrumental mass fractionation using

'internal normalisation' adopting a true $^{146}Nd/^{144}Nd$ ratio of 0.7219 and the exponential mass fractionation law, as well as for potential isobaric interferences from Sm. All corrected ratios are normalised to the international reference material JNdi-1 using a $^{143}Nd/^{144}Nd$ ratio of 0.512115 after Tanaka et al. (2000). Repeat analyses of the in-house HPS secondary standard were used to perform error propagation after normalisation. International reference materials from the USGS (United States) and GSJ (Japan) were used to monitor the veracity of the analyses and gave $^{146}Nd/^{144}Nd$ isotope ratios that overlap with reported values, within error (**Appendix A**, **Figure 3.9**). Total procedural replicates (3 digestions each for Kinloch, Motuoapa Dacite, and 1520C 24R 1W 91/93) were used to assess external precision (**Appendix A**, **Figure 3.7**). The 2SE uncertainties include the analytical uncertainties of the sample and normalising standards. Estimates of reproducibility of Nd isotope analyses are based on replicate analyses of standard JNdi-1 yielding $^{143}Nd/^{144}Nd = 0.512115 \pm 0.000009$ (2 SD, n=14).

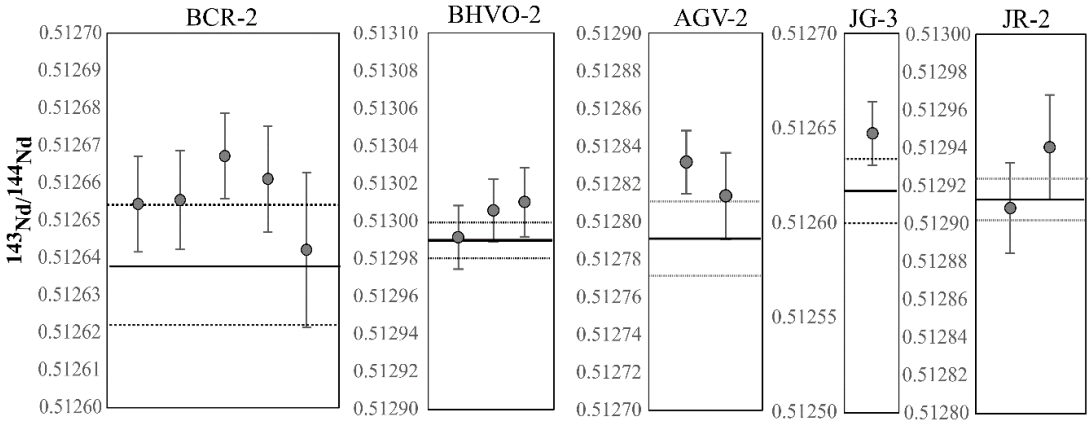

Figure 3.9: Reference materials compared to $^{143}Nd/^{144}Nd$ reported ratios. BCR-2, BHVO-2, and AGV-2 ratios are from Weis et al. (2006), JG-3 and JR-2 ratios are from Miyazaki and Shuto (1998).

3.8.4 Hf isotopic analysis

After the Hf chemical separation process, all samples were diluted with 3% HF-HNO_3 to contain 30 ppb of Hf and analysed in 'dry plasma' mode. Unknown samples were analysed together with the primary standard JMC-475 and the secondary standard HPS at

the beginning and end of each analytical session, and within-run between every four samples and reference materials. All $^{176}Hf/^{177}Hf$ ratios were corrected for instrumental mass fractionation using 'internal normalisation' adopting a true $^{179}Hf/^{177}Hf$ ratio of 0.7325 and the exponential mass fractionation law, as well as for potential isobaric interferences from Lu, Yb, W, and Ta. All corrected ratios are normalised to the international reference material JMC-475 using a $^{176}Hf/^{177}Hf$ ratio of 0.282160 after Vervoort and Blichert-Toft (1999). Repeat analyses of the in-house HPS secondary standard were used to perform error propagation after normalisation. International reference materials from the USGS (United States), and GSJ (Japan) were used to monitor the veracity of the analyses and gave $^{176}Hf/^{177}Hf$ isotope ratios that overlap with reported values, within error (**Appendix A**, **Figure 3.10**). Total procedural replicates (3 digestions each for Kinloch, Motuoapa Dacite, and 1520C 24R 1W 91/93) were used to assess external precision (**Appendix A**, **Figure 3.7**). The 2SE uncertainties include the analytical uncertainties of the sample and normalising standards. Estimates of reproducibility of Nd isotope analyses are based on replicate analyses of standard JNdi-1 yielding $^{176}Hf/^{177}Hf$ = 0.282160±0.000004 (2 SD, n=21).

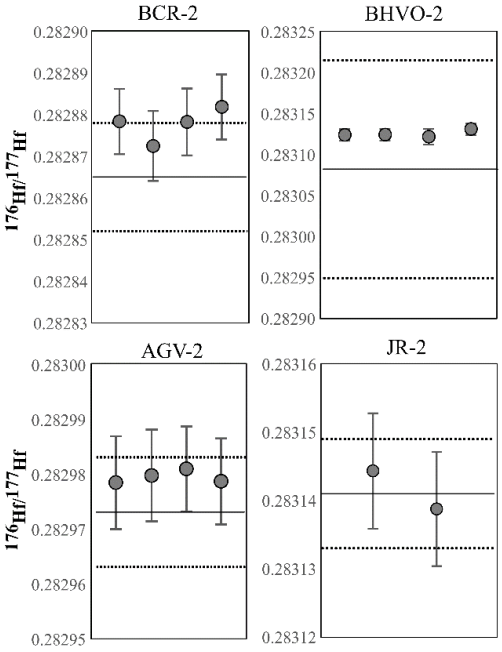

Figure 3.10: Reference materials compared to $^{176}Hf/^{177}Hf$ preferred ratios from GeoREM, and after Hanyu et al. (2005) for JR-2. Note the large range of reference material BHVO-2, this may be due to insufficient Ti elution in some reported ratios as it causes results to be irreproducible.

3.9 Assimilation-fractional crystallisation modelling in the TVZ

In this study, an energy- and mass-constrained modelling approach was applied to the TVZ, using the Magma Chamber Simulator (MCS, Bohrson et al. (2014), Bohrson et al. (2020), Heinonen et al. (2020)) to investigate whether chemical variations are primarily controlled by AFC from basaltic precursors, as suggested by most previous studies. The PC version of MCS_PhaseEQ_2019AC.xlsm employing rhyolite-MELTS+H_2O-CO_2 fluid (v1.1.0) was selected (Ghiorso & Gualda, 2015, Gualda et al., 2012) due to the presence of intermediate and felsic quartz saturated magmas. This tool is used to model fractional crystallisation and assimilation in an energy-constrained environment. It employs MELTS to thermodynamically generate the phases that crystallise in the magma at each step, to calculate the stability and partial melting temperatures of the wall rock, and the partial melt composition before assimilation occurs. Based on the crystallised mineralogy generated with the major element compositions and their partition coefficients, MCS calculates the trace element concentrations and the isotopic ratios of selected elements at each step for both the wall rock and the magma. To run each model simulation, the following input parameters are required: (i) a starting composition that represents the magma before AFC occurs, (ii) a wall rock composition that will be partially melted and assimilated, (iii) a pressure at which this process is being modelled, (iv) the initial temperatures of wall rock and magma, (v) wall rock mass and (vi) percolation threshold (FmZero). The simulation finishes when thermal equilibrium is reached between the magma and wall rock, once assimilation ends, or once a pre-defined hardstop temperature has been reached.

For **Chapter 4** the starting compositions of the parental melt were: (i) the lowest silica sample in the TVZ *i.e.*, Kakuki (major and trace elements from Zellmer et al. (2020) and

$^{87}Sr/^{86}Sr$, $^{206}Pb/^{204}Pb$, $^{207}Pb/^{204}Pb$ and $^{208}Pb/^{204}Pb$ isotopic ratios from Price et al. (2012); (ii) a high Mg# (molar 100*(Mg/(Mg + Fe^{2+}))) and a Sr-Pb isotopically less radiogenic intermediate sample *i.e.*, Karangahape (major and trace element compositions from Zellmer et al. (2020), $^{87}Sr/^{86}Sr$, $^{206}Pb/^{204}Pb$, $^{207}Pb/^{204}Pb$ and $^{208}Pb/^{204}Pb$ isotopic ratios from this study), and (iii) a primitive sample from the Kermadec Volcanic Zone, representative of a magma that likely did not experience any interaction with Torlesse crust *i.e.*, Rumble IV (major and trace element compositions and $^{87}Sr/^{86}Sr$, $^{206}Pb/^{204}Pb$, $^{207}Pb/^{204}Pb$ and $^{208}Pb/^{204}Pb$ isotopic ratios from Gamble et al. (1996), Gamble et al. (1993).

For the wall rock compositions, the Kaweka and Pahau sub-terranes of the Torlesse basement from Price et al. (2015) were used, which represent the main crustal components beneath the TVZ (**Figure 3.11**). Magma-to-wall rock mass ratios of 1:0.5 cause the thermal equilibrium to occur sooner than observed in the data in this study but with high amounts of assimilation, whereas ratios of 1:2 cause the thermal equilibrium to occur later than observed in the data with low amounts of assimilation. For the models shown here, the ratio was set to 1:1, representing an equal amount of starting magma and wall rock before heating. The water content of the parental melt was assumed to be low with ~1 wt% H_2O, consistent with previous studies (Arpa et al., 2017, Kilgour et al., 2013, Lormand et al., 2020, Zellmer et al., 2020).

As previous studies have suggested (*e.g.*, Deering et al. (2011), Graham et al. (1995)), a single-stage model is not effective in reproducing the chemical variation of the TVZ, and thus a multi-stage approach similar to that of Heinonen et al. (2019) was taken. To this end, for each starting composition two paths were modelled with different pressure

constraints. Decreasing pressure steps represent the magma moving to an upper level of the crust and having contact with another wall rock. Wall rock temperatures were chosen based on the need for early assimilation to reproduce the observed behaviour in the mafic members of the TVZ, and thus temperatures close to the solidus of the material were taken for each step, consistent with the high heat flux of 800 mW/m^2 in the TVZ (Stern, 1987).

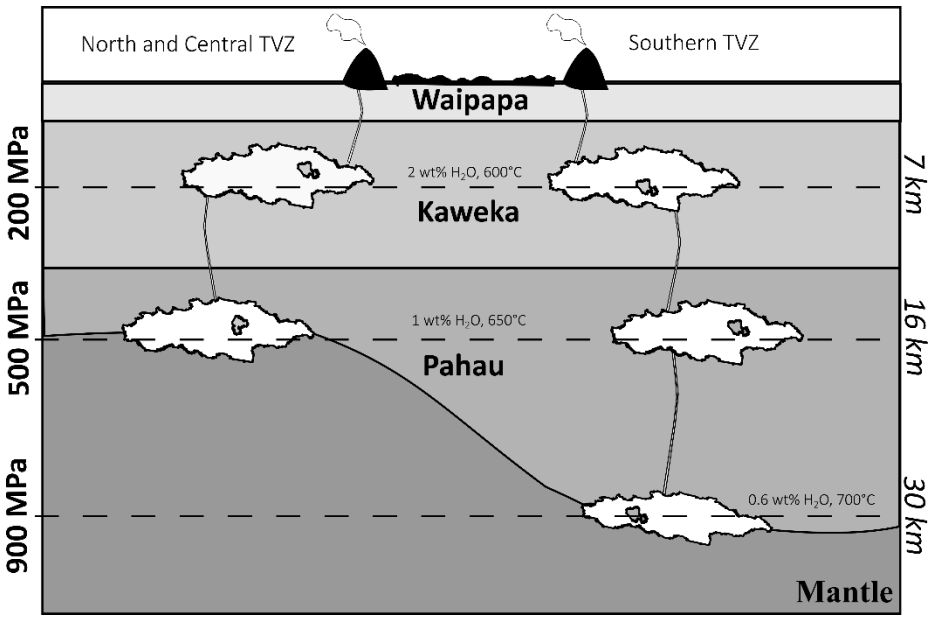

Figure 3.11: Schematic section of the crust under the TVZ separated into the North and the Central TVZ, and the Southern TVZ due to the different crustal thicknesses. Crustal composition is from Price et al. (2015).

Two paths were modelled based on the crustal thickness variation, as shown and simplified in **Figure 3.11**. The first path started at 900 MPa (~30 km depth, with a crustal thickness equivalent to the southern TVZ (Salmon et al., 2011)), with a magma water content of ~1 wt%, a wall rock water content of ~0.6 wt%, a wall rock starting temperature of 700 °C simulating a pre-heated crust, and a hardstop temperature of 1160 °C or when thermal equilibrium achieved. The second stage commenced at 500 MPa (~16 km depth), with a wall rock water content of ~1 wt% and a starting temperature of 650 °C, with a hardstop temperature of 980 °C or when thermal equilibrium was reached. A final third stage started at 200 MPa (~7 km depth), with a wall rock water content of ~2 wt%, a starting temperature of 600 °C and a hardstop temperature of 700 °C or when thermal

equilibrium was achieved. The second modelled path started at 500 MPa (~16 km depth, with the crustal thickness observed in the central and northern TVZ, Stratford and Stern (2004)), with a magma water content of ~1 wt%, wall rock water content of ~1 wt% and a starting temperature of 650 °C, with a hardstop temperature of 980 °C or when thermal equilibrium was reached. The second stage commenced at 200 MPa, with a wall rock water content of ~2 wt%, a starting temperature of 600 °C, and a hardstop temperature of 700 °C or when thermal equilibrium was achieved. The central North Island crust is mainly comprised of the Torlesse and Waipapa terranes; the Torlesse composite terrane is dominant below the TVZ, while Waipapa is only present close to the surface (Price et al., 2015). Within the Torlesse terrane, the Pahau subterrane is dominant in the lower portion of the crust, while the Kaweka subterrane is dominant in the upper portion of the crust. Thus, for the models at 900 MPa and 500 MPa, a wall rock composition based on the Pahau subterrane was employed, while for the 200 MPa models, the wall rock composition of the Kaweka subterrane was chosen, both after Price et al. (2015). The trace element partition coefficients (Kd) employed were taken from the GERM repository (see **Appendix B**, Bacon and Druitt (1988), Bea et al. (1994), Boudreau (1999), Ewart and Griffin (1994), Green et al. (2000), Mahood and Hildreth (1983), Olin and Wolff (2010), Sisson and Bacon (1992), Stimac and Hickmott (1994), Taylor et al. (2015), Tiepolo et al. (2007)). A summary of the modelling approach and results are presented in **Chapter 4**. The presence of water-bearing minerals, such as amphiboles and phyllosilicates, in some of the samples, limits the scope of these models, as it is known that MELTS is not always capable of stabilizing these minerals. However, they are present as accessory phases in a limited number of samples, and thus their effects are expected to change the model results significantly.

3.10 Calculation of bulk compositions of tectonically eroded and subducting materials

To approximate the composition of the subducting plate cover and the eroding crust, the method of Plank (2014) was used. This method considers the relative thickness of the different materials to approximate a bulk composition of the sedimentary column. Here, samples were taken from all units from drill cores U1520 and U1518 and further divided into three groups based on the position of the *décollement* identified by Barnes et al. (2020) (**Figure 3.12**). This bulk composition approximation allows to consider which members and their proportions are involved in the magma generation processes of the TVZ. Samples below the *décollement* represent the material that is being subducted without the need for tectonic erosion. Samples above the *décollement* represent material that is being accreted to the accretionary prism and subsequently eroded, while samples from the forearc represent material from the accretionary prism. The average chemical composition of each unit was calculated based on the thicknesses presented by Barnes et al. (2020), Saffer et al. (2019). The chemical composition of the tectonically eroded crust represents a composite of the samples above the *décollement* and the accretionary prism, considering their relative thicknesses.

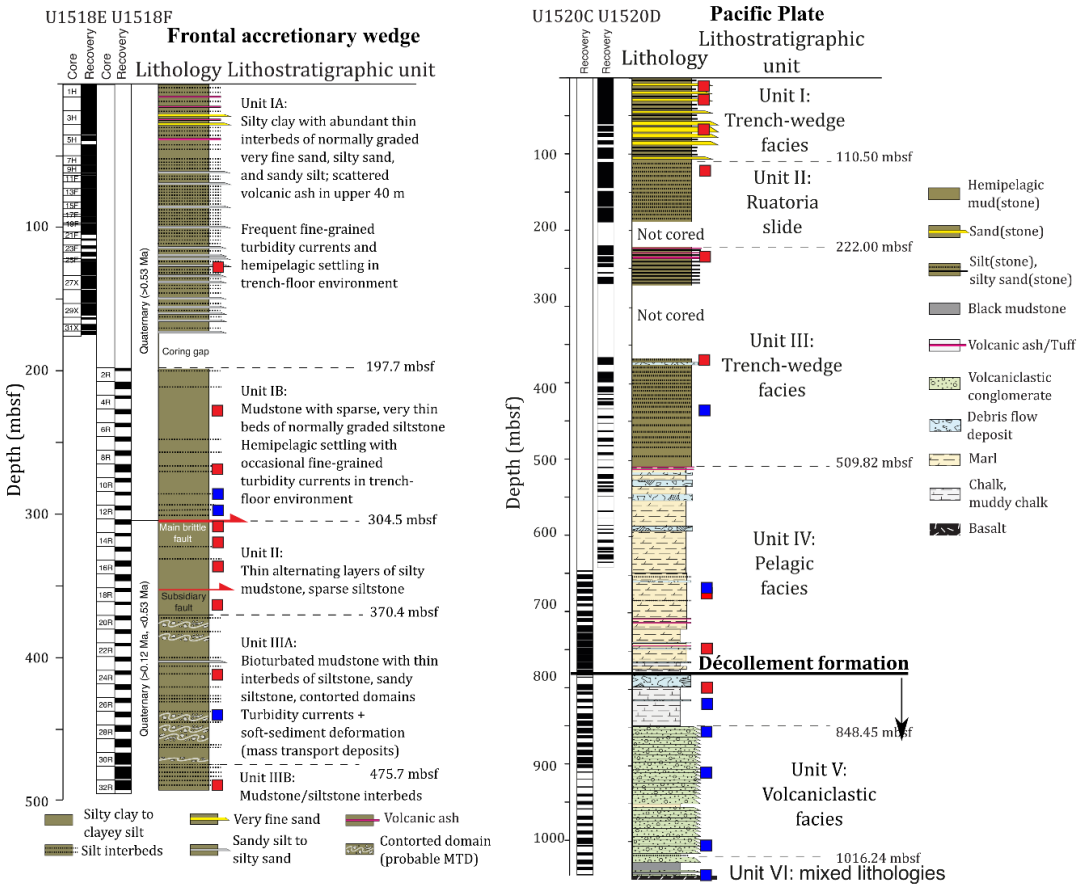

Figure 3.12: Site recovery columns after Saffer et al. (2019). The selected samples are shown in squares. Red squares represent samples with only major elements reported; blue squares represent samples with major and trace elements, as well as selected isotopic ratios. *Décollement* formation after Barnes et al. (2020).

Chapter 4 - Transcrustal and source processes affecting the chemical characteristics of magmas in a hyperactive volcanic zone

Carlos R. Corella Santa Cruz[1]; Georg F. Zellmer[1]; Claudine H. Stirling[2,3]; Susanne M. Straub[4]; Marco Brenna[3]; Malcolm R. Reid[2,3]; Károly Németh[1,5]; David Barr[2,3]

[1]Massey University, Private Bag 11222, Palmerston North 4442, New Zealand

[2]Centre for Trace Element Analysis and Department of Geology, University of Otago, PO Box 56, Dunedin 9054, New Zealand

[3]Department of Geology, University of Otago, PO Box 56, Dunedin 9054, New Zealand

[4]Lamont-Doherty Earth Observatory of Columbia University, 61 Route 9W, Palisades, NY 10964, USA

[5]Institute of Earth Physics and Space Science, Csatkai E. út 6-8., Sopron 9400, Hungary

Abstract

Arc magma generation and evolution are affected by transcrustal processes, such as assimilation and fractional crystallisation, and source processes like slab influx into the mantle wedge. However, the relative contribution of these mechanisms remains contentious. The Pleistocene to Holocene Taupo Volcanic Zone (TVZ) is unusually dominated by felsic volcanism with more than 95% of the total eruptive volume corresponding to rhyolitic magmas. Despite the relatively thin crustal basement (~16-30 km), combined wall rock assimilation and fractional crystallization (AFC) of primary basalt has previously been presented as a necessary means to generate the chemical characteristics of these magmas. This petrogenetic model is here assessed using a new, internally consistent set of major and trace element concentrations, and Sr-Pb isotope data from a suite of basaltic to rhyolitic samples that are representative of the entire TVZ with respect to geographical distribution and age. The dataset was modelled for AFC using the energy- and mass-constrained Magma Chamber Simulator (MCS) and the local Permian to Early Jurassic Torlesse composite terrane basement used as the principal assimilant. Regardless of the intensive parameters employed, the energy- and mass-constrained models presented here fail to realistically reproduce the combined major oxide, trace element, and isotope systematics of the sample set. The Pb isotope ratios of TVZ basalts to rhyolites reveal a broadly linear trend ranging from an unradiogenic ($^{206}Pb/^{204}Pb$: 18.77) to a more radiogenic crustal endmember ($^{206}Pb/^{204}Pb$: 18.84). This trend can be reproduced by a composite mélange dominated by the Torlesse terrane

(representative of tectonically eroded forearc crust), with some contribution of subducting sediments (GLOSS-II), interacting with the sub-arc mantle to generate the source of the magmas observed in the TVZ. This model is also consistent with Sr-Pb isotope systematics. At New Zealand's active margin, tectonic erosion has been reported based on geophysical data. Therefore, it is proposed that slab input can have a stronger relevance in the magma generation of the TVZ than previously thought. The broad compositional variations in the TVZ may result from source contamination by a subduction mélange, with differentiation processes within the overriding crust being subordinate.

4.1 Introduction

Subduction-related magmatism is considered as the primary process responsible for crustal growth on Earth. The average continental crust has an andesitic composition and approximately 80% of it is generated at convergent margins (*e.g.*, Barth et al., 2000; Plank and Langmuir, 1998; Rudnick and Gao, 2003; Stern, 2002; Taylor, 1967). A variety of processes can generate magma diversity in subduction zones. These processes can be broadly divided into two types: (i) slab additions to the mantle source, such as melts, fluids and solid material, leading to crustal input in the source generating some geochemical diversity (*e.g.*, Marschall and Schumacher, 2012; Plank, 2014; Turner and Langmuir, 2022), and (ii) transcrustal processes in the crustal basement, where mafic mantle magmas become progressively more felsic due to fractional crystallisation and crustal assimilation (AFC) and magma mixing (*e.g.*, DePaolo, 1981; Farner and Lee, 2017; Leeman, 1983).

Variations caused by the mantle wedge thermal structure and slab inputs are important factors controlling the composition of arc magmas, in some cases to a greater extent than transcrustal processes (Kelemen, 1995; Plank and Langmuir, 1988; Turner and Langmuir, 2015a, b). Slab inputs can originate from the sediment cover, the oceanic crust (Plank,

2014; Turner and Langmuir, 2022), or any mixture of materials known as *mélange* (Marschall and Schumacher, 2012). Further, melts and silica-rich slab fluids can contribute to the compositional diversity found in global arcs, consistent with experimental data (*e.g.*, Drummond et al., 1996; Förster and Selway, 2021; Hauff et al., 2003; Johnson and Plank, 2000; Martin et al., 2005; Rebaza et al., 2023; Schiano et al., 1995; Shimoda et al., 1998; Skora and Blundy, 2010; Tatsumi, 2001; Tatsumi and Hanyu, 2003; Yogodzinski et al., 1995). Interactions of the slab with the mantle can occur at their interface or, if the subducted material detaches and ascends diapirically, between the mantle and the diapir. Diapirs can contribute to mantle heterogeneity, partially melt due to ascent-related decompression, and generate melts with chemical variations ranging from basalt to dacite (Castro et al., 2010; Castro and Gerya, 2008; Marschall and Schumacher, 2012; Parolari et al., 2018; Parolari et al., 2021; Straub et al., 2015).

Following melt generation in the mantle, transcrustal processes are the next key factor in controlling magma composition. These processes are strongly influenced by crustal thickness as melts typically become more silicic with increasing crustal thickness, because the crust acts as a density filter, causing longer storage times that promote magmatic fractionation and magma-crust interactions, ultimately modifying the magmatic compositions (*e.g.*, Leeman, 1983; Plank and Langmuir, 1988). This causes arcs with thick crust to have, on average, more silicic compositions than arcs with thin crust (Farner and Lee, 2017). An important transcrustal process controlling magmatic evolution is AFC, which, together with magma mixing, has been traditionally proposed to explain the compositional and isotopic diversity of magmas observed in nature. However, the generation of felsic magmas from mafic precursor magmas requires large amounts of crustal assimilation and fractional crystallisation, in turn producing large

quantities of ultramafic-mafic cumulates (*e.g.*, Nandedkar et al., 2014). These cumulates are often absent in arcs, typically interpreted as a result of lower crustal delamination (Hawkesworth and Kemp, 2006; Magni and Király, 2020), although recent work has shown that the presence of interstitial partial melts may make the bulk of this material buoyant, hindering delamination (Bowman et al., 2021).

Active volcanic zones in arc settings are natural laboratories where the two above-mentioned processes affecting magma generation and evolution can be examined. The active Taupo Volcanic Zone (TVZ) is located on a variably thin crust (~16 km) in the northern and central regions, compared to the ~35 km in the southern regions (Eberhart-Phillips et al., 2019; Gase et al., 2019; Salmon et al., 2011; Stratford and Stern, 2004). Variations in the crustal thickness along the TVZ are caused by the development of a southwards propagating intra-arc rift (*e.g.*, Villamor et al., 2017), with a high heat flux of up to 800 mW/m^2 (Stern, 1987). Intra-arc rifting may facilitate magma generation by decompression and flux melting in the mantle wedge under New Zealand's North Island (Reyners, 2013; Seebeck et al., 2013). The TVZ is dominated by rhyolitic volcanism (>95 % of the total erupted volume) found in the thin central TVZ but not in the thicker southern TVZ. This does not conform with the general global hypothesis that crustal thickness is correlated with a greater abundance of evolved silicic magmas (Leeman, 1983), but may be related to the rifting process that may facilitate melting and assimilation. Complex transcrustal processes including AFC, magma mixing, and crustal anatexis have thus been proposed as the main process controlling the magmatic compositions and their variations observed in the TVZ (*e.g.*, Deering et al., 2011; Gamble et al., 1990; Gamble et al., 1993; Graham et al., 1995; Graham and Hackett, 1987; McCulloch et al., 1994; Reid, 1983; Reid and Cole, 1983). Alongside the complex

transcrustal processing, mantle source heterogeneities and source addition of subducted sediments have also been proposed by several authors to explain some of the variations observed, particularly in the mafic magmas (*e.g.*, Gamble et al., 1996; Gamble et al., 1993; Graham et al., 1995; Rooney and Deering, 2014). Both, source and transcrustal processes, may hence be important contributors to variations in magmatic compositions. Here we aim to further assess the role of these two mechanisms with a sample suite with a wide range of geographical locations, chemical composition ranging from mafic to felsic, and an age range representative of the whole TVZ volcanism. This is an internally consistent sample set subjected to identical analytical techniques to minimise inter-laboratory bias, providing the opportunity to re-evaluate some of the existing models and hypotheses of the petrogenetic processes within the TVZ. Transcrustal AFC is here evaluated based on energy-constrained Magma Chamber Simulator AFC modelling (MCS-AFC) employing major and trace element compositions, as well as Sr-Pb isotope ratios. Slab input is here evaluated based on the isotopic compositions of the magmas observed in the TVZ.

4.2 Geological background

The TVZ is at the southern tip of the Tonga-Kermadec-Hikurangi subduction zone that extends for 2,700 km from Samoa to North Island, New Zealand with a NNE-SSW orientation. It accommodates convergence between the Pacific and Australian plates with the highest rates of subduction and back-arc extension on Earth (Bevis et al., 1995). The magmatic expression of the northern and central portions are intra-oceanic arcs, whereas the southern portion of this subduction zone, the Hikurangi segment, represents a continental arc: the TVZ (Turner et al., 1997). Along the Hikurangi trench, the convergence rate ranges from 57 mm/yr in the north to 27 mm/yr in the south (Clark et al., 2019). In the Tonga and Kermadec portions the subducting plate consists of a typical

oceanic crust, while in the Hikurangi portion, the ~15 km thick Hikurangi Plateau is currently subducting (Mortimer and Parkinson, 1996). This plateau is a fragment of the Cretaceous Ontong Java-Manihiki-Hikurangi plateau Large Igneous Province (LIP), has a sediment cover of ~2 km and abundant seamounts that are thought to have a strong effect on subduction erosion (Davy and Wood, 1994; Timm et al., 2014). The Hikurangi Plateau started subducting beneath the Gondwana margin along the Chatham Rise in the Late Cretaceous and caused subduction there to cease (Davy, 2014; Davy et al., 2008; Reyners, 2013; Worthington et al., 2006). Subduction recommenced at about 24-30 Ma beneath the east coast of North Island, with slab dip steepening over time beneath the central North Island (Nicol et al., 2007; Seebeck et al., 2013).

The basement of central North Island consists of the Waipapa and Torlesse composite terranes (**Figure 4.1**a). These terranes are weakly metamorphosed greywacke-dominated accretionary prisms with localised sub-marine fans (Adams et al., 2002; Adams et al., 2007; Roser and Korsch, 1999). The Torlesse composite terrane is comprised of successions of quartzose, turbidite-dominated greywackes and consists of the Early Jurassic Kaweka subterrane and the Early Cretaceous Pahau subterrane (Adams et al., 2009; Mortimer et al., 2014). Although the boundaries between the Waipapa and Torlesse composite terranes are covered by the TVZ, Price et al. (2015) proposed that the base of the crust corresponds to the Torlesse composite terrane, overlain by the Waipapa composite terrane in the uppermost portion of the crust. These terranes dominate the crust under the TVZ, though there is also evidence for other units such as granulites, older volcanic and plutonic lithologies (*e.g.*, Price et al., 2012; Price et al., 2005). However, the geographical and depth distribution of these units, and their bulk composition, have not yet been systematically established.

The TVZ is divided into the northern, central and southern TVZ (Figure 4.1**b**) (Wilson et al., 1995). The northern and southern segments are dominated by andesitic volcanism and the central segment is dominated by rhyolitic volcanism (Wilson et al., 1984). Volcanism started at *c.* 2 Ma with andesitic activity, which was succeeded by voluminous rhyolitic activity and minor dacitic and basaltic activity (Wilson et al., 1995). Silicic volcanism has been reported to occur as early as at 1.88 – 1.84 Ma (Chambefort et al., 2014; Milicich et al., 2020). The volcanism in the TVZ is subdivided into the old (2 Ma-0.34 Ma) and the young TVZ (0.34 Ma-Present). Eight caldera centres have been identified in the TVZ: Okataina, Rotorua, Kapenga, Reporoa, Mangakino, Maroa, Whakamaru and Taupo (Wilson et al., 1995). Volumetrically, the TVZ is dominantly felsic, with rhyolitic volcanism accounting for 97.8% of the total volume, dacitic volcanism <0.1% and andesitic volcanism 2.1%; in comparison, mafic volcanism represents <0.1% (Cole, 1979). The occurrence of ignimbrite flare-ups has been correlated with high mantle flux and crustal rifting, producing ~3,000 km^3 of magma in the central TVZ between ~350 to ~280 ka, with a rate of 38 km^3/kyr (Gravley et al., 2016), making the TVZ an extraordinarily productive centre of high-silica volcanism compared with other volcanic systems around the globe.

4.3 Previously proposed petrogenetic processes of TVZ eruptives

In the central TVZ, mafic magmas are high-alumina basalts (HAB) generated by the partial melting of mantle peridotite and, in some cases, they have been shown to have interacted with crustal material (*e.g.*, Cole, 1973; Graham et al., 1995; Hiess et al., 2007). Fractionation of HAB is thought to generate basaltic andesites and further AFC generates andesitic melts (*e.g.*, Gamble et al., 1990; Graham and Hackett, 1987). Based on Nd-Sr isotope ratios, Gamble et al. (1993) proposed that the Torlesse composite terrane was the main contaminant for the TVZ magmas, and that the Waipapa composite terrane was not

involved. Crustal anatexis and fractionation were proposed to generate the dacites and rhyolites (*e.g.*, Reid, 1983; Reid and Cole, 1983), but it was later proposed, based on Sr-Nd-Pb-O isotopes, that rhyolites are instead generated by 15-25% assimilation of Torlesse roof rock by a basaltic magma plus ~70% fractional crystallisation (McCulloch et al., 1994).

The concept of an 'extraction window' in crystal mushes, together with the subordinate assimilation of Mesozoic crustal lithologies, has been considered for the TVZ by Deering et al. (2011). In this model, andesitic melts can be generated by 50-80% crystallisation of pyroxenes, plagioclase and Fe-Ti oxides from dry basaltic primary melts in the lower crust. Dacites can be produced by a similar extent of crystallisation of hornblende and Fe-Ti oxides. Following extraction from the lower crustal hot zone, these dacitic melts would then rise into the upper crust and further crystallise by >50%, forming a mush body in which interstitial rhyolitic melts are stored. Mixing of mafic minerals with a felsic crustal mush body has been proposed to generate high-magnesium intermediate samples in the southern TVZ (Beier et al., 2017; Conway et al., 2020; Svoboda et al., 2021). Sas et al. (2021b) studied Sr isotope ratios in plagioclase crystals in the Okataina Volcanic Centre (OVC) in the northern TVZ and found that crystals were formed in intermediate melts, suggesting ~20% crustal contamination. It was argued that the similar isotopic compositional ranges in plagioclase crystals imply consistent relative contributions from isotopically varied sources across the lifespan of the OVC system. Despite resorption textures, Sas et al. (2021a) found $\delta^{18}O$ homogeneity in quartz crystals (to within ~0.2‰, 2σ) in the OVC rhyolites, suggesting these melts derived from an isotopically homogeneous source, supporting invariable relative contributions from the mantle and

crust. They suggested a basaltic parent with variable subduction flux and significant deep crustal assimilation of >25% of Torlesse-like metasediments.

Mantle heterogeneities have also been proposed to explain some of the chemical characteristics of magmas in the TVZ. An increase of subduction components in the TVZ basalts compared to the Tonga-Kermadec magmas suggests that all basalts have geochemical input from the slab (Gamble et al., 1993). This input may come from the recycling of subducted sediments, with variations seen in individual volcanoes reflecting variable efficiency of melt transfer in the crust (Gamble et al., 1996). Furthermore, the transition from oceanic crust to continental crust from the Kermadec arc to the TVZ does not correlate with a significant increase in trace element concentrations or isotope ratios that are sensitive to crustal contamination (Gamble et al., 1996). Graham et al. (1995) observed that crustal assimilation does not reproduce the observed characteristics of HAB and thus that these variations must originate in the source region. Rooney and Deering (2014) showed that variable slab melt and fluid addition can generate the characteristics observed in the TVZ basalts, which by further AFC processing would generate the voluminous rhyolitic volcanism. Using Nd-Sr-Hf isotope ratios, Waight et al. (2017) proposed that variable degrees of source addition of sediment melts or bulk sediment to mantle sources plus AFC (10-15%) are required to explain variations observed in the TVZ. In summary, the processes taking place to generate the geochemical variations observed in the TVZ are still debated, but most studies agree on a link to slab flux into the mantle wedge followed by overprinting through transcrustal processes.

4.4 Methods

4.4.1 Sampling

Sampling targeted a diverse suite in geographical distribution, age and geochemical characteristics. Samples were taken from lava flows, volcanic cones, domes and pyroclastic deposits representative of the TVZ (**Figure 4.1**b**, Table 4.1**). In the central and northern TVZ, samples are mafic, intermediate and felsic, representing different eruptive styles such as monogenetic phreatomagmatic eruptions, volcanic cones, domes, lava flows, and pyroclastic deposits. In the present sample set, the southern TVZ is mostly represented by intermediate lava samples and one felsic (dacitic) lava-dome. Maungatautari volcano at the western edge of the TVZ was also included as it was part of the subduction-related volcanic front at *c.* 2 Ma (Prentice et al., 2020), contemporary to the initiation of the TVZ. Here we focus on mafic samples due to the petrogenetic information that can be determined from them as clearly mantle-derived melts, although we acknowledge that they represent a small percentage of the total erupted volume and stress that the entire TVZ geochemical diversity is presented in this sample suite.

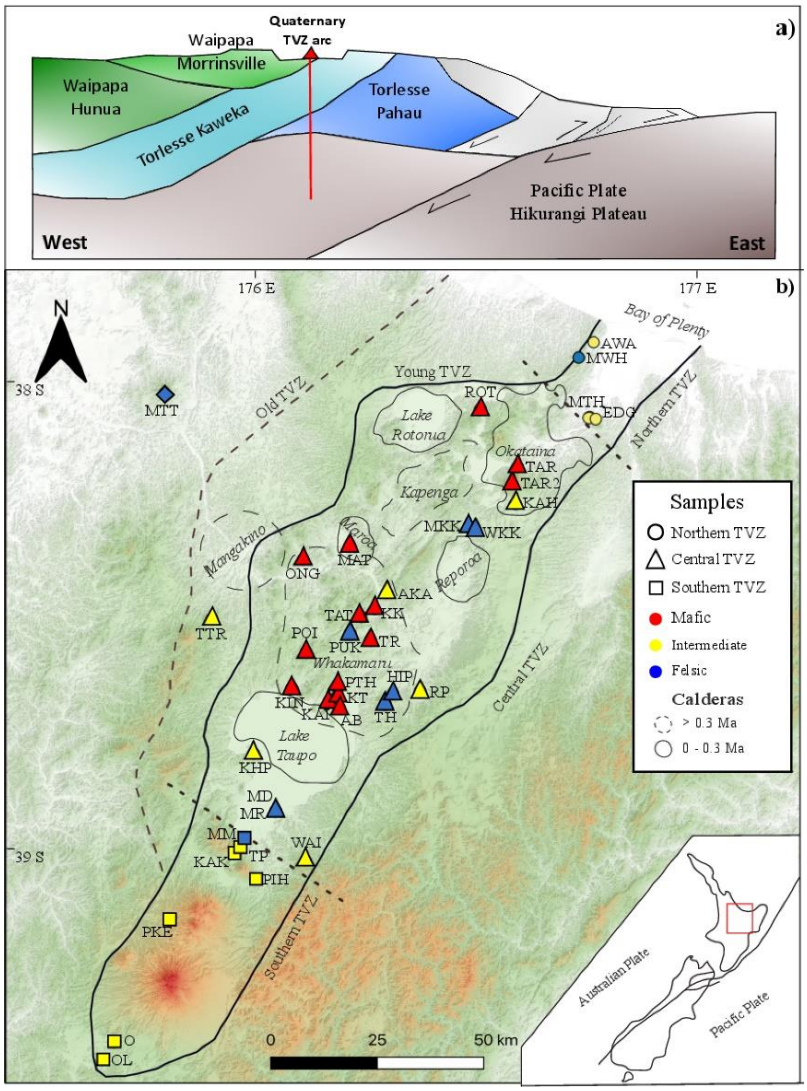

Figure 4.1: (a) Schematic view of the crust of the Central North Island, after Price et al. (2015). (b) Sample locations, using Land Information New Zealand (LINZ) 3m digital elevation model (DEM), with brown representing the elevated regions. Calderas delimited within Lake Taupo and Lake Rotorua correspond to Taupo and Rotorua calderas respectively. Young and old TVZ and southern, central and northern TVZ after Wilson et al. (1995). Coordinate reference system WGS84/UTM zone 60S. Map abbreviations: KT = K-TRIG, PTH = Punatekahi, TAT = Tatua, AB = Acacia Bay, TR = TramRoad, POI = Poihipi, KAI = Kaiapo, ROT = Rotokawau, TAR = Tarawera, KIN = Kinloch, MAT = Matipan, MTH = Matahi, AKA = Akatarewa, RP = Rolles Peak, OL = Ohakune Lakes, O = Ohakune, TTR = Titiraupenga, PIH = Pihanga, KAK = Kakaramea, EDG = Edgecumbe, TP = Te Ponanga, AWA = Awakaponga, MKK = Maungakakaramea, MWH = Manawahe, WKK = Waikokomuka, MTT = Maungatautari, TH = Tauhara, HIP = Hipaua, MM = Maungamanu Mosquito, MD = Motuoapa Dacite, MR = Motuoapa Rhyolite, PUK = Puketarata, WAI = Waimarino, KHP = Karangahape, PKE = Pukeonake, KAH = Kaharoa, KK = Kakuki, ONG = Ongaroto.

Table 4.1: Selected samples from the northern, central and southern TVZ. Maungatautari is not part of the TVZ.

Sample	Rock	Age	Comment
		Northern TVZ	
Matahi	Basaltic tephra	*c*. 42 ka	(Pullar & Nairn, 1972)
Manawahe	Dacitic dome	*c*. 0.75 Ma	(Nairn & Beanland, 1989)
Awakaponga	Andesitic flow	*c*. 0.75 Ma	(Nairn & Beanland, 1989)
Edgecumbe	Andesitic flow	*c*. 6 ka	(Carroll et al., 1997)
		Central TVZ	
Kakuki	Scoria	0.221 Ma	(Tanaka et al., 1996)
K-TRIG	Basaltic scoria	0.137 Ma	(Tanaka et al., 1996)
Ongaroto	Basalt	0.086 Ma	(Tanaka et al., 1996)
Acacia Bay	Basaltic tephra	0.1-0.2 Ma	(Wilson & Smith, 1985)
Kinloch	Basaltic lapilli tuff	< 9. 5 Ka	(Matheson, 2010)
Matipan	Basaltic lapilli tuff	-	-
Poihipi	Basaltic scoria	-	-
Tarawera	Basaltic tephra	A.D. 1886	Historic, (Walker et al., 1984)
Kaiapo	Basaltic scoria	-	(Matheson, 2010)
Tatua	Basalt	Late	(Houghton et al., 1987)
Rotokawau	Basaltic lapilli tuff	*c*. 3 ka	(Cole, 1973)
TramRoad	Basaltic lapilli tuff	-	-
Punatekahi	Basaltic scoria cone	45-300 ka	(Matheson, 2010)
Waimarino	Basalt	-	-
Karangahape	Andesite scoria cone	*c*. 290 ka	(Wilson et al., 1984)
Titiraupenga	Andesitic cone	1.89 Ma	(Stipp, 1968)
Rolles Peak	Andesitic cone	0.712 Ma	(Tanaka et al., 1996)
Kaharoa	Lapilli tuff	AD 1305	(Leonard et al., 2002)
Akatarewa	Lapilli tuff	-	-
Hipaua	Dacitic dome	58 ka	(Rosenberg et al., 2020)
Tauhara	Dacitic dome	58 ka	(Rosenberg et al., 2020)
Waikokomuka	Dacitic dome	-	-
Puketerata	Rhyolitic dome	14 ka	(Brooker et al., 1993, Kósik et al.,
Maungakakaramea	Dacitic dome	-	-
Motuoapa Dacite	Dacitic dome	*c*. 35 ka	(Kósik et al., 2021)
Motuoapa Rhyolite	Rhyolitic pyroclastic	*c*. 80 ka	(Kósik et al., 2021)
		Southern TVZ	
Te Ponanga	Andesite	Late	Inferred
Pukeonake	Scoria cone	Late	(Cole, 1978)
Ohakune	Scoria cone	Late	(Kósik et al., 2016)
Ohakune lakes	Andesite	Late	Inferred
Pihanga	Andesite	< 0.2 Ma	(Cole, 1978)
Kakaramea	Andesite	*c*. 0.2 Ma	(Stipp, 1968)
Maungamanu	Dacitic dome	-	-
Maungatautari	Dacite	1.8 Ma	(Robertson, 1983)

4.4.2 Analytical methods

Major element compositions were determined using a Wavelength Dispersive X-ray Fluorescence (WD-XRF) S8 Tiger spectrometer from Bruker-AXS (Germany) at Massey University, New Zealand. Reproducibility is ± 0.5-1.0% relative for major element oxides and better than ± 3% relative for minor element oxides, except for P_2O_5 (± 5-10%). Selected samples were analysed for trace element concentrations using an inductively coupled plasma mass spectrometer with a quadrupole mass analyser (Q-ICP-MS) and a 7900 instrument (Agilent Technologies, USA) at the Centre for Trace Element Analysis, University of Otago, New Zealand. Results of reference materials are within 90% of reported values, individual elements %RSD are typically from 1 to 5%, for details see **Appendix A**. Strontium and lead isotope analysis were performed by multiple-collector ICP-MS (MC-ICP-MS) at the Centre for Trace Element Analysis, University of Otago, using a Nu Plasma-HR instrument (Nu Instruments Ltd, UK) modified from previously reported methods (Scholes et al., 2016; Woodhead, 2002). Total procedural replicates and reference materials are reported in **Chapter 3 and Appendix A**. Estimates of reproducibility of Sr and Pb isotope analyses are based on replicate analyses of standards SRM987 yielding $^{87}Sr/^{86}Sr$ = 0.710247 0±0.000013 (2 SD, n = 18) and Pb981 yielding $^{208}Pb/^{204}Pb$ = 36.7184±0.0032, $^{207}Pb/^{204}Pb$ = 15.4957±0.0013, and $^{206}Pb/^{204}Pb$ = 16.9406±0.0012 (2 SD, n=20). Previously reported Pb isotope values for the TVZ from Gamble et al. (1996); Price et al. (2012); Sas et al. (2021b); Shane et al. (2017) were re-normalised to the NIST 981 values of Yuan et al. (2016) to have comparable results, including those of the Torlesse subterranes after Price et al. (2015) and those of Rumble IV, a primitive sample from the Kermadec arc that is thought not to have experienced any crustal assimilation, after Gamble et al. (1996) (see **Appendix A**). Results for major elements are presented in **Table 4.2**, results for trace element

concentrations in **Table 4.3** and Sr-Pb isotope ratios in **Table 4.4**.

Table 4.2: XRF major oxides results, all values are in wt%.

Sample name*	SiO_2	TiO_2	Al_2O_3	Fe_2O_3	MnO	MgO	CaO	Na_2O	K_2O	P_2O_5	LOI	Total
KT2	49.45	1.13	17.33	11.88	0.20	5.97	11.30	2.55	0.34	0.22	0.39	100.77
KT1	49.57	1.12	17.3	11.94	0.20	6.29	11.26	2.62	0.35	0.21	0.39	101.25
PTH	49.69	0.99	17.31	10.72	0.18	7.27	12.15	2.35	0.33	0.18	0.00	101.17
TAT	50.02	1.35	17.14	10.71	0.19	6.49	10.55	3.23	0.33	0.30	0.70	101.01
AB	50.22	1.02	19.32	8.36	0.16	4.47	13.50	2.28	0.32	0.29	1.21	101.15
TR	50.22	1.31	17.05	10.63	0.19	6.78	11.01	2.94	0.45	0.29	0.32	101.20
POI	50.57	1.15	17.34	10.73	0.17	6.10	10.41	2.74	0.33	0.22	1.16	100.92
KAI	51.01	1.34	16.63	10.57	0.18	6.59	10.73	3.12	0.57	0.24	0.31	101.30
ROT	51.15	0.78	17.91	9.58	0.17	6.36	11.96	2.18	0.59	0.15	0.14	100.98
TAR	51.79	0.82	17.36	10.34	0.18	6.25	11.27	2.22	0.6	0.17	0.27	101.27
KIN	51.79	1.21	16.68	10.51	0.19	5.95	10.81	2.89	0.49	0.23	0.40	101.15
MAT	51.87	1.15	17.10	10.17	0.18	5.73	10.40	2.93	0.75	0.24	0.68	101.20
MTH	52.58	0.84	17.95	9.61	0.17	5.03	11.71	2.32	0.63	0.17	0.26	101.26
AKA	55.33	1.14	16.17	9.17	0.17	3.98	7.77	3.03	1.02	0.40	2.57	100.76
RP	57.30	0.63	19.14	6.86	0.11	4.13	8.35	3.00	0.76	0.19	0.69	101.16
OL	57.36	0.58	16.28	8.45	0.14	5.78	8.60	2.71	0.75	0.13	0.26	101.03
O1	57.37	0.55	15.49	8.38	0.14	6.62	8.96	2.64	0.72	0.13	0.41	101.41
TTR	57.37	0.57	15.23	8.14	0.13	7.28	8.36	2.49	0.94	0.14	0.71	101.37
O2	57.49	0.58	16.09	8.36	0.14	5.95	8.67	2.76	0.73	0.14	0.44	101.34
PH	57.71	0.65	17.52	7.69	0.11	4.78	7.67	2.97	1.21	0.16	0.61	101.08
KAK	59.33	0.74	16.64	7.28	0.12	3.53	5.50	2.95	1.76	0.17	2.86	100.90
EDG	60.76	0.73	16.56	7.35	0.14	3.53	6.86	2.83	1.61	0.17	0.44	100.98
TP	61.31	0.71	16.44	7.29	0.11	3.36	5.74	3.13	1.77	0.16	1.23	101.26
AWA	62.14	0.53	16.70	6.65	0.12	3.20	6.84	2.77	1.25	0.12	0.90	101.21
MKK	64.62	0.85	16.59	4.89	0.07	0.39	2.30	4.22	2.28	0.27	4.06	100.54
MWH	65.16	0.58	16.20	5.57	0.10	1.57	4.63	3.62	2.29	0.19	0.75	100.66
WKK	65.22	0.80	15.91	5.83	0.14	1.62	4.53	4.11	1.84	0.26	0.53	100.79
MTT	65.52	0.61	16.37	5.28	0.08	1.08	2.81	3.11	2.84	0.17	2.62	100.48
TH	66.52	0.37	15.64	4.36	0.09	2.41	4.79	3.50	2.17	0.13	0.91	100.90
HIP	67.08	0.41	15.15	4.49	0.09	2.76	4.86	3.71	2.18	0.15	0.08	100.96
MM	67.92	0.42	15.06	3.73	0.07	0.93	3.06	3.03	3.45	0.15	2.65	100.48
MD	69.17	0.39	15.05	3.72	0.08	0.91	3.30	4.02	2.50	0.14	1.56	100.83
MR	72.82	0.14	13.17	1.92	0.05	0.11	1.43	3.99	3.39	0.07	3.26	100.36
PUK	72.46	0.24	14.01	1.86	0.07	0.33	1.47	4.15	3.53	0.06	2.38	100.58
WAI	52.58	0.49	13.00	9.07	0.16	13.18	9.97	1.73	0.45	0.11	0.39	101.12
KHP	56.04	0.57	13.98	7.98	0.15	8.75	9.57	2.36	0.75	0.13	0.94	101.23
PKE	57.15	0.70	14.45	7.66	0.14	8.91	7.34	2.88	1.45	0.18	0.37	101.22
KAH	57.89	0.84	17.43	8.01	0.19	3.55	7.64	3.59	1.23	0.27	0.34	100.99
KK	49.20	1.14	17.55	9.81	0.17	7.76	11.47	2.69	0.34	0.24	0.67	101.04
KT	49.71	1.09	18.10	11.52	0.19	6.01	11.60	2.43	0.31	0.22	0.14	101.32
PTH2	50.10	0.98	17.31	10.43	0.18	7.14	11.92	2.43	0.38	0.18	0.01	101.07
TAT2	50.84	1.34	17.23	10.66	0.19	6.34	10.63	3.32	0.40	0.32	0.22	101.49
ONG	50.94	1.08	15.76	10.09	0.18	9.44	10.29	2.61	0.56	0.32	0.00	101.28
ROT2	51.50	0.78	18.14	9.54	0.17	6.31	11.80	2.29	0.61	0.15	0.21	101.50
TAR2	51.69	0.83	17.41	10.52	0.19	6.26	11.33	2.25	0.60	0.18	0.00	101.26
KIN2	52.08	1.21	16.71	10.50	0.19	5.85	10.67	2.86	0.50	0.23	0.28	101.08
MTH2	55.15	0.98	17.24	8.90	0.16	4.35	8.23	2.54	0.81	0.27	2.13	100.76
O3	56.76	0.55	15.45	8.52	0.15	6.86	8.68	2.58	0.71	0.13	0.58	100.96

*KT2 = K-TRIG 2, KT1 = K-TRIG 1, PTH = Punatekahi, TAT = Tatua, AB = Acacia Bay, TR = TramRoad, POI = Poihipi, KAI = Kaiapo, ROT = Rotokawau, TAR = Tarawera, KIN = Kinloch, MAT = Matipan, MTH = Matahi, AKA = Akatarewa, RP = Rolles Peak, OL = Ohakune Lakes, O1 = Ohakune 1, TTR = Titiraupenga, O2 = Ohakune 2, PIH = Pihanga, KAK = Kakaramea, EDG = Edgecumbe, TP = Te Ponanga, AWA = Awakaponga, MKK = Maungakakaramea, MWH = Manawahe, WKK = Waikokomuka, MTT = Maungatautari, TH = Tauhara, HIP = Hipaua, MM = Maungamanu Mosquito, MD = Motuoapa Dacite, MR = Motuoapa Rhyolite, PUK = Puketarata, WAI = Waimarino, KHP = Karangahape, PKE = Pukeonake, KAH = Kaharoa, KK = Kakuki, KT = K-TRIG, PTH2 = Punatekahi 2, TAT2 = Tatua 2, ONG = Ongaroto, ROT2 = Rotokawau 2, TAR2 = Tarawera 2, KIN2 = Kinloch 2, MTH2 = Matahi 2, O3 = Ohakune 3

Table 4.3: ICP-MS trace elements results. All values are in µg/g.

	KT2	KT1	PTH	TAT	AB	TR	POI	KAI	ROT	TAR	KIN	MAT	MTH	AKA	RP	OL	O1	TTR	O2	PIH
Ba	95	98	72	160	170	110	130	130	210	160	160	200	190	270	180	150	130	170	130	280
Rb	<5	7.5	6.3	6.3	7.4	7.2	6	12	13	12	11	18	14	31	13	16	16	16	13	34
Th	0.89	0.76	0.79	0.97	0.61	0.85	1.2	1.4	1.5	1.3	1.1	1.9	1.6	3.7	2.6	2.3	2.2	2.8	1.9	4.2
Nb	2.6	2.5	2	4.9	<2	3.6	2.9	5.8	<2	2	4.2	4	2.3	4.6	3.1	2.5	2.3	<2	2.1	3.8
Sr	400	400	300	330	430	330	360	340	340	250	360	350	270	280	940	380	400	280	390	480
Zr	66	64	54	140	51	91	78	110	47	47	100	91	52	120	66	62	62	65	44	95
Y	18	19	15	24	23	22	24	22	14	13	23	22	14	25	8.7	14	13	14	13	16
Cr	42	41	100	34	72	140	40	150	79	16	74	63	20	17	23	120	180	260	120	120
V	250	260	260	230	300	270	260	260	240	200	320	240	230	220	130	200	200	190	150	180
Ni	17	17	25	27	10	37	24	28	20	<5	26	17	<5	<5	26	27	37	60	29	42
Co	34	34	32	32	22	33	35	34	29	25	36	30	22	21	21	28	29	29	26	25
Sc	34	34	33	29	32	29	30	32	32	27	33	29	32	25	12	24	25	21	24	21
Pb	1.9	1.8	1.5	2.4	1.5	1.7	2.4	2.7	2.2	2.8	2.5	3.5	3	7.6	3.8	3.4	3	4.3	1.1	5
Cu	37	38	28	36	34	33	46	32	32	11	41	21	11	14	100	95	35	90	98	43
Li	5.4	5.5	4.9	7.3	8	5.4	8.2	8.2	6	7	8	9.1	8	21	7.4	9.9	8.3	7.9	8.4	13
Cs	<0.5	<0.5	<0.5	<0.5	0.88	<0.5	1	0.68	<0.5	0.85	0.87	0.87	1.2	3.6	0.61	0.91	0.99	<0.5	0.61	0.97
Be	0.5	0.48	0.52	0.68	0.35	0.49	0.46	0.8	0.35	0.39	0.55	0.63	0.62	0.99	0.54	0.31	0.27	0.45	0.32	0.72
Ta	0.14	0.14	0.15	0.29	0.099	0.21	0.16	0.35	0.096	0.12	0.21	0.23	0.16	0.32	0.18	0.14	0.14	0.12	0.16	0.28
Hf	1.7	1.7	1.5	3.6	1.3	2.4	1.9	2.6	1.4	1.4	2.3	2.5	1.8	3.6	1.9	1.8	1.6	1.8	1.3	3.1
U	<0.5	<0.5	<0.5	<0.5	<0.5	<0.5	<0.5	<0.5	<0.5	<0.5	<0.5	<0.5	<0.5	0.94	0.67	0.6	0.5	0.68	<0.5	0.88
W	0.18	0.34	0.37	0.18	0.41	0.25	0.39	0.39	0.26	0.27	0.39	0.41	0.43	0.88	0.36	0.4	0.39	0.34	0.28	0.72
La	7.7	7.1	5.4	11	7.8	7.9	9.8	8.6	6.3	5.4	7.3	9.3	6.9	14	11	6.6	6.3	7.4	6.8	12
Ce	18	17	13	25	16	20	18	21	14	13	18	22	16	27	23	14	14	14	14	25
Pr	2.7	2.4	1.9	3.7	2.4	3	3.3	3	2	1.8	2.5	3.1	2.3	4.4	2.8	1.7	1.7	1.9	1.8	3.2
Nd	13	12	9.5	17	12	14	16	14	9.1	8.2	12	14	11	19	12	7.8	7.4	8.5	7.8	13
Sm	3.3	3	2.7	4.3	3	3.8	4	3.6	2.4	2.1	3.1	3.7	2.9	4.6	2.5	1.8	1.9	2.2	2	2.9
Eu	1.1	1.1	0.89	1.4	1.1	1.2	1.2	1.2	0.87	0.69	1.1	1.2	0.88	1.5	0.73	0.59	0.57	0.64	0.54	0.85
Gd	3.5	3.4	2.9	4.7	3.6	4.1	4.5	4.3	2.7	2.3	3.5	4.1	2.9	4.7	2.2	2.2	2	2.2	2.2	3.1
Tb	0.55	0.57	0.46	0.7	0.56	0.66	0.68	0.64	0.43	0.39	0.58	0.6	0.47	0.75	0.31	0.35	0.35	0.34	0.35	0.51
Dy	3.4	3.5	3.2	4.8	3.6	4.3	4.2	4.3	2.8	2.5	3.7	4.1	3.2	4.8	1.8	2.2	2.4	2.4	2.4	3
Ho	0.72	0.7	0.66	0.95	0.73	0.83	0.85	0.83	0.6	0.51	0.78	0.85	0.67	0.92	0.35	0.5	0.52	0.51	0.51	0.65
Er	2.1	2	1.9	2.8	2.1	2.4	2.4	2.4	1.7	1.5	2.3	2.4	1.9	2.8	1.1	1.6	1.5	1.6	1.5	1.9
Tm	0.3	0.3	0.26	0.38	0.29	0.34	0.33	0.35	0.25	0.21	0.32	0.32	0.27	0.4	0.14	0.22	0.19	0.21	0.23	0.28
Yb	2	1.8	1.7	2.5	1.9	2.3	2.3	2.2	1.6	1.4	2.3	2.2	1.8	2.5	0.93	1.7	1.5	1.5	1.6	1.8
Lu	0.27	0.26	0.27	0.4	0.27	0.34	0.32	0.35	0.25	0.23	0.32	0.34	0.27	0.37	0.14	0.24	0.26	0.23	0.24	0.28

Table 4.3 (continued):

	KAK	EDG	TP	AWA	MKK	MWH	WKK	MTT	TH	HIP	MM	MD	MR	PUK
Ba	320	410	370	320	610	560	500	830	450	370	460	480	610	910
Rb	56	48	59	38	44	72	56	89	57	48	91	86	110	120
Th	6.4	4.7	5.4	3.4	7.3	7.1	5.2	11	7.2	6.9	10	8.2	11	12
Nb	5.7	3.7	5.4	2.9	8.1	6.2	6.4	12	4	3.7	6	5.9	7.6	7.8
Sr	190	230	230	140	210	220	280	280	310	270	150	160	87	130
Zr	150	85	140	74	190	150	150	99	80	70	110	100	110	63
Y	23	17	27	16	17	24	27	13	15	13	20	22	31	18
Cr	23	30	30	14	3.8	4.3	<3	15	18	38	4.8	3.5	<3	<3
V	150	180	170	160	49	91	61	85	70	67	41	36	3.2	11
Ni	7.4	<5	11	<5	<5	<5	<5	7.4	11	28	<5	<5	<5	<5
Co	18	15	20	15	4.3	8.9	5.6	9.3	9.6	9.3	5.1	4.6	<2	<2
Sc	18	21	19	21	11	13	17	8.5	9.1	9.9	8.5	8.9	8.8	3.9
Pb	9.3	7.6	7	6.3	12	9.4	9.6	9.2	9	8.1	12	13	18	15
Cu	17	10	22	11	<5	5.2	<5	21	8.9	14	<5	<5	<5	<5
Li	21	24	14	11	9.7	19	18	13	19	15	10	40	43	41
Cs	2.9	2.6	2.2	2.3	1.3	2.1	1.2	1.9	2.8	2	4.8	4.8	7	5.6
Be	0.98	0.73	0.85	0.52	1.2	1.1	1.3	1.2	1.1	1.1	1.3	1.4	1.8	1.6
Ta	0.41	0.29	0.38	0.2	0.56	0.45	0.41	0.89	0.37	0.37	0.56	0.46	0.59	0.72
Hf	4.3	2.6	3.9	2.2	5.7	4.3	4.2	2.9	2.5	2.6	3.7	3.2	4.1	2.7
U	1.4	1.1	1.3	0.82	1.4	1.6	1.1	2.3	1.6	1.4	2.1	1.9	2.3	2.7
W	0.71	0.92	0.61	0.67	0.83	1	0.73	0.98	0.84	0.84	1.2	1.1	1.6	1.7
La	16	12	18	7.9	22	18	18	32	16	16	21	18	26	24
Ce	34	25	29	17	50	37	38	46	31	32	43	39	56	49
Pr	4.3	2.9	4.7	2	6.4	4.7	4.8	6.2	3.7	3.8	4.9	4.5	6.5	4.9
Nd	17	12	20	8.7	28	19	20	22	14	14	20	18	26	17
Sm	3.7	2.9	4.2	2.1	5.4	4.3	4.7	3.7	2.9	2.9	4	3.9	5.6	3.4
Eu	0.89	0.82	1.1	0.64	1.2	1	1.3	0.98	0.72	0.69	0.83	0.86	0.8	0.71
Gd	4	3.1	4.6	2.5	4.1	4.1	4.9	3.1	3	2.8	4	3.8	5.2	3
Tb	0.63	0.47	0.74	0.38	0.58	0.65	0.75	0.46	0.43	0.45	0.67	0.59	0.86	0.48
Dy	4.1	3.1	4.7	2.7	3.5	4.2	4.9	2.7	2.8	2.7	3.9	3.8	5.5	3.2
Ho	0.87	0.64	0.96	0.59	0.72	0.85	1	0.5	0.57	0.58	0.82	0.78	1.2	0.72
Er	2.5	2	2.7	1.8	2.1	2.6	3	1.5	1.8	1.7	2.4	2.4	3.6	2.1
Tm	0.37	0.29	0.4	0.25	0.31	0.38	0.41	0.19	0.25	0.23	0.36	0.35	0.5	0.32
Yb	2.4	2	2.8	1.9	2.3	2.5	3	1.5	1.7	1.8	2.4	2.6	3.4	2.4
Lu	0.34	0.28	0.4	0.3	0.31	0.41	0.45	0.19	0.29	0.27	0.37	0.38	0.49	0.38

4.4.3 AFC modelling

Given that AFC has been proposed to be one of the main processes generating the chemical diversity seen in the TVZ, modelling it starting from basaltic precursors should be able to explain some of the variations observed. To assess this, the Magma Chamber Simulator (MCS, Bohrson et al. (2014); Bohrson et al. (2020); Heinonen et al. (2020)) was employed to have an energy- and mass-constrained modelling approach. This allows for a more robust evaluation of the processes involved compared to models constrained by chemistry alone (DePaolo, 1981). Due to the presence of intermediate and felsic quartz-saturated magmas, the PC version of MCS_PhaseEQ_2019AC.xlsm with rhyolite-MELTS+H_2O-CO_2 fluid (v1.1.0) (Ghiorso and Gualda, 2015; Gualda et al., 2012) was employed. MCS employs MELTS to thermodynamically calculate the phases that crystallise in the magma at each step, approximate the stability and partial melting temperatures of the wall rock, and the partial melt composition to be assimilated. Based on the partition coefficients of the crystallised mineralogy generated with the major element compositions, it calculates the trace element concentrations and selected isotope ratios at each step for both the wall rock and the magma. To run each model, the following are required: (i) a starting composition that represents the magma before AFC occurs, (ii) a wall rock composition that will be partially melted and assimilated, (iii) a system pressure, (iv) the initial temperatures of both bodies, (v) wall rock mass, and (vi) percolation threshold (FmZero). Modelling finishes when thermal equilibrium is reached between the magma and wall rock, or with a hardstop temperature selected by the user. Limitations for the MCS include those inherent to MELTS such as the stabilisation of water-bearing minerals and the user input data. Input data depends on the availability of

well-constrained data for the initial magma and wall rock compositions, including their water contents.

4.5 Results

4.5.1 Major and trace elements

Major oxide compositions are presented in **Table 4.2**, **Figure 4.2** and **Figure 4.3**, and are consistent with previously published data from the TVZ (Beier et al., 2017; Briggs et al., 1993; Browne et al., 1992; Cameron et al., 2010; Cole et al., 2010; Deering et al., 2011; Gamble et al., 1993; Graham and Hackett, 1987; Milner et al., 2003; Nairn et al., 2004; Nakagawa et al., 1998; Price et al., 2012; Schmitz and Smith, 2004; Shane et al., 2007; Shane et al., 2005; Smith et al., 2002; Sutton et al., 1995; Waight et al., 2017). The basalts and three basaltic andesites correspond to HAB according to the definition of Crawford et al. (1987), are found in the central TVZ, and vary in Mg# (molar 100*(Mg/(Mg + Fe^{2+})) from 74 to 50. Andesites, which show diverse crystal histories, are found across the whole volcanic zone and show Al_2O_3 compositions (~16 wt%) similar to HAB, with a Mg# range from 70 to 46. Dacites and rhyolites are more abundant in the central TVZ and show a Mg# range from 58 to 11. As a general trend, SiO_2 compositions increase with the decrease of Mg# but three groups can be observed: basalts with ~50 wt% SiO_2; an intermediate group, with ~57 wt% SiO_2 corresponding to andesites and basaltic andesites, and a more felsic group, with >63 wt% SiO_2 corresponding to dacites and rhyolites. Andesites and basaltic andesites, as well as two dacitic samples with unusually high Mg#, have the same Mg# range as basalts. Variation diagrams (**Figure 4.3**) show the enrichment of K_2O and Na_2O and depletion of MgO, CaO and FeO_t with decreasing Mg#.

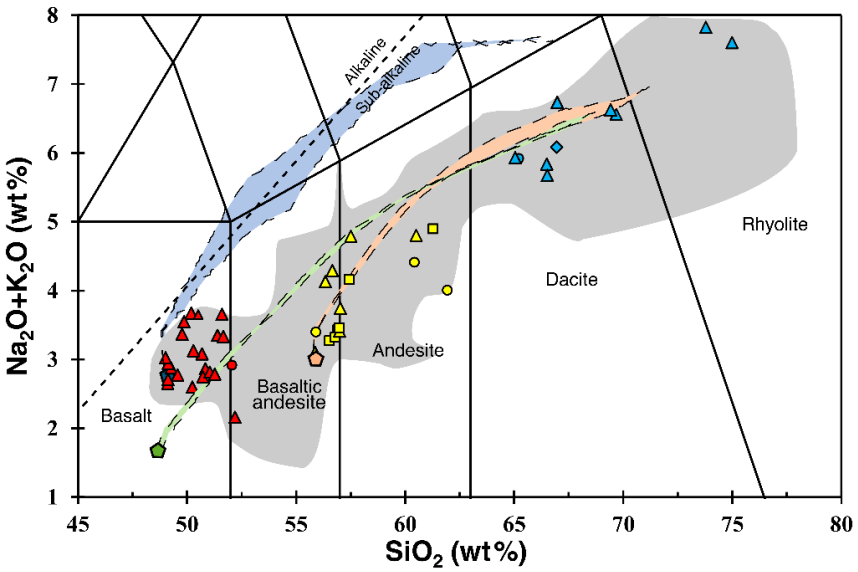

Figure 4.2: Total alkali versus silica (TAS) classification for extrusive igneous rocks (Le Maitre et al., 2002), dashed line discriminates between alkaline and sub-alkaline suites (Irvine & Baragar, 1971). Rhomb represents Maungatautari, to the west of the TVZ. The grey area corresponds to previously reported data for the TVZ (Beier et al., 2017, Briggs et al., 1993, Browne et al., 1992, Cameron et al., 2010, Cole et al., 2010, Deering et al., 2011, Gamble et al., 1993, Graham & Hackett, 1987, Milner et al., 2003, Nairn et al., 2004, Nakagawa et al., 1998, Price et al., 2012, Schmitz & Smith, 2004, Shane et al., 2007, Shane et al., 2005, Smith et al., 2002, Sutton et al., 1995, Waight et al., 2017). Squares correspond to southern TVZ, triangles to central TVZ and circles to northern TVZ; red samples are mafic, yellow are intermediate, and blue are felsic. Coloured areas correspond to the models of MCS-AFC.

Basalts have Cr contents from ~20 to 140 µg/g, basaltic andesites from 23 to 260 µg/g, andesites from 14 to 30 µg/g, and the felsic members have a maximum of 18 µg/g. For nickel, basalts range from 10 to 37 µg/g, while basaltic andesites range between 25 and 60 µg/g, and andesites and felsic members have a maximum of 11 µg/g, with most of them below detection limits. An exception in the felsic members for both Cr and Ni is Hipaua, which has 38 µg/g and 28 µg/g, respectively, in line with its high Mg#. Trace element ratios have similar behaviour to major elements (**Figure 4.4**), where Th/La, La/Yb and Nb/Yb show a range of ratios for the same silica content in the mafic and intermediate members (~50 and 57 wt% SiO_2). Light rare earth elements (LREE) show enrichment ($(La/Sm)_N$ = 1.5 to 5) as well as flat normalised patterns in the heavy rare earth elements (HREE, $(Gd/Yb)_N$ ~1.3). Europium negative anomalies in the most differentiated samples are also seen (Eu/Eu* = 1 to 0.4) (**Figure 4.5**a). Trace element compositions of all samples show negative Nb-Ta anomalies, typical of arc settings

(**Figure 4.5**b). Lead has a noticeable positive anomaly that is more significant in felsic samples ($(Ce/Pb)_N$ = 0.5 to 0.12); Sr and Nd have minor positive anomalies in a few samples, and Ti shows negative anomalies that are more significant in the felsic samples.

4.5.2 Lead and Strontium isotope ratios

When comparing Pb isotope ratios with SiO_2 compositions (**Figure 4.6**a-c), an important variation is seen in all three isotope ratios for the mafic and intermediate samples at a given silica content (~50 and ~57 wt% SiO_2, respectively). For $^{206}Pb/^{204}Pb$, mafic samples vary from ~18.774 to 18.837 and intermediate samples vary from ~18.767 to 18.841; $^{207}Pb/^{204}Pb$ varies from ~15.613 to 15.630 in mafic samples, and from ~15.604 to 15.637 in intermediate samples; $^{208}Pb/^{204}Pb$ varies from ~38.644 to 38.732 in the mafic group and from ~38.646 to 38.759 in the intermediate group. Some felsic members show similar isotope signatures to mafic and intermediate samples, while others are more radiogenic. The least radiogenic samples correspond to those of older andesitic volcanoes (Titiraupenga and Rolles Peak) followed by mafic members and members with high Mg# (Ohakune, Ohakune lakes, Acacia Bay, K-TRIG, TramRoad, Punatekahi and Waimarino). The most radiogenic samples correspond to the younger and more felsic Motuoapa Dacite and Rhyolite. The measured or approximated age of the samples is shown in **Table 4.1**.

A similar behaviour is seen in the strontium isotopic ratio ($^{87}Sr/^{86}Sr$) (**Figure 4.6**d). In general, felsic samples are more radiogenic ($^{87}Sr/^{86}Sr$ ~0.7060) than their mafic counterparts ($^{87}Sr/^{86}Sr$ ~0.7040), but the suite does not follow a monotonous trend of enrichment. Samples from the mafic and intermediate groups show the same range of $^{87}Sr/^{86}Sr$ varying from 0.7040 to 0.7053, while some felsic samples have similar isotopic

compositions to mafic and intermediate samples, and some others are more radiogenic. A broadly linear trend is observed in the lead isotopic space, although it does not always correspond to an increase in SiO_2 content (**Figure 4.7**a and b).

Table 4.4: Pb-Sr MC-ICP-MS isotopic ratios results. Uncertainties are 2SE and are comparable to the 2SD based on replicate analyses. All uncertainties are in the last 2 decimal places.

Sample name	$^{87}Sr/^{86}Sr$	$^{206}Pb/^{204}Pb$	$^{207}Pb/^{204}Pb$	$^{208}Pb/^{204}Pb$
KT1	0.704855±22	18.7937±22	15.6180±20	38.6689±59
PTH	0.704612±18	18.7737±16	15.6217±19	38.6642±67
AB	0.704686±20	18.7829±25	15.6126±22	38.6443±80
TR	0.704229±19	18.7903±24	15.6145±22	38.6457±72
POI	0.704339±23	18.8144±19	15.6204±20	38.6868±59
KAI	0.704120±17	18.8279±24	15.6233±22	38.6894±75
KIN	0.704414±23	18.8156±20	15.6182±17	38.6818±63
MAT	0.704651±18	18.8371±21	15.6313±20	38.7319±69
MTH	0.705272±23	18.8092±21	15.6301±21	38.7151±78
AKA	0.705167±21	18.8401±21	15.6352±21	38.7461±69
RP	0.704352±22	18.7649±15	15.6038±18	38.6479±63
OL	0.704341±22	18.7865±19	15.6152±20	38.6733±65
O1	0.704284±22	18.7778±26	15.6207±23	38.6762±76
TTR	0.704537±21	18.7666±20	15.6140±20	38.6462±73
PIH	0.704861±20	18.8412±21	15.6370±21	38.7587±72
EDG	0.706123±22	18.8318±18	15.6373±17	38.7483±49
TP	0.705225±22	18.8406±24	15.6392±22	38.7590±83
MWH	0.706214±17	18.8427±19	15.6392±17	38.7580±61
WKK	0.705779±14	18.8551±15	15.6396±19	38.7625±71
MTT	0.704518±16	18.8457±17	15.6252±17	38.7311±51
HIP	0.704896±19	18.8119±21	15.6197±24	38.7021±81
MM	0.705823±21	18.8499±19	15.6394±18	38.7654±67
MD	0.706401±17	18.8639±20	15.6448±19	38.7903±67
MR	0.707054±18	18.8708±22	15.6477±21	38.7986±64
PUK	0.705431±23	18.8464±25	15.6374±24	38.7519±78
WAI	0.704346±23	18.7912±26	15.6234±25	38.6977±85
KHP	0.704303±16	18.8039±25	15.6301±24	38.7093±78
PKE	0.704817±15	18.8131±21	15.6316±19	38.7219±67
KAH	0.705237±17	18.8208±22	15.6324±22	38.7264±73

4.6 **Discussion**

The drivers of magmatic differentiation in volcanic arcs have long been a topic of research and debate. Traditional AFC models were constructed using arithmetic approaches that considered the chemical behaviour of a variety of elements and isotopes (*e.g.*, DePaolo, 1981). Although source processes have been proposed to generate the chemical and

isotopic diversity found in mafic magmas of the TVZ (*e.g.*, Gamble et al., 1993; Waight et al., 2017), the generation of the chemical and isotopic compositions of more evolved members has tended to favour AFC from a basaltic parent together with magma mixing (*e.g.*, Gamble et al., 1990; Graham and Hackett, 1987). While these AFC models have provided important insights into magmatic evolution processes and first-order thermodynamic constraints based on the value of 'r', they have limitations compared to more recent tools build around robust thermodynamic constraints, such as MELTS, EC-AFC and MCS, which were previously unavailable. Here, thermodynamically constrained MCS-AFC modelling is performed to test the extent to which AFC influences the magmatic evolution of the TVZ. Furthermore, the viability of a slab-link in the TVZ magmatism, as has previously been proposed in several studies (*e.g.*, Gamble et al., 1993; Waight et al., 2017) is also evaluated, taking into consideration the occurrence of tectonic erosion in the Hikurangi margin (Barker et al., 2009; Collot and Davy, 1998; Collot et al., 1996; Lewis et al., 1998; Pedley et al., 2010).

4.6.1 Modelled AFC processes in the TVZ

Firstly, an attempt was made to reproduce the major oxide variability of the TVZ magmas, as this, together with intensive parameters (*e.g.*, pressure and temperature), controls the crystallising mineral phases. Secondly, the trace element concentrations were calculated at each step based on the mineral phases derived from the major element models. The behaviour of trace elements is controlled for each step by the elemental partition coefficient for each mineral at a given temperature, for each body (magma and wall rock). The Sr and Pb isotope ratios are calculated for each step depending on the wall rock partial melt generated before assimilation. All modelling parameters and results are presented in **Appendix B**, simplified in **Table 4.5**.

In attempting to reproduce the TVZ chemical range, three starting parental melt compositions were used based on: (i) the lowest silica sample (49 wt% SiO_2, Mg# = 59) in the TVZ, *i.e.*, Kakuki basalt (major and trace element concentrations from Zellmer et al. (2020) and Sr-Pb isotope ratios from Price et al. (2012)); (ii) a primitive sample from the Kermadec Volcanic Zone (49 wt% SiO_2, Mg# = 57), representative of a magma that is unlikely to have experienced any interaction with Torlesse crust, *i.e.*, Rumble IV (major and trace element concentrations and Sr-Pb isotope ratios from Gamble et al. (1996); Gamble et al. (1993)), and (iii) a high Mg# and less radiogenic intermediate sample (56 wt% SiO_2, Mg# = 68), *i.e.*, Karangahape basaltic andesite (major and trace element concentrations from Zellmer et al. (2020), Sr-Pb isotope ratios from this study). The water content of the parental melt was assumed to be low with ~1 wt% H_2O, consistent with previous studies (Arpa et al., 2017; Kilgour et al., 2013; Lormand et al., 2020; Zellmer et al., 2020).

For wall rock compositions, those of the Kaweka and Pahau sub-terranes of the Torlesse basement from Price et al. (2015) were selected, representing the main crustal components beneath the TVZ (**Figure 4.1**a). Although the wall rock mass is adjustable, the magma-to-wall rock mass ratio was set to 1:1 for all models, representing an equal amount of starting magma and wall rock to heat. A multi-stage approach similar to that of Heinonen et al. (2019) was employed: for each starting composition, two pressure paths were modelled based on the variation in crustal thickness. Decreasing pressure steps represent magma ascent in the crust followed by interaction with a new wall rock. Wall rock temperatures were chosen based on the need for early assimilation to reproduce the observed behaviour in the mafic members of the TVZ, thus each step had temperatures close to the crust solidus. The first path started at 900 MPa (~30 km depth, crustal

thickness in the southern TVZ (Salmon et al., 2011)) with a wall rock water content of ~0.6 wt%, a starting temperature of 700 °C, and a hardstop temperature of 1160 °C or when thermal equilibrium is achieved. The second stage was at 500 MPa (~16 km depth), with a wall rock water content of ~1 wt% and a starting temperature of 650 °C, with a hardstop temperature of 980 °C or when thermal equilibrium was reached. The final third stage was at 200 MPa (~7 km depth), with a wall rock water content of ~2 wt%, a starting temperature of 600 °C, and a hardstop temperature of 700 °C or when thermal equilibrium was achieved. For the second modelled path, parameters were identical to the previous model except for starting at shallower depths (500 – 200 MPa) due to the thinner crust present in the central and northern TVZ (~16 km depth, Stratford and Stern (2004)) compared to the southern TVZ.

Within the Torlesse terrane, the Pahau subterrane is dominant in the lower portion of the crust, while the Kaweka subterrane is dominant in the upper portion of the crust (Price et al., 2015). Thus, the composition of the Pahau subterrane was used for the models at 900 MPa and 500 MPa, while that of the Kaweka subterrane was used for the 200 MPa models, both after Price et al. (2015). The Kaweka subterrane has a higher SiO_2 content and is more radiogenic in both Sr- and Pb- isotope systems than the Pahau subterrane, thus the assimilation of these terranes yields different results. Trace element partition coefficients (Kd) employed were taken from the GERM repository (see **Appendix B**, Bacon and Druitt, 1988; Bea et al., 1994; Boudreau, 1999; Ewart and Griffin, 1994; Green et al., 2000; Mahood and Hildreth, 1983; Olin and Wolff, 2010; Sisson and Bacon, 1992; Stimac and Hickmott, 1994; Taylor et al., 2015; Tiepolo et al., 2007). A summary of the modelling is presented in **Table 4.5**.

Mineral phases present in these models mostly fit those observed in the samples. Mafic samples show dominance in plagioclase (pl) and clinopyroxene (cpx) with minor orthopyroxene (opx), Fe-Ti oxides and olivine (ol). Intermediate samples have abundant pl, cpx and opx with minor Fe-Ti oxides and trace amphibole. Felsic samples show pl, cpx and opx with minor Fe-Ti oxides, as well as trace amphibole and biotite in some samples. The presence of trace amounts of ol in mafic magmas, amphibole in intermediate magmas, and amphibole and biotite in felsic magmas are not reproduced by the models presented here. However, these minerals are only present in some samples and in minor proportions, thus their effect on the chemistry of the magmas can be assumed as being insignificant.

4.6.1.1 Modelled major element compositions

A detailed compilation of the crystallising phases, their relative proportions and the assimilated volumes is presented in **Table 4.5**. For models starting at 900 MPa, an increase in CaO wt.% is caused due to the fractionation of cpx in Kakuki and Rumble IV, while the fractionation of opx in Karangahape causes a decrease in CaO until cpx becomes stable. Except for CaO and MgO, all major oxides increase during these early stages of crystallisation (**Figure 4.3**). At the end of this first step, Kakuki had assimilated 8% crust and fractionated 38% crystalline material, Rumble IV assimilated 9% crust and fractionated 46% crystals, while Karangahape assimilated 11% crust and fractionated 35% crystals. During the second step, at 500 MPa, the fractionation of pl causes a decrease in CaO and Al_2O_3, and an increase of TiO_2, at different rates for each starting composition. When fractionation of cpx occurs, it causes the decrease to be more gradual. At the end of this second step, Kakuki had assimilated an additional 9% crust and fractionated 29% crystalline material, Rumble IV assimilated 9% crust and fractionated 25% crystals, while Karangahape assimilated 8% crust and fractionated 22% crystals.

During the third step, Na_2O decreases due to the fractionation of more sodic plagioclase. After step three, Kakuki assimilated an extra 18% crust and fractionated 17% crystalline material, Rumble IV assimilated 18% crust and fractionated 16% crystals, while Karangahape assimilated 23% crust and fractionated 20% crystals. In total, Kakuki assimilated 35% crust and fractionated 84% crystalline material. Rumble IV assimilated 36% crust and fractionated 87% crystals. Karangahape assimilated 42% assimilation and fractionated 77% crystals (**Table 4.5**).

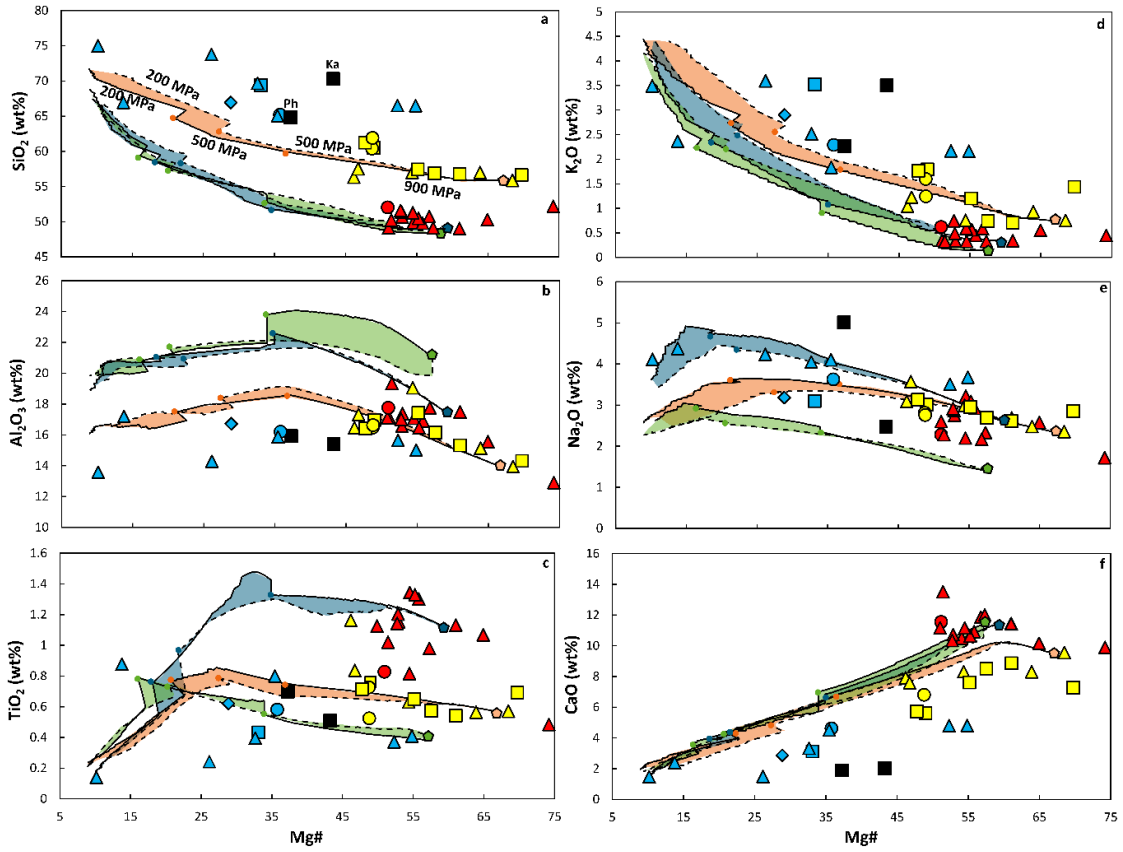

Figure 4.3: Major oxide variation diagrams for (a) SiO_2, (b) Al_2O_3, (c) TiO_2, (d) K_2O, (e) Na_2O, (f) CaO wt%, with Mg# as differentiation index (molar 100*(Mg/(Mg + Fe^{2+})) calculated using 0.8998 ferric iron). Pentagons represent the different starting compositions: Blue corresponds to Kakuki, green to Rumble IV and orange to Karangahape. The coloured shaded areas correspond to these starting compositions, continuous lines represent a starting pressure of 900 MPa followed by 500 MPa and 200 MPa during the first, second and third stages of AFC, respectively; discontinuous lines represent a starting pressure of 500 MPa followed by 200 MPa for the first and second stages, respectively. Coloured circles represent the end of each step. Squares correspond to southern TVZ, triangles to central TVZ and circles to northern TVZ; red samples are mafic, yellow are intermediate, and blue are felsic; Maungatautari is represented as a rhomb. Ka = Kaweka subterrane, Ph = Pahau subterrane.

Table 4.5: Multi-step AFC modelling results. See footnote* for units and abbreviations.

	SC	P	T	Mineral phases				Fractionated		Assimilated		Liquid
				MIN	Tin	Tout	mu	F	MC	A	MC	
1	Kakuki	900	1292	Cpx	1292	N/A	38	38	38	8	8	70
		500	1126	Pl	1126	N/A	28	42	29	13	9	71
				Cpx	1095	1075	3.5					
				Spl	1090	N/A	3.4					
				Opx	1062	N/A	5.6					
				Ap	1034	N/A	0.4					
				RhOx	1026	N/A	0.6					
		200	977	Spl	977	N/A	1.3	34	17	37	18	102
				Pl	962	N/A	27					
				RhOx	962	N/A	0.7					
				Ol	937	N/A	5.6					
				Opx	804	799	0.1					
2	Kakuki	500	1229	Cpx	1229(1040)	1075(1018)	38	66	66	20	20	54
				Pl	1114	N/A	22					
				Spl	1087	N/A	2.4					
				Opx	1074	N/A	4					
				Ap	1034	N/A	0.2					
				RhOx	1018	N/A	0.3					
		200	995	Spl	995	N/A	1.4	35	19	37	20	102
				RhOx	985	N/A	1					
				Pl	980	N/A	27					
				Opx	955	820	2.4					
				Ol	940	N/A	3.5					
3	KHP	900	1362	Opx	1362	1282	9.7	35	35	11	11	76
				Cpx	1282	N/A	25					
		500	1102	Pl	1102	N/A	19	29	22	10	8	81
				Cpx	1097	1011	7.5					
				Spl	1030	N/A	0.9					
				Opx	1019	N/A	1.8					
		200	969	Spl	969	N/A	1.3	32	20	37	23	104
				Pl	955	N/A	25.5					
				Opx	935	N/A	4					
				RhOx	930	N/A	0.8					
				Ol	814	N/A	0.4					
4	KHP	500	1295	Opx	1295(1040)	1196(N/A)	11.2	49	49	21	21	72
				Cpx	1212	1040	28					
				Pl	1073	N/A	9.7					
				Spl	1035	N/A	0.3					
		200	1009	Spl	1009	N/A	1.9	35	25	37	27	102
				Pl	999	N/A	27					
				Opx	979	N/A	5.4					
				RhOx	913	N/A	0.6					
5	Rumble IV	900	1289	Cpx	1289	N/A	32.5	46	46	9	9	63
				Pl	1241	N/A	10					
				Grt	1172	N/A	3.4					
		500	1153	Pl	1153	N/A	28	40	25	14	9	74
				Cpx	1089	1017	5.7					
				Opx	1033	999	1.5					
				Grt	1005	N/A	5.3					
		200	971	Spl	971	N/A	1.4	34	16	37	18	102
				Pl	961	N/A	26.2					
				RhOx	931	N/A	0.7					
				Ol	926	N/A	5.6					
				Opx	849	799	0.6					
6	Rumble IV	500	1248	Pl	1248(1165)	1182(N/A)	31	67	67	20	20	53
				Cpx	1223	N/A	36					
		200	1001	Pl	1001	N/A	25	36	19	36	19	100
				Spl	996	N/A	1.9					
				Opx	971(883)	946(819)	2.4					
				Ol	951	N/A	5.3					
				RhOx	893	N/A	0.4					

*SC = starting composition, P = pressure (MPa), T = temperature (°C), MC = mass constrained, Tin = Temperature the mineral appears, Tout = Temperature the mineral stops crystallising. Fractionation and assimilation are in mass units (mu) respective to the initial 100 mu of melt and wall rock; mass constrained is calculated based on the total liquid and wall rock masses left from the previous step. Mineralogy: Cpx = clinopyroxene, Opx = orthopyroxene, Pl = Plagioclase, Spl = spinel, Grt = Garnet, Ap = Apatite, Ol = Olivine, RhOx = rhombohedral oxides.

For models starting at 500 MPa, the major oxide behaviour is parallel to that of the previous model, but with slightly lower concentrations of TiO_2, Na_2O and CaO and higher concentrations of K_2O, Al_2O_3 and SiO_2 (**Figure 4.3**). At the end of this first step, Kakuki had assimilated 20% crust and fractionated 66% crystalline material, Rumble IV assimilated 20% crust and fractionated 67% crystals, while Karangahape assimilated 21% crust and fractionated 49% crystals. At 200 MPa the major oxide behaviour is also parallel to that of the previous model, with the same considerations as the first step. At the end of this second step, Kakuki assimilated an extra 20% crust and fractionated 19% crystalline material, Rumble IV assimilated 19% crust and fractionated 19% crystals, while Karangahape assimilated 27% crust and fractionated 25% crystals. After both steps, Kakuki starting composition assimilated a total of 40% crust and fractional crystallisation was 85%, Rumble IV assimilated 39% and fractionated 86%, and Karangahape assimilated 48% and fractionated 74% (**Table 4.5**).

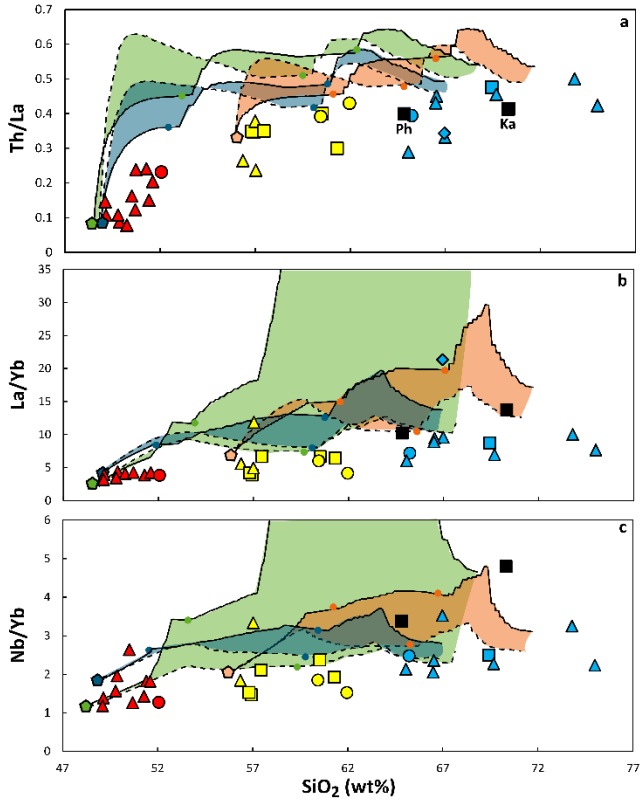

Figure 4.4: Bivariate variation diagrams for selected trace element ratios (a) Th/La, (b) Nb/Yb and (c) La/Yb, vs SiO_2 as differentiation index. Pentagons represent the different starting compositions: Blue corresponds to Kakuki, green to Rumble IV and orange to Karangahape. The coloured shaded areas correspond to these starting compositions, continuous lines represent a starting pressure of 900 MPa followed by 500 MPa and 200 MPa during the first, second and third stages of AFC, respectively; discontinuous lines represent a starting pressure of 500 MPa followed by 200 MPa for the first and second stages, respectively. Coloured circles represent the end of each step. Squares correspond to southern TVZ, triangles to central TVZ and circles to northern TVZ; red samples are mafic, yellow are intermediate, and blue are felsic; Maungatautari is represented as a rhomb. Ka = Kaweka subterrane, Ph = Pahau subterrane.

4.6.1.2 Modelled trace elements

Regardless of the starting pressure, either 900 MPa or 500 MPa, the behaviour of the trace element ratio patterns is very similar in all models (**Figure 4.4**). Of the modelled trace element ratios, Th/La seems to be the most sensitive to the assimilation process. Compared to La, Th behaves more mobile when the wall rock melts. This is reflected in an extremely rapid increase of Th/La due to a significant increase in the Th content of the magma. This is more pronounced in the 500 MPa models due to a higher content of Th in the wall rock partial melt and a higher addition of partial melt to the magma triggered by the high temperature of the magma in a lower pressure/temperature environment. While this ratio increases significantly in the MCS-AFC models, this behaviour is not observed in the TVZ samples, where the increase is more gradual. The La/Yb and Nb/Yb ratios also show an increase when assimilation begins, followed by a decrease when partial melting of the wall rock increases and thus Yb becomes more abundant in the partial melt. Rumble IV models show a particular behaviour for La/Yb and Nb/Yb that is not followed by the other two starting compositions (**Figure 4.4**). The wall rock partial melt composition is similar for all three starting compositions; however, Rumble IV has a ~50% lower Yb concentration than the other two starting compositions. When assimilation occurs in this magma, the La/Yb and Nb/Yb ratios rapidly increase due to its lower Yb concentration compared to the high La and Nb concentrations in the partial melts.

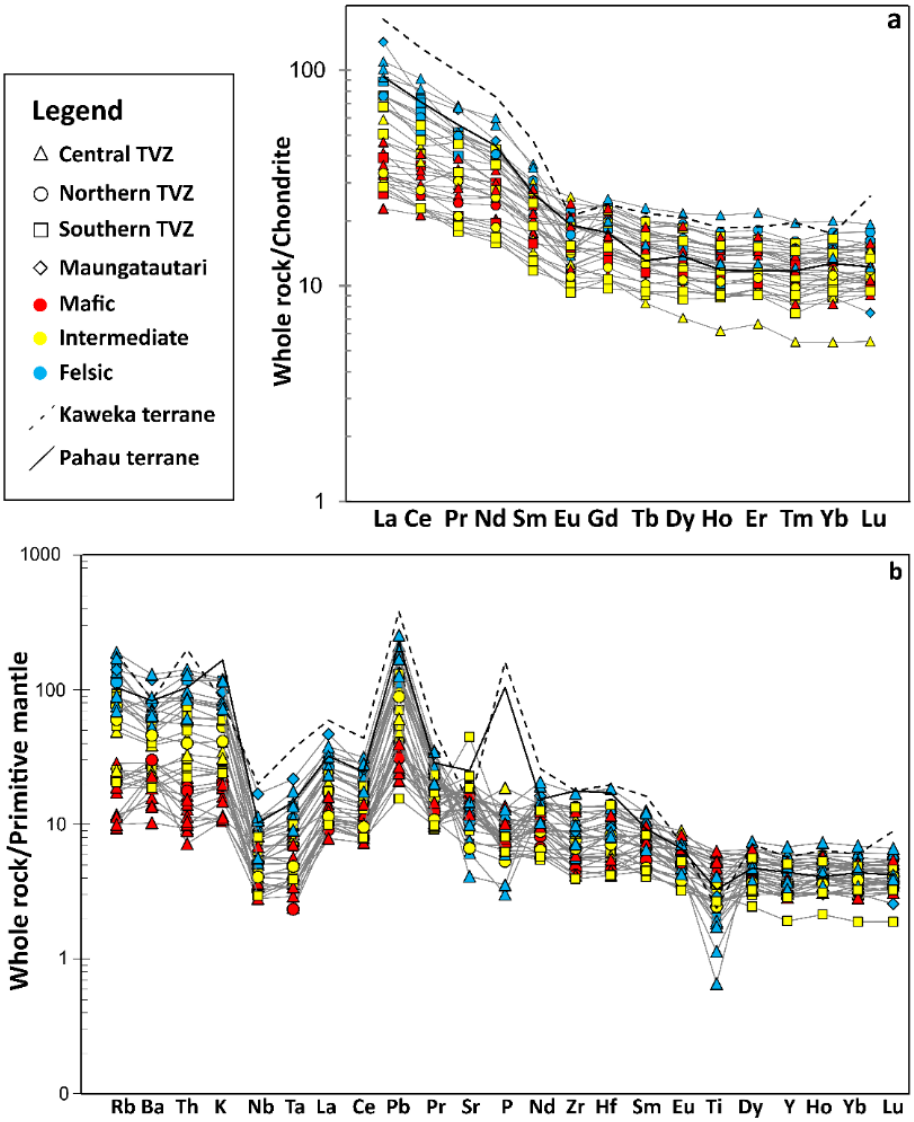

Figure 4.5: (a) Rare earth elements (REE) normalized to chondrite, (b) Multi-element diagram normalised to the primitive mantle composition of Sun and McDonough (1989). Squares correspond to southern TVZ, triangles to central TVZ and circles to northern TVZ; red samples are mafic, yellow are intermediate, and blue are felsic; Maungatautari is represented as a rhomb. Continuous lines correspond to the Pahau terrane composition and discontinuous lines to the Kaweka terrane, after Price et al. (2015).

4.6.1.3 Modelled isotope ratios

The modelled behaviour of the Sr-Pb isotope ratios is similar at different pressures and starting compositions (**Figure 4.6**). The narrow difference in the Sr isotopic composition of the magma and the Pahau wall rock causes the magma to become more radiogenic but with a minimal increase even at 20% of assimilation. In contrast, the large $^{87}Sr/^{86}Sr$ isotopic difference between the magma and Kaweka wall rock causes a significantly more radiogenic magma after assimilation. Models following a lower-pressure constraint for

the same starting composition become marginally more radiogenic than their higher-pressure counterparts due to earlier assimilation. The behaviour observed in the TVZ data can partially be reproduced by these models in the case of the least radiogenic members and the felsic samples; however, the heterogeneities observed at ~50 and ~57 wt% SiO_2 are not reproduced by any of the models.

The lead isotope ratios ($^{208}Pb/^{204}Pb$, $^{207}Pb/^{204}Pb$ and $^{206}Pb/^{204}Pb$) are very sensitive to crustal inputs. For all three starting compositions, the $^{206}Pb/^{204}Pb$ and $^{208}Pb/^{204}Pb$ isotope ratios increase when assimilation starts but rapidly become stable as the magma gets closer to the isotopic composition of the Pahau terrane (**Figure 4.6**). Particularly for Rumble IV, the increase is larger as this starting composition is less radiogenic than the other two compositions. Karangahape has similar $^{206}Pb/^{204}Pb$ and $^{208}Pb/^{204}Pb$ isotope ratios to the Pahau subterrane, causing minor increases in these ratios. On the other hand, for Karangahape $^{207}Pb/^{204}Pb$ ratios decrease as the magma is more radiogenic than the wall rock, while Kakuki and Rumble IV show a similar behaviour as with the other ratios. At lower pressure, when the Kaweka terrane is assimilated, all three Pb isotope ratios become more radiogenic regardless of the starting composition. As with the Sr isotopic ratio, these MCS-AFC models only reproduce the least radiogenic members of the observed data from the TVZ and do not explain the heterogeneities observed at the mafic and intermediate members (~50 and 57 wt% SiO_2). In conclusion, AFC in the overriding crust alone is not able to explain the isotopic diversity of the eruption products, pointing to an isotopic diversity of the primary melts.

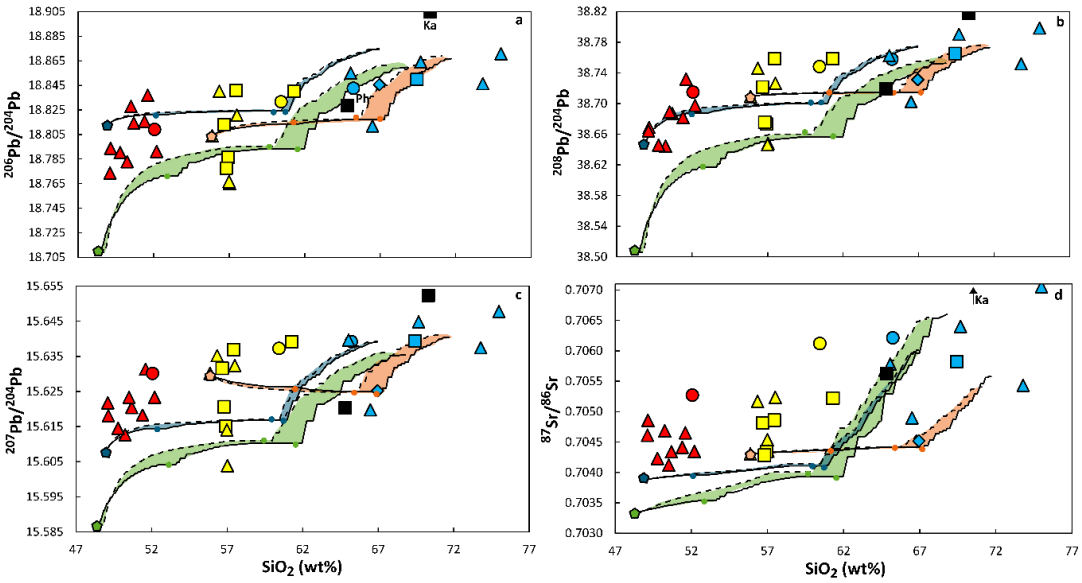

Figure 4.6: Lead isotopic ratios (a) $^{206}Pb/^{204}Pb$, (b) $^{208}Pb/^{204}Pb$ and (c) $^{207}Pb/^{204}Pb$ plotted against SiO_2 wt%; (d) Strontium isotopic ratio ($^{87}Sr/^{86}Sr$) plotted against SiO_2 wt%. Pentagons represent the different starting compositions: Blue corresponds to Kakuki, green to Rumble IV and orange to Karangahape. The coloured shaded areas correspond to these starting compositions, continuous lines represent a starting pressure of 900 MPa followed by 500 MPa and 200 MPa during the first, second and third stages of AFC, respectively; discontinuous lines represent a starting pressure of 500 MPa followed by 200 MPa for the first and second stages, respectively. Coloured circles represent the end of each step. Squares correspond to southern TVZ, triangles to central TVZ and circles to northern TVZ; red samples are mafic, yellow are intermediate, and blue are felsic; Maungatautari is represented as a rhomb. Ka = Kaweka subterrane, Ph = Pahau subterrane. Uncertainties of isotopic ratios are smaller than symbol size.

4.6.1.4 MCS-AFC modelling limitations

The MCS-AFC models presented here have the following technical limitations: i) The water content of the wall rocks is not well constrained and may not be suitable for all three starting compositions. For consistency, water content was selected to achieve the same wall rock water content at a given pressure for the different models. ii) The modelled presence or absence of minerals may contrast with the observed mineral assemblages of the samples. For example, the general absence of olivine in the models contrasts with its presence in the samples, and the presence of amphibole in some felsic samples also contrasts with the modelled mineralogy. Other minerals appear at the final stages of the modelling, such as garnet and spinel in minor proportions, but are not observed in the samples. iii) Although the water content of the starting compositions is low, these models only provide limited information on the case of the more water-rich felsic endmembers

due to difficulties in modelling their mineral assemblages. iv) The existence of more complex paths with more magma chambers than those represented in the models may influence the modelling results.

Other limitations include the unknown lithological structure of the crust under the TVZ. In particular, although the most significant members of the crust correspond to the Pahau and Kaweka subterranes of the Torlesse terrane, as well as the Waipapa terrane (Price et al., 2015), other under-reported members may also be present. For example, older volcanic units may be assimilated in the intermediate and felsic members of the TVZ (Price et al., 2005). Further, lower crustal meta-igneous xenoliths occur in magmas from the southern TVZ (Price et al., 2012) and their contribution to the lithologies may also lead to chemical heterogeneity that is not captured by the models. Although these lithologies may be of importance in the transcrustal processes of the TVZ, there are no systematic constraints on their chemical and isotopic compositions, and their distribution within the crust. Thus, the lack of this information makes using these lithologies as wall rock compositions difficult at present. Another important limitation of the MCS-AFC models is that the samples investigated here are not derived from the same volcanic edifice, therefore they do not represent an approximation of a singular liquid line of descent (LLD). Thus, the models reported here are not valid as individual LLDs, and only serve as a general overview of the thermodynamically constrained AFC paths considering the different starting compositions that may be involved in the general magmatic process of the TVZ as a whole.

However, despite these limitations, the MCS-AFC modelling results reveal that several challenges arise in terms of the genesis of the TVZ magmas by AFC alone. Mafic magmas

show variations in their major oxide compositions, trace element concentrations, and Sr-Pb isotope ratios that cannot be reproduced by any of the presented MCS-AFC models. The Sr-Pb isotopic heterogeneities at ~50 wt% and ~57 wt% SiO_2 cannot be reproduced by any of the starting compositions, regardless of the pressure employed. The variations in the major and trace element concentrations, as well as Sr-Pb isotope ratios of the mafic magmas (~50 wt% SiO_2) of the TVZ (**Figure 4.6**), indicate an isotopically heterogeneous mantle source, consistent with observations from previous studies (*e.g.*, Gamble et al., 1993; Rooney and Deering, 2014). Some intermediate samples (~57 wt% SiO_2) have high Mg# and major and trace elements concentrations as well as isotopic signatures that cannot be achieved through AFC when using a mafic starting composition but are instead reproduced if the primary melt has intermediate affinities.

To reproduce the felsic endmembers, the MCS-AFC modelling shows that fractional crystallisation needs to be up to ~90 % together with wall rock assimilation between 30 and 50 %, much higher than the 70 % fractional crystallisation and 15-25 % assimilation proposed by McCulloch et al. (1994). To generate the volumetrically dominant (>95 %) felsic volcanism from mafic magmas that undergo extensive AFC, the original volume of magma would be close to 10 times that of the observed erupted felsic volume. The occurrence of AFC and mixing for the generation of the felsic endmembers is supported by the complex history of their crystals, as well as their chemical characteristics, such as negative Eu anomalies (1 to 0.4 Eu/Eu*). However, the large amounts of assimilation required here (up to 50%), that is unlikely to occur in a thin crust, together with large amounts of fractionation needed (up to 90%), indicate that source heterogeneities are also likely to play an important role in the isotope characteristics of felsic magmas, though to a lesser extent than for mafic and intermediate magmas.

In summary, although some crustal assimilation and magma mixing has been reported to occur at mid-crustal levels in the southern TVZ with evident diversity in crystal histories and incorporation of crustal material (Beier et al., 2017; Conway et al., 2020; Svoboda et al., 2021), our thermodynamically constrained AFC alone cannot reproduce some of the fundamental chemical variations observed in the TVZ and additional processes are required to adequately explain the datasets.

4.6.2 Slab-mantle interactions

The Sr-Pb isotope characteristics of the mafic and some intermediate members cannot be reproduced following the presented MCS-AFC approach or transcrustal mixing, and instead agree with the presence of mantle heterogeneities as previously reported (Gamble et al., 1996; Gamble et al., 1993; Graham et al., 1995; Rooney and Deering, 2014). Bivariate plots of the lead isotopic ratios ($^{206}Pb/^{204}Pb$, $^{207}Pb/^{204}Pb$ and $^{208}Pb/^{204}Pb$) of volcanic samples yield a broadly linear trend (**Figure 4.7a, b**) in the datasets presented here, especially in the composition reported by Sas et al. (2021b). Such a broadly linear trend in Pb isotope space suggests that these magmas may be related to the mixing of two compositionally distinct endmembers: a mantle component and a crustal component. Both transcrustal and source processes are involved in the magma generation and evolution of the TVZ, and thus this raises the question of how much of this crustal component is caused by the former, and how much is caused by the latter as input of crustal material in the form of subducted sediments and/or tectonically eroded crust.

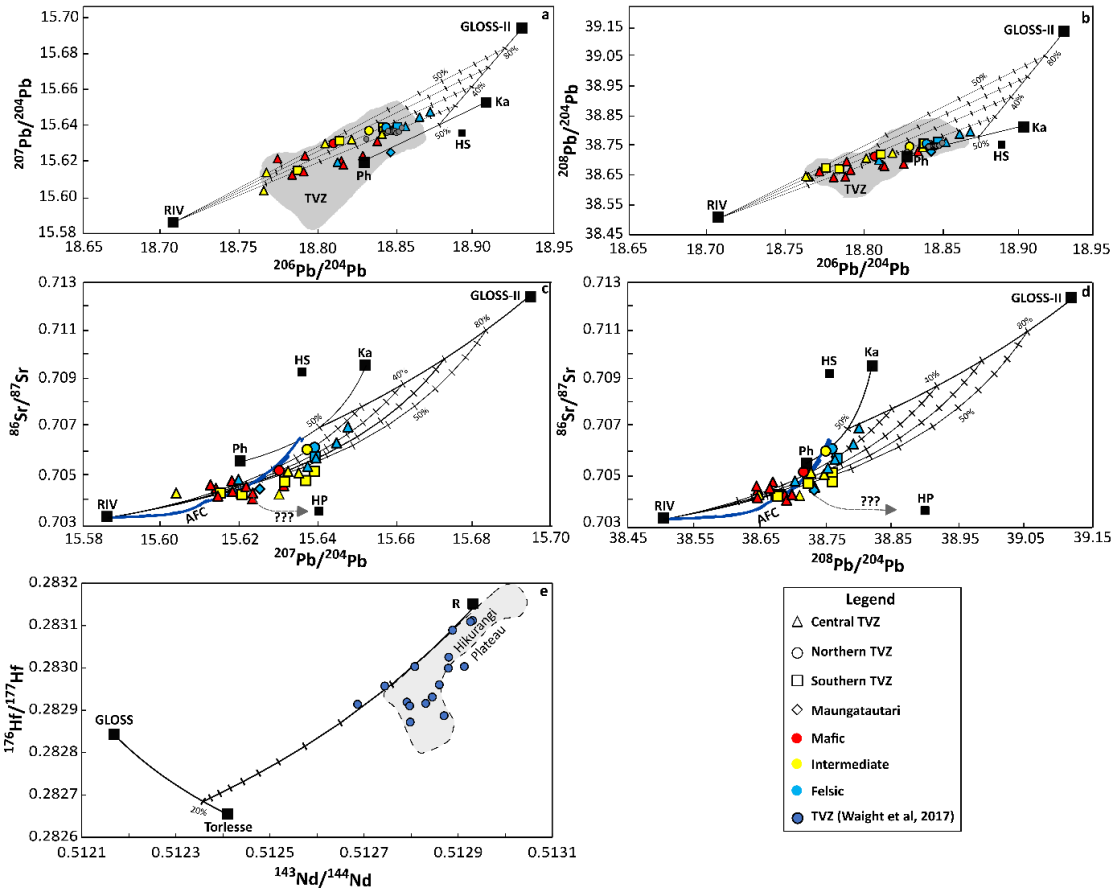

Figure 4.7: Mixing models for the TVZ data based on lead isotopic ratios a) $^{207}Pb/^{204}Pb$ vs $^{206}Pb/^{204}Pb$, b) $^{208}Pb/^{204}Pb$ vs $^{206}Pb/^{204}Pb$, grey areas correspond to renormalised previously reported old data from the TVZ after Gamble et al. (1996), Price et al. (2012), Shane et al. (2017), grey dots correspond to renormalised previously reported new data from Sas et al. (2021b); c) $^{87}Sr/^{86}Sr$ vs $^{207}Pb/^{204}Pb$; d) $^{87}Sr/^{86}Sr$ vs $^{208}Pb/^{204}Pb$. Squares correspond to southern TVZ, triangles to central TVZ and circles to northern TVZ; red samples are mafic, yellow are intermediate, and blue are felsic; Maungatautari is represented as a rhomb. Uncertainties of isotopic ratios are smaller than symbol size. Isotopic ratios for Rumble IV after Gamble et al. (1996), Torlesse (Pahau and Kaweka) after Price et al. (2015), GLOSS-II and HS after Plank (2014), HP after Timm et al. (2014). Blue lines correspond to AFC models, continuous when starting at 900 MPa, discontinuous when starting at 500 MPa, RIV = Rumble IV, Ph = Pahau subterrane, Ka = Kaweka subterrane, HS = Hikurangi sediment, HP = Hikurangi Plateau. e) $^{176}Hf/^{177}Hf$ vs $^{143}Nd/^{144}Nd$ of the TVZ, Torlesse after Waight et al. (2017), Rumble after Todd et al. (2010) and GLOSS after Chauvel et al. (2008). The field of the Hikurangi Plateau is after Hoernle et al. (2010).

Dehydration of the subducting sediments has been proposed by several studies (*e.g.*, Gamble et al., 1993; Waight et al., 2017). However, crustal recycling may include not only subducting sediments but also tectonically eroded crust, and not only release fluids but also melts. Melting of subducting material has been a common process in modern volcanic arcs: melting of the basalt-gabbro portion of the subducting slab in eclogite facies has been reported to generate Adak-type magnesian andesites (*e.g.*, Defant and

Drummond, 1990; Drummond et al., 1996; Yogodzinski et al., 1995), although crustal differentiation has also been proposed to generate these enigmatic rocks (*e.g.*, Atherton and Petford, 1993; Dreher et al., 2005; Garrison and Davidson, 2003; Shellnutt and Zellmer, 2010). In addition to the oceanic crust, fluids and melts from the cover of the subducting plate, consisting of sediments or a mixture of materials (*mélange*), have been reported to be involved in magma generation in the SW Japan, Cascadia, Izu and Marianas arcs (*e.g.*, Förster and Selway, 2021; Hauff et al., 2003; Shimoda et al., 1998; Tatsumi, 2001). Detachment of subducting material from the slab, followed by diapiric ascent and subsequent fluid and melt interaction with the mantle can also contribute to magma generation processes (Marschall and Schumacher, 2012; Nielsen and Marschall, 2017; Parolari et al., 2018; Parolari et al., 2021).

In the Southern Kermadec and Northern Hikurangi margins, strike-slip and compressional faulting from seamount and scarp collisions followed by subsequent extensional faulting and collapse of the overriding plate have been reported as a control on effective tectonic erosion (Barker et al., 2009; Collot and Davy, 1998; Collot et al., 1996; Lewis et al., 1998; Pedley et al., 2010). This tectonic erosion affects the crust of the North Island, New Zealand, which may be eroded, mixed, and dragged into the subduction channel where it would mix with the subducting sediments and later with the mantle wedge to variable degrees. The presence of ridges and seamounts in the subduction zone directly causes a more significant fracturing of upper plate rocks (von Huene and Scholl, 1991). This widens the subduction channel and allows more effective transport of trench sediments and debris into the mantle (Cande and Leslie, 1986; Laursen et al., 2002; Stern, 2011; von Huene et al., 2004). The process of tectonic erosion is responsible for returning parts of the overriding crust into the mantle, of which about 10%

may then be recycled through arc magmatism (Stern, 2011), but due to the geochemical similarities may be misinterpreted as transcrustal assimilation during magma ascent (von Huene et al., 2004). Recycling of this material by arc magmatism would then reduce the amount of crust lost by erosion (*e.g.*, Castro et al., 2010; Castro et al., 2013).

Thus, it is possible that the crust being recycled in the Hikurangi margin may not correspond to the subducting sediments, but instead be a mixture of these with the tectonically eroded Torlesse crust from the overriding plate, generating a *mélange*. This *mélange* may then be recycled back into the mantle through interaction at the mantle-slab interface through the release of fluids and melts and/or by having a diapiric ascent (Marschall and Schumacher, 2012; Nielsen and Marschall, 2017). Regardless of whether mantle-slab or mantle-diapir interactions are at play, melts from the *mélange* would react with the peridotitic mantle. Experimental studies on peridotite-siliceous melt reactions have shown the development of pyroxenitic zones and veins (*e.g.*, Corgne et al., 2018; Gervasoni et al., 2017; Rebaza et al., 2023). These pyroxenites can melt and generate a diverse range of compositions in primary arc magmas, as was first conceptualized by Straub et al. (2008) and later expanded to include silica-excess and silica-deficient pyroxenitic zones (Straub et al., 2011). Experimental studies have shown that melting of these pyroxenites, which occurs at a lower temperature than peridotite at a given pressure, generates melts ranging from strongly Ne-normative to quartz-normative magmas (Borghini and Fumagalli, 2020; Kogiso et al., 2004; Pertermann and Hirschmann, 2003; Rapp et al., 1999). The type of material in the *mélange* also affects the type of magmas generated by melting: from primitive tholeiitic to calc-alkaline magmas, generated by melting of a mantle hybridized by a serpentine- or sediment-dominated *mélange*, respectively (Codillo et al., 2018).

4.6.3 Crustal recycling in the Hikurangi margin

In the southern Kermadec arc, north of the TVZ, the presence of cold diapirs of a subduction *mélange* containing tectonically eroded material from the overriding plate, metasediments and fragments of the Hikurangi Plateau, has been proposed by Timm et al. (2014). This was inferred based on a systematic enrichment in Sr-Pb and depletion in Nd isotopic signatures of the arc lavas, and geophysical information supporting the subduction of a fragment of the Hikurangi Plateau beneath the Kermadec arc. In the southernmost portion of this zone, Timm et al. (2014) also reported an increase in a sediment component diluting the signature of the Hikurangi Plateau. If crustal recycling of tectonically eroded crust is also responsible for the heterogeneities found in the source of the TVZ magmatism, the signature of the overriding crust may be stronger than in the Kermadec arc and could be misinterpreted as crustal assimilation. This idea is consistent with earlier observations from Gamble et al. (1996), who indicated that sediment recycling is the main process controlling the trace element concentrations and isotopic ratios in the TVZ basalts. More recently, Codillo et al. (2018) noted that andesites from New Zealand are consistent with melting experiments of a sediment-dominated *mélange*.

Following Faure (1986), mixing lines for different isotope systems were derived (**Figure 4.7**). Rumble IV after Gamble et al. (1996) was chosen as the least radiogenic endmember, representing a magma without Torlesse crustal addition. Kaweka and Pahau sub-terrane averages after Price et al. (2015) were selected to represent the tectonically eroded crust. Subducting sediments in the Hikurangi margin have been reported by Plank (2014) and were calculated from ODP Sites 1123 and 1124, ~500 km from the trench and separated from it by the Hikurangi channel. The presence of this channel means that the sediments found in this core may have different sources than the sediments found to its

west, which are eventually subducted. Plank (2014) indicated that there is substantial uncertainty as to what material fills the Hikurangi trough. Therefore, the globally subducting sediments II (GLOSS-II) was employed as a mixing endmember. However, further information about the local subducting sediments is required to support or discard their involvement in the magma generation of the TVZ.

The Sr and particularly Pb isotope systems offer the ability to identify crustal material involved in magmatic systems (*e.g.*, Hart, 1988; Kobayashi et al., 2004; Kokfelt et al., 2006). However, Sr and Pb are both fluid-mobile elements and thus would only provide limited information. More immobile elements, such as Nd and Hf, are also of interest. Thus, the Sr-Pb isotope data presented here, as well as previously published Nd-Hf isotope data (Waight et al., 2017) provide more robust information about the interactions between the mantle and the subducting material. For all of these isotope systems, the composition of the subducting sediments (GLOSS-II) is too enriched and cannot reproduce the isotopic range observed in the TVZ volcanics (**Figure 4.7**). This may indicate that if crustal recycling is occurring, the recycled material is not dominated by subducting sediments. However, when considering tectonically eroded material alongside subducting sediments in a ~5:1 ratio, this 'crustal component' would be a fitting endmember to explain the Sr-Pb isotope systematics of the TVZ samples (**Figure 4.7**a-d). In particular, in Pb isotope space the samples follow a broadly linear trend that is consistent with a mixture of crustal and mantle endmembers. Although this trend is reproduced by this mixture, some variation within this trend can be seen in **Figure 4.7**a, where $^{207}Pb/^{204}Pb$ isotopic ratios show some dispersion. Such variation may be caused by two main processes that are not mutually exclusive: i) variation in the proportions of tectonically eroded material and subducting sediments and ii) additional

transcrustal processes such as magma mixing and AFC. Therefore, it is likely that a combination of both source input variations and transcrustal processes are occurring in the magma generation and evolution of the TVZ.

When combining Pb and Sr isotope ratios (**Figure 4.7**c, d), two observations can be made: i) Some minor interaction of the Hikurangi Plateau causing dispersion of the data appears possible and, ii) AFC by itself generates isotopic compositions that have less radiogenic Pb signatures for a given Sr isotopic ratio than what is observed from TVZ volcanism. The observed trend has more enriched Pb isotope ratios and is closer to the trend of a mixture between the *mélange* and the mantle, but the variations seen in these ratios also indicate variations in the sediment-crust proportions and that AFC may also play a role. In these two isotope systems, a contribution ranging from 10 to 30% for the 'crustal component' would be required for the mafic members, less than 10 to 40% for the intermediate members, and 30 to 80% for the felsic members. This does not mean that up to 80% of the mass of these magmas correspond to the recycled crust, but only that the elemental budget of fluid mobile elements such as Sr and Pb, may be dominated by fluids from the *mélange*, with some subsequent contributions of transcrustal assimilation.

When considering Nd and Hf isotope systematics (**Figure 4.7**e), a mixture between the 'crustal component' and the mantle yields similar isotopic signatures to some of the reported samples, but the relation is less clear than for the Sr-Pb isotope systems. In the samples that do follow the mantle-*mélange* mixing line, Nd-Hf isotopes reveal a smaller input of the 'crustal component' of up to 20%. This may indicate that the contribution of melts from the subducting material is much smaller than the contribution from dehydrating fluids to the mantle underneath the North Island of New Zealand.

Interestingly however, these isotope systems also reveal a possible interaction with material from the Hikurangi Plateau, with a stronger signature than what is seen in the Sr-Pb isotope systems.

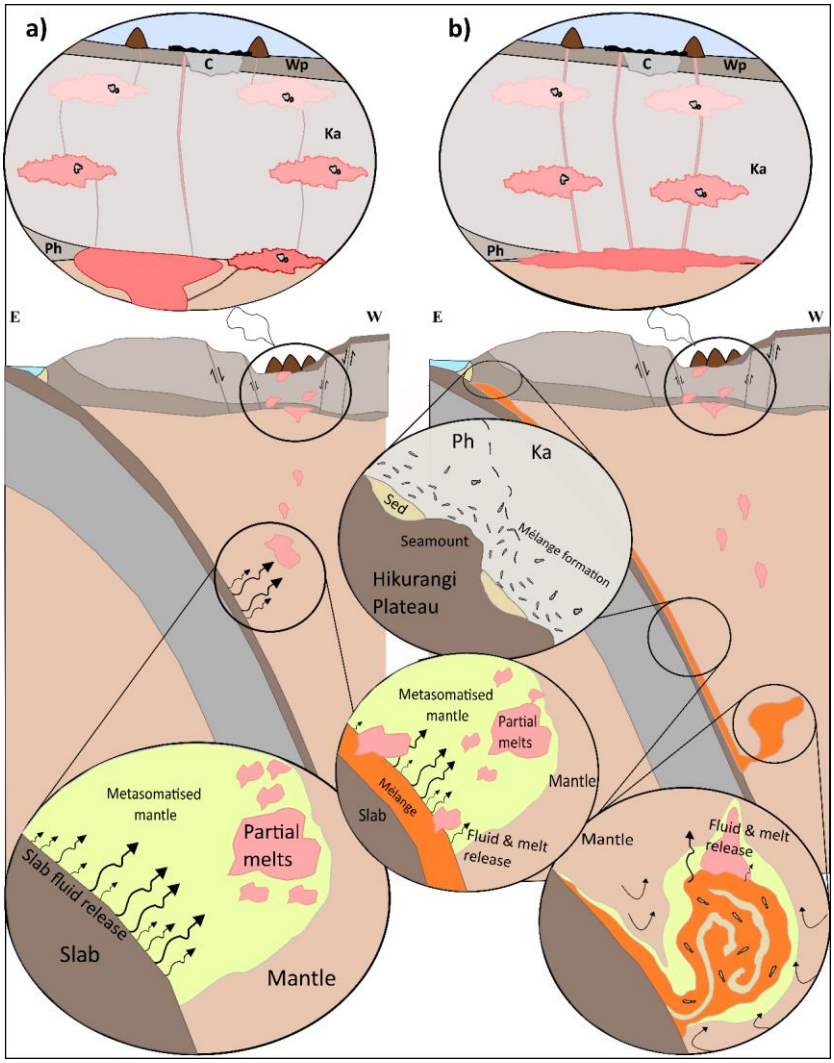

Figure 4.8: Representation of the two different models (a) partial melting of the mantle by slab fluid release, followed by extensive AFC, (b) formation of subduction *mélange* by crustal erosion and sediment subduction, followed by a mix with the wedge mantle, melting and subsequent ascent and eruption with little to no AFC, Ph = Pahau, Ka = Kaweka, Wp = Waipapa, C = Calderas. Not to scale.

The contribution of subducting sediments and tectonically eroded material into the mantle can reproduce the Sr-Pb isotope systematics of the TVZ, together with subsequent transcrustal processing. The occurrence of crustal recycling would drastically reduce the amount of assimilation, and thus the thermal limitations, required to generate some of the Sr-Pb isotopic variations of the TVZ. Although these fluid-mobile elements support the

hypothesis of source contamination, and fluid immobile Nd-Hf isotope systematics appear to be consistent with this in some cases, the recycling of tectonically eroded crust, subducting sediments and the Hikurangi Plateau remains elusive. Additionally, it remains uncertain if these interactions occur as mantle-diapir or at the mantle-slab interface (**Figure 4.8**). Further investigations of the chemical composition of the subducting sediments and forearc, as well as more extensive Nd-Hf isotope systematics of the TVZ volcanics, are required to further elucidate subcrustal processes.

Crustal recycling of eroded crust has the potential to provide the large amounts of crustal contamination and thermal energy required, without the same limitations as in the overriding crust. In recent years, similar observations of the thermal limitations of crustal assimilation, and the occurrence of crustal recycling, have been seen around the globe. Based on the Famatinian continental arc, Argentina, Cornet et al. (2022) reported that the contribution of subducted sediments to arc magmas has the potential to generate the observed isotopic diversity which is traditionally attributed to trans-crustal processes. Around the circum-Pacific belt, crustal recycling of subducting sediments by fluid and melt addition to the mantle has been proposed in magma generation in the SW Japan, Cascadia, Izu and the Marianas arcs (*e.g.*, Förster and Selway, 2021; Hauff et al., 2003; Shimoda et al., 1998; Tatsumi, 2001). In the circum-Pacific belt, this process is not limited to subducting sediments, and tectonically eroded material has been reported to make an important contribution to mantle heterogeneities in the central and southern Andes (Holm et al., 2014; Kay et al., 2005; Risse et al., 2013). Magmas in Costa Rica and Panama, Central America are also linked to the incorporation of forearc crust into the mantle by tectonic erosion of ophiolites (Goss and Kay, 2006). Another example of the input of tectonically eroded material into subduction-related magmatism is found in the

Trans-Mexican Volcanic Belt. Here, tectonically eroded material is thought to interact with the mantle, causing pyroxenitization and subsequent melting (Straub et al., 2011; Straub et al., 2008) or undergoing diapiric ascent and subsequent melting, thereby contributing to arc magma generation (Parolari et al., 2018; Parolari et al., 2021; Straub et al., 2015). In Mexico, up to 70% of peridotite mass could be part of a mixture between the mantle and siliceous flux from the tectonically eroded material without significantly modifying its isotopic signatures due to the low concentrations of incompatible elements such as Sr, Nd, Hf and Pb in the peridotite (Parolari et al., 2018). There, it was proposed that ~40% melting of a hybrid pyroxene-rich mantle source with ~50% of the eroded material reproduces the entire compositional characteristics of the Mexican andesitic volcanoes (Parolari et al., 2018; Parolari et al., 2021).

Thus, it appears that crustal recycling of tectonically eroded material is not unique to the TVZ and may be a globally important process in magma generation at subduction zones (Straub et al., 2020). However, the active production of silicic volcanism in the TVZ is the largest on Earth at present, with at least 3,900 km^3 of material produced in the past 350 ky (Kósik et al., 2021, and references therein). If some proportion of this material corresponds to the recycled crust, this will have major implications on the balance between crustal growth and material 'lost' into the deep mantle at the Hikurangi margin.

4.7 Conclusions

1) Our MCS-AFC models reveal that unrealistically large amounts of crustal assimilation (30-50%) and large amounts of fractional crystallisation (~90%) in the thin continental crust are required to obtain compositions similar to those of the dominantly felsic eruptives of the TVZ (>95% total volume) if AFC was occurring alone.

2) The broadly linear relationship seen in Pb isotope space suggests that volcanism in the TVZ may be related to the mixing of two compositionally distinct endmembers: a mantle component and a crustal component. To generate this trend, it is plausible that an unradiogenic mantle endmember is mixing with a *mélange* dominated by tectonically eroded crust (Torlesse terrane), with some contribution of subducting sediments (GLOSS-II). Possible interactions of the mantle source with the Hikurangi Plateau are also revealed when combining the Sr-Pb and Nd-Hf isotope systems.
3) The major element, trace element and Sr-Pb isotope characteristics seen in the volcanism of the TVZ can be reproduced by a combination of source and transcrustal processes, including AFC, mixing, and slab additions to the mantle. However, further studies are required to better quantify the processes here proposed. A more systematic Nd-Hf isotope work on the TVZ as well as Sr-Pb-Nd-Hf isotope systematics of the forearc and subducting materials would help to strengthen and test possible source heterogeneity caused by tectonic erosion and sediment subduction.

Chapter 5 - Geochemical characterisation of material in the Hikurangi Margin from IODP Expedition 375 drill sites U1518 and U1520

Carlos R. Corella Santa Cruz[1]; Susanne M. Straub[2]; Georg F. Zellmer[1]; Claudine H. Stirling[3,4]; Malcolm R. Reid[3,4]; David Barr[3,4]; Candace E. Martin[4]; Marco Brenna[4]; Karoly Nemeth[5]

[1]Massey University, Private Bag 11222, Palmerston North 4442, New Zealand

[2]Lamont-Doherty Earth Observatory of Columbia University, 61 Route 9W, Palisades, NY
10964, USA

[3]Centre for Trace Element Analysis and Department of Geology, University of Otago, PO Box 56, Dunedin 9054, New Zealand

[4]Department of Geology, University of Otago, PO Box 56, Dunedin 9054, New Zealand

[5]Institute of Earth Physics and Space Science, Csatkai E. út 6-8., Sopron 9400, Hungary

Abstract

The composition of the subducting sediments at convergent margins is of major importance due to their link to arc magmatism. At the Hikurangi margin, east of the North Island, New Zealand, the Hikurangi Plateau and its sedimentary cover have been subducting for the last 20 Ma. A first approximation to the composition of the subducting sediments was proposed 10 years ago based on drill sites 1123 and 1124 from ODP Expedition 181 located c.500 km from the trench. Recent drilling (IODP Expedition 375) recovered sediment closer to the trench. Here, major and trace element concentrations, and Sr–Pb–Nd isotope ratios are reported for drill sites U1518 and U1520, with samples of the accretionary prism of the forearc on the upper plate and the sedimentary cover of the subducting plate. A well–defined décollement allows material that has already been accreted or is prone to future accretion, and material that is in the process of being subducted to be distinguished. Tectonic erosion has been reported in the Hikurangi margin, suggesting that the material that is accreted to the forearc can be subsequently subducted. Therefore, this characterisation is of prime importance to reliably identify crustal recycling along the Hikurangi margin through associated arc magmatism.

Keywords: subducting sediments, bulk composition, tectonic erosion, *décollement*, isotopes

5.1 Introduction

The chemical characterization of local trench sediments is essential to constrain the chemical budget of arc magmatism globally (*e.g.*, Plank 2014). However, materials from the forearc and accretionary prism can also affect the chemical budget of arc magmatism globally, as they can be subducted by tectonic erosion (*e.g.*, Jicha et al. 2004; Risse et al. 2013; Straub et al. 2015; Straub et al. 2020). Subducted materials play a significant role in magma generation processes and the formation of new, or recycling of existing crust in subduction zones (*e.g.*, Plank and Langmuir 1998; Kay et al. 2005; Risse et al. 2013; Holm et al. 2014; Plank 2014; Parolari et al. 2018; Straub et al. 2020; Parolari et al. 2021; Cornet et al. 2022). Locally, in the Tonga–Kermadec–Hikurangi subduction system, a general increase in subducted material input into the mantle towards the south is displayed, with a large increase along the Hikurangi margin (Gamble et al. 1996). In the southern Kermadec arc, this material was proposed to be a mélange of subducting sediments, tectonically eroded forearc crust, and material from the Hikurangi Plateau (Timm et al. 2014). The presence of mantle heterogeneities caused by mantle–slab interactions, particularly the addition of subducting sediments, have been proposed to also have an effect in the Taupo Volcanic Zone (TVZ) (Gamble et al. 1993; Graham et al. 1995; Gamble et al. 1996; Rooney and Deering 2014). As with the Kermadec arc, tectonic erosion of forearc crust and subsequent interaction with the mantle source has been suggested to affect the geochemistry of volcanic products of the TVZ (**Chapter 4**).

Until 2018, Ocean Drilling Program (ODP) sites 1123 and 1124 were located nearest to the Hikurangi trench, but c. 500 km to the east (**Figure 5.1**) and separated from it by the Hikurangi channel. These sites were used to estimate the bulk geochemical composition of the Hikurangi margin subducting sediments by Plank (2014) and integrated into the

composition of the estimated Global Subducting Sediments II (GLOSS–II). Materials and units of the Hikurangi Margin were identified by Davy et al. (2008) based on seismic and ODP site 1124 logging data. They reported six units varying from sediments to the basaltic basement, described as follows. The first unit corresponds to Cenozoic sediments with interbeds of tephra and clays, and an age range of 32 to 0 Ma. The second unit corresponds to their Sequence Y, comprised of chalks and mudstones with an age range of 70 to 32 Ma. Below this unit are laminar Mesozoic sediments ranging from 100 to 70 Ma containing volcaniclastic sediments with basalt interbeds aged 100 to 90 Ma. The fifth unit corresponds to Cretaceous volcaniclastic sediments with an uncertain age range, but likely to be 125 to 100 Ma old. Finally, the basaltic basement corresponds to the sixth unit and has an age range of 125 to 120 Ma.

For Plank's (2014) estimation of the bulk composition of the subducting material, the composition was taken to be 50% carbonate–rich Cenozoic sediments and 50% volcaniclastics from the Hikurangi Plateau. The composition of the carbonate–rich Cenozoic sediments was calculated based on geochemical analyses (major and trace elements, Sr–Nd–Pb isotopes) of ODP Sites 1123 and 1124, supplemented by geochemical analyses of surface sediments from the Hikurangi Plateau. As samples of the volcaniclastic sequence of the Hikurangi Plateau were not available, the geochemical composition of the volcaniclastic section was based on the volcaniclastic sediments of the genetically related Manihiki Plateau (Deep Sea Drilling Project (DSDP) 317) and other intraplate and basement volcaniclastic sediments (ODP 801, DSDP 417) as well as basalts reported by Hoernle et al. (2010).

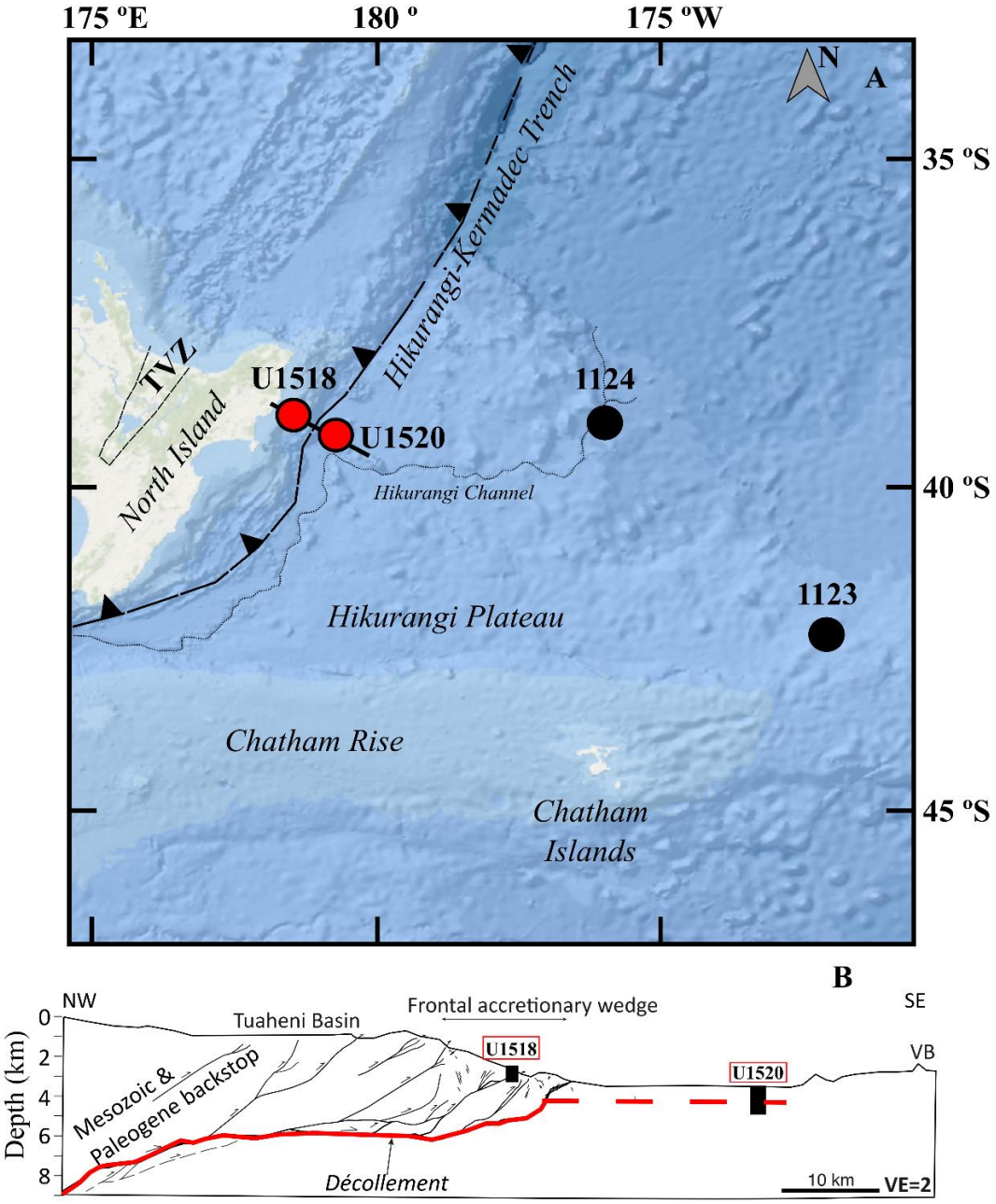

Figure 5.1: Location map of ODP sites 1123 and 1124, and IODP sites U1518 and U1520. For reference, the Taupo Volcanic Zone (TVZ), Chatham Rise, Chatham Islands, the Hikurangi Plateau, and the Hikurangi-Kermadec Trench are shown. Cross section of the trench and location of sites U1518 and U1520 after Saffer et al. (2019), discontinuous line indicating the formation of the *décollement* after Barnes et al. (2020).

In late 2017–2018, Expedition 372B/375 of the International Ocean Drilling Program (IODP) took place at the Hikurangi Trough, drilling sites U1518, U1519, U1520, and U1526 in a trench–perpendicular transect, including both the subducting plate and the accretionary prism (Barnes et al. 2019; Saffer et al. 2019; Wallace et al. 2019). Thus,

material closer to the trench became available along with the volcaniclastic sequence (**Figure 5.2**), enabling a more accurate estimate of the geochemical composition of the subducting trench sediment to be determined. In addition, recent tectonic and structural observations became relevant to determine subducting and accreting materials, due to the identification of the development of a *décollement* zone (Barnes et al. 2020). Accreting material is located above the *décollement* zone, while subducting material is located below. However, the presence of tectonic erosion in the Hikurangi margin, as reported by *e.g.*, Collot et al. (1996); Collot and Davy (1998); Lewis et al. (1998); Barker et al. (2009); Pedley et al. (2010), implies that accreted material can also be ultimately subducted. Thus, material that is currently subducting and material that is prone to ultimate tectonic erosion can now be distinguished. Bulk major and trace element concentrations, and Sr–Pb–Nd isotope compositions are presented in this study, to geochemically characterise the drilled sequences above and below the *décollement* zone which may impact the composition of the magmas erupted in the TVZ.

5.2 General description of the lithostratigraphic units at the Hikurangi margin

Lithostratigraphic units found in IODP Expedition 372B/375 can be divided into three main groups: hemipelagic and terrigenous facies (Units I–III), pelagic facies (Unit IV) and the Hikurangi Plateau volcaniclastic facies (Units V and VI). Based on expedition reports (Barnes et al. 2019; Saffer et al. 2019; Wallace et al. 2019), Unit I, a trench–wedge facies with a Quaternary age (< 2.58 Ma) is composed of silty clay to clayey silt interbedded with silt and sand, indicating turbidity current activity and hemipelagic settling during deposition. Unit II with a Quaternary age (< 2.58 Ma), the Ruatoria slide, is composed of silty clay to clayey silt interbedded with silt, deposited at the distal edges of the Ruatoria debris avalanche. Unit III, a trench–wedge facies with a Quaternary – late Miocene age (< 11.63 Ma), is composed of mud and mudstone interbedded with silt,

indicative of hemipelagic settling and dilute turbidity currents during deposition. Unit IV, a pelagic facies of early Paleocene to late Miocene age (66–5.333 Ma), is composed of marl, calcareous mudstone, and chalk, and represents pelagic sedimentation. Minor horizons of airborne volcanic ash are found in Units I to IV. Unit V, a volcaniclastic facies with a late Cretaceous age (100.5–66 Ma), is composed of volcaniclastic conglomerate associated with the Hikurangi Plateau. Unit VI has mixed lithologies with a Cretaceous age (145–66 Ma) and is composed of volcaniclastic conglomerate, siltstone, limestone, mudstone, and basalt.

A good correlation is found in the drilled units and those identified by Davy et al. (2008): Units I, II, and III correlate to their Cenozoic sediments, Unit IV correlates with their sequence Y and Units V and VI may correspond to the basement and volcaniclastic units. Barnes et al. (2020) identified the formation of a *décollement* zone based on seismic line data and deformation in drill sites U1520 and U1526. They reported that the Hikurangi Plateau, its volcaniclastic sequence, and the lowest portion of the pelagic sequence are located below the plate boundary fault, and thus currently subducted. In contrast, the terrigenous sequence and the rest of the pelagic sequence are located above the plate boundary, and therefore accreted to the forearc complex. However, the accreted material may subsequently be subducted, as the accretionary forearc is tectonically eroded by the seamount–studded subducting plate, as reported by *e.g.*, Collot et al. (1996); Collot and Davy (1998); Lewis et al. (1998); Barker et al. (2009); Pedley et al. (2010).

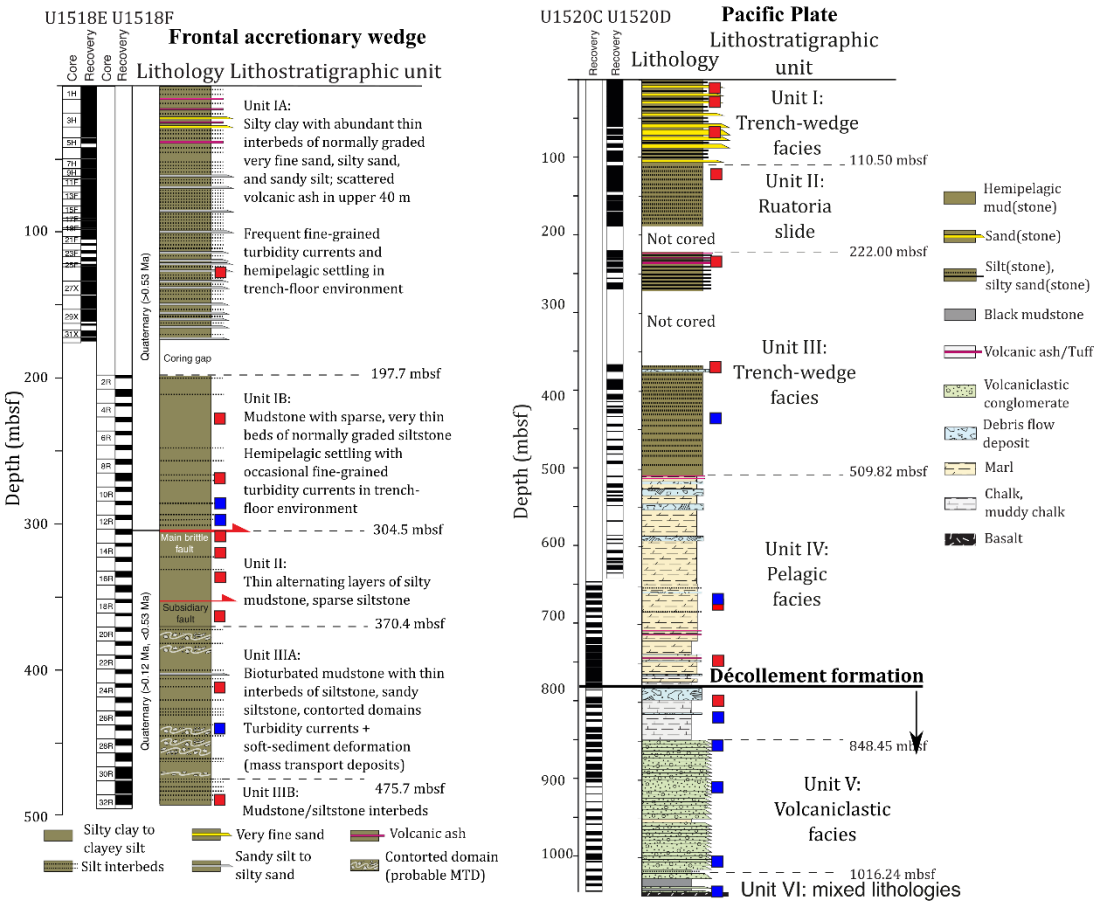

Figure 5.2: Site recovery columns after Saffer et al. (2019). The selected samples are shown in squares. Red squares represent samples with only major elements reported; blue squares represent samples with major and trace elements, as well as selected isotopic ratios. Décollement formation after Barnes et al. (2020). Details are in **Table 5.1**.

5.3 Methods

5.3.1 Sample selection

The subducting and accreted sediments were sampled from IODP drill holes U1518E and F, and U1520C and D (**Figure 5.1**, **Figure 5.2** and **Table 5.1**). A total of 28 samples were selected which fully represent the lithological units present in the subducting complex as well as the accretionary prism. Twelve samples from drill holes U1518E and F correspond to Units IA–B, II, and IIIA–B and represent the accreted material, with associated lithological descriptions given in Saffer et al. (2019). At site U1518, Unit IA (1 sample) has a thickness of 197.7 m and Unit IB (4 samples) is 106.8 m thick, giving a total

thickness of 304.5 m for Unit I. Unit II has a thickness of 65.9 m and is represented by 4 samples. Unit IIIA (2 samples) has a thickness of 105.30, and Unit IIIB (1 sample) is 16.6 m thick, giving a minimum thickness of 121.86 m for Unit III. Sixteen samples from drill holes U1520D and C correspond to units I, II, III, IV, V, and VI with unit descriptions reported in Barnes et al. (2019) and representing material from the subducting plate above and below the *décollement* based on Barnes et al. (2020). Here, thicknesses of 110.5 m (1 sample) for Unit I, 109.5 m (1 sample) for Unit II, 289.8 m (3 samples) for Unit III and 338.6 m (5 samples) for Unit IV are given. Unit V has a thickness of 137.8 m (3 samples), and Unit VI has a minimum thickness of 29.5 m (1 sample). Samples were carefully selected to avoid the presence of volcanic ashes.

All samples were analysed for their major element compositions. A subset of ten representative samples was selected for trace element concentration and Sr–Pb–Nd isotope analysis, including three samples from the accretionary prism, two samples from above the *décollement*, and five samples from below the *décollement* (**Figure 5.2**; **Table 5.1**).

5.3.2 Analytical methods

Major element analyses were carried out with a Wavelength Dispersive X–ray Fluorescence (WD–XRF) S8 Tiger spectrometer from Bruker–AXS (Germany) at Massey University, New Zealand, using glass beads made with a sample:flux ratio of 1:10 ratio, with 12:22 X–Ray flux (35.3% Lithium Tetraborate and 64.7% Lithium Metaborate). Interference–corrected spectral intensities were converted to oxide concentrations using calibration curves consisting of natural standards. The long–term reproducibility of the oxide analyses was assessed using the basaltic OREAS 24c and granodioritic OREAS 24b reference materials (OREAS, Australia). The 1σ

reproducibility is typically ±0.5–1% for major oxides and better than ±3% for minor oxides, except for P2O5 (±5–10%).

Table 5.1: Selected samples from IODP cores. Numeric age is based on the fossils present in the samples; the period is present when no approximation is available. The position corresponds to forearc (FA), above the *décollement* (AD), and below the *décollement* (BD) based on Barnes et al. (2020). Rock description, age, unit, and depth interval after Barnes et al. (2019), and Saffer et al. (2019). Bold samples correspond to those selected for trace element concentrations and Sr-Pb analyses while the rest is only major elements.

Sample	Rock	Age (Ma)	Unit	Position	Depth interval
		U1518E			
26X 6W 69/71	Sandy silt	Quaternary	IA	FA	123 – 133
		U1518F			
5R 1W 12/14	Clayey silt	Quaternary	IB	FA	226 – 236
9R 5W 24/26	Sandy silt	0.63	IB	FA	264 – 274
11R 2W 47/49	Silty clay	Quaternary	IB	FA	284 – 294
12R 2 18/20	Silty clay	0.53 – 2.17	IB	FA	294 – 304
13R 1W 59/61	Clayey silt	Quaternary	II	FA	304 – 313
14R 1W 133/135	Clayey silt	Quaternary	II	FA	313 – 323
16R 4W 24/26	Silty clay	Quaternary	II	FA	332 – 342
19R 3W 33/35	Clayey silt	Quaternary	II	FA	360 – 370
24R 2W 66/68	Silty clay	Quaternary	IIIA	FA	408 – 418
27R 3W 8/10	Sandy silt	Quaternary	IIIA	FA	437 – 447
32R 7 29/31	Silty clay	0.126 – 0.53	IIIB	FA	485 – 495
		U1520D			
2H 7W 67/69	Silty sand	0.011	I	AD	14.15 – 15.15
4H 5W 104/106	Silty sand	0.011 – 0.29	I	AD	30 – 32.5
8H 5W 55/57	Sand	0.011 – 0.53	I	AD	68 – 69
14H 3W 54/56	Silty clay	Quaternary	II	AD	121 – 122
28F 4W 33/35	Sandy silt	Quaternary	III	AD	236.7 – 238
35X 1W 66/68	Silty clay	0.53	III	AD	366.6 – 368
44X 1W 83/85	Silty clay	0.53 – 0.62	III	AD	443.2 – 444.7
		U1520C			
5R 1W 72/74	Marl	10.66	IV	AD	670.4 – 671.9
5R 1W 105/107	Marl	10.66	IV	AD	670.4 – 671.9
13R 2W 51/53	Marl	24.67	IV	AD	748.6 – 750.1
19R 3W 34/36	Muddy chalk	54.4	IV	BD	807.6 – 809
21R 1W 71/73	Chalk	55	IV	BD	823.9 – 825.41
24R 1W 91/93	Silty claystone	<72	V	BD	852.6 – 853.6
31R 1W 58/60	Coarse	Cretaceous	V	BD	919.7 – 920.6
41R 1W 119/121	Siltstone	100	VI	BD	1015.7 – 1017.2
44R 1W 116/118	Basalt	Cretaceous	VI	BD	1044.5 – 1045.45

5.3.2.1 Trace element concentration and Sr–Pb–Nd isotope analysis

Trace element concentration and isotopic analyses were performed at the Centre for Trace Element Analysis, University of Otago, New Zealand. Selected samples were analysed for their trace element concentrations using inductively coupled plasma mass spectrometry with a quadrupole mass analyser (Q–ICP–MS) and a 7900 instrument (Agilent Technologies, USA). Strontium and lead isotope analyses were performed by multiple–collector ICP–MS (MC–ICP–MS), using a Nu Plasma–HR instrument (Nu Instruments Ltd, UK). For all samples, aliquots of powdered material of c.0.5 g were taken for combined trace element concentrations and Sr–Pb–Nd isotope analyses. All samples were chemically processed within ISO 4 ducted laminar flow workstations (ISO 5 for Nd separation) housed in an ISO 5 metal–free cleanroom. All reagents used (HF, HNO3, and HCl) were purified in–house using Teflon and Quartz sub–boiling distillation, and ultra–high purity H2O was dispensed from a Milli–Q Element water purification system (Millipore, Ltd, USA).

Each sample was digested sequentially using HCl–HNO3–HF following routine procedures (Stirling et al. 2005; Stirling et al. 2006; Stirling et al. 2007; Corella Santa Cruz et al. 2023). Total procedural replicates were within errors (**Appendix A**). Values for limits of detection (LOD) were 5 µg/g for Ni, Zn, Ga, Rb, Sr, Zr, Cd, Sn, Sb, and Ba, 3 µg/g for V and Cr, 2 µg/g for Co, Y and Nb, 1 µg/g for Li, 0.5 µg/g for Cs, Pb, Th, and U, 0.1 µg/g for Be and Ta, 0.06 µg/g for REE, Hf and W.

Separation of Sr and Pb from the sample matrix was performed using ion exchange chromatographic columns loaded with 250 µl of Sr.spec resin (100–150 µm) (Eichrom Technologies, USA), while that of Nd was performed following a protocol modified from

Pin and Zalduegui (1997); Baker et al. (2002). Procedural blanks yielded < 60 pg, < 10 pg and <50 pg, all of which are negligible compared to the 300 ng, 10 ng and 30 ng load sizes for Sr, Pb and Nd respectively. For Sr isotope analysis, all $^{87}Sr/^{86}Sr$ ratios were corrected for instrumental mass fractionation using a 'true' $^{86}Sr/^{88}Sr$ value of 0.1194 and the exponential mass fractionation law (Hart and Zindler 1989; Habfast 1998), as well as for potential isobaric interferences from Kr and Rb across the Sr mass range. All $^{87}Sr/^{86}Sr$ results were normalised to the NIST SRM 987 Sr reference value of 0.710248 (McArthur et al. 2001). For Pb isotopic analysis, the $^{206}Pb/^{204}Pb$, $^{207}Pb/^{204}Pb$, and $^{208}Pb/^{204}Pb$ ratios were corrected for instrumental mass fractionation using thallium (Tl) normalisation and the exponential mass fractionation law with a NIST–Tl997 $^{205}Tl/^{203}Tl$ value of 2.3875 and a Pb:Tl ratio of 5:1. All Pb isotope ratios are reported relative to NIST SRM 981 Pb reference values of $^{206}Pb/^{204}Pb = 16.9406 \pm 0.0003$, $^{207}Pb/^{204}Pb = 15.4957 \pm 0.0002$, and $^{208}Pb/^{204}Pb = 36.7184 \pm 0.0007$ (Yuan et al. 2016). All $^{143}Nd/^{144}Nd$ values were corrected for instrumental mass fractionation adopting a 'true' $^{146}Nd/^{144}Nd$ ratio of 0.7219 and applying the exponential mass fractionation law, as well as for potential interferences from Sm across the Nd mass range. All corrected Nd isotopic ratios were normalised to the international reference material JNdi–1 using a $^{143}Nd/^{144}Nd$ ratio of 0.512115 after Tanaka et al. (2000). All uncertainties for individual samples are reported as ± 2 SE, unless stated otherwise, and include the analytical uncertainties of sample and normalising standards combined in quadrature, using standard error propagation techniques.

Analytical performance for Sr, Pb and Nd isotope analysis was assessed on the basis of replicate analyses of the primary standards SRM 987 Sr, SRM 981 Pb and JNdi–1, respectively, yielding average compositions of 0.710247 ± 0.000013 (2 SD, n = 18) for

$^{87}Sr/^{86}Sr$, 36.7184 ± 0.0032, 15.4957 ± 0.0013 and 16.9406 ± 0.0012 (2 SD, n=20) respectively for $^{208}Pb/^{204}Pb$, $^{207}Pb/^{204}Pb$ and $^{206}Pb/^{204}Pb$, and 0.512115 ± 0.000009 (2 SD, n=14) for $^{143}Nd/^{144}Nd$. The BHVO–2, BCR–2, AGV–2 (USGS, United States), JR–2, and JG–3 (GSJ, Japan) reference materials were also used for quality control purposes, giving Sr, Pb and Nd isotopic compositions that are identical, within error, to reported values (**Appendix A**). The results for all trace element concentrations and Sr–Pb–Nd isotope compositions are presented in **Table 5.3**.

5.3.3 Bulk composition calculations

The method of Plank (2014) was employed to estimate the bulk composition of the different materials in the accretionary prism (U1518) and subducting plate (U1520), based on published values for sediment unit thicknesses (Barnes et al. 2019; Saffer et al. 2019; Wallace et al. 2019) as well as the major and trace element concentrations and Sr–Pb–Nd isotope ratios determined in the present study. Based on the *décollement* zone reported by Barnes et al. (2020), a bulk composition of the material located below and above the current *décollement* in site U1520 was obtained. Subsequently, the material located in the accretionary prism and above the *décollement* were combined to represent the material that may be recycled via tectonic erosion. The results of these calculations are presented in **Table 5.4**. However, we note that the *décollement* zone is a dynamic feature and as such, it may have migrated over the evolution of the Hikurangi subduction system. Thus, there remains some uncertainty about the material located below and above the *décollement* in the past.

5.4 Results

For simplicity, the results are presented in three groups instead of individual units, as hemipelagic and terrigenous facies (Units I–III), pelagic facies (Unit IV), and the

Hikurangi Plateau associated volcaniclastic facies (Units V and VI). For the compilation of results for the individual samples within each unit, the reader is referred to **Table 5.2** and **Table 5.3**.

Table 5.2: Major elements results from IODP cores. All results are in wt.%

Sample Name	SiO_2	Al_2O_3	TiO_2	MnO	Fe_2O_3	MgO	CaO	Na_2O	K_2O	P_2O_5	LOI	Total
U1518E 26X 6W 69/71	57.71	13.85	0.61	0.05	4.49	1.93	6.70	2.92	2.53	0.19	9.06	100.10
U1518F 5R 1W 12/14	59.63	13.90	0.60	0.06	4.48	1.82	5.95	2.93	2.49	0.20	8.10	100.20
U1518F 9R 5W 24/26	62.23	13.53	0.56	0.05	4.12	1.66	4.79	3.10	2.43	0.18	7.21	99.90
U1518F 11R 2W 47/49	62.76	13.09	0.53	0.05	3.89	1.63	5.39	2.94	2.40	0.17	7.18	100.08
U1518F 12R 2 18/20	59.30	16.64	0.72	0.07	5.93	2.34	2.88	3.09	3.30	0.22	5.60	100.14
U1518F 13R 1W 59/61	61.34	15.94	0.70	0.07	5.21	2.17	2.80	3.24	2.99	0.22	5.33	100.04
U1518F 14R 1W 133/135	59.65	14.20	0.61	0.05	4.51	1.88	5.72	3.03	2.54	0.18	7.77	100.22
U1518F 16R 4W 24/26	58.03	14.60	0.63	0.05	4.67	1.89	6.29	2.98	2.64	0.18	8.23	100.25
U1518F 19R 3W 33/35	58.80	14.38	0.63	0.06	5.16	1.99	5.06	2.98	2.61	0.19	8.33	100.25
U1518F 24R 2W 66/68	58.80	14.78	0.65	0.06	5.40	2.06	4.75	3.00	2.66	0.20	7.97	100.37
U1518F 27R 3W 8/10	55.26	14.36	0.62	0.06	4.85	1.99	7.42	2.88	2.66	0.19	9.97	100.29
U1518F 32R 7 29/31	59.24	14.78	0.66	0.07	4.94	1.96	5.11	3.16	2.74	0.20	7.23	100.17
U1520D 2H 7W 67/69	72.06	11.08	0.38	0.04	2.57	1.03	3.45	3.31	2.07	0.19	3.96	100.17
U1520D 4H 5W 104/106	72.83	10.94	0.39	0.04	2.56	1.05	3.23	3.24	1.99	0.13	3.82	100.23
U1520D 8H 5W 55/57	72.58	10.80	0.32	0.04	2.31	0.98	3.98	3.25	1.98	0.12	4.04	100.45
U1520D 14H 3W 54/56	58.70	15.25	0.66	0.06	5.05	2.14	4.51	3.17	2.88	0.19	7.66	100.30
U1520D 28F 4W 33/35	61.76	14.39	0.56	0.05	4.13	1.72	4.56	3.39	2.91	0.17	6.72	100.38
U1520D 35X 1W 66/68	70.08	12.31	0.47	0.04	3.07	1.05	2.98	3.68	2.14	0.16	3.58	99.71
U1520D 44X 1W 83/85	61.75	15.44	0.68	0.06	4.75	2.00	3.49	3.35	2.93	0.21	5.39	100.10
U1520C 5R 1W 72/74	26.37	7.66	0.32	0.09	2.95	1.29	31.79	1.40	0.74	0.14	27.24	100.00
U1520C 5R 1W 105/107	24.59	7.11	0.29	0.08	2.74	1.20	33.26	1.37	0.62	0.14	28.31	99.71
U1520C 13R 2W 51/53	30.13	8.14	0.41	0.10	3.11	1.55	28.94	1.25	1.32	0.14	24.92	100.02
U1520C 19R 3W 34/36	1.86	0.49	0.02	0.04	0.22	0.30	51.79	0.07	0.02	0.07	42.91	97.83
U1520C 21R 1W 71/73	2.38	0.58	0.02	0.05	0.26	0.35	51.63	0.06	0.02	0.09	42.66	98.12
U1520C 24R 1W 91/93	51.01	14.55	3.31	0.24	13.07	4.12	1.84	2.43	2.08	0.94	6.79	100.38
U1520C 31R 1W 58/60	30.30	10.02	2.18	0.15	9.12	3.73	21.92	1.88	1.58	0.93	18.60	100.45
U1520C 41R 1W 119/121	56.51	15.05	0.87	0.03	6.53	5.22	3.41	2.54	1.76	0.30	7.73	100.04
U1520C 44R 1W 116/118	55.33	18.15	1.36	0.05	5.23	1.53	4.66	4.44	5.69	0.95	3.37	100.76

Even though the terrigenous facies is subdivided into three different units, their geochemical characteristics are similar due to analogous detrital lithologies and depositional environments (**Figure 5.3**). SiO_2 content varies from 60 to 80 wt.% but commonly is around 65 wt.%. The content of Al_2O_3 varies from 11–18 wt.%, while TiO_2 and MgO contents are both low with values of <1 wt.% and ≤2 wt.%, respectively. The

concentrations of K_2O and Na_2O vary from 2–4 wt.% and 3–4 wt.% respectively (**Figure 5.3**). The terrigenous facies also has the least variable trace element concentrations between samples, with the highest concentrations being observed for Rb and Cs, and intermediate concentrations being recorded for the remaining elements (**Figure 5.4**). The Sr–Pb–Nd isotope signatures are also well constrained, with ratios from 18.87 to 18.89 for $^{206}Pb/^{204}Pb$, from 15.65 to 15.66 for $^{207}Pb/^{204}Pb$, and from 38.82 to 38.83 for $^{208}Pb/^{204}Pb$, while $^{87}Sr/^{86}Sr$ varies from 0.70909 to 0.71095, and $^{143}Nd/^{144}Nd$ ranges from 0.51238 to 0.51251 (εNd from -5 to -2.5) (**Figure 5.5**).

The pelagic facies (Unit IV) shows a large variation in major element concentrations due to differences in the types of sediments comprising this unit (**Figure 5.3**). A higher detrital input causes SiO_2 to increase from around 5 wt.% for calcareous sediments to between 30 and 40 wt.% for siliceous sediments, while Al_2O_3 increases from around 1.5 wt.% for the former to 11 wt.% for the latter. Similar distributions are seen for TiO_2, MgO, $Fe_2O_3^T$, K_2O, and Na_2O, while CaO has the highest concentrations of the entire sequence. Trace element concentrations also show larger variations in the pelagic facies compared to the terrigenous facies, and give the lowest concentration of the sequence for virtually all elements, except for Sr, which has the highest concentrations in the sequence. In Pb isotope space, the pelagic facies is slightly more radiogenic but similar in composition to the terrigenous facies, with values ranging from 18.816 to 19.005 for $^{206}Pb/^{204}Pb$, 15.657 to 15.661 for $^{207}Pb/^{204}Pb$ and 38.888 to 39.007 for $^{208}Pb/^{204}Pb$ (**Figure 5.5**). Both $^{87}Sr/^{86}Sr$ and $^{143}Nd/^{144}Nd$ ratios are slightly less radiogenic in the pelagic facies than the terrigenous sequence, varying from 0.70784 to 0.70892 and 0.51235 to 0.51248 (εNd from -5.5 to -3.1), respectively (**Figure 5.5**).

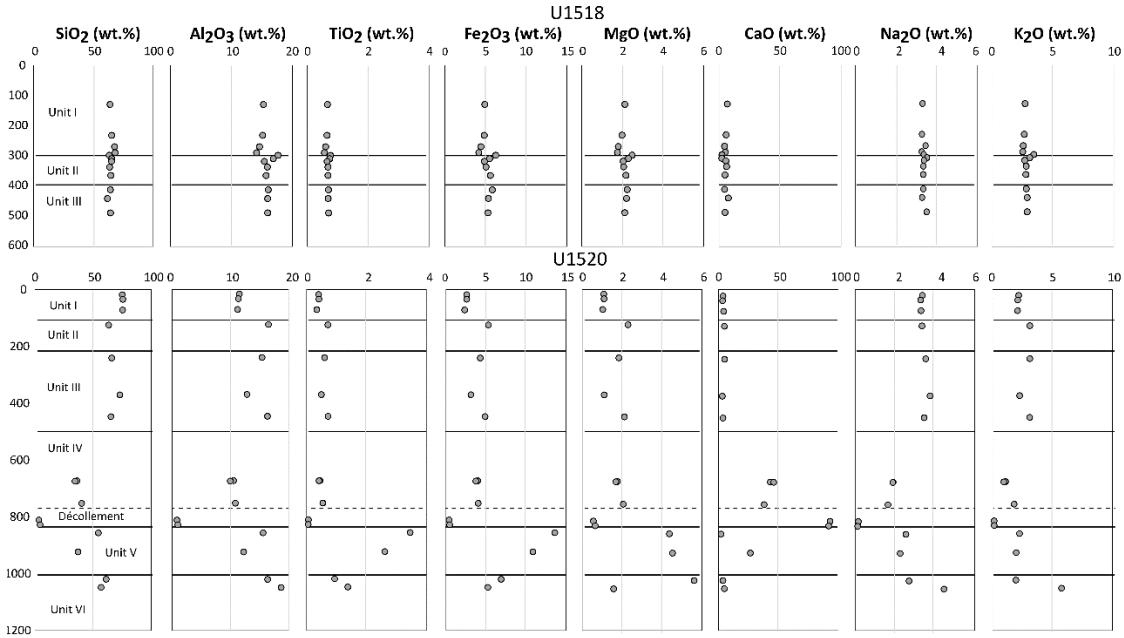

Figure 5.3: Major element plots (wt.%) against depth in mbsf. All oxides are plotted normalised to 100 in anhydrous base. *Décollement* formation after Barnes et al. (2020).

The oldest units correspond to the sequences associated with the Hikurangi Plateau (Units V and VI) where SiO_2 content varies from 35 to 65 wt.%, Al_2O_3 varies from 12 to 19 wt.%. TiO_2, MgO, and $Fe_2O_3^T$ are all higher in Unit V than Unit VI and correspond to the highest values of the entire sequence, while Na_2O and K_2O show the opposite behaviour and are higher in Unit VI than Unit V (**Figure 5.3**). This facies has the highest trace element concentrations of the sequence, except for Ba and Sr, which have the lowest contents (**Figure 5.4**). In Pb isotopic space, this facies is extremely variable and more radiogenic than the pelagic and terrigenous facies, with values ranging from 18.816 to 21.050 for $^{206}Pb/^{204}Pb$, 15.635 to 15.769 for $^{207}Pb/^{204}Pb$, and 38.817 to 40.569 for $^{208}Pb/^{204}Pb$ (**Figure 5.5**). Only one sample from Unit VI, corresponding to a siltstone located at the upper limit of the mafic material of the Hikurangi Plateau, has a similar Pb isotope composition to the pelagic and terrigenous facies. Both $^{87}Sr/^{86}Sr$ and $^{143}Nd/^{144}Nd$ show large variations with values ranging from 0.70388 to 0.70806 and 0.51235 to 0.51291 (εNd from 1 to 5.2), respectively (**Figure 5.5**).

5.5 Discussion

The thickness of the units in the subducting plate found in site U1520 differ from those used by Plank (2014), causing differences in the calculated geochemical bulk composition (**Table 5.4**, **Figure 5.5** and **Figure 5.6**). The estimation by Plank (2014) assumed that 50% of the material in the subducting plate is made of the volcaniclastic sequence, but this is only around 30% in site U1520. Detrital units correspond to around 50% of the U1520 sequence and carbonate units to around 20%. Higher contents in SiO_2, CaO, Na_2O, and K_2O along with lower $Fe_2O_3^T$ and MgO in site U1520 are due to the smaller proportion of the volcaniclastic material when comparing it with the estimation by Plank (2014).

Trace element concentrations are also different. The elements most abundant in the volcaniclastic sequence, such as Cr, Co, and Ni, are significantly lower than in the Plank (2014) composite, while others are more abundant in the pelagic and terrigenous facies, such as Rb, Cs, Ce and Li that are all higher in U1520 (**Figure 5.4** and **Figure 5.6**). Other elements, like Ba and Sr, have similar concentrations in U1520 and in the Plank (2014) composite. Isotopically, $^{206}Pb/^{204}Pb$, $^{207}Pb/^{204}Pb$, and $^{208}Pb/^{204}Pb$ are more radiogenic compared to the estimate of Plank (2014) (**Table 5.3**, **Table 5.4** and **Figure 5.5**). Large and variable isotopic compositions are also seen in $^{87}Sr/^{86}Sr$ and $^{143}Nd/^{144}Nd$, but their weighted averages of 0.70892 and 0.51250 respectively, are slightly less radiogenic than the corresponding Plank (2014) values of 0.70928 and 0.51259 (**Figure 5.5**).

Table 5.3: Selected trace elements and Pb-Sr isotopic ratios results from IODP cores. All trace results are in µg/g. Pb-Sr isotopes 2se indicated in parenthesis.

	Unit I U1518F 11R 2W 47/49	Unit II U1518F 12R 2 18/20	Unit III U1518F 27R 3W 8/10	Unit III U1520D 44X 1W 83/85	Unit IV U1520C 5R 1W 72/74	Unit IV U1520C 21R 1W 71/73	Unit V U1520C 24R 1W 91/93	Unit V U1520C 31R 1W 58/60	Unit VI U1520C 41R 1W 119/121	Unit VI U1520C 44R 1W 116/118
Li (µg/g)	47.79	61.95	57.59	60.73	30.06	8.23	48.79	26.60	80.08	14.50
V	75.99	101.81	96.99	91.13	46.08	<3	86.59	76.83	47.26	40.84
Cr	38.88	53.83	46.28	46.83	14.06	<3	151.63	115.34	19.69	<3
Co	5.57	8.74	5.61	8.64	5.14	2.79	38.13	21.02	8.66	6.35
Ni	15.64	22.03	16.88	21.36	13.30	6.54	98.58	83.78	25.56	6.51
Zn	58.70	83.58	68.34	80.09	35.64	24.02	200.69	93.80	140.05	53.57
Ga	16.37	21.88	18.68	20.55	8.54	<5	25.16	18.87	23.78	27.06
Rb	89.45	127.88	104.95	115.65	39.50	<5	39.39	26.93	30.97	69.04
Sr	296.96	263.26	372.44	314.88	969.66	854.90	152.83	409.09	176.39	364.02
Y	15.90	21.41	18.35	21.76	13.84	10.93	40.37	28.51	21.82	24.50
Zr	*81.97*	*71.58*	*87.69*	*85.27*	*44.13*	*5.86*	*531.44*	*399.62*	*288.82*	*499.40*
Nb	6.96	10.59	8.56	10.34	3.13	<2	111.90	86.54	26.21	96.03
Cs	4.76	7.57	6.23	6.56	2.22	<0.5	0.83	0.54	0.81	0.68
Ba	458.35	589.43	463.89	548.22	442.22	1109.15	98.92	215.74	2207.21	561.72
La	18.48	28.46	22.02	29.10	11.16	7.72	91.04	63.76	25.73	82.79
Ce	39.08	58.70	46.65	60.35	23.75	10.23	160.54	120.91	48.65	143.99
Pr	4.59	6.66	5.40	7.03	2.57	1.71	19.95	14.12	6.64	15.09
Nd	17.42	25.47	20.42	26.78	10.52	6.97	76.76	54.63	26.57	51.41
Sm	3.39	5.21	3.97	5.39	2.22	1.56	13.99	9.90	5.35	8.14
Eu	0.82	1.12	0.92	1.12	0.54	0.40	4.18	2.91	1.41	2.45
Gd	3.14	4.56	3.59	4.66	2.41	1.53	11.73	8.34	4.75	6.39
Dy	2.77	3.85	3.22	3.94	2.17	1.46	8.18	5.92	3.79	4.58
Ho	0.56	0.74	0.64	0.77	0.44	0.31	1.49	1.05	0.76	0.84
Er	1.64	2.11	1.91	2.18	1.34	0.85	3.93	2.82	2.13	2.55
Tm	0.23	0.30	0.26	0.31	0.21	0.13	0.52	0.36	0.29	0.35
Yb	1.57	1.91	1.75	2.02	1.30	0.82	3.21	2.27	1.93	2.09
Lu	0.25	0.28	0.27	0.30	0.18	0.12	0.48	0.34	0.30	0.36
Hf	*2.30*	*2.05*	*2.47*	*2.51*	*1.18*	*0.14*	*10.26*	*8.07*	*7.22*	*11.29*
W	1.03	1.57	1.23	1.57	0.64	0.24	0.51	0.89	0.58	0.63
Pb	11.38	18.62	13.10	18.29	2.46	1.38	4.19	3.32	15.79	4.72
Th	7.48	11.21	9.05	11.02	3.37	0.69	9.92	7.75	9.21	12.13
U	1.80	2.40	2.19	2.55	0.63	<0.5	1.10	1.69	1.31	2.90
$^{206}Pb/^{204}Pb$	18.8876	18.8746	18.8881	18.8942	19.0054	18.8162	20.7920	21.0496	18.9035	21.0324
(±2SE)	0.0023	0.0023	0.0025	0.0016	0.0021	0.0022	0.0028	0.0026	0.0019	0.0026
$^{207}Pb/^{204}Pb$	15.6511	15.6568	15.6538	15.6567	15.6572	15.6616	15.7549	15.7687	15.6353	15.7691
(±2SE)	0.0011	0.0011	0.0013	0.0007	0.0009	0.0022	0.0011	0.0023	0.0008	0.0012
$^{208}Pb/^{204}Pb$	38.8219	38.8258	38.8343	38.8322	39.0067	38.8885	40.3204	40.3032	38.8172	40.5693
(±2SE)	0.0040	0.0040	0.0043	0.0027	0.0035	0.0056	0.0044	0.0057	0.0031	0.0044
$^{87}Sr/^{86}Sr$	0.709092	0.710953	0.709694	0.710082	0.708923	0.707843	0.708057	0.704792	0.707026	0.703878
(±2SE)	0.000020	0.000022	0.000020	0.000023	0.000021	0.000020	0.000019	0.000019	0.000025	0.000017
$^{143}Nd/^{144}Nd$	0.512510	0.512382	0.512456	0.512400	0.512479	0.512358	0.512886	0.512907	0.512688	0.512803
(±2SE)	0.000023	0.000021	0.000024	0.000015	0.000013	0.000015	0.000019	0.000016	0.000020	0.000014
εNd	-2.5	-5.0	-3.5	-4.5	-3.1	-5.5	4.8	5.2	1.0	3.2

Forearc site U1518, has higher SiO_2 and Al_2O_3 than the trench site U1520 due to the influence of the detrital sequence, with lower TiO_2 and CaO from the volcanic material and carbonated sequences that are not involved in the accretionary prism (**Figure 5.3** and **Figure 5.4**). For the same reason, Cr, Co, Ni, Sr, and Ba are less abundant at site U1518 (**Figure 5.4**). However, site U1518 sediments have much more homogenous and less radiogenic Pb isotope ratios ($^{206}Pb/^{204}Pb$ of c.18.885, $^{207}Pb/^{204}Pb$ of c.15.653, and $^{208}Pb/^{204}Pb$ of c.38.826), while also having more radiogenic Sr and Nd isotope ratios ($^{87}Sr/^{86}Sr$ of c.0.70949, $^{143}Nd/^{144}Nd$ of c.0.51247) compared to Plank (2014) and U1520 (**Figure 5.5**).

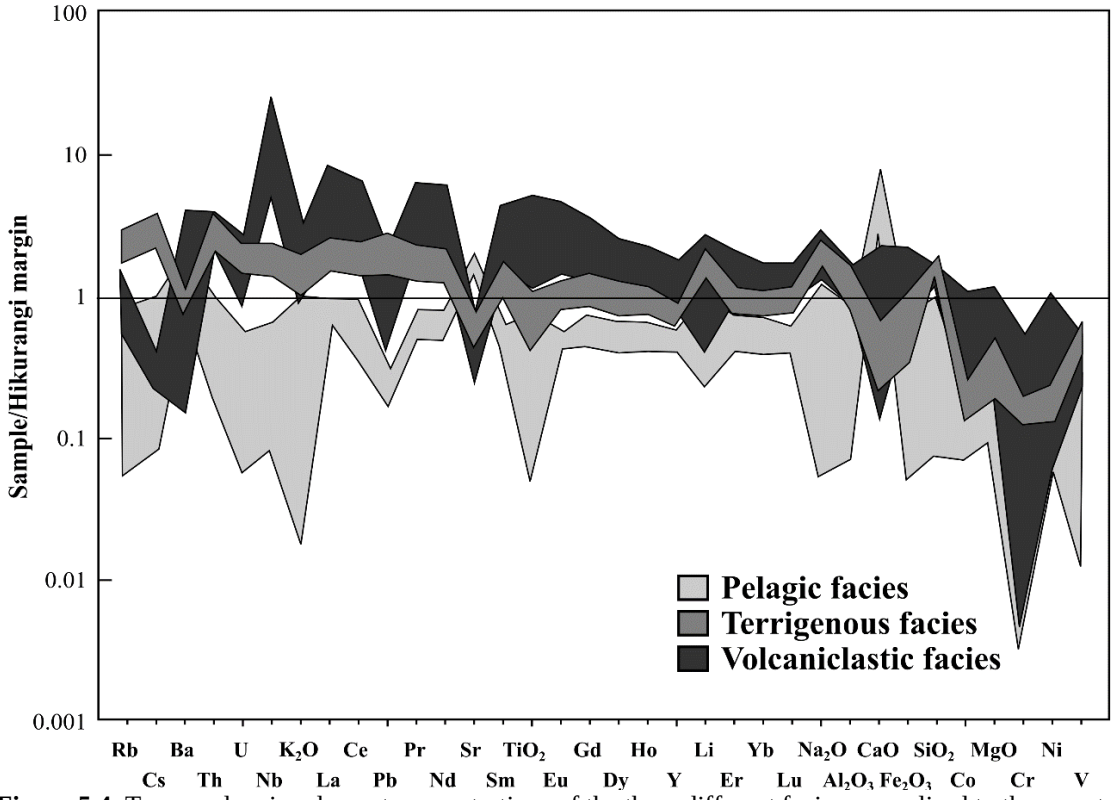

Figure 5.4: Trace and major element concentrations of the three different facies normalised to the reported bulk composition of the Hikurangi margin by Plank (2014).

The development of a *décollement* zone has been reported at site U1520 by Barnes et al. (2020). Dividing this site into the material located above and below the *décollement* may have a greater significance in the present–day tectonic distribution than the bulk composition of the site (**Figure 5.6**). This can help to elucidate if the subducted material, the tectonically eroded material, or both, are involved in the magma generation of the associated volcanic arc of the TVZ. The composition of the material located below the *décollement* is controlled by both the pelagic and volcaniclastic units. For example, the low SiO_2 and high CaO (38 wt.% and 31 wt.%, respectively) are controlled by the carbonate unit, while the high TiO_2 (2.13 wt.%) is influenced by the volcaniclastic sequence (**Figure 5.3**). In general, the trace element concentrations are dominated by the volcaniclastic sequence, having for example, the highest contents of Ni, Co, and Cr (**Figure 5.4**). The material located below the *décollement* zone is thought to be currently subducting, but large discrepancies are evident when compared to the Plank (2014)

composite (**Figure 5.6**). The Pb isotope composition of the material below the *décollement* is highly variable, but the bulk composition is around 20.4826 for $^{206}Pb/^{204}Pb$, 15.7355 for $^{207}Pb/^{204}Pb$ and 39.9833 for $^{208}Pb/^{204}Pb$, and is much more radiogenic than the Plank (2014) estimate (**Table 5.4** and **Figure 5.5**). Both Sr and Nd isotope compositions are highly variable and less radiogenic than those reported by Plank (2014) (**Table 5.4** and **Figure 5.5**).

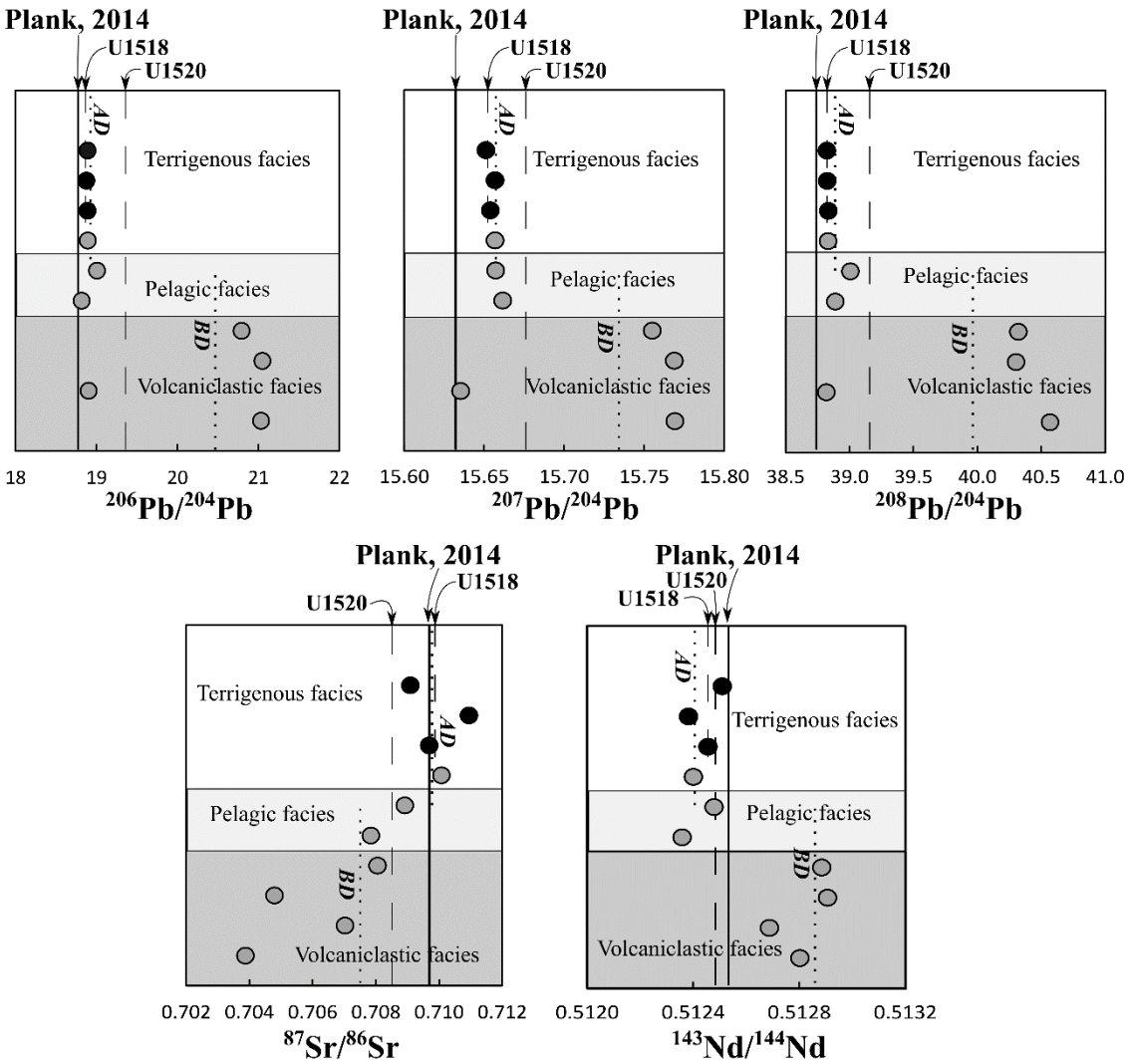

Figure 5.5: Pb-Sr-Nd isotope ratios of the samples and calculated bulk compositions. Black circles correspond to samples from site U1518 (accretionary prism), and grey circles correspond to samples from site U1520 (subducting plate). The bulk composition of sites U1520 and U1518, as well as above and below *décollement* (AD and BD, respectively) of the subducting plate, as well as the bulk composition of the Hikurangi Margin after Plank (2014), are shown as lines for reference. Analytical uncertainty is within symbol size.

On the other hand, the material located above the *décollement* has a weighted average composition that is SiO_2–rich (58 wt.%), with lower CaO and TiO_2 (17 wt.% and 0.54 wt.%, respectively) due to the more detrital nature of these units, with less carbonate material and without input of material from the Hikurangi Plateau. The trace elements related to mafic volcanism, like Ni, Co, and Cr, have lower concentrations here compared to those below the *décollement*, but higher levels of incompatible elements, such as Li, Rb, Cs, and Pb (**Figure 5.6**). The material above the *décollement* has a much more limited and less radiogenic range in Pb isotope ratios ($^{206}Pb/^{204}Pb$ of c.18.902, $^{207}Pb/^{204}Pb$ of c.15.657 and $^{208}Pb/^{204}Pb$ of c.38.844) than the weighted average of the material below the *décollement*. On the other hand, the $^{87}Sr/^{86}Sr$ and $^{143}Nd/^{144}Nd$ isotope ratios are more radiogenic than the estimate by Plank (2014) and the material below the *décollement* (**Figure 5.5**).

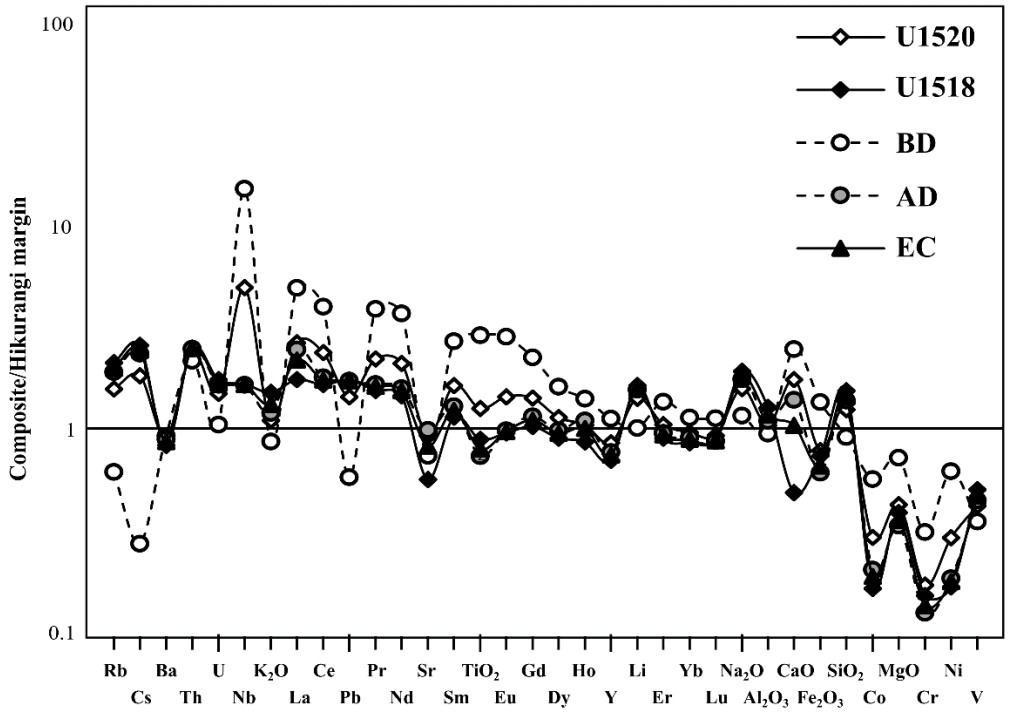

Figure 5.6: Multi-element diagram of the calculated bulk composition normalised to the Hikurangi bulk composition by Plank (2014). The bulk composition of the sites U1518 and U1520 are shown alongside the composition of the material above and below the *décollement* in the subducting plate (AD and BD, respectively) and the composition of material prone to tectonic erosion (AD and U1518 composite, shown as EC).

Table 5.4: Bulk composition of sites U1520 and U1518 as well as the composition of the material below *décollement* (BD) and above *décollement* (AD) in site U1520, and the tectonically erodible material (EC). Major elements are in wt.% and normalized to 100 on an anhydrous basis. Trace elements are reported in µg/g. Data from the New Zealand margin by Plank (2014).

	U1520	U1518	BD	AD	EC	Plank's
SiO_2	52.15	64.75	38.36	57.77	60.48	42.21
Al_2O_3	12.44	15.26	11.30	13.07	13.92	12.01
TiO_2	0.93	0.65	2.13	0.54	0.58	0.74
MnO	0.10	0.06	0.17	0.08	0.07	0.15
$Fe_2O_3^T$	5.27	4.96	9.12	4.09	4.42	6.77
MgO	2.20	2.02	3.76	1.74	1.85	5.24
CaO	21.88	6.05	30.84	17.36	12.98	12.55
Na_2O	2.68	3.25	1.96	2.97	3.08	1.70
K_2O	2.02	2.78	1.60	2.21	2.43	1.85
P_2O_5	0.33	0.21	0.76	0.19	0.19	0.13
Li	45.19	52.20	32.32	49.85	50.76	32.13
V	70.66	84.83	59.01	75.15	78.90	170.00
Cr	48.21	42.77	87.74	35.20	38.13	285.00
Co	10.67	6.00	20.69	7.40	6.86	36.80
Ni	29.34	16.81	62.40	18.50	17.85	101.50
Zn	76.11	64.47	112.99	64.33	64.39	115
Ga	16.51	19.77	17.78	16.29	17.64	-
Rb	73.35	98.53	28.52	88.65	92.48	46.80
Sr	512.32	312.08	408.59	547.10	456.01	557.00
Y	21.06	17.26	27.69	18.95	18.29	24.80
Nb	23.48	7.86	72.06	7.78	7.81	4.75
Cs	3.91	5.51	0.58	5.02	5.21	2.15
Ba	521.00	477.06	530.64	510.62	497.62	577.00
La	31.49	20.72	58.73	29.10	25.85	11.90
Ce	62.74	43.63	105.63	47.36	45.92	26.50
Pr	7.24	5.07	12.79	5.45	5.30	3.29
Nd	27.85	19.26	49.03	21.02	20.33	13.30
Sm	5.40	3.78	8.93	4.26	4.07	3.32
Eu	1.33	0.88	2.63	0.91	0.90	0.93
Gd	4.76	3.44	7.54	3.86	3.70	3.37
Dy	3.82	3.03	5.42	3.31	3.20	3.38
Ho	0.74	0.61	0.99	0.77	0.71	0.71
Er	2.07	1.77	2.68	1.88	1.84	1.98
Yb	1.86	1.66	2.21	1.76	1.72	1.95
Lu	0.27	0.26	0.33	0.26	0.26	0.30
W	1.07	1.15	0.59	1.24	1.20	-
Pb	10.60	12.81	4.25	12.70	12.75	7.40
Th	7.99	8.38	7.24	8.30	8.33	3.36
U	1.69	1.98	1.19	1.87	1.91	1.14
$^{206}Pb/^{204}Pb$	19.2719	18.8852	20.4826	18.9018	18.8953	18.8910
$^{207}Pb/^{204}Pb$	15.6753	15.6529	15.7355	15.6567	15.6552	15.6360
$^{208}Pb/^{204}Pb$	39.1417	38.8260	39.9833	38.8442	38.8371	38.7540
$^{87}Sr/^{86}Sr$	0.70892	0.70949	0.70752	0.70935	0.70939	0.70928
$^{143}Nd/^{144}Nd$	0.51250	0.51247	0.51286	0.51241	0.51243	0.51259

Since the material located above the *décollement* is eventually accreted to the accretionary prism and may be subsequently eroded tectonically, a composite of the accretionary prism (U1518) and the above *décollement* material in site U1520 may be useful (**Figure 5.6**; **Table 5.4**, referred to here as EC for erodible crust). The material above the *décollement* shares the same major oxide and trace element characteristics as the material in the forearc. The biggest difference is a higher concentration of CaO and Sr in the material above *décollement*, thus the material prone to tectonic erosion is similar to both sequences

in all elements and major oxides other than these two (**Figure 5.6**). This composite has a weighted average of c.18.895 for $^{206}Pb/^{204}Pb$, c.15.655 for $^{207}Pb/^{204}Pb$, c.38.837 for $^{208}Pb/^{204}Pb$, c.0.70939 for $^{87}Sr/^{86}Sr$ and c.0.51243 for $^{143}Nd/^{144}Nd$ (**Figure 5.5**). The homogeneity seen in the major oxide and trace element characteristics between the materials prone to tectonic erosion is also observed in the Sr–Pb–Nd isotope characteristics, contrasting with the large variations of the material located below the *décollement*. Although the *décollement* zone is a dynamic feature that is prone to migrate over time, the geochemical homogeneity seen in the material that has already been accreted (U1518) and material that is yet to be accreted (above *décollement*) (**Figure 5.3**; **Figure 5.4** and **Figure 5.5**), indicates that the structural characteristics of the subducting plate in the Hikurangi margin may not have significantly changed over time. However, this remains a hypothesis that cannot be tested based on the data of the present study.

ODP sites 1123 and 1124, used by Plank (2014) to estimate the bulk composition of the subducting sequence, are located up to 500 km away from the trench. This newly calculated estimate is based on IODP sites U1518 and U1520, located on the trench, improving relative to the previous estimate. The information about the lithological units and their thicknesses in these two sites is also well–constrained and slightly differs from that of sites 1123 and 1124, particularly in the proportion of the volcaniclastic sequence which is smaller than thought. Further, there was no information regarding which part of the sequence is accreted to the Hikurangi margin and which part of the sequence is subducted. The information provided by the identification of the *décollement* by Barnes et al. (2020) in site U1520 helps to identify and separate the material that is going to be accreted from the one that is going to be subducted. Due to the lack of information on the *décollement* when Plank's estimate was calculated, using it to test recycling of subducted

sediments in the TVZ may lead to erroneous results. Instead, with this new data it is now possible to test if recycling is occurring in the source of the TVZ in the form of subducting sediments or if instead, it corresponds to accreted material that suffered tectonic erosion.

5.6 Conclusions

New geochemical datasets for major oxide compositions, trace element concentrations, and Sr–Pb–Nd isotope ratios of the material in the Hikurangi margin were obtained for drill sites U1518 and U1520 retrieved during IODP Expedition 372B/375. The material in the subducting plate can be divided into two groups, namely material that is being subducted, and accreted or accreting material that may only be subducted by tectonic erosion, improving over previous estimates. These two groups show important differences in their compositional ranges for trace element concentrations and particularly their isotopic compositions. The material below the *décollement* shows large variations in Sr–Pb–Nd isotope signatures, whereas the material prone to tectonic erosion is much more homogeneous and less radiogenic in Sr–Pb–Nd isotope space. The geochemical differences between material above and below the *décollement* presented here may be employed for assessment of the composition and relative contribution of the subducted components in studies of elemental cycling through arc magmatism at the Hikurangi margin.

Chapter 6 - Crustal recycling of tectonically eroded sediments and its impact on magma generation of the Taupo Volcanic Zone, New Zealand

Carlos R. Corella Santa Cruz[1]; Georg F. Zellmer[1]; Claudine H. Stirling[2,3]; Susanne M. Straub[4]; Malcolm R. Reid[2,3]; Candace E. Martin[3]; Marco Brenna[3]; Karoly Nemeth[5]

[1]Massey University, Private Bag 11222, Palmerston North 4442, New Zealand

[2]Centre for Trace Element Analysis and Department of Geology, University of Otago, PO Box 56, Dunedin 9054, New Zealand

[3]Department of Geology, University of Otago, PO Box 56, Dunedin 9054, New Zealand

[4]Lamont-Doherty Earth Observatory of Columbia University, 61 Route 9W, Palisades, NY

10964, USA

[5]Institute of Earth Physics and Space Science, Csatkai E. út 6-8., Sopron 9400, Hungary

Abstract

The Taupo Volcanic Zone (TVZ) is a young volcanic arc producing large volumes of silicic volcanism. The TVZ is unusually dominated by rhyolitic eruptions in more than 90% of the total erupted volume and occurs in a rifting thin crust dominated by greywackes from the Torlesse composite terrane. New Pb-Sr-Nd-Hf isotopic data of the TVZ and Hikurangi margin sediments is in line with earlier observations of sediment input into the mantle source of the TVZ. However, the data here presented shows for the first time that this interaction does not occur with the subducting material but instead with tectonically eroded material from the accretionary prism. The composition of the subducting material is too variable in the isotope spaces and inconsistent when compared with TVZ samples. In contrast, the material prone to tectonic erosion not only has an isotopic composition that is consistent with mixing with the mantle to generate the signature of the TVZ volcanics but also is much less variable in isotope spaces. Thus, the isotopic behaviour of the magmas of the TVZ may be controlled by crustal recycling of tectonically eroded material, with subsequent transcrustal processing adding to the diversity generated subcrustally.

6.1 Introduction

Crustal recycling is an important process in the dynamic evolution of the Earth. Crustal material can be brought back into the mantle via subduction or crustal delamination and reduces the amount of continental crust destruction through subsequent partial melting and magma generation (*e.g.*, Patchett & Samson, 2003). The generation of new crust and its destruction by subaerial or tectonic erosion occurs in subduction zones, making them a pivotal part of the crustal recycling process (*e.g.*, Armstrong, 1981, Straub et al., 2020, von Huene & Scholl, 1993). The material recycled into the mantle consists of subducting trench sediments, subducting oceanic crust, and tectonically eroded material. This crustal material may then contribute to the newly generated overriding crust in subduction zones (*e.g.*, Johnson & Plank, 2000, Plank, 2014, Tollstrup & Gill, 2005, White & Dupré, 1986) and to intraplate volcanism around the globe (*e.g.*, Hofmann & White, 1982, Kawabata et al., 2011, Loubet et al., 1988, Weaver, 1991). Further, dehydration of the subducting material transports fluid-mobile elements back into the mantle and can affect the geochemistry of all arc magmas as well as oceanic island basalts (OIB) (*e.g.*, Aizawa et al., 1999, White & Dupré, 1986).

Interactions between the subducting material and the mantle are not restricted to hydrous fluids but also include melts, which can recycle a portion of the element budget from the subducted material (*e.g.*, Ben Othman et al., 1989, Plank, 2014, Plank & Langmuir, 1993). Melting of material in the subducting slab is known to generate magnesian andesites (*e.g.*, Defant & Drummond, 1990, Drummond et al., 1996, Shimoda et al., 1998, Tatsumi, 2001, Yogodzinski et al., 1995). However, melt generation by crustal recycling goes beyond the production of magnesian andesites, and its influence can be seen in different magmas. Specifically, a clear correlation between the chemical and isotopic compositions of the

trench sediments and associated volcanic arc magmas can be seen globally (Cornet et al., 2022, Förster & Selway, 2021, Hauff et al., 2003, Plank, 2014, Plank & Langmuir, 1993, Shimoda et al., 1998, Tatsumi, 2001). Tectonically eroded material from the overriding crust also plays an important role in the magma generation processes in volcanic arcs worldwide (*e.g.*, Straub et al., 2020). The influence of tectonically eroded material in the isotopic compositions of arc magmatism has been proposed around the circum-pacific belt in the Andes, Central America, the Trans-Mexican Volcanic Belt (TMVB), and in the Kermadec arc (Goss & Kay, 2006, Holm et al., 2014, Kay et al., 2005, Parolari et al., 2018, Parolari et al., 2021, Risse et al., 2013, Straub et al., 2015, Timm et al., 2014). Silicic partial melts of the slab react with the surrounding mantle, causing pyroxenitization and subsequent melting (Straub et al., 2008, Tatsumi, 2001). Evidence for the presence of rhyolitic melts within a veined mantle, caused by the interaction between the mantle and crustal melts, has been found in melt inclusions within mantle xenoliths (Dallai et al., 2022). The resulting melts of these pyroxenitic sources can be high magnesium basalts, magnesian andesites, and dacites (Rebaza et al., 2023, Straub et al., 2011, Tatsumi, 2001).

Further, the subducted material can detach from the slab and undergo diapiric ascent, followed by partial melting of the rising diapir in the hot core of the mantle wedge (Marschall & Schumacher, 2012, Nielsen & Marschall, 2017). For example, crustal recycling in the Trans-Mexican Volcanic Belt is thought to progress through tectonically eroded material, which subsequently detaches from the subducting plate, undergoes diapiric ascent, and contributes to arc magma generation (Parolari et al., 2018, Parolari et al., 2021, Straub et al., 2015). In the southern Kermadec arc, the Sr-Pb-Nd isotopic characteristics of the arc magmas have been linked to the presence of cold diapirs made

of material from the subducting plate and tectonically eroded crust from the overriding plate (Timm et al., 2014). This arc forms part of the 2,700 km long Tonga-Kermadec-Hikurangi subduction system, accommodating the convergence between the Pacific and Australian plates with the highest rates of subduction and back-arc extension on Earth (Bevis et al., 1995).

In the southernmost portion of this system, represented by the southern Kermadec and the Hikurangi margin, the subduction of the ~15 km thick Hikurangi Plateau (HP), a fragment of the Cretaceous Ontong Java-Manihiki-Hikurangi plateau Large Igneous Province (LIP), is currently occurring (Mortimer & Parkinson, 1996). This plateau has a sediment cover of ~2 km and abundant seamounts that are thought to have a strong effect on tectonic erosion (Barker et al., 2009, Davy & Wood, 1994, Lewis et al., 1998, Pedley et al., 2010, Timm et al., 2014). The subduction of the Hikurangi Plateau in the eastern margin of the North Island, New Zealand, is inferred to begin at *c.* 10 Ma (Reyners, 2013) and has reached depths of ~150 km (Reyners et al., 2011). The effects of the subduction of this plateau and tectonically eroded material have been reported in the southern Kermadec arc (Timm et al., 2014), while in the Taupo Volcanic Zone (TVZ), the arc associated with the Hikurangi margin, only subducted sediments have been reported to be involved in magma generation (*e.g.*, Gamble et al., 1996, Rooney & Deering, 2014). Recently, a possible link of subducted sediments and tectonically eroded material with the chemical and isotopic characteristics of the TVZ was hypothesised (**Chapter 4**). The occurrence of crustal recycling of subducting sediments and tectonically eroded material north of this volcanic arc, makes the TVZ an ideal location to test the input of not only the subducting sediments but also tectonically eroded material.

The TVZ is remarkably unusual in its overwhelming volumetric proportion of felsic eruptions (>95%, Cole, 1979) sourced from an overriding crust with a thin non-crystalline basement (~15-35 km, Eberhart-Phillips et al., 2019, Gase et al., 2019, Salmon et al., 2011, Stratford & Stern, 2004). Both, transcrustal processes such as assimilation-fractional crystallisation (AFC) and mixing are thought to be important contributors to the chemical and isotopic diversity of the TVZ (*e.g.*, Beier et al., 2017, Conway et al., 2020, Gamble et al., 1990, Graham et al., 1995, Hiess et al., 2007, McCulloch et al., 1994, Svoboda et al., 2021), and source processes like sediment (*e.g.*, Gamble et al., 1996, Rooney & Deering, 2014) and/or tectonically eroded crust addition to the mantle (**Chapter 4**) have been considered as important contributors. Recently, the International Ocean Discovery Program (IODP) Expedition 372B/375 drilled into the Hikurangi margin, greatly increasing the availability of material from the subducting plate and accretionary prism (Wallace et al., 2019). An approximation of the bulk chemical and isotopic composition of the subducting material and material prone to tectonic erosion has been presented in **Chapter 5**. These approximations to the bulk compositions are useful to determine potential links between the subducting material and tectonically eroded material with the magma generation processes occurring in the TVZ. Because this volcanic zone is the largest producer of silicic volcanism on Earth, with at least 3,900 km^3 of material produced only in the past 350 ky (Kósik et al., 2021, and references therein), crustal recycling in this margin has major implications for the generation of new crust and the balance between crustal growth and subducted material 'lost' into the mantle.

6.2 Sample selection and methods

Although the majority of the magmatic expressions of the TVZ have a felsic composition, intermediate and mafic magmas can still provide insight to better understand the magma

generation processes occurring in this volcanic zone (**Figure 6.1**). A coherent high-quality combined Sr-Pb-Nd-Hf data set, with all results being acquired from the same laboratory, allows for an internally consistent suite of compositions. Major element oxide and trace element concentrations, and Sr-Pb isotopic data for the TVZ are after **Chapter 4**, while major element oxide and trace element concentrations, and Sr-Pb isotopic data for IODP samples are after **Chapter 5**, and new Nd-Hf isotopic data for the TVZ and IODP samples are presented here. Nd-Hf isotopic analyses were performed at the Centre for Trace Element Analysis, University of Otago, New Zealand by multiple-collector ICP-MS (MC-ICP-MS), using a Nu Plasma-HR instrument (Nu Instruments Ltd, UK).

Chemical separation of Nd was performed following a protocol modified from Baker et al. (2002), Pin and Zalduegui (1997), whereas Hf chemical separation followed a procedure modified from Münker et al. (2001). All $^{143}Nd/^{144}Nd$ and $^{176}Hf/^{177}Hf$ ratios were corrected for instrumental mass fractionation adopting a true $^{146}Nd/^{144}Nd$ ratio of 0.7219 and a true $^{179}Hf/^{177}Hf$ ratio of 0.7325, applying the exponential mass fractionation law. Isobaric interferences for Nd (Sm) and Hf (Lu, Yb, W, and Ta) were monitored during analysis. All corrected Nd and Hf isotopic ratios were normalised to the international reference materials JNdi-1 using a $^{143}Nd/^{144}Nd$ ratio of 0.512115 after Tanaka et al. (2000), and JMC-475 using a $^{176}Hf/^{177}Hf$ ratio of 0.282160 after Vervoort and Blichert-Toft (1999), respectively. The international reference materials BHVO-2, BCR-2, AGV-2 (USGS, United States), JR-2, and JG-3 (GSJ, Japan) together with the in-house HPS secondary standard were employed to ensure data quality (see **Chapter 3**), while total procedural replicates (3 digestions each for Kinloch, Motuoapa Dacite, and 1520C 24R 1W 91/93) were used to assess external precision (see **Chapter 3**). Procedural blanks yielded <50 pg for Nd and <60 pg for Hf, negligible compared to the 30 ng used

for the measurement of both elements. The reported 2SE uncertainties include the analytical uncertainties of the sample and normalising standards. Lead isotopic data are shown in **Figure 6.2**, while the data of all isotopic systems (Sr-Pb-Nd-Hf) are shown in **Figure 6.3**, Nd-Hf isotope data reported in **Table 6.1**.

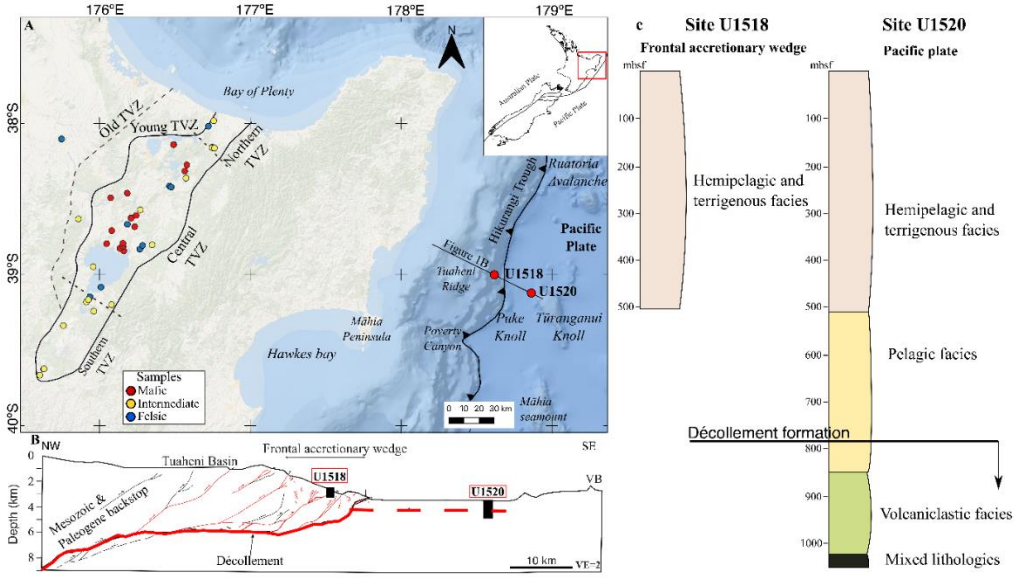

Figure 6.1: Sample locations, (A) details in **Chapter 4**. Basemap from ESRI Ocean, overview sourced from QMap repository. Young and old TVZ, and southern, central, and northern TVZ after Wilson et al. (1995). Coordinate reference system WGS84/UTM zone 60S. (B) Depth-converted seismic profile 05CM-04 showing locations and depths of sites drilled during Expedition 375 and structural interpretation (Saffer et al., 2019). Details in **Chapter 5**. (C) Schematic section of drill sites U1520 and U1518. Red circles highlighting sites U1518 and U1520. VB = volcanic cone. VE = vertical exaggeration.

6.3 Results

The TVZ ranges in $^{143}Nd/^{144}Nd$ from 0.51295 to 0.51255 and in $^{176}Hf/^{177}Hf$ from 0.28310 to 0.28280, consistent with previous results reported by Waight et al. (2017). Mafic magmas have $^{143}Nd/^{144}Nd$ ranging between 0.51295 and 0.51275, and $^{176}Hf/^{177}Hf$ varying between 0.28310 and 0.28297. Intermediate magmas display $^{143}Nd/^{144}Nd$ ranging between 0.51285 and 0.51265, and $^{176}Hf/^{177}Hf$ varying between 0.28310 and 0.28288. Felsic magmas display $^{143}Nd/^{144}Nd$ ranging between 0.5128 and 0.51255, however, no $^{176}Hf/^{177}Hf$ ratios are reported here for felsic samples because of the possibility of residual undissolved zircon following digestion. The compositions of the intermediate and mafic groups show significant overlap. Calculation of the bulk composition of the material

below and above the *décollement* follows that reported in **Chapter 5**. The samples from IODP Expedition 375 show a strong variation in the Nd isotopic system. Here, samples below the *décollement* show a strong variation in $^{143}Nd/^{144}Nd$, with values ranging between 0.5123 and 0.5129, while the material above the *décollement* and from the accretionary prism, have a much more constrained $^{143}Nd/^{144}Nd$ variation of between 0.5123 and 0.5125. This behaviour is also observed in the Pb-Sr isotopic systems, where the material below the *décollement* is highly heterogeneous while the material above the *décollement* and from the accretionary prism, is more homogeneous. The mafic material located below the *décollement* has a $^{176}Hf/^{177}Hf$ ratio ~0.2828, while the felsic material located above the *décollement* is not reported, as discussed above.

6.4 Crustal recycling in the Hikurangi margin

Crustal recycling of subducting sediments has been demonstrated to occur in the Kermadec-Hikurangi subduction system, with increasing input of subducted sediments towards the TVZ, as indicated by the trace element concentration and Pb isotopic characteristics (Gamble et al., 1996, Gamble et al., 1993, Rooney & Deering, 2014). The tectonically eroded material is a strong component of the recycled crust, based on the Sr-Pb-Nd isotopic systematics of the Kermadec arc (Timm et al., 2014) and Sr-Pb isotopic systematics of the TVZ (**Chapter 4**). Although the chemical and isotopic compositions of the magmas may be strongly influenced by recycled material, this may be subsequently masked by further transcrustal processing before eruption (**Chapter 4**). Recent studies have provided important information on the structure of the subducting plate and accretionary prism (Barnes et al., 2020), and its chemical and isotopic composition (**Chapter 5**). Together with the occurrence of tectonic erosion and subsidence in the Hikurangi margin (Barker et al., 2009, Collot & Davy, 1998, Collot et al., 1996, Lewis et

al., 1998, Pedley et al., 2010), the data presented here may provide further insights into the effect of recycled material on the magma generation in the TVZ.

Table 6.1: Results of $^{143}Nd/^{144}Nd$ and $^{176}Hf/^{177}Hf$ for samples from the TVZ and Hikurangi Margin (IODP); approximated bulk composition of drill cores U1520 and U1518, samples below (BD) and above (AD) the decollement, and material prone to tectonic erosion (EC).

	$^{143}Nd/^{144}Nd$	±2se	$^{176}Hf/^{177}Hf$	±2se
Kinloch	0.512886	0.000015	0.283061	0.000009
Matipan	0.512773	0.000014	0.282994	0.000008
Akatarewa	0.512784	0.000014	0.282952	0.000009
Acacia Bay	0.512861	0.000016	0.283069	0.000008
Poihipi	0.512863	0.000015	0.283071	0.000007
KTRIG	0.512837	0.000016	0.282989	0.000007
Tram Road	0.512865	0.000019	0.283055	0.000009
Kaipio	0.512919	0.000012	0.283026	0.000007
Pihanga	0.512735	0.000016	0.282900	0.000010
Ohakune	0.512846	0.000014	0.283047	0.000008
Te Ponanga	0.512724	0.000015	0.282928	0.000009
Pukeonaki	0.512804	0.000015	0.282989	0.000009
Waimarino	0.512802	0.000016	0.283032	0.000009
Ohakune Lakes	0.512819	0.000013	0.283058	0.000010
Karangahape	0.512783	0.000017	0.282960	0.000009
Manawahe	0.512655	0.000015		
Waikokomuka	0.512694	0.000017		
Edgecumbe	0.512641	0.000017	0.282891	0.000009
Maungatautari	0.512820	0.000019		
Punatekahi	0.512857	0.000016	0.283011	0.000010
Titiraupenga	0.512812	0.000013	0.283064	0.000008
Matahi	0.512759	0.000016	0.282993	0.000009
Rolles Peak	0.512765	0.000016	0.283001	0.000008
Kaharoa	0.512765	0.000018	0.282940	0.000008
Maunganamu Mosquito	0.512677	0.000021		
Hipaua	0.512758	0.000020		
Motuoapa Dacite	0.512635	0.000019		
Puketarata	0.512721	0.000019		
Motuoapa Rhyolite	0.512580	0.000022		
U1518F 11R 2W 47/49	0.512510	0.000023		
U1518F 12R 2 18/20	0.512382	0.000021		
U1518F 27R 3W 8/10	0.512456	0.000024		
U1520D 44X 1W 83/85	0.512400	0.000015		
U1520C 5R 1W 72/74	0.512479	0.000013		
U1520C 21R 1W 71/73	0.512358	0.000015		
U1520C 24R 1W 91/93	0.512886	0.000019	0.282845	0.000008
U1520C 31R 1W 58/60	0.512907	0.000016	0.282849	0.000009
U1520C 41R 1W 119/121	0.512688	0.000020	0.282845	0.000009
U1520C 44R 1W 116/118	0.512803	0.000014	0.282824	0.000007
U1520 bulk	0.512507			
U1518 bulk	0.512473			
BD bulk	0.512867		0.282849	
AD bulk	0.512421			
EC bulk	0.512446			

The first and most obvious indication of eroded material being involved in the magma generation processes of the TVZ is the broadly linear relationships shown by the samples in lead isotope space. To this end, the Pb isotope systematics show a line between the mantle and the material prone to tectonic erosion from the accretionary prism and above the *décollement* of the subducting plate, but not with the material below the *décollement* (**Figure 6.2a, b**). The Pb isotopic signature of the material located below the

décollement is not only highly variable but also has some extreme enrichments that would not reproduce the broadly linear distribution found in the TVZ.

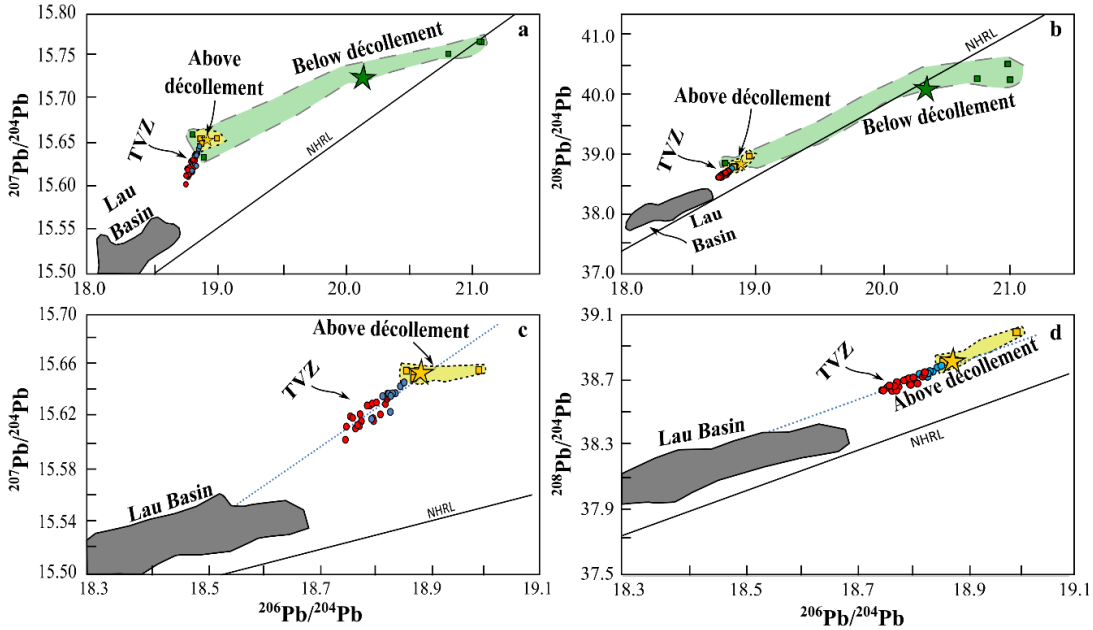

Figure 6.2: Lead isotopic spaces a) $^{208}Pb/^{204}Pb$ vs $^{206}Pb/^{204}Pb$ and b) $^{207}Pb/^{204}Pb$ vs $^{206}Pb/^{204}Pb$, c and d) are insights of a and b) respectively, showing a broadly linear behaviour of the TVZ consistent with a mixing of tectonically eroded recycled crust and mantle. Below and above the *décollement* after **Chapter 5**, TVZ after **Chapter 4** together with Lau Basin data (Ewart et al., 1998, Haase et al., 2002, Pearce et al., 2007, Todd et al., 2011, Turner et al., 1997, Wu et al., 2020). Red and blue circles are samples from the TVZ with <60 SiO_2 wt.% and >60 SiO_2 wt.%, respectively. Yellow and green squares are samples above and below the *décollement*, respectively. Yellow and green stars are the bulk composition above and below the *décollement*, respectively.

Conversely, the material that is located in the accretionary prism and above the *décollement* has tightly constrained Pb isotopic signatures, giving a composition that can feasibly be considered as a crustal endmember generating the Pb isotopic variation seen in the TVZ (**Figure 6.2c, d**). The observed correlation suggests that the lead isotopic diversity of the TVZ may correspond to the recycling of tectonically eroded material, with input from subducted material, including from the Hikurangi Plateau itself, being minimal (**Figure 6.3**). Subsequent transcrustal processing can generate the slight scatter in the Pb isotopic variations seen in **Figure 6.2c**, which is difficult to differentiate from source contamination due to the similar isotopic signatures of the materials (**Figure 6.3**).

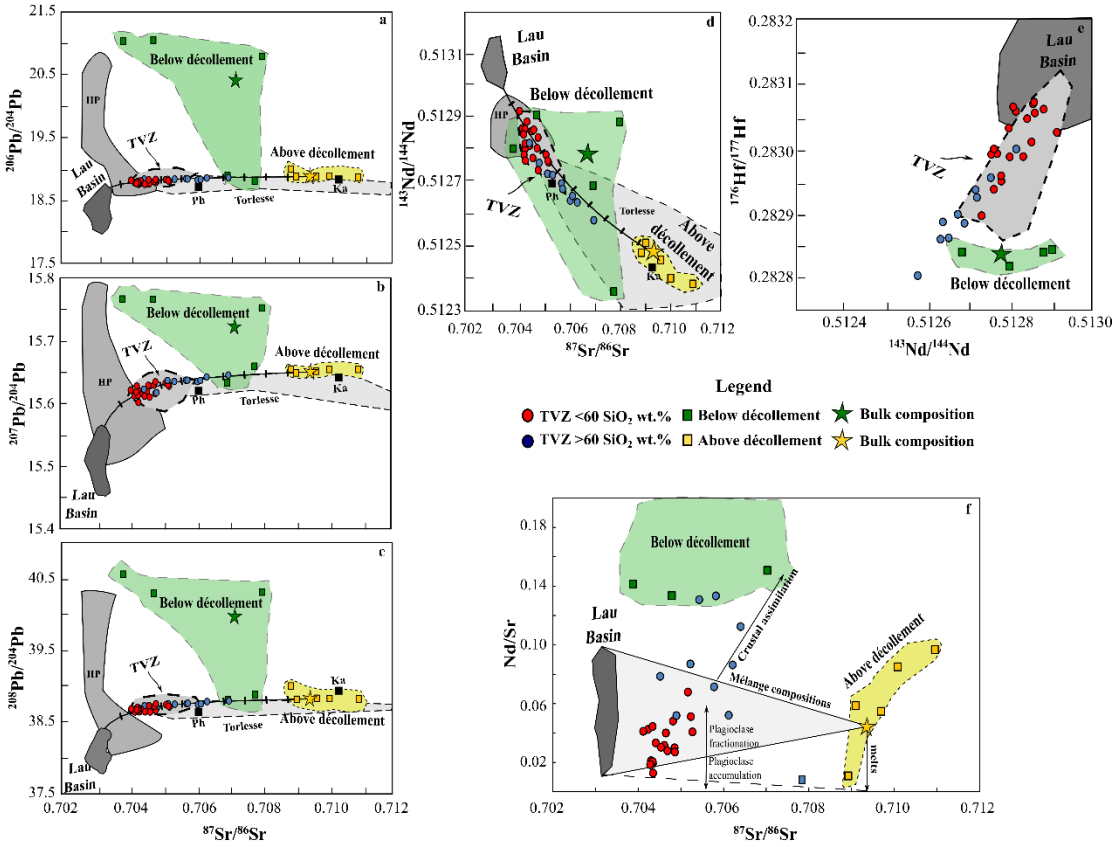

Figure 6.3: Sr-Pb-Nd-Hf isotope spaces. Strontium-Lead isotopic space a) $^{87}Sr/^{86}Sr$ vs $^{206}Pb/^{204}Pb$, b) $^{87}Sr/^{86}Sr$ vs $^{207}Pb/^{204}Pb$, and c) $^{87}Sr/^{86}Sr$ vs $^{208}Pb/^{204}Pb$, strontium-neodymium isotopic space d) $^{87}Sr/^{86}Sr$ vs $^{143}Nd/^{144}Nd$ and neodymium-hafnium isotopic space e) $^{143}Nd/^{144}Nd$ vs $^{176}Hf/^{177}Hf$ showing the behaviour of the TVZ inconsistent with the mixing of subducting material and mantle. f) Nd/Sr elemental ratio vs $^{87}Sr/^{86}Sr$ showing the mixing between the mantle and eroded material. Hikurangi Plateau (HP) after Hoernle et al. (2010), Torlesse after Graham et al. (1992), McCulloch et al. (1994), Price et al. (2015), Waight et al. (2017). Sr and Nd isotope ratios reported at **Chapter 4**. TVZ field after Shane et al. (2017), Gamble et al. (1996), Price et al. (2012), Sas et al. (2021).

Dehydration of the tectonically eroded material during erosion and subduction affects the concentration of fluid-mobile elements. Therefore, the concentration of Sr in the eroded material required adjustment to account for the hyperbolic trend seen in the TVZ volcanism, as done in previous studies of other volcanic zones (*e.g.*, Parolari et al., 2021). Despite this correction, the Pb and Sr isotopic relationship in the TVZ can be reproduced by mixing a mantle-like composition with the material prone to tectonic erosion (**Figure 6.3a-c**). Here, the material below the *décollement* is once again extremely variable and does not act as a plausible endmember when considering its bulk composition. The clear correlation between the TVZ and mixing between the mantle and tectonically eroded

crust, as seen in the Sr-Pb isotope systematics, indicates that the eroded material may be responsible for the isotopic characteristics of fluid mobile elements in the TVZ volcanics. The Sr-Pb isotope composition of the Torlesse composite terrane is similar to that of the eroded material, but it has a stronger variation (**Figure 6.3a-c**). Thus, although transcrustal processing also provides some isotopic input, it is likely that the main contributor to the Sr-Pb isotope diversity corresponds to source contamination, particularly in the mafic and some intermediate members.

The inclusion of the isotopic compositions of other more fluid immobile elements, such as Nd and Hf, can help to elucidate if the input of tectonically eroded material only appears in the form of fluid interactions or if melts of this material are also involved in the generation of magmas in the TVZ. In the Nd-Sr isotopic space (**Figure 6.3d**), mixing between the mantle and the material prone to tectonic erosion is also capable of reproducing the signatures seen in the TVZ. Once again, the material that is located below the *décollement* is too variable and its bulk composition is not consistent with the Nd-Sr isotopic signatures of the TVZ. In the Hf-Nd isotopic space (**Figure 6.3e**), neither the material located below the *décollement*, nor the Hikurangi Plateau are plausible endmembers. This indicates that not only fluids from the tectonically eroded material are interacting with the mantle under New Zealand's North Island, but also that melts of tectonically eroded material may be contaminating the source and contribute importantly to the Hf-Nd isotopic signatures seen in the TVZ. In **Figure 6.3d**, it can be again seen that although the isotope composition of the Torlesse composite terrane can be similar to that of the eroded material, it is more variable, and this is not reflected in the signature of the TVZ. Particularly, **Figure 6.3f** shows that the Sr isotopic signature of the TVZ magmas and their Nd/Sr ratios can be reproduced by either melting of a mixture between

the mantle and ‘crustal material’ or by interactions of melts from the ‘crustal material’ with the mantle, with transcrustal processing causing further variations in the chemical and isotopic compositions of the TVZ. Thus, the data here presented is not conclusive as to whether melt addition to the mantle, or mixing within the mantle and subsequent melting, is the dominant process (**Figure 6.4**).

Following subcrustal generation of the isotopic signature of the magmas of the TVZ by crustal recycling, transcrustal processing can also then add to the chemical and isotopic diversity, as many studies have highlighted (*e.g.*, Beier et al., 2017, Conway et al., 2020, Gamble et al., 1990, Graham et al., 1995, Hiess et al., 2007, McCulloch et al., 1994, Svoboda et al., 2021, Waight et al., 2017). The similar characteristics of the North Island basement and the tectonically eroded material make it difficult to quantify and differentiate how much transcrustal and source assimilation, influence the isotopic composition of the TVZ magmas. However, the large amounts of assimilation required to generate some of the isotopic signatures seen in the TVZ, and the isotopic variations seen especially in the mafic and intermediate members (**Chapter 4**), indicate that source processing may have a strong control on the isotopic variations observed, with transcrustal processing only modifying these compositions afterwards.

Lead isotopic data reported by Sas et al. (2021b) for the Okataina Volcanic Centre lies within the broadly linear trend seen in the TVZ data, consistent with mixing between the mantle and ‘crustal material’ (**Figure 6.2**). These authors found that the Sr isotopic ratios in plagioclase crystals were formed in intermediate melts rather than mafic melts, and with ~20 % crustal contamination, implying consistent relative contributions across the lifespan of the Okataina Volcanic Centre. Similarly, quartz crystals in rhyolites erupted

over the 600 kyr histories of the Okataina Volcanic Centre and across several caldera cycles show oxygen isotope ($\delta^{18}O$) homogeneity (to within ~0.2 ‰, 2σ) despite resorption textures, suggesting that these melts are derived from an isotopically homogeneous source with invariable relative contributions from the mantle and the crust (Sas et al., 2021a). Thus, it is possible that the Pb and Sr isotopic signatures seen in the Okataina Volcanic Centre are inherited from source processes and only slightly modified by subsequent transcrustal processing.

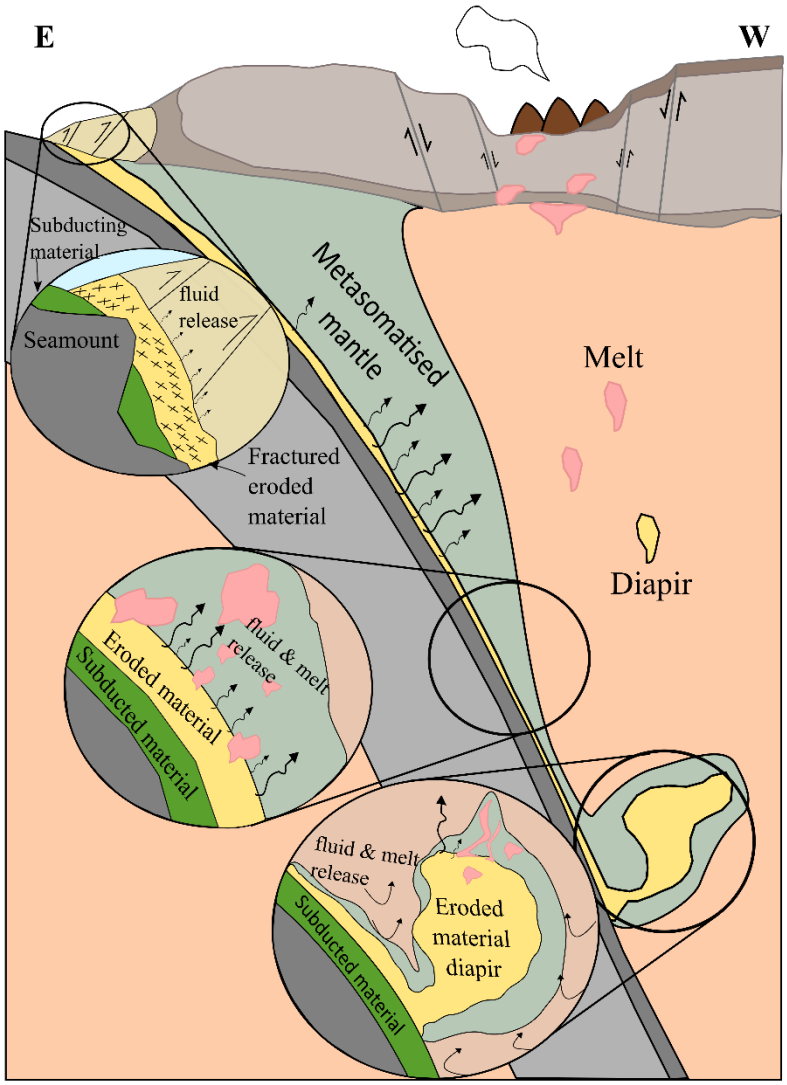

Figure 6.4: Schematic model of crustal recycling of tectonically eroded material, showing slab melting and diapir melting. Material from the accretionary prism is tectonically eroded and brought into the mantle, where fluids and melts are released either in the slab-mantle interface or having a diapiric ascent. Subducted material below the *décollement* zone, does not contribute to the melts and fluids interacting with the mantle underneath the TVZ.

6.5 Global perspectives on crustal recycling

Crustal recycling of tectonically eroded material in the TVZ, the largest producer of silicic subduction zone volcanism on Earth, has major implications for the generation of continental crust. The TVZ has produced at least 3,900 km^3 of material in the past 350 ky (Kósik et al., 2021, and references therein), and as has been proposed here, a portion of this material corresponds to the recycled crust. This implies that although tectonic erosion occurs in the Hikurangi margin, some of the eroded material is not lost and instead is recycled back into the crust, reducing the amount of crust 'lost' to the deep mantle.

Recycling pre-existing crustal material is not an uncommon process in the circum-Pacific belt. Here, the recycling of subducted sediments and tectonically eroded material from the overriding crust has been extensively reported. Around the circum-Pacific belt, crustal recycling of subducting sediments and oceanic crust by fluid and melt addition to the mantle, has been proposed to be involved in magma generation in SW Japan, Cascadia, Izu, and the Mariana arcs (*e.g.*, Förster & Selway, 2021, Hauff et al., 2003, Shimoda et al., 1998, Tatsumi, 2001). In the Miocene Setouchi volcanic belt, SW Japan, partial melting of subducting sediments and the altered oceanic crust has been shown to reproduce the Sr-Pb-Nd-Hf isotopic characteristics of the magmas, due to the subduction of a young lithosphere (*e.g.*, Tatsumi & Hanyu, 2003). Silicic melts from the sediments can react with mantle peridotite and create orthopyroxenites, which upon melting generate high-Mg andesites with signatures overlapping with those of terrigenous trench sediments (Tatsumi, 2001). Similarly, in the Izu-Mariana arcs, the recycling of subducting sediments and oceanic crust by fluid and melt release into the mantle has been

reported to generate the isotopic characteristics of the arc magmas (Hauff et al., 2003 and references therein).

However, crustal recycling in the circum-Pacific Belt is not restricted to sediments and oceanic crust, but also tectonically eroded material has been shown to have important inputs in the geochemical diversity of the magmas. Specifically, tectonically eroded material provides an important contribution to mantle heterogeneities in the central and southern Andes (Holm et al., 2014, Kay et al., 2005, Risse et al., 2013). Magmas in Costa Rica and Panama, Central America are linked to the incorporation of the forearc crust into the mantle by tectonic erosion of forearc ophiolites (Goss & Kay, 2006). In the TMVB, tectonically eroded material is thought to interact with the mantle, causing pyroxenitization and subsequent melting similar to what has been reported in SW Japan (Straub et al., 2011, Straub et al., 2008), or to undergo diapiric ascent and subsequent melting, thereby contributing to arc magma generation (Parolari et al., 2018, Parolari et al., 2021, Straub et al., 2015).

Recent research has questioned if transcrustal processes are actually the main driver in the chemical and isotopic evolution of magmatism, and instead propose that crustal recycling is a major contributor of characteristics usually attributed to transcrustal processing (*e.g.*, Cornet et al., 2022). Furthermore, the recycling of tectonically eroded forearc crust is an important contributor to arc magmatism around the globe (Straub et al., 2020), and the TVZ is not an exception to this observation. Subsequent transcrustal processes also add to the isotopic and chemical diversity seen in the TVZ, but it is for now difficult to distinguish source processes involving crustal material and transcrustal processes.

6.6 Conclusions

1. The broadly linear trend followed by the TVZ eruptives in lead isotope space is consistent with a subcrustal mixture of two homogenized endmembers: the mantle and crustal material.
2. The crustal endmember does not correspond with the subducting material (below the *décollement*) due to the different and large variations in the Sr-Pb-Nd-Hf isotopic compositions, inconsistent with the isotopic behaviour of the TVZ. Instead, it strongly correlates with tectonically eroded material from the accretionary prism and above the *décollement* of the subducted plate, which has a tightly constrained isotopic composition in the Pb-Sr-Nd systematics.
3. Crustal recycling of tectonically eroded material from the accretionary prism caused by the subduction of the thick Hikurangi Plateau and seamount collision is a feasible petrogenetic process, generating the isotopic variations seen in the hyperactive TVZ. This has major implications for the generation of a more evolved crust.

Chapter 7 - Synthesis

Here, the results of the three studies and their implications on the magmatism of the TVZ are presented in relation to their implications on our understanding of arc magmatism on a global scale. In **Chapter 4**, whole-rock major and trace element concentrations together with Sr-Pb isotope ratios were combined with MCS modelling and show that: i) Crustal assimilation and fractional crystallisation alone, with the presented parameters, require large amounts of crustal assimilation and fractionation to reproduce similar compositions to those of the volumetrically dominant rhyolites. ii) Based on the Pb-Sr isotopic behaviour of the TVZ samples, it is likely that the geochemical diversity is generated dominantly by crustal recycling of tectonically eroded crust and additional transcrustal processing (*e.g.*, AFC and magma mixing). In **Chapter 5**, whole rock major and trace element concentrations together with Sr-Pb isotope ratios of the IODP drill cores U1520 and U1518 are used to approximate the bulk composition of the tectonically eroded material and the subducted material. In **Chapter 6**, Nd-Hf isotopic ratios of the TVZ and IODP samples, together with the results of previous chapters, show a relation between the TVZ and the tectonically eroded material that is not limited to fluid mobile elements and also show that the subducted material is not involved in the Sr-Pb-Nd-Hf isotope systematics. Together, these studies represent a new, comprehensive model for the petrogenesis of primary magmas that feed the eruptions of TVZ.

7.1 Global perspectives on the limitations of transcrustal assimilation

Transcrustal assimilation is traditionally viewed as the key process occurring in the subsurface that explains the geochemical diversity seen during magmatic evolution, not only in arc volcanism but also in other tectonic settings. It is conventionally thought that mafic magmas generated in the mantle are injected into the base of the crust and then start

to assimilate the surrounding crustal material and mix, generating the entire range of geochemical variation observed in magmas ranging in composition from basalts to rhyolites. An important factor controlling the magmatic evolution in the crust is the crustal thickness. A thicker crust would act as a density filter and cause longer fractionation and cooling times, thereby permitting more magma-crust interactions which modify the chemical composition of the magmas (*e.g.*, Leeman, 1983, Plank & Langmuir, 1988). As a result, arcs with thick crust have, on average, more silicic compositions than arcs with thin crusts (Farner & Lee, 2017). However, there remain some open questions about the petrogenetic, and evolution processes involved in the formation of new crust that cannot be explained by the differentiation of mafic magmas. For example, the bulk composition of the continental crust is estimated to be andesitic (*e.g.*, Rudnick & Gao, 2003, Taylor, 1967, Taylor & McLennan, 1985) with high Mg# and Ni contents that cannot be reproduced by crustal differentiation. This composition is similar to that of high-Mg# andesites, and thus a significant proportion of the crust may be composed of high Mg# andesites (*e.g.*, Kelemen, 1995, Rudnick, 1995), making source processes pivotal in crustal growth. Thus, the classical approach used to explain magmatic differentiation in many arcs, including the TVZ (**Figure 7.1**), where mafic mantle magmas assimilate crustal materials, may not be capable of explaining all of the diversity seen in nature.

Most previous studies evaluate assimilation-fractional crystallisation by employing the method from DePaolo (1981b). Although this method uses parameter approximations (*e.g.*, the ‘r’ value), it does not incorporate thermodynamic constraints, such as the temperature of the magma and the wall rocks, amongst others. Recent work has noted that not only are the amounts of assimilation required to reproduce the isotopic compositions

of arc magmas in the Famatinian continental arc (Argentina) unreasonably high, but also that no existing crustal endmembers fit as interacting with the mafic rocks (Cornet et al., 2022). Similar observations have been made in other areas such as the Dovyren layered intrusion, Eastern Siberia (Amelin et al., 1996), and the gabbroic complex from Yinan, Shandong Province, China (Xu et al., 2004).

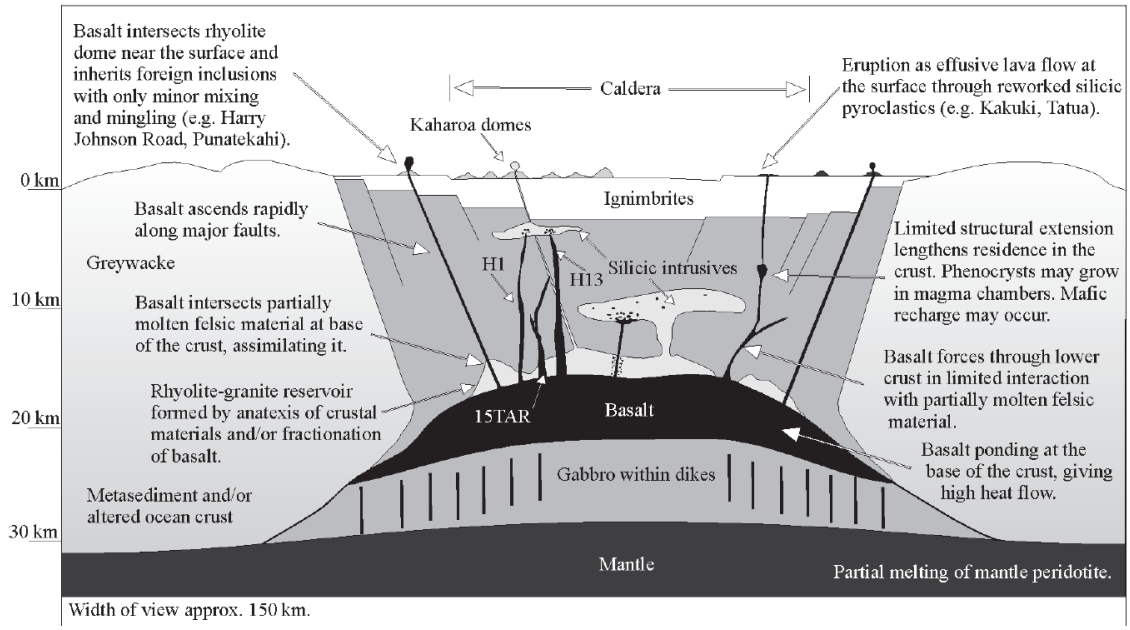

Figure 7.1: Schematic view of the TVZ from Hiess et al. (2007), showing the role of transcrustal processes in the magmatic generation and evolution.

This project identifies that although transcrustal assimilation has been proposed as a necessary means to generate the isotopic diversity seen in the TVZ, including the most felsic members (*e.g.*, Deering et al., 2011, Gamble et al., 1990, Gamble et al., 1993, Graham et al., 1995, Graham & Hackett, 1987, McCulloch et al., 1994, Reid, 1983, Reid & Cole, 1983), the significance of transcrustal assimilation may be smaller than previously thought. Transcrustal assimilation would require up to 50% of the original volume of magma assimilating the wall rock composition, paired with up to 90% of fractional crystallisation requiring at least 10 times more mafic starting material than the observed felsic materials. This is inconsistent with the thin, non-crystalline basement of

the Central North Island and the presence of extension faults that act as conduits facilitating rapid magma ascent through the crust. Transcrustal assimilation also does not conform with the hypothesis that more evolved magmas dominate in thicker crusts (Leeman, 1983); instead, the dominant volume of rhyolitic eruptions is found in the extended ~16 km thick crust in the northern and central regions, compared to ~35 km in the southern regions (Eberhart-Phillips et al., 2019, Gase et al., 2019, Salmon et al., 2011, Stratford & Stern, 2004). Furthermore, the presence of silicic volcanism has been reported to occur as early as at 1.88 – 1.84 Ma (Chambefort et al., 2014, Milicich et al., 2020), indicating that there may not be a clear gradual temporal evolution from mafic to more evolved volcanism in the TVZ.

Complex transcrustal processes including assimilation, fractional crystallisation, magma mixing, and crustal anatexis have been proposed to explain the chemical and isotopic variations seen in the TVZ (Beier et al., 2017, Conway et al., 2020, Deering et al., 2011, Gamble et al., 1990, Gamble et al., 1993, Graham et al., 1995, Graham & Hackett, 1987, McCulloch et al., 1994, Reid, 1983, Reid & Cole, 1983, Svoboda et al., 2021). Although these processes explain some of the variations observed, they cannot explain: i) the variations observed in the mafic members, linked to source heterogeneities (*e.g.*, Gamble et al., 1996, Gamble et al., 1993, Rooney & Deering, 2014), ii) the Sr-Pb isotope signatures of some intermediate members, which are more unradiogenic than mafic members, and iii) the large amounts of transcrustal assimilation required to generate the isotopic signatures observed in felsic magmas. Instead, we showed that these characteristics may be related to the source of these magmas which may have a larger control on the diversity in TVZ magmatism than previously thought, with subsequent complex transcrustal processing overprinting these signatures.

7.2 Global perspectives on crustal recycling

An alternative process to transcrustal assimilation generating the chemical and isotopic diversity seen in magmas around the globe is the source assimilation of crustal material. Crustal material can be transported into the mantle via subduction or crustal delamination and subsequently contribute to crustal growth (*e.g.*, Patchett & Samson, 2003). Thus, crustal recycling is an important process in the dynamic evolution of the Earth. Particularly, subduction zones generate new crust by magma addition to the overlying plate and also result in its destruction through subaerial and tectonic erosion, making subduction zones a pivotal part of this process (*e.g.*, Armstrong, 1981, Straub et al., 2020, von Huene & Scholl, 1993). The crust generated in arcs can be the result of recycled subducted material, corresponding to the subducting trench sediments, oceanic crust and/or tectonically eroded material (*e.g.*, Johnson & Plank, 2000, Plank, 2014, Tollstrup & Gill, 2005, White & Dupré, 1986). Recycling of this material is not restricted to subduction zones and also has an important input to intraplate volcanism around the globe (*e.g.*, Hofmann & White, 1982, Kawabata et al., 2011, Loubet et al., 1988, Weaver, 1991).

The type of interactions occurring between the subducted material and the mantle wedge are variable (**Figure 7.2**). These can occur as dehydration fluids from the slab transporting fluid-mobile elements back into the mantle (*e.g.*, Aizawa et al., 1999, White & Dupré, 1986), melts transporting fluid-immobile elements (*e.g.*, Ben Othman et al., 1989, Defant & Drummond, 1990, Drummond et al., 1996, Plank, 2014, Plank & Langmuir, 1993, Shimoda et al., 1998, Tatsumi, 2001, Yogodzinski et al., 1995), or even solid material mixing with the mantle to variable degrees (Parolari et al., 2018, Parolari et al., 2021, Straub et al., 2015). A correlation between the trench sediments and the associated volcanic arc chemical and isotopic compositions is seen globally (Cornet et al., 2022,

Förster & Selway, 2021, Hauff et al., 2003, Plank, 2014, Plank & Langmuir, 1993, Shimoda et al., 1998, Tatsumi, 2001). Tectonically eroded material with diverse compositions can also play an important role in the magma generation processes (*e.g.*, Goss & Kay, 2006, Holm et al., 2014, Kay et al., 2005, Parolari et al., 2018, Parolari et al., 2021, Risse et al., 2013, Straub et al., 2015, Straub et al., 2020, Timm et al., 2014).

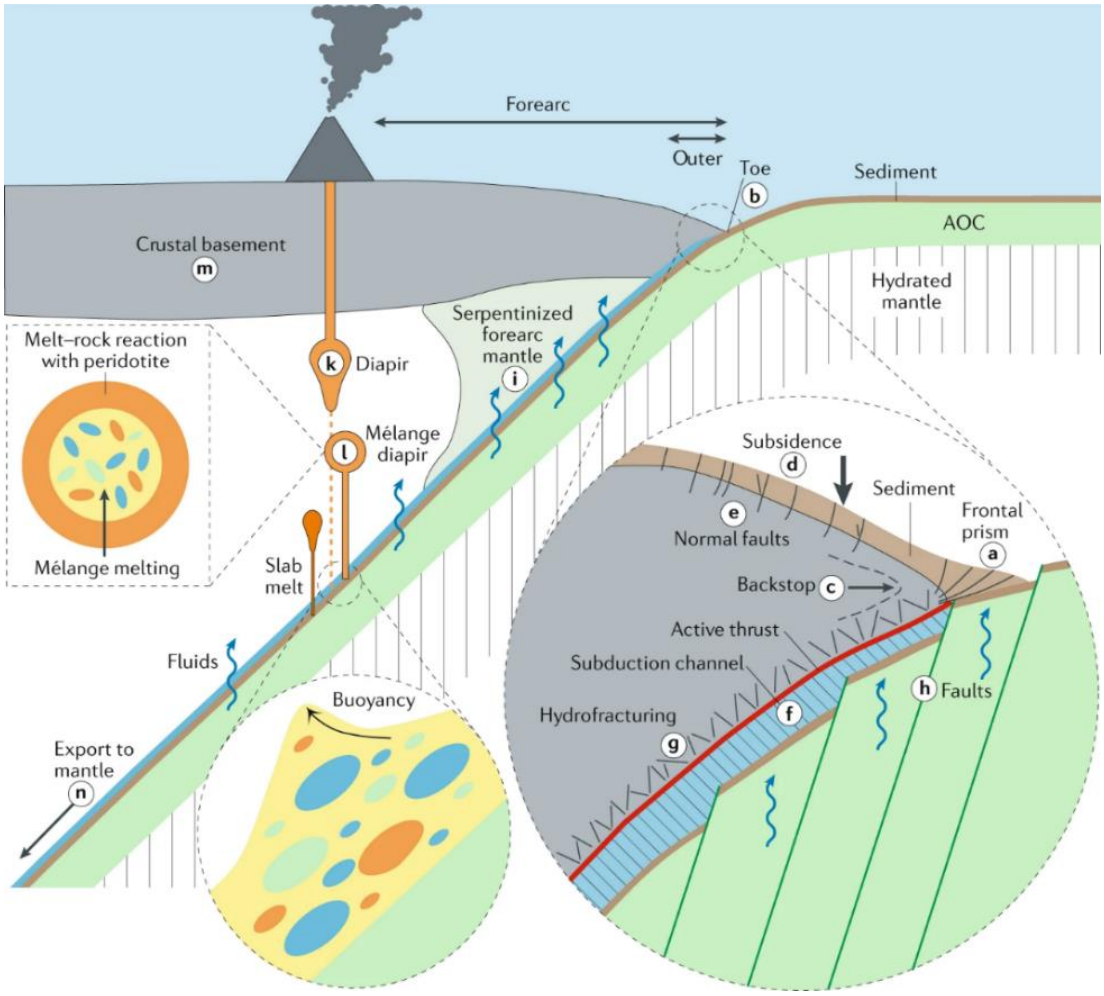

Figure 7.2: Schematic diagram showing the different types of materials and processes involved in crustal recycling in arc settings, from Straub et al. (2020). The material involved in these processes includes the altered oceanic crust, the sedimentary cover and basal or frontal tectonically eroded material from the overlying crust. These materials interact with the mantle wedge by fluid and melt releases and by the formation of *mélange* diapirs.

The occurrence of rhyolitic melts has been reported in melt inclusions within mantle xenoliths from a veined mantle, due to the interaction between crustal melts and the mantle (Dallai et al., 2022). These rhyolitic melts can originate from interactions at the slab-mantle interface or from ascending diapirs (Marschall & Schumacher, 2012, Nielsen

& Marschall, 2017). Melts of the crustal material react with the surrounding mantle, causing pyroxenitization and subsequent melting (Straub et al., 2008, Tatsumi, 2001). The resulting melts of the pyroxenitic sources can range from high-Mg# basalts and magnesian andesites to dacites and even rhyolites, after multiple reactions (Rebaza et al., 2023, Straub et al., 2011, Tatsumi, 2001).

7.2.1 Mantle diapirs in subduction zones

Modelling the detachment of material from the subducting slab and subsequent diapiric ascent and interaction with the mantle was first performed by Castro & Gerya, 2008. It was found that at 1.5 – 2.5 GPa, the material may reach temperatures of around 1000 °C due to thermal re-equilibration. Under these conditions, it is expected that large melt fractions are produced, up to 50% in a dry mantle and 80% in a hydrated mantle. Irrespective of whether the composition of the diapir is mafic, intermediate or felsic, all modelled diapirs with 1, 2, 3 and 4 km radius show melt fractions between 20 – 30% for around 80% of the volume, while the outermost volume loses up to 80% (Klein and Behn, 2021). These melts can have compositions varying from basalts to rhyolites coming from variable sources, with more felsic magmas being generated when multiple reactions occur (Rebaza et al., 2023).

Evidence for the occurrence of mantle diapirs by seismic techniques is typically absent, likely due to the low resolution of tomographic images. However, recent work has shown the presence of several diapirs with radii of ~1 km at between 60 – 95 km depth beneath two active volcanoes in the northern Taiwan area and may be directly associated with magma generation in the mantle (Lin et al., 2021). Thus, the occurrence of diapirs

underneath arc volcanoes may be more common than previously thought, but the lack of high-resolution images makes it difficult to detect them using geophysical techniques.

7.2.2 Influence of tectonic erosion in arc magmatism

As presented above, subducting material and tectonically eroded material have important inputs into arc magmatism around the globe. However, tectonically eroded material has been reported to have a greater influence than the subducting material in some arcs, *i.e.*, subducting sediments and oceanic crust (*e.g.*, Goss & Kay, 2006, Parolari et al., 2018, Parolari et al., 2021, Straub et al., 2020). At the Trans-Mexican Volcanic Belt, it has been reported that crustal recycling is dominated by tectonically eroded material and not by subducting sediments (Parolari et al., 2018, Parolari et al., 2021, Straub et al., 2015).m Regionally, in the Tonga-Kermadec-Hikurangi subduction system, tectonic erosion has been reported to be caused by the subduction of the thick Hikurangi Plateau and its seamounts in the Hikurangi margin (Barker et al., 2009, Collot & Davy, 1998, Collot et al., 1996, Lewis et al., 1998, Pedley et al., 2010), and the Louisville Seamount Chain in the limit between the Tonga-Kermadec margins (Clift & Vannucchi, 2004, Contreras-Reyes et al., 2011). Recycling of tectonically eroded material, together with subducting sediments and material from the Hikurangi Plateau, was reported by Timm et al. (2014) in the southern Kermadec arc, caused by interactions of cold diapirs with the mantle and revealed by Sr-Nd-Pb systematics.

In the TVZ, crustal recycling of subducting sediments has been previously reported (*e.g.*, Gamble et al., 1996, Gamble et al., 1993). Instead, this project found that the material possibly being recycled in the TVZ corresponds to tectonically eroded material from the accretionary prism and not to the subducting material (**Figure 7.3**). This is consistent with

previous findings, although at first glance it may be at odds. Recent information about the *décollement* zone being developed in the subducting plate (Barnes et al., 2020) indicates that the material that was used by previous studies may have been located above the *décollement* and thus would not be subject to subduction unless tectonic erosion takes place.

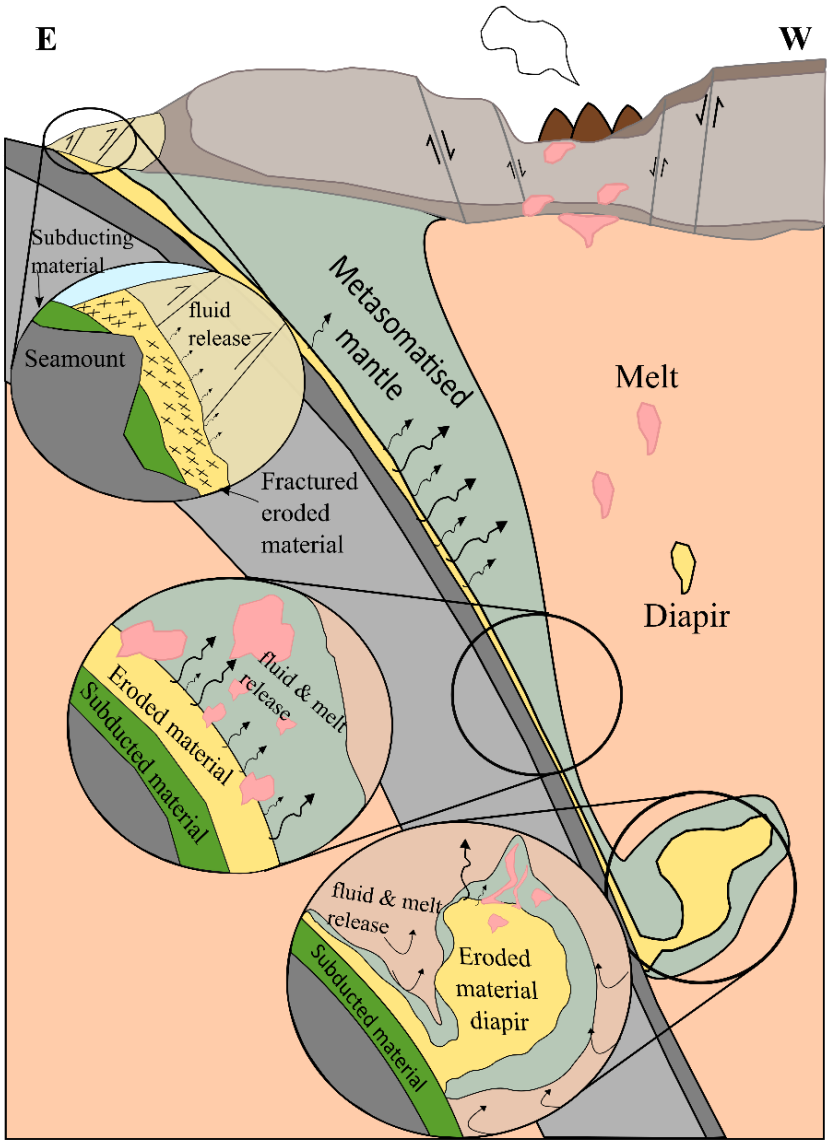

Figure 7.3: Same as **Figure 6.4**,. Schematic model of crustal recycling of tectonically eroded material, showing slab melting and diapir melting. Material from the accretionary prism is tectonically eroded and brought into the mantle, where fluids and melts are released either in the slab-mantle interface or having a diapiric ascent. Subducted material below the *décollement* zone, does not contribute to the melts and fluids interacting with the mantle underneath the TVZ.

Results reported here indicate that the isotopic variations seen in the TVZ magmas may be primarily controlled by crustal recycling of tectonically eroded material from the accretionary prism. This is not only valid for the fluid mobile elements such as Sr and Pb, but also for fluid immobile elements such as Nd. Thus, not only does fluid release of the subducting slab influence the source characteristics, but also melt and/or material interactions with the mantle have an important influence. A clear disconnection between the isotopic signatures of the TVZ and the subducting material shown by all Sr-Pb-Nd-Hf isotopic systematics is in strong contrast with that of the material prone to tectonic erosion, which robustly correlates with the volcanic samples of the TVZ. The compositional link between the magmatism of the TVZ and the tectonically eroded material may not only explain the isotopic heterogeneities seen in mafic magmas, but also some of the isotopic signatures that are seen in andesitic magmas, which cannot be explained by transcrustal processes alone. Furthermore, the isotopic link between the mantle and tectonically eroded material is also seen in the felsic members of the TVZ, and although some variation is caused by subsequent transcrustal processes, the model developed here greatly reduces the amount of crustal material required to be assimilated in the overlying plate. Thus, source processes may be of significant importance, not only in magma generation processes, but also in the magmatic evolution of the TVZ. However, due to the similarities between the tectonically eroded material and the basement of the Central North Island, source and transcrustal assimilation remain difficult to distinguish based on the data here reported.

7.2.3 Implications in mass balance and crustal growth

Tectonic erosion and subduction of different materials are thought to be destructive processes. However, the occurrence of crustal recycling of both subducting and

tectonically eroded materials implies that material that would otherwise be ‘lost’ to the deep mantle, is being inserted back into the crust. In actuality, the TVZ is the largest producer of silicic subduction zone volcanism on Earth and has produced at least 3,900 km^3 of material in the past 350 ky (Kósik et al., 2021, and references therein). A portion of this material may correspond to recycled tectonically eroded crust and has important implications in the mass balance of crustal destruction and crustal growth. During the phanerozoic, 1.1 km^3/yr and 1.8 km^3/yr of subducting and tectonically eroded material, respectively, have been globally ‘lost’ (Stern & Scholl, 2010). However, crustal recycling implies that a considerable proportion of these volumes can be brought back into the crust, limiting the amount of crust that is ‘lost’ to the deep mantle by tectonic erosion.

Chapter 8 - Conclusions and outlook

This study integrates the whole rock major and trace element concentrations and Sr-Pb-Nd-Hf isotopic systematics of the Taupo Volcanic Zone and the Hikurangi margin sediments from the IODP Expeditions to gain an insight into the crustal recycling processes involved in magma generation at this subduction margin. The following conclusions are derived from this research:

1. Thermodynamically constrained assimilation-fractional crystallisation modelling using the Magma Chamber Simulator revealed that AFC alone, following the models here presented, has several limitations in reproducing the isotopic diversity of the TVZ.
    a. The isotopic variations observed in the mafic members cannot be reproduced by transcrustal processes, indicating that these variations are source related.
    b. Some intermediate magmas can be generated by transcrustal processes, such as AFC and magma mixing, while others, with more unradiogenic Sr-Pb isotope signatures, require a source origin.
    c. To reproduce the signatures similar to that of most evolved magmas of the TVZ, up to 90% of fractional crystallisation and 50% of crustal assimilation is required. This would require a starting volume of mafic magma more than 10 times the volume represented by rhyolitic eruptions. The abundant volume of rhyolitic eruptions is not correlated with an increase in crustal thickness.
    d. Altogether, this indicates that source processes may be involved in the magma generation and isotope characteristics of the TVZ to a greater extent than previously thought.

2. Lead isotopic systematics show a clear two-member mixing between radiogenic and unradiogenic materials, even in the most mafic endmembers. These mixing members may be the mantle and a ‘crustal material’ being recycled subcrustally.
    a. The subducting material, below the *décollement*, is too heterogeneous and too enriched to be a suitable endmember in this mixture.
    b. Instead, material from the accretionary prism and above the *décollement* has the required lead isotopic composition to generate the observed trend and is consistently homogenous.
3. Inferences from the strontium, neodymium and hafnium isotopic systematics are consistent with those based on the lead isotopic systematics:
    a. The Sr, Nd and Hf isotopic systematics of the subducting material are highly variable, and its bulk composition is inconsistent as an endmember causing the isotopic diversity observed in the TVZ.
    b. However, the Sr and Nd isotopic systematics of the accretionary prism and above the *décollement* are consistent as an end member, not only in their bulk value, but also in their constrained behaviour.
4. The occurrence of tectonic erosion in the Hikurangi margin has been previously reported in several studies but never linked to the magma generation of the TVZ. The material subducting in this margin shows no link to the magmatism of the TVZ. Instead, a link between the material from the accretionary prism and the TVZ is observed. This material can be tectonically eroded and brought into the mantle to be then recycled back into the TVZ, affecting the composition of the TVZ magmas, particularly that of mafic and some intermediate magmas. Recycled material may also contribute to the isotope composition of the felsic magmas.

a. Strontium and lead isotope systematics are consistent with fluid interaction between the tectonically eroded material and the mantle.

b. Neodymium isotope systematics are consistent with melt interaction between the eroded material and the mantle.

c. Whether these interactions occur at the slab-mantle interface or within a diapir remains uncertain.

8.1 Ongoing work

Although the $^{176}Hf/^{177}Hf$ isotopic systematics of the samples from the TVZ were constrained (**Figure 8.1**), that of the material from the IODP drill cores U1518 and U1520 may have been affected by the presence of refractory minerals that were not digested by the traditional HCl-HNO_3-HF method used in this work. High-pressure parr bombs, used to digest these minerals at high pressures for long periods, were not available for this project. The material from these cores has a $^{176}Hf/^{177}Hf$ variation of between 0.2828 and 0.2829, with the same variations seen in the material located above and below the *décollement*. This is inconsistent with the Pb-Sr-Nd isotope data.

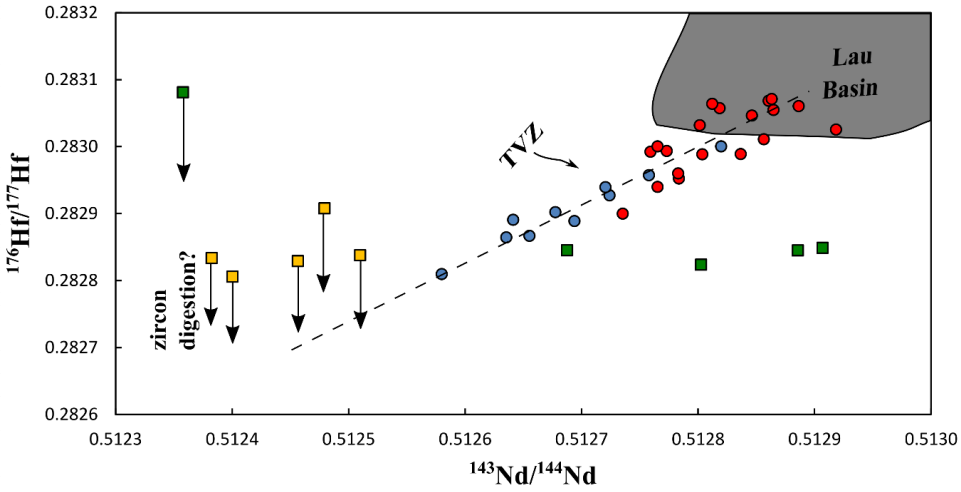

Figure 8.1: $^{143}Nd/^{144}Nd$ vs $^{176}Hf/^{177}Hf$ showing the behaviour of the TVZ and IODP material divided into below the *décollement* and material prone to tectonic erosion (accretionary prism and above the *décollement*). Reference materials and procedural replicates are present in **Chapter 3**. Lau Basin data corresponds to that of Ewart et al. (1998), Todd et al. (2011), Turner et al. (1997). The discontinuous line corresponds to a possible mixing line between the mantle and possibly the tectonically eroded crust.

The presence of residual zircon would not only cause the material to show larger isotopic variations but would also make it more radiogenic if the zircons are older (**Figure 8.1**). The determination of the $^{176}Hf/^{177}Hf$ ratio of the IODP samples may be resolved by employing the flux melted disks used for major oxide determination by XRF (Ulfbeck et al., 2003, Waight et al., 2017), which overcomes the need to digest a zircon-bearing phase under high pressure. If this approach is successful, the Hf isotopic results obtained will be included in the manuscript presented in **Chapter 6** before journal submission. If this flux-based approach is unsuccessful, the option remains to re-digest the samples employing high-pressure parr bombs to fully digest very refractory phases, including zircons for further Hf isotope analysis. However, even if zircon residue is present in the samples located below the *décollement*, their $^{176}Hf/^{177}Hf$ isotopic composition is inconsistent with the samples from the TVZ when compared with $^{143}Nd/^{144}Nd$, and thus consistent with the interpretations based on the Sr-Pb-Nd isotope variations.

8.2 Outlook

To expand our understanding of the magmatic generation of the TVZ and arc magmatism globally, future work may include:

1. Determining the $^{176}Hf/^{177}Hf$ isotopic systematics of the material located above the *décollement* and in the accretionary prism using more appropriate sample digestion methods, as described above.
2. Other isotopic systems can be useful to detect crustal recycling in the magmas of the TVZ. For example, $^{41}K/^{39}K$ ($\delta^{41}K$), $^{7}Li/^{6}Li$ ($\delta^{7}Li$), $^{98}Mo/^{95}Mo$ ($\delta^{98}Mo$), $^{11}B/^{10}B$ ($\delta^{11}B$), and ^{10}Be isotopic systematics can show evidence of crustal material involved in the source, and their variable behaviour can elucidate the different fluid and melt processes that may be occurring (see Freymuth et al., 2015, Hu et al., 2021, Li et al.,

2021, Moriguti & Nakamura, 1998, Palmer, 1991, Plank, 2014, Sun et al., 2020). Particularly, combining $\delta^{41}K$ with other isotope systematics (such as Sr-Pb-Nd-Hf) and elemental concentrations can help differentiate between source and transcrustal assimilation (Hu et al., 2021). Further, high $\delta^{41}K$ values are attributed to the input of slab-derived fluids, while low values are attributed to sediment melts (Hu et al., 2021, Sun et al., 2020). Although there is limited data, a strong correlation between $\delta^{7}Li$ and Y/Li has been reported to indicate mixing between a mantle component and a slab component in different subduction zones around the globe (Plank, 2014). Differentiating between the fluid component and the melt component can also be done with $\delta^{98}Mo$, where isotopically heavy Mo compositions are expected by fluid fluxes from the slab to the mantle, and isotopically light Mo signatures indicate the presence of melts from a slab that underwent dehydration (Freymuth et al., 2015, Li et al., 2021). $\delta^{98}Mo$ together with Ce/Mo ratios can differentiate between melts from Ca-rich and Ca-poor sediments, as the first retains Ce when melting, but not Mo (Casalini et al., 2019).

3. A systematic study of O and Hf isotope compositions together with U-Pb dating of the zircons contained in the subducting material, eroding material, and the TVZ volcanic products could yield interesting results linking these materials (see Cornet et al., 2022, Gómez-Tuena et al., 2018). Crustal recycled could be better constrained if zircon is collected in samples without crustal interactions but still show cores with isotopic characteristics of those of the accretionary prism, with magmatic regrowth, for example, shown in the TMVB (Gómez-Tuena et al., 2018).
4. Mineral chemistry of magmatic olivine and spinel crystals in mafic and intermediate samples may show interactions between the mantle and crustal material when combining the Fo%, Ni, CaO, Al_2O_3 content, Mg#, Cr#, $^{3}He/^{4}He$ and $\delta^{18}O$ of the

crystals. These, combined with whole rock data, including the isotopic systems employed in this study, may help elucidate the interactions between the mantle and the crustal material (see Nielsen et al., 2002, Straub et al., 2011, Xu, 2002). The characteristics of these minerals, when compared with the whole rock can show a source contaminated with 'crustal material'. For example, Cr-spinel inclusions, olivines and even some pyroxenes from a norite dyke in Isua, West Greenland, show primitive compositions in equilibrium with the mantle, but the isotopic characteristics of the rock have strong crustal-like signatures that would require extensive assimilation and are inconsistent with the minerals (Nielsen et al., 2002). Similar observations were acquired for the Trans-Mexican Volcanic Belt when comparing the $^{3}He/^{4}He$ and $\delta^{18}O$ isotope compositions, and elemental concentrations of olivines with the whole rock systematics (Straub et al., 2015, Straub et al., 2011).

5. Crustal recycling of tectonically eroded material has been reported along the Hikurangi margin in the southern Kermadec arc (Timm et al., 2014), and is now reported in this study for the TVZ. However, recycling of either subducted or tectonically eroded material should also be examined along the length of Tonga-Kermadec margin. Tectonic erosion has been reported to be caused by the collision of the Louisville Ridge (Clift & Vannucchi, 2004, Contreras-Reyes et al., 2011). Material from this seamount chain is thought to be recycled based on $^{206}Pb/^{204}Pb$, $^{208}Pb/^{204}Pb$ and $^{87}Sr/^{86}Sr$ (Timm et al., 2013), but it should be assessed if tectonically eroded crust, and consequently crustal recycling may also play a role.

References

Adams, C. J., Barley, M. E., Maas, R. & Doyle, M. G. (2002). Provenance of Permian-Triassic volcaniclastic sedimentary terranes in New Zealand: Evidence from their radiogenic isotope characteristics and detrital mineral age patterns. *New Zealand Journal of Geology and Geophysics* **45**, 221-242.

Adams, C. J., Campbell, H. J. & Griffin, W. L. (2007). Provenance comparisons of Permian to Jurassic tectonostratigraphic terranes in New Zealand: perspectives from detrital zircon age patterns. *Geological Magazine* **144**, 701-729.

Adams, C. J., Mortimer, N., Campbell, H. J. & Griffin, W. L. (2009). Age and isotopic characterisation of metasedimentary rocks from the Torlesse Supergroup and Waipapa Group in the central North Island, New Zealand. *New Zealand Journal of Geology and Geophysics* **52**, 149-170.

Aizawa, Y., Tatsumi, Y. & Yamada, H. (1999). Element transport by dehydration of subducted sediments: Implication for arc and ocean island magmatism. *Island Arc* **8**, 38-46.

Allègre, C. J. (1987). Isotope geodynamics. *Earth and Planetary Science Letters* **86**, 175-203.

Amelin, Y. V., Neymark, L. A., Ritsk, E. Y. & Nemchin, A. A. (1996). Enriched Nd-Sr-Pb isotopic signatures in the Dovyren layered intrusion (eastern Siberia, Russia): evidence for source contamination by ancient upper-crustal material. *Chemical Geology* **129**, 39-69.

Andrews, P. B., Speden, I. G. & Bradshaw, J. D. (1976). Lithological and paleontological content of the Carboniferous-Jurassic Canterbury Suite, South Island, New Zealand. *New Zealand Journal of Geology and Geophysics* **19**, 791-819.

Armstrong, R. (1981). Radiogenic isotopes: the case for crustal recycling on a near-steady-state no-continental-growth Earth. *Philosophical Transactions of the Royal Society of London. Series A, Mathematical and Physical Sciences* **301**, 443 - 472.

Arpa, M. C., Zellmer, G. F., Christenson, B., Lube, G. & Shellnutt, G. (2017). Variable magma reservoir depths for Tongariro Volcanic Complex eruptive deposits from 10,000 years to present. *Bulletin of Volcanology* **79**, 56.

Bacon, C. R. (1990). Calc-alkaline, Shoshonitic, and Primitive Tholeiitic Lavas from Monogenetic Volcanoes near Crater Lake, Oregon. *Journal of Petrology* **31**, 135-166.

Bacon, C. R. & Druitt, T. H. (1988). Compositional evolution of the zoned calcalkaline magma chamber of Mount Mazama, Crater Lake, Oregon. *Contributions to Mineralogy and Petrology* **98**, 224-256.

Baker, J., Waight, T. & Ulfbeck, D. (2002). Rapid and highly reproducible analysis of rare earth elements by multiple collector inductively coupled plasma mass spectrometry. *Geochimica et Cosmochimica Acta* **66**, 3635-3646.

Barker, D. H. N., Sutherland, R., Henrys, S. & Bannister, S. (2009). Geometry of the Hikurangi subduction thrust and upper plate, North Island, New Zealand. *Geochemistry, Geophysics, Geosystems* **10**.

Barnes, P., Wallace, L., Saffer, D., Pecher, I., Petronotis, K., LeVay, L., Bell, R., Crundwell, M., Engelmann de Oliveira, C. & Fagereng, A., et al. (2019). Site U1520. In: Wallace LM, Saffer DM, Barnes PM, Pecher IA, Petronotis KE, LeVay LJ, and the Expedition 372/375 Scientists; Hikurangi Subduction Margin Coring, Logging, and Observatories. Proceedings of the International Ocean Discovery Program, 372B/375: College Station (TX) (International Ocean Discovery Program).

Barnes, P. M., Wallace, L. M., Saffer, D. M., Bell, R. E., Underwood, M. B., Fagereng, A., Meneghini, F., Savage, H. M., Rabinowitz, H. S., Morgan, J. K., Kitajima, H., Kutterolf, S., Hashimoto, Y., Engelmann de Oliveira, C. H., Noda, A., Crundwell, M. P., Shepherd, C. L., Woodhouse, A. D., Harris, R. N., Wang, M., Henrys, S., Barker, D. H. N., Petronotis, K. E., Bourlange, S. M., Clennell, M. B., Cook, A. E., Dugan, B. E., Elger, J., Fulton, P. M., Gamboa, D., Greve, A., Han, S., Hüpers, A., Ikari, M. J., Ito, Y., Kim, G. Y., Koge, H., Lee, H., Li, X., Luo, M., Malie, P. R., Moore, G. F., Mountjoy, J. J., McNamara, D. D., Paganoni, M., Screaton, E. J., Shankar, U., Shreedharan, S., Solomon, E. A., Wang, X., Wu, H.-Y., Pecher, I. A. & LeVay, L. J. (2020). Slow slip source characterized by lithological and geometric heterogeneity. *Science Advances* **6**, eaay3314.

Barth, M. G., McDonough, W. F. & Rudnick, R. L. (2000). Tracking the budget of Nb and Ta in the continental crust. *Chemical Geology* **165**, 197-213.

Bea, F., Pereira, M. D. & Stroh, A. (1994). Mineral/leucosome trace-element partitioning in a peraluminous migmatite (a laser ablation-ICP-MS study). *Chemical Geology* **117**, 291-312.

Behn, M. D., Kelemen, P. B., Hirth, G., Hacker, B. R. & Massonne, H.-J. (2011). Diapirs as the source of the sediment signature in arc lavas. *Nature Geoscience* **4**, 641-646.

Beier, C., Haase, K. M., Brandl, P. A. & Krumm, S. H. (2017). Primitive andesites from the Taupo Volcanic Zone formed by magma mixing. *Contributions to Mineralogy and Petrology* **172**, 33.

Belshaw, N. S., Freedman, P. A., O'Nions, R. K., Frank, M. & Guo, Y. (1998). A new variable dispersion double-focusing plasma mass spectrometer with performance illustrated for Pb isotopes. *International Journal of Mass Spectrometry* **181**, 51-58.

Ben Othman, D., White, W. M. & Patchett, J. (1989). The geochemistry of marine sediments, island arc magma genesis, and crust-mantle recycling. *Earth and Planetary Science Letters* **94**, 1-21.

Beresford, S. W. & Cole, J. W. (2000). Kaingaroa Ignimbrite, Taupo Volcanic Zone, New Zealand: Evidence for asymmetric caldera subsidence of the Reporoa Caldera. *New Zealand Journal of Geology and Geophysics* **43**, 471-481.

Bevis, M., Taylor, F. W., Schutz, B. E., Recy, J., Isacks, B. L., Helu, S., Singh, R., Kendrick, E., Stowell, J., Taylor, B. & Calmantli, S. (1995). Geodetic observations of very rapid convergence and back-arc extension at the Tonga arc. *Nature* **374**, 249-251.

Billen, M. I. & Stock, J. (2000). Morphology and origin of the Osbourn Trough. *Journal of Geophysical Research: Solid Earth* **105**, 13481-13489.

Black, P. (1994). The "Waipapa Terrane", North Island, New Zealand : Subdivision and correlation. *Geoscience Reports of Shizuoka University* **20**.

Blichert-Toft, J. & Albarède, F. (1997). The Lu-Hf isotope geochemistry of chondrites and the evolution of the mantle-crust system. *Earth and Planetary Science Letters* **148**, 243-258.

Bohrson, W. A., Spera, F. J., Ghiorso, M. S., Brown, G. A., Creamer, J. B. & Mayfield, A. (2014). Thermodynamic Model for Energy-Constrained Open-System Evolution of Crustal Magma Bodies Undergoing Simultaneous Recharge, Assimilation and Crystallization: the Magma Chamber Simulator. *Journal of Petrology* **55**, 1685-1717.

Bohrson, W. A., Spera, F. J., Heinonen, J. S., Brown, G. A., Scruggs, M. A., Adams, J. V., Takach, M. K., Zeff, G. & Suikkanen, E. (2020). Diagnosing open-system magmatic processes using the Magma Chamber Simulator (MCS): part I—major elements and phase equilibria. *Contributions to Mineralogy and Petrology* **175**, 104.

Borghini, G. & Fumagalli, P. (2020). Melting relations of anhydrous olivine-free pyroxenite Px1 at 2 GPa. *Eur. J. Mineral.* **32**, 251-264.

Boudreau, A. E. (1999). PELE—a version of the MELTS software program for the PC platform. *Computers & Geosciences* **25**, 201-203.

Bowman, E. E., Ducea, M. N. & Triantafyllou, A. (2021). Arclogites in the Subarc Lower Crust: Effects of Crystallization, Partial Melting, and Retained Melt on the Foundering Ability of Residual Roots. *Journal of Petrology* **62**, egab094.

Briggs, R. M., Gifford, M. G., Moyle, A. R., Taylor, S. R., Norman, M. D., Houghton, B. F. & Wilson, C. J. N. (1993). Geochemical zoning and eruptive mixing in ignimbrites from Mangakino volcano, Taupo Volcanic Zone, New Zealand. *Journal of Volcanology and Geothermal Research* **56**, 175-203.

Briggs, R. M., Houghton, B. F., McWilliams, M. & Wilson, C. J. N. (2005). 40Ar/39Ar ages of silicic volcanic rocks in the Tauranga-Kaimai area, New Zealand: Dating the transition between volcanism in the Coromandel Arc and the Taupo Volcanic Zone. *New Zealand Journal of Geology and Geophysics* **48**, 459-469.

Brooker, M. R., Houghton, B. F., Wilson, C. J. N. & Gamble, J. A. (1993). Pyroclastic phases of a rhyolitic dome-building eruption: Puketarata tuff ring, Taupo Volcanic Zone, New Zealand. *Bulletin of Volcanology* **55**, 395-406.

Brown, S. J. A., Wilson, C. J. N., Cole, J. W. & Wooden, J. (1998). The Whakamaru group ignimbrites, Taupo Volcanic Zone, New Zealand: evidence for reverse tapping of a zoned silicic magmatic system. *Journal of Volcanology and Geothermal Research* **84**, 1-37.

Browne, P. R. L., Graham, I. J., Parker, R. J. & Wood, C. P. (1992). Subsurface andesite lavas and plutonic rocks in the Rotokawa and Ngatamariki geothermal systems, Taupo Volcanic Zone, New Zealand. *Journal of Volcanology and Geothermal Research* **51**, 199-215.

Cameron, E., Gamble, J., Price, R., Smith, I., McIntosh, W. & Gardner, M. (2010). The petrology, geochronology and geochemistry of Hauhungatahi volcano, S.W. Taupo Volcanic Zone. *Journal of Volcanology and Geothermal Research* **190**, 179-191.

Cande, S. C. & Leslie, R. B. (1986). Late Cenozoic tectonics of the southern Chile Trench. *Journal of Geophysical Research* **91**, 471-496.

Carroll, L. D., Gamble, J. A., Houghton, B. F., Thordarson, T. & Higham, T. F. G. (1997). A radiocarbon age determination for Mount Edgecumbe (Putauaki) volcano, Bay of Plenty, New Zealand. *New Zealand Journal of Geology and Geophysics* **40**, 559-562.

Casalini, M., Avanzinelli, R., Tommasini, S., Elliott, T. & Conticelli, S. (2019). Ce/Mo and Molybdenum Isotope Systematics in Subduction-Related Orogenic Potassic Magmas of Central-Southern Italy. *Geochemistry, Geophysics, Geosystems* **20**, 2753-2768.

Castro, A., Gerya, T., García-Casco, A., Fernández, C., Díaz-Alvarado, J., Moreno-Ventas, I. & Löw, I. (2010). Melting Relations of MORB–Sediment Mélanges in Underplated Mantle Wedge Plumes; Implications for the Origin of Cordilleran-type Batholiths. *Journal of Petrology* **51**, 1267-1295.

Castro, A. & Gerya, T. V. (2008). Magmatic implications of mantle wedge plumes: Experimental study. *Lithos* **103**, 138-148.

Castro, A., Vogt, K. & Gerya, T. (2013). Generation of new continental crust by sublithospheric silicic-magma relamination in arcs: A test of Taylor's andesite model. *Gondwana Research* **23**, 1554-1566.

Chambefort, I., Lewis, B., Wilson, C. J. N., Rae, A. J., Coutts, C., Bignall, G. & Ireland, T. R. (2014). Stratigraphy and structure of the Ngatamariki geothermal system from new zircon U–Pb geochronology: Implications for Taupo Volcanic Zone evolution. *Journal of Volcanology and Geothermal Research* **274**, 51-70.

Chauvel, C., Lewin, E., Carpentier, M., Arndt, N.T., Marini, J.-C., 2008. Role of recycled oceanic basalt and sediment in generating the Hf–Nd mantle array. Nat. Geosci. 1(1), 64-67. doi.org/10.1038/ngeo.2007.51.

Clark, K., Howarth, J., Litchfield, N., Cochran, U., Turnbull, J., Dowling, L., Howell, A., Berryman, K. & Wolfe, F. (2019). Geological evidence for past large earthquakes and tsunamis along the Hikurangi subduction margin, New Zealand. *Marine Geology* **412**, 139-172.

Clift, P. & Vannucchi, P. (2004). Controls on tectonic accretion versus erosion in subduction zones: Implications for the origin and recycling of the continental crust. *Reviews of Geophysics* **42**.

Codillo, E. A., Le Roux, V. & Marschall, H. R. (2018). Arc-like magmas generated by mélange-peridotite interaction in the mantle wedge. *Nature Communications* **9**, 2864.

Cole, J. W. (1970). Structure and eruptive history of the Tarawera Volcanic Complex. *New Zealand Journal of Geology and Geophysics* **13**, 879-902.

Cole, J. W. (1973). High-alumina basalts of Taupo Volcanic Zone, New Zealand. *Lithos* **6**, 53-64.

Cole, J. W. (1978). Andesites of the Tongariro volcanic centre, North Island, New Zealand. *Journal of Volcanology and Geothermal Research* **3**, 121-153.

Cole, J. W. (1979). Structure, petrology, and genesis of Cenozoic volcanism, Taupo Volcanic Zone, New Zealand—a review. *New Zealand Journal of Geology and Geophysics* **22**, 631-657.

Cole, J. W., Gamble, J. A., Burt, R. M., Carroll, L. D. & Shelley, D. (2001). Mixing and mingling in the evolution of andesite–dacite magmas; evidence from co-magmatic plutonic enclaves, Taupo Volcanic Zone, New Zealand. *Lithos* **59**, 25-46.

Cole, J. W., Spinks, K. D., Deering, C. D., Nairn, I. A. & Leonard, G. S. (2010). Volcanic and structural evolution of the Okataina Volcanic Centre; dominantly silicic volcanism associated with the Taupo Rift, New Zealand. *Journal of Volcanology and Geothermal Research* **190**, 123-135.

Cole, J. W. & Teoh, L. H. (1975). Petrography, mineralogy, and chemistry of Pureora andesite volcano, North Island, New Zealand. *New Zealand Journal of Geology and Geophysics* **18**, 259-272.

Cole, J. W., Thordarson, T. & Burt, R. M. (2000). Magma Origin and Evolution of White Island (Whakaari) Volcano, Bay of Plenty, New Zealand. *Journal of Petrology* **41**, 867-895.

Collot, J.-Y. & Davy, B. (1998). Forearc structures and tectonic regimes at the oblique subduction zone between the Hikurangi Plateau and the southern Kermadec margin. *Journal of Geophysical Research: Solid Earth* **103**, 623-650.

Collot, J.-Y., Delteil, J., Lewis, K. B., Davy, B., Lamarche, G., Audru, J.-C., Barnes, P., Chanier, F., Chaumillon, E., Lallemand, S., de Lepinay, B. M., Orpin, A., Pelletier, B., Sosson, M., Toussaint, B. & Uruski, C. (1996). From oblique subduction to intra-continental transpression: Structures of the southern Kermadec-Hikurangi margin from multibeam bathymetry, side-scan sonar and seismic reflection. *Marine Geophysical Researches* **18**, 357-381.

Contreras-Reyes, E., Grevemeyer, I., Watts, A. B., Flueh, E. R., Peirce, C., Moeller, S. & Papenberg, C. (2011). Deep seismic structure of the Tonga subduction zone: Implications for mantle hydration, tectonic erosion, and arc magmatism. *Journal of Geophysical Research: Solid Earth* **116**.

Conway, C. E., Chamberlain, K. J., Harigane, Y., Morgan, D. J. & Wilson, C. J. N. (2020). Rapid assembly of high-Mg andesites and dacites by magma mixing at a continental arc stratovolcano. *Geology* **48**, 1033-1037.

Cooper, G. F., Wilson, C. J. N., Millet, M.-A. & Baker, J. A. (2016). Generation and Rejuvenation of a Supervolcanic Magmatic System: a Case Study from Mangakino Volcanic Centre, New Zealand. *Journal of Petrology* **57**, 1135-1170.

Coote, A., Shane, P., Stirling, C. & Reid, M. (2018). The origin of plagioclase phenocrysts in basalts from continental monogenetic volcanoes of the Kaikohe-Bay of Islands field, New Zealand: implications for magmatic assembly and ascent. *Contributions to Mineralogy and Petrology* **173**, 14.

Corgne, A., Schilling, M. E., Grégoire, M. & Langlade, J. (2018). Experimental constraints on metasomatism of mantle wedge peridotites by hybridized adakitic melts. *Lithos* **308-309**, 213-226.

Cornet, J., Laurent, O., Wotzlaw, J. F., Antonelli, M. A., Otamendi, J., Bergantz, G. W. & Bachmann, O. (2022). Reworking subducted sediments in arc magmas and the isotopic diversity of the continental crust: The case of the Ordovician Famatinian crustal section, Argentina. *Earth and Planetary Science Letters* **595**, 117706.

Crawford, A. J., Falloon, T. J. & Eggins, S. (1987). The origin of island arc high-alumina basalts. *Contributions to Mineralogy and Petrology* **97**, 417-430.

Currie, C. A., Beaumont, C. & Huismans, R. S. (2007). The fate of subducted sediments: A case for backarc intrusion and underplating. *Geology* **35**, 1111-1114.

Dallai, L., Bianchini, G., Avanzinelli, R., Deloule, E., Natali, C., Gaeta, M., Cavallo, A. & Conticelli, S. (2022). Quartz-bearing rhyolitic melts in the Earth's mantle. *Nature Communications* **13**, 7765.

Darby, D. J., Hodgkinson, K. M. & Blick, G. H. (2000). Geodetic measurement of deformation in the Taupo Volcanic Zone, New Zealand: The north Taupo network revisited. *New Zealand Journal of Geology and Geophysics* **43**, 157-170.

Davy, B. (2014). Rotation and offset of the Gondwana convergent margin in the New Zealand region following Cretaceous jamming of Hikurangi Plateau large igneous province subduction. *Tectonics* **33**, 1577-1595.

Davy, B., Hoernle, K. & Werner, R. (2008). Hikurangi Plateau: Crustal structure, rifted formation, and Gondwana subduction history. *Geochemistry, Geophysics, Geosystems* **9**.

Davy, B. & Wood, R. (1994). Gravity and magnetic modelling of the Hikurangi Plateau. *Marine Geology* **118**, 139-151.

De Astis, G., Peccerillo, A., Kempton, P., Volpe, L. & Wu, T. (2000). Transition from calc-alkaline to potassium-rich magmatism in subduction environments: geochemical and Sr, Nd, Pb isotopic constraints from the island of Vulcano (Aeolian arc). *Contributions to Mineralogy and Petrology* **139**, 684-703.

Deering, C. D., Bachmann, O., Dufek, J. & Gravley, D. M. (2011). Rift-Related Transition from Andesite to Rhyolite Volcanism in the Taupo Volcanic Zone (New Zealand) Controlled by Crystal–melt Dynamics in Mush Zones with Variable Mineral Assemblages. *Journal of Petrology* **52**, 2243-2263.

Defant, M. J. & Drummond, M. S. (1990). Derivation of some modern arc magmas by melting of young subducted lithosphere. *Nature* **347**, 662-665.

DePaolo, D. J. (1981a). Nd Isotopic Studies: Some new perspectives on Earth structure and evolution. *Eos, Transactions American Geophysical Union* **62**, 137-137.

DePaolo, D. J. (1981b). Trace element and isotopic effects of combined wallrock assimilation and fractional crystallization. *Earth and Planetary Science Letters* **53**, 189-202.

Druce, M., Stirling, C. H., Bostock, H. C. & Rolison, J. M. (2022). Examining the effects of chemical cleaning, leaching, and partial dissolution on zinc and cadmium isotope fractionation in marine carbonates. *Chemical Geology* **592**, 120738.

Drummond, M. S., Defant, M. J. & Kepezhinskas, P. K. (1996). Petrogenesis of slab-derived trondhjemite–tonalite–dacite/adakite magmas. *Earth and Environmental Science Transactions of the Royal Society of Edinburgh* **87**, 205-215.

Eberhart-Phillips, D., Bannister, S. & Reyners, M. (2019). Attenuation in the mantle wedge beneath super-volcanoes of the Taupo Volcanic Zone, New Zealand. *Geophysical Journal International* **220**, 703-723.

Ewart, A., Brothers, R. N. & Mateen, A. (1977). An outline of the geology and geochemistry, and the possible petrogenetic evolution of the volcanic rocks of the Tonga-Kermadec-New Zealand island arc. *Journal of Volcanology and Geothermal Research* **2**, 205-250.

Ewart, A., Collerson, K. D., Regelous, M., Wendt, J. I. & Niu, Y. (1998). Geochemical Evolution within the Tonga–Kermadec–Lau Arc–Back-arc Systems: the Role of Varying Mantle Wedge Composition in Space and Time. *Journal of Petrology* **39**, 331-368.

Ewart, A. & Griffin, W. L. (1994). Application of proton-microprobe data to trace-element partitioning in volcanic rocks. *Chemical Geology* **117**, 251-284.

Ewart, A. & Hawkesworth, C. J. (1987). The Pleistocene-Recent Tonga-Kermadec Arc Lavas: Interpretation of New Isotopic and Rare Earth Data in Terms of a Depleted Mantle Source Model. *Journal of Petrology* **28**, 495-530.

Farner, M. J. & Lee, C.-T. A. (2017). Effects of crustal thickness on magmatic differentiation in subduction zone volcanism: A global study. *Earth and Planetary Science Letters* **470**, 96-107.

Faure, G. (1986). *Principles of isotope geology. Second edition*. United States: John Wiley and Sons Inc.,New York, NY.

Förster, M. W. & Selway, K. (2021). Melting of subducted sediments reconciles geophysical images of subduction zones. *Nature Communications* **12**, 1320.

Freymuth, H., Vils, F., Willbold, M., Taylor, R. N. & Elliott, T. (2015). Molybdenum mobility and isotopic fractionation during subduction at the Mariana arc. *Earth and Planetary Science Letters* **432**, 176-186.

Froude, D. O. & Cole, J. W. (1985). Petrography, mineralogy and chemistry of Titiraupenga volcano, North Island, New Zealand. *New Zealand Journal of Geology and Geophysics* **28**, 487-496.

Gamal El Dien, H., Li, Z. X., Kil, Y. & Abu-Alam, T. (2019). Origin of arc magmatic signature: A temperature-dependent process for trace element (re)-mobilization in subduction zones. *Scientific Reports* **9**.

Gamble, J., Woodhead, J., Wright, I. & Smith, I. (1996). Basalt and Sediment Geochemistry and Magma Petrogenesis in a Transect from Oceanic Island Arc to Rifted Continental Margin Arc: the Kermadec—Hikurangi Margin, SW Pacific. *Journal of Petrology* **37**, 1523-1546.

Gamble, J. A., Smith, I. E. M., Graham, I. J., Peter Kokelaar, B., Cole, J. W., Houghton, B. F. & Wilson, C. J. N. (1990). The petrology, phase relations and tectonic setting of basalts from the taupo volcanic zone, New Zealand and the Kermadec Island arc - havre trough, SW Pacific. *Journal of Volcanology and Geothermal Research* **43**, 253-270.

Gamble, J. A., Smith, I. E. M., McCulloch, M. T., Graham, I. J. & Kokelaar, B. P. (1993). The geochemistry and petrogenesis of basalts from the Taupo Volcanic Zone and Kermadec Island Arc, S.W. Pacific. *Journal of Volcanology and Geothermal Research* **54**, 265-290.

Gase, A. C., Van Avendonk, H. J. A., Bangs, N. L., Luckie, T. W., Barker, D. H. N., Henrys, S. A., Bassett, D., Okaya, D. A., Jacobs, K. M., Kodaira, S., Fujie, G., Arnulf, A. F. & Yamamoto, Y. (2019). Seismic Evidence of Magmatic Rifting in the Offshore Taupo Volcanic Zone, New Zealand. *Geophysical Research Letters* **46**, 12949-12957.

Gervasoni, F., Klemme, S., Rohrbach, A., Grützner, T. & Berndt, J. (2017). Experimental constraints on mantle metasomatism caused by silicate and carbonate melts. *Lithos* **282-283**, 173-186.

Ghiorso, M. S. & Gualda, G. A. R. (2015). An H2O–CO2 mixed fluid saturation model compatible with rhyolite-MELTS. *Contributions to Mineralogy and Petrology* **169**, 53.

Gómez-Tuena, A., Cavazos-Tovar, J. G., Parolari, M., Straub, S. M. & Espinasa-Pereña, R. (2018). Geochronological and geochemical evidence of continental crust 'relamination' in the origin of intermediate arc magmas. *Lithos* **322**, 52-66.

Goss, A. R. & Kay, S. M. (2006). Steep REE patterns and enriched Pb isotopes in southern Central American arc magmas: Evidence for forearc subduction erosion? *Geochemistry, Geophysics, Geosystems* **7**.

Graham, I. J. & Cole, J. W. (1991). Petrogenesis of andesites and dacites of White Island volcano, Bay of Plenty, New Zealand, in the light of new geochemical and isotopic data. *New Zealand Journal of Geology and Geophysics* **34**, 303-315.

Graham, I. J., Cole, J. W., Briggs, R. M., Gamble, J. A. & Smith, I. E. M. (1995). Petrology and petrogenesis of volcanic rocks from the Taupo Volcanic Zone: a review. *Journal of Volcanology and Geothermal Research* **68**, 59-87.

Graham, I. J., Gulson, B. L., Hedenquist, J. W. & Mizon, K. (1992). Petrogenesis of Late Cenozoic volcanic rocks from the Taupo Volcanic Zone, New Zealand, in the light of new lead isotope data. *Geochimica et Cosmochimica Acta* **56**, 2797-2819.

Graham, I. J. & Hackett, W. R. (1987). Petrology of Calc-alkaline Lavas from Ruapehu Volcano and Related Vents, Taupo Volcanic Zone, New Zealand. *Journal of Petrology* **28**, 531-567.

Graham, I. J. & Worthington, T. (1988). Petrogenesis of Tauhara Dacite (Taupo Volcanic Zone, New Zealand) - Evidence for magma mixing between high-alumina andesite and rhyolite. *Journal of Volcanology and Geothermal Research* **35**, 279-294.

Gravley, D. M., Deering, C. D., Leonard, G. S. & Rowland, J. V. (2016). Ignimbrite flare-ups and their drivers: A New Zealand perspective. *Earth-Science Reviews* **162**, 65-82.

Green, T. H., Blundy, J. D., Adam, J. & Yaxley, G. M. (2000). SIMS determination of trace element partition coefficients between garnet, clinopyroxene and hydrous basaltic liquids at 2–7.5 GPa and 1080–1200°C. *Lithos* **53**, 165-187.

Gribble, C. D. (1990). ASSIMILATIONAssimilation. *Petrology*. Boston, MA: Springer US, 39-40.

Gualda, G. A. R., Ghiorso, M. S., Lemons, R. V. & Carley, T. L. (2012). Rhyolite-MELTS: a Modified Calibration of MELTS Optimized for Silica-rich, Fluid-bearing Magmatic Systems. *Journal of Petrology* **53**, 875-890.

Haase, K. M., Worthington, T. J., Stoffers, P., Garbe-Schönberg, D. & Wright, I. (2002). Mantle dynamics, element recycling, and magma genesis beneath the Kermadec Arc-Havre Trough. *Geochemistry, Geophysics, Geosystems* **3**, 1-22.

Habfast, K. (1998). Fractionation correction and multiple collectors in thermal ionization isotope ratio mass spectrometry. *International Journal of Mass Spectrometry* **176**, 133-148.

Hanyu, T., Nakai, S. i. & Tatsuta, R. (2005). Hafnium isotope ratios of nine GSJ reference samples. *GEOCHEMICAL JOURNAL* **39**, 83-90.

Hart, S. R. (1988). Heterogeneous mantle domains: signatures, genesis and mixing chronologies. *Earth and Planetary Science Letters* **90**, 273-296.

Hart, S. R. & Zindler, A. (1989). Isotope fractionation laws: a test using calcium. *International Journal of Mass Spectrometry and Ion Processes* **89**, 287-301.

Hauff, F., Hoernle, K. & Schmidt, A. (2003). Sr-Nd-Pb composition of Mesozoic Pacific oceanic crust (Site 1149 and 801, ODP Leg 185): Implications for alteration of ocean crust and the input into the Izu-Bonin-Mariana subduction system. *Geochemistry, Geophysics, Geosystems* **4**.

Hawkesworth, C. J. & Kemp, A. I. S. (2006). Evolution of the continental crust. *Nature* **443**, 811-817.

Heinonen, J. S., Bohrson, W. A., Spera, F. J., Brown, G. A., Scruggs, M. A. & Adams, J. V. (2020). Diagnosing open-system magmatic processes using the Magma Chamber Simulator (MCS): part II—trace elements and isotopes. *Contributions to Mineralogy and Petrology* **175**, 105.

Heinonen, J. S., Luttinen, A. V., Spera, F. J. & Bohrson, W. A. (2019). Deep open storage and shallow closed transport system for a continental flood basalt sequence revealed with Magma Chamber Simulator. *Contributions to Mineralogy and Petrology* **174**, 87.

Hiess, J., Cole, J. W. & Spinks, K. D. (2007). Influence of the crust and crustal structure on the location and composition of high-alumina basalts of the Taupo Volcanic Zone, New Zealand. *New Zealand Journal of Geology and Geophysics* **50**, 327-342.

Hildyard, S. C., Cole, J. W. & Weaver, S. D. (2000). Tikorangi Ignimbrite: A 0.89 Ma mixed andesite-rhyolite ignimbrite, Matahana Basin, Taupo Volcanic Zone, New Zealand. *New Zealand Journal of Geology and Geophysics* **43**, 95-107.

Hoernle, K., Hauff, F., van den Bogaard, P., Werner, R., Mortimer, N., Geldmacher, J., Garbe-Schönberg, D. & Davy, B. (2010). Age and geochemistry of volcanic rocks from the Hikurangi and Manihiki oceanic Plateaus. *Geochimica et Cosmochimica Acta* **74**, 7196-7219.

Hofmann, A. W. & White, W. M. (1982). Mantle plumes from ancient oceanic crust. *Earth and Planetary Science Letters* **57**, 421-436.

Holm, P. M., Søager, N., Dyhr, C. T. & Nielsen, M. R. (2014). Enrichments of the mantle sources beneath the Southern Volcanic Zone (Andes) by fluids and melts derived from abraded upper continental crust. *Contributions to Mineralogy and Petrology* **167**, 1004.

Houghton, B., Wilson, C., lloyd, e., Gamble, J. & Kokelaar, B. (1987). A catalogue of basaltic deposits within the Central Taupo Volcanic Zone. *New Zealand Geological Survey* **Record 18**, 95–101.

Houghton, B. F., Wilson, C. J. N., McWilliams, M. O., Lanphere, M. A., Weaver, S. D., Briggs, R. M. & Pringle, M. S. (1995). Chronology and dynamics of a large silicic magmatic system: Central Taupo Volcanic Zone, New Zealand. *Geology* **23**, 13-16.

Hu, Y., Teng, F.-Z. & Chauvel, C. (2021). Potassium isotopic evidence for sedimentary input to the mantle source of Lesser Antilles lavas. *Geochimica et Cosmochimica Acta* **295**, 98-111.

Irvine, T. N. & Baragar, W. R. A. (1971). A Guide to the Chemical Classification of the Common Volcanic Rocks. *Canadian Journal of Earth Sciences* **8**, 523-548.

Jicha, B. R., Singer, B. S., Brophy, J. G., Fournelle, J. H., Johnson, C. M., Beard, B. L., Lapen, T. J. & Mahlen, N. J. (2004). Variable Impact of the Subducted Slab on Aleutian Island Arc Magma Sources: Evidence from Sr, Nd, Pb, and Hf Isotopes and Trace Element Abundances. *Journal of Petrology* **45**, 1845-1875.

Johnson, M. C. & Plank, T. (2000). Dehydration and melting experiments constrain the fate of subducted sediments. *Geochemistry, Geophysics, Geosystems* **1**.

Kawabata, H., Hanyu, T., Chang, Q., Kimura, J.-I., Nichols, A. R. L. & Tatsumi, Y. (2011). The Petrology and Geochemistry of St. Helena Alkali Basalts: Evaluation of the Oceanic Crust-recycling Model for HIMU OIB. *Journal of Petrology* **52**, 791-838.

Kay, S. M., Godoy, E. & Kurtz, A. (2005). Episodic arc migration, crustal thickening, subduction erosion, and magmatism in the south-central Andes. *GSA Bulletin* **117**, 67-88.

Kelemen, P. B. (1995). Genesis of high Mg# andesites and the continental crust. *Contributions to Mineralogy and Petrology* **120**, 1-19.

Kelemen, P. B. & Behn, M. D. (2016). Formation of lower continental crust by relamination of buoyant arc lavas and plutons. *Nature Geoscience* **9**, 197-205.

Kelley, K. A., Plank, T., Ludden, J. & Staudigel, H. (2003). Composition of altered oceanic crust at ODP Sites 801 and 1149. *Geochemistry, Geophysics, Geosystems* **4**.

Keppler, H. (1996). Constraints from partitioning experiments on the composition of subduction-zone fluids. *Nature* **380**, 237-240.

Kessel, R., Schmidt, M. W., Ulmer, P. & Pettke, T. (2005a). Trace element signature of subduction-zone fluids, melts and supercritical liquids at 120–180 km depth. *Nature* **437**, 724-727.

Kessel, R., Ulmer, P., Pettke, T., Schmidt, M. W. & Thompson, A. B. (2005b). The water-basalt system at 4 to 6 GPa: Phase relations and second critical endpoint in a K-free eclogite at 700 to 1400 degrees C. *Earth and Planetary Science Letters* **237**, 873-892.

Kilgour, G., Blundy, J., Cashman, K. & Mader, H. M. (2013). Small volume andesite magmas and melt–mush interactions at Ruapehu, New Zealand: evidence from melt inclusions. *Contributions to Mineralogy and Petrology* **166**, 371-392.

King, P. R. (2000). Tectonic reconstructions of New Zealand: 40 Ma to the Present. *New Zealand Journal of Geology and Geophysics* **43**, 611-638.

Klein, B.Z., Behn, M.D., 2021. On the Evolution and Fate of Sediment Diapirs in Subduction Zones. Geochem. Geophys. Geosyst. 22(11), e2021GC009873. doi.org/https://doi.org/10.1029/2021GC009873.

Kobayashi, K., Tanaka, R., Moriguti, T., Shimizu, K. & Nakamura, E. (2004). Lithium, boron, and lead isotope systematics of glass inclusions in olivines from Hawaiian lavas: evidence for recycled components in the Hawaiian plume. *Chemical Geology* **212**, 143-161.

Kogiso, T., Hirschmann, M. M. & Pertermann, M. (2004). High-pressure Partial Melting of Mafic Lithologies in the Mantle. *Journal of Petrology* **45**, 2407-2422.

Koide, Y. & Nakamura, E. (1990). Lead Isotope Analyses of Standard Rock Samples. *Journal of the Mass Spectrometry Society of Japan* **38**, 241-252.

Kokfelt, T. F., Hoernle, K., Hauff, F., Fiebig, J., Werner, R. & Garbe-Schonberg, D. (2006). Combined Trace Element and Pb-Nd–Sr-O Isotope Evidence for Recycled Oceanic Crust (Upper and Lower) in the Iceland Mantle Plume. *Journal of Petrology* **47**, 1705-1749.

Kósik, S., Németh, K., Danišík, M., Procter, J. N., Schmitt, A. K., Friedrichs, B. & Stewart, R. B. (2021). Shallow subaqueous to emergent intra-caldera silicic volcanism of the Motuoapa Peninsula, Taupo Volcanic Zone, New Zealand – New constraints from geologic mapping, sedimentology and zircon geochronology. *Journal of Volcanology and Geothermal Research* **411**, 107180.

Kósik, S., Németh, K., Kereszturi, G., Procter, J. N., Zellmer, G. F. & Geshi, N. (2016). Phreatomagmatic and water-influenced Strombolian eruptions of a small-volume parasitic cone complex on the southern ringplain of Mt. Ruapehu, New Zealand: Facies architecture and eruption mechanisms of the Ohakune Volcanic Complex

controlled by an unstable fissure eruption. *Journal of Volcanology and Geothermal Research* **327**, 99-115.

Kósik, S., Németh, K., Lexa, J. & Procter, J. N. (2019). Understanding the evolution of a small-volume silicic fissure eruption: Puketerata Volcanic Complex, Taupo Volcanic Zone, New Zealand. *Journal of Volcanology and Geothermal Research* **383**, 28-46.

Kósik, S., Németh, K., Procter, J. N. & Zellmer, G. F. (2017). Maar-diatreme volcanism relating to the pyroclastic sequence of a newly discovered high-alumina basalt in the Maroa Volcanic Centre, Taupo Volcanic Zone, New Zealand. *Journal of Volcanology and Geothermal Research* **341**, 363-370.

Kushiro, I. (2007). Origin of magmas in subduction zones: a review of experimental studies. *Proceedings of the Japan Academy. Series B, Physical and biological sciences* **83**, 1-15.

Laursen, J., Scholl, D. W. & von Huene, R. (2002). Neotectonic deformation of the central Chile margin: Deepwater forearc basin formation in response to hot spot ridge and seamount subduction. *Tectonics* **21**, 2-1-2-27.

Law, S., Bromiley, G. D., Kilgour, G. N. & Fitton, J. G. (2021). Tracing mantle source variation through xenocrystic olivine in the Taupo Volcanic Zone, New Zealand: A role for lithospheric mantle in the shift from andesitic to rhyolitic compositions. *Lithos* **394-395**, 106185.

Le Maitre, R., Streckeisen, A., Zanettin, B. , Le Bas, M., Bonin, B. & Bateman, P. E. (2002). *Igneous Rocks: A Classification and Glossary of Terms: Recommendations of the International Union of Geological Sciences Subcommission on the Systematics of Igneous Rocks*. Cambridge: Cambridge University Press.

Leeman, W. P. (1983). The influence of crustal structure on compositions of subduction-related magmas. *Journal of Volcanology and Geothermal Research* **18**, 561-588.

Leonard, G. S. (2003). The evolution of Maroa Volcanic Centre, Taupo Volcanic Zone, New Zealand. University of Canterbury.

Leonard, G. S., Cole, J. W., Nairn, I. A. & Self, S. (2002). Basalt triggering of the c. AD 1305 Kaharoa rhyolite eruption, Tarawera Volcanic Complex, New Zealand. *Journal of Volcanology and Geothermal Research* **115**, 461-486.

Lewis, K. B., Collot, J.-Y. & Lallem, S. E. (1998). The dammed Hikurangi Trough: a channel-fed trench blocked by subducting seamounts and their wake avalanches (New Zealand–France GeodyNZ Project). *Basin Research* **10**, 441-468.

Li, C.-F., Li, X.-H., Li, Q.-L., Guo, J.-H., Li, X.-H. & Yang, Y.-H. (2012). Rapid and precise determination of Sr and Nd isotopic ratios in geological samples from the same filament loading by thermal ionization mass spectrometry employing a single-step separation scheme. *Analytica Chimica Acta* **727**, 54-60.

Li, W. & Ni, H. (2020). Dehydration at subduction zones and the geochemistry of slab fluids. *Science China Earth Sciences* **63**, 1925-1937.

Li, X., Yan, Q., Zeng, Z., Fan, J., Li, S., Li, J., Yang, H. & Wang, X. (2021). Across-arc variations in Mo isotopes and implications for subducted oceanic crust in the source of back-arc basin volcanic rocks. *Geology* **49**, 1165-1170.

Lin, C.-H., Shih, M.-H., Lai, Y.-C., 2021. Mantle wedge diapirs detected by a dense seismic array in Northern Taiwan. Sci. Rep. 11(1), 1561. doi.org/10.1038/s41598-021-81357-7.

Lormand, C., Zellmer, G. F., Kilgour, G. N., Németh, K., Palmer, A. S., Sakamoto, N., Yurimoto, H., Kuritani, T., Iizuka, Y. & Moebis, A. (2020). Slow ascent of unusually hot intermediate magmas triggering Strombolian to sub-Plinian eruptions. *Journal of Petrology*.

Loubet, M., Sassi, R. & Di Donato, G. (1988). Mantle heterogeneities: a combined isotope and trace element approach and evidence for recycled continental crust materials in some OIB sources. *Earth and Planetary Science Letters* **89**, 299-315.

Mackinnon, T. C. (1983). Origin of the Torlesse terrane and coeval rocks, South Island, New Zealand. *GSA Bulletin* **94**, 967-985.

Magni, V. & Király, Á. (2020). *Reference Module in Earth Systems and Environmental Sciences*: Elsevier.

Mahood, G. & Hildreth, W. (1983). Large partition coefficients for trace elements in high-silica rhyolites. *Geochimica et Cosmochimica Acta* **47**, 11-30.

Marini, J.-C., Chauvel, C. & Maury, R. C. (2005). Hf isotope compositions of northern Luzon arc lavas suggest involvement of pelagic sediments in their source. *Contributions to Mineralogy and Petrology* **149**, 216-232.

Marschall, H. R. & Schumacher, J. C. (2012). Arc magmas sourced from mélange diapirs in subduction zones. *Nature Geoscience* **5**, 862-867.

Martin, H., Smithies, R. H., Rapp, R., Moyen, J. F. & Champion, D. (2005). An overview of adakite, tonalite–trondhjemite–granodiorite (TTG), and sanukitoid: relationships and some implications for crustal evolution. *Lithos* **79**, 1-24.

Martin, R. C. (1961). Stratigraphy and structural outline of the Taupo Volcanic Zone. *New Zealand Journal of Geology and Geophysics* **4**, 449-478.

Matheson, M. A. (2010). Eruption Dynamics and Hydrological Implications of Basaltic Volcanic Centres at Lake Taupo. University of Waikato, 287.

McArthur, J. M., Howarth, R. J. & Bailey, T. R. (2001). Strontium Isotope Stratigraphy: LOWESS Version 3: Best Fit to the Marine Sr-Isotope Curve for 0–509 Ma and Accompanying Look-up Table for Deriving Numerical Age. *The Journal of Geology* **109**, 155-170.

McCulloch, M. T., Kyser, T. K., Woodhead, J. D. & Kinsley, L. (1994). Pb−Sr−Nd−O isotopic constraints on the origin of rhyolites from the Taupo Volcanic Zone of New Zealand: evidence for assimilation followed by fractionation from basalt. *Contributions to Mineralogy and Petrology* **115**, 303-312.

Mibe, K., Kawamoto, T., Matsukage, K. N., Fei, Y. & Ono, S. (2011). Slab melting versus slab dehydration in subduction-zone magmatism. *Proceedings of the National Academy of Sciences* **108**, 8177-8182.

Milicich, S. D., Chambefort, I., Wilson, C. J. N., Alcaraz, S., Ireland, T. R., Bardsley, C. & Simpson, M. P. (2020). A zircon U-Pb geochronology for the Rotokawa geothermal system, New Zealand, with implications for Taupō Volcanic Zone evolution. *Journal of Volcanology and Geothermal Research* **389**, 106729.

Milner, D. M., Cole, J. W. & Wood, C. P. (2003). Mamaku Ignimbrite: a caldera-forming ignimbrite erupted from a compositionally zoned magma chamber in Taupo Volcanic Zone, New Zealand. *Journal of Volcanology and Geothermal Research* **122**, 243-264.

Miyazaki, T. & Shuto, K. (1998). Sr and Nd isotope ratios of twelve GSJ rock reference samples. *GEOCHEMICAL JOURNAL* **32**, 345-350.

Moriguti, T. & Nakamura, E. (1998). Across-arc variation of Li isotopes in lavas and implications for crust/mantle recycling at subduction zones. *Earth and Planetary Science Letters* **163**, 167-174.

Mortimer, N. & Parkinson, D. (1996). Hikurangi Plateau: A Cretaceous large igneous province in the southwest Pacific Ocean. *Journal of Geophysical Research: Solid Earth* **101**, 687-696.

Mortimer, N., Rattenbury, M. S., King, P. R., Bland, K. J., Barrell, D. J. A., Bache, F., Begg, J. G., Campbell, H. J., Cox, S. C., Crampton, J. S., Edbrooke, S. W., Forsyth,

P. J., Johnston, M. R., Jongens, R., Lee, J. M., Leonard, G. S., Raine, J. I., Skinner, D. N. B., Timm, C., Townsend, D. B., Tulloch, A. J., Turnbull, I. M. & Turnbull, R. E. (2014). High-level stratigraphic scheme for New Zealand rocks. *New Zealand Journal of Geology and Geophysics* **57**, 402-419.

Münker, C., Weyer, S., Scherer, E. & Mezger, K. (2001). Separation of high field strength elements (Nb, Ta, Zr, Hf) and Lu from rock samples for MC-ICPMS measurements. *Geochemistry, Geophysics, Geosystems* **2**.

Nairn, I. A. & Beanland, S. (1989). Geological setting of the 1987 Edgecumbe earthquake, New Zealand. *New Zealand Journal of Geology and Geophysics* **32**, 1-13.

Nairn, I. A., Kobayashi, T. & Nakagawa, M. (1998). The ~10 ka multiple vent pyroclastic eruption sequence at Tongariro Volcanic Centre, Taupo Volcanic Zone, New Zealand:: Part 1. Eruptive processes during regional extension. *Journal of Volcanology and Geothermal Research* **86**, 19-44.

Nairn, I. A., Shane, P. R., Cole, J. W., Leonard, G. J., Self, S. & Pearson, N. (2004). Rhyolite magma processes of the ~AD 1315 Kaharoa eruption episode, Tarawera volcano, New Zealand. *Journal of Volcanology and Geothermal Research* **131**, 265-294.

Nakagawa, M., Nairn, I. A. & Kobayashi, T. (1998). The ~10 ka multiple vent pyroclastic eruption sequence at Tongariro Volcanic Centre, Taupo Volcanic Zone, New Zealand: Part 2. Petrological insights into magma storage and transport during regional extension. *Journal of Volcanology and Geothermal Research* **86**, 45-65.

Nicol, A., Mazengarb, C., Chanier, F., Rait, G., Uruski, C. & Wallace, L. (2007). Tectonic evolution of the active Hikurangi subduction margin, New Zealand, since the Oligocene. *Tectonics* **26**.

Nielsen, S. G., Baker, J. A. & Krogstad, E. J. (2002). Petrogenesis of an early Archaean (3.4 Ga) norite dyke, Isua, West Greenland: evidence for early Archaean crustal recycling? *Precambrian Research* **118**, 133-148.

Nielsen, S. G. & Marschall, H. R. (2017). Geochemical evidence for mélange melting in global arcs. *Science Advances* **3**, e1602402-e1602402.

Olin, P. H. & Wolff, J. A. (2010). Rare earth and high field strength element partitioning between iron-rich clinopyroxenes and felsic liquids. *Contributions to Mineralogy and Petrology* **160**, 761-775.

Palmer, M. R. (1991). Boron-isotope systematics of Halmahera arc (Indonesia) lavas: Evidence for involvement of the subducted slab. *Geology* **19**, 215-217.

Parolari, M., Gómez-Tuena, A., Cavazos-Tovar, J. G. & Hernández-Quevedo, G. (2018). A balancing act of crust creation and destruction along the western Mexican convergent margin. *Geology* **46**, 455-458.

Parolari, M., Gómez-Tuena, A., Errázuriz-Henao, C. & Cavazos-Tovar, J. G. (2021). Orogenic andesites and their link to the continental rock cycle. *Lithos* **382-383**, 105958.

Patchett, P. J. & Bridgwater, D. (1984). Origin of continental crust of 1.9-1.7 Ga age defined by Nd isotopes in the Ketilidian terrain of South Greenland. *Contributions to Mineralogy and Petrology* **87**, 311-318.

Patchett, P. J. & Samson, S. D. (2003). In: Holland, H. D. & Turekian, K. K. (eds.) *Treatise on Geochemistry*. Oxford: Pergamon, 321-348.

Pearce, J. A., Kempton, P. D. & Gill, J. B. (2007). Hf–Nd evidence for the origin and distribution of mantle domains in the SW Pacific. *Earth and Planetary Science Letters* **260**, 98-114.

Pedley, K. L., Barnes, P. M., Pettinga, J. R. & Lewis, K. B. (2010). Seafloor structural geomorphic evolution of the accretionary frontal wedge in response to seamount subduction, Poverty Indentation, New Zealand. *Marine Geology* **270**, 119-138.

Pertermann, M. & Hirschmann, M. M. (2003). Partial melting experiments on a MORB-like pyroxenite between 2 and 3 GPa: Constraints on the presence of pyroxenite in basalt source regions from solidus location and melting rate. *Journal of Geophysical Research: Solid Earth* **108**.

Pin, C. & Zalduegui, J. S. (1997). Sequential separation of light rare-earth elements, thorium and uranium by miniaturized extraction chromatography: Application to isotopic analyses of silicate rocks. *Analytica Chimica Acta* **339**, 79-89.

Plank, T. (2014). In: Holland, H. D. & Turekian, K. K. (eds.) *Treatise on Geochemistry (Second Edition)*. Oxford: Elsevier, 607-629.

Plank, T. & Langmuir, C. H. (1988). An evaluation of the global variations in the major element chemistry of arc basalts. *Earth and Planetary Science Letters* **90**, 349-370.

Plank, T. & Langmuir, C. H. (1993). Tracing trace elements from sediment input to volcanic output at subduction zones. *Nature* **362**, 739-743.

Plank, T. & Langmuir, C. H. (1998). The chemical composition of subducting sediment and its consequences for the crust and mantle. *Chemical Geology* **145**, 325-394.

Potts, P. J. (1987). X-ray fluorescence analysis: principles and practice of wavelength dispersive spectrometry. In: Potts, P. J. (ed.) *A Handbook of Silicate Rock Analysis*. Dordrecht: Springer Netherlands, 226-285.

Prentice, M. L., Pittari, A., Barker, S. L. L. & Moon, V. G. (2020). Volcanogenic processes and petrogenesis of the early Pleistocene andesitic-dacitic Maungatautari composite cone, Central Waikato, New Zealand. *New Zealand Journal of Geology and Geophysics* **63**, 210-226.

Price, R. C., Gamble, J. A., Smith, I. E. M., Maas, R., Waight, T., Stewart, R. B. & Woodhead, J. (2012). The Anatomy of an Andesite Volcano: a Time–Stratigraphic Study of Andesite Petrogenesis and Crustal Evolution at Ruapehu Volcano, New Zealand. *Journal of Petrology* **53**, 2139-2189.

Price, R. C., Gamble, J. A., Smith, I. E. M., Stewart, R. B., Eggins, S. & Wright, I. C. (2005). An integrated model for the temporal evolution of andesites and rhyolites and crustal development in New Zealand's North Island. *Journal of Volcanology and Geothermal Research* **140**, 1-24.

Price, R. C., Mortimer, N., Smith, I. E. M. & Maas, R. (2015). Whole-rock geochemical reference data for Torlesse and Waipapa terranes, North Island, New Zealand. *New Zealand Journal of Geology and Geophysics* **58**, 213-228.

Pullar, W. A. & Nairn, I. A. (1972). Matahi Basaltic Tephra member, Rotoiti Breccia Formation. *New Zealand Journal of Geology and Geophysics* **15**, 446-450.

Rapp, R. P., Shimizu, N., Norman, M. D. & Applegate, G. S. (1999). Reaction between slab-derived melts and peridotite in the mantle wedge: experimental constraints at 3.8 GPa. *Chemical Geology* **160**, 335-356.

Rebaza, A. M., Mallik, A. & Straub, S. M. (2023). Multiple episodes of rock-melt reaction at the slab-mantle interface: Formation of high silica primary magmas in intermediate to hot subduction zones. *Journal of Petrology*, egad011.

Regelous, M., Collerson, K. D., Ewart, A. & Wendt, J. I. (1997). Trace element transport rates in subduction zones: evidence from Th, Sr and Pb isotope data for Tonga-Kermadec arc lavas. *Earth and Planetary Science Letters* **150**, 291-302.

Reid, F. (1983). Origin of the rhyolitic rocks of the taupo volcanic zone, New Zealand. *Journal of Volcanology and Geothermal Research* **15**, 315-338.

Reid, F. W. & Cole, J. W. (1983). Origin of dacites of Taupo Volcanic Zone, New Zealand. *Journal of Volcanology and Geothermal Research* **18**, 191-214.

Reyners, M. (2013). The central role of the Hikurangi Plateau in the Cenozoic tectonics of New Zealand and the Southwest Pacific. *Earth and Planetary Science Letters* **361**, 460-468.

Reyners, M., Eberhart-Phillips, D. & Bannister, S. (2011). Tracking repeated subduction of the Hikurangi Plateau beneath New Zealand. *Earth and Planetary Science Letters* **311**, 165-171.

Ribeiro, J., MacLeod, C., Lissenberg, J., Ryan, J. & Macpherson, C. (2022). Origin and evolution of the slab fluids since subduction inception in the Izu-Bonin-Mariana: A comparison with the southeast Mariana fore-arc rift. *Chemical Geology* **601**, 120813.

Risse, A., Trumbull, R. B., Kay, S. M., Coira, B. & Romer, R. L. (2013). Multi-stage Evolution of Late Neogene Mantle-derived Magmas from the Central Andes Back-arc in the Southern Puna Plateau of Argentina. *Journal of Petrology* **54**, 1963-1995.

Robertson, D. (1983). Paleomagnetism and geochronology of volcanics in the northern North Island. University of Auckland.

Rollinson, H. & Pease, V. (2021). Using Trace Element Data. In: Rollinson, H. & Pease, V. (eds.) *Using Geochemical Data: To Understand Geological Processes*. Cambridge: Cambridge University Press, 96-156.

Rooney, T. O. & Deering, C. D. (2014). Conditions of melt generation beneath the Taupo Volcanic Zone: The influence of heterogeneous mantle inputs on large-volume silicic systems. *Geology* **42**, 3-6.

Rosenberg, M. D., Wilson, C. J. N., Bignall, G., Ireland, T. R., Sepulveda, F. & Charlier, B. L. A. (2020). Structure and evolution of the Wairakei–Tauhara geothermal system (Taupo Volcanic Zone, New Zealand) revisited with a new zircon geochronology. *Journal of Volcanology and Geothermal Research* **390**, 106705.

Roser, B. P. & Korsch, R. J. (1999). Geochemical characterization, evolution and source of a Mesozoic accretionary wedge: the Torlesse terrane, New Zealand. *Geological Magazine* **136**, 493-512.

Rudnick, R. L. (1995). Making continental crust. *Nature* **378**, 571-578.

Rudnick, R. L. & Gao, S. (2003). In: Holland, H. D. & Turekian, K. K. (eds.) *Treatise on Geochemistry*. Oxford: Pergamon, 1-64.

Saffer, D. M., Wallace, L. M., Barnes, P. M., Pecher, I. A., Petronotis, K. E., LeVay, L. J., Bell, R. E., Crundwell, M. P., Engelmann de Oliveira, C. H., Fagereng, A., Fulton, P. M., Greve, A., Harris, R. N., Hashimoto, Y., Hüpers, A., Ikari, M. J., Ito, Y., Kitajima, H., Kutterolf, S., Lee, H., Li, X., Luo, M., Malie, P. R., Meneghini, F., Morgan, J. K., Noda, A., Rabinowitz, H. S., Savage, H. M., Shepherd, C. L., Shreedharan, S., Solomon, E. A., Underwood, M. B., Wang, M., Woodhouse, A. D., Bourlange, S. M., Brunet, M. M. Y., Cardona, S., Clennell, M. B., Cook, A. E., Dugan, B., Elger, J., Gamboa, D., Georgiopoulou, A., Han, S., Heeschen, K. U., Hu, G., Kim, G. Y., Koge, H., Machado, K. S., McNamara, D. D., Moore, G. F., Mountjoy, J. J., Nole, M. A., Owari, S., Paganoni, M., Rose, P. S., Screaton, E. J., Shankar, U., Torres, M. E., Wang, X. & Wu, H.-Y. (2019). Expedition 372B/375 summary. *International Ocean Discovery Program* **372B/375**.

Salmon, M. L., Stern, T. A. & Savage, M. K. (2011). A major step in the continental Moho and its geodynamic consequences: the Taranaki-Ruapehu line, New Zealand. *Geophysical Journal International* **186**, 32-44.

Sas, M., Shane, P., Kawasaki, N., Sakamoto, N., Zellmer, G. F. & Yurimoto, H. (2021a). Inter- and intra-crystal quartz δ18O homogeneity at Okataina volcano, Aotearoa New Zealand: Implications for rhyolite genesis. *Journal of Volcanology and Geothermal Research*, 107430.

Sas, M., Shane, P., Kuritani, T., Zellmer, G. F., Kent, A. J. R. & Nakagawa, M. (2021b). Mush, Melts and Metasediments: a History of Rhyolites from the Okataina Volcanic Centre, New Zealand, as Captured in Plagioclase. *Journal of Petrology* **62**.

Schellart, W. P., Lister, G. S. & Toy, V. G. (2006). A Late Cretaceous and Cenozoic reconstruction of the Southwest Pacific region: Tectonics controlled by subduction and slab rollback processes. *Earth-Science Reviews* **76**, 191-233.

Schiano, P., Clocchiatti, R., Shimizu, N., Maury, R. C., Jochum, K. P. & Hofmann, A. W. (1995). Hydrous, silica-rich melts in the sub-arc mantle and their relationship with erupted arc lavas. *Nature* **377**, 595-600.

Schmitz, M. D. & Smith, I. E. M. (2004). The Petrology of the Rotoiti Eruption Sequence, Taupo Volcanic Zone: an Example of Fractionation and Mixing in a Rhyolitic System. *Journal of Petrology* **45**, 2045-2066.

Scholes, R. C., Hageman, K. J., Closs, G. P., Stirling, C. H., Reid, M. R., Gabrielsson, R. & Augspurger, J. M. (2016). Predictors of pesticide concentrations in freshwater trout – The role of life history. *Environmental Pollution* **219**, 253-261.

Seebeck, H., Nicol, A., Giba, M., Pettinga, J. & Walsh, J. (2013). Geometry of the subducting Pacific plate since 20 Ma, Hikurangi margin, New Zealand. *Journal of the Geological Society* **171**, 131-143.

Shane, P., Maas, R. & Lindsay, J. (2017). History of Red Crater volcano, Tongariro Volcanic Centre (New Zealand): Abrupt shift in magmatism following recharge and contrasting evolution between neighboring volcanoes. *Journal of Volcanology and Geothermal Research* **340**, 1-15.

Shane, P., Martin, S. B., Smith, V. C., Beggs, K. F., Darragh, M. B., Cole, J. W. & Nairn, I. A. (2007). Multiple rhyolite magmas and basalt injection in the 17.7 ka Rerewhakaaitu eruption episode from Tarawera volcanic complex, New Zealand. *Journal of Volcanology and Geothermal Research* **164**, 1-26.

Shane, P., Nairn, I. A. & Smith, V. C. (2005). Magma mingling in the ~50 ka Rotoiti eruption from Okataina Volcanic Centre: implications for geochemical diversity and chronology of large volume rhyolites. *Journal of Volcanology and Geothermal Research* **139**, 295-313.

Shimoda, G., Tatsumi, Y., Nohda, S., Ishizaka, K. & Jahn, B. M. (1998). Setouchi high-Mg andesites revisited: geochemical evidence for melting of subducting sediments. *Earth and Planetary Science Letters* **160**, 479-492.

Sisson, T. W. & Bacon, C. R. (1992). Garnet/high-silica rhyolite trace element partition coefficients measured by ion microprobe. *Geochimica et Cosmochimica Acta* **56**, 2133-2136.

Skora, S. & Blundy, J. (2010). High-pressure Hydrous Phase Relations of Radiolarian Clay and Implications for the Involvement of Subducted Sediment in Arc Magmatism. *Journal of Petrology* **51**, 2211-2243.

Smith, V. C., Shane, P. & Nairn, I. A. (2005). Trends in rhyolite geochemistry, mineralogy, and magma storage during the last 50 kyr at Okataina and Taupo volcanic centres, Taupo Volcanic Zone, New Zealand. *Journal of Volcanology and Geothermal Research* **148**, 372-406.

Smith, V. C., Shane, P. & Smith, I. E. M. (2002). Tephrostratigraphy and geochemical fingerprinting of the Mangaone Subgroup tephra beds, Okataina Volcanic Centre, New Zealand. *New Zealand Journal of Geology and Geophysics* **45**, 207-219.

Spandler, C. & Pirard, C. (2013). Element recycling from subducting slabs to arc crust: A review. *Lithos* **170-171**, 208-223.

Speden, I. G. (1976). Fossil localities in Torlesse rocks of the North Island, New Zealand. *Journal of the Royal Society of New Zealand* **6**, 73-91.

Staudigel, H. (2003). In: Holland, H. D. & Turekian, K. K. (eds.) *Treatise on Geochemistry*. Oxford: Pergamon, 511-535.

Stern, C. R. (2011). Subduction erosion: Rates, mechanisms, and its role in arc magmatism and the evolution of the continental crust and mantle. *Gondwana Research* **20**, 284-308.

Stern, R. J. (2002). Subduction zones. *Reviews of Geophysics* **40**, 3-1.

Stern, R. J. & Scholl, D. W. (2010). Yin and yang of continental crust creation and destruction by plate tectonic processes. *International Geology Review* **52**, 1-31.

Stern, T. A. (1987). Asymmetric back-arc spreading, heat flux and structure associated with the Central Volcanic Region of New Zealand. *Earth and Planetary Science Letters* **85**, 265-276.

Stimac, J. & Hickmott, D. (1994). Trace-element partition coefficients for ilmenite, orthopyroxene and pyrrhotite in rhyolite determined by micro-PIXE analysis. *Chemical Geology* **117**, 313-330.

Stipp, J. J. (1968). The geochronology and petrogenesis of the Cenozoic volcanics of the North Island, New Zealand. *Ph. D. Thesis, Australian National University, Canberra*.

Stirling, C. H., Andersen, M. B., Potter, E.-K. & Halliday, A. N. (2007). Low-temperature isotopic fractionation of uranium. *Earth and Planetary Science Letters* **264**, 208-225.

Stirling, C. H., Halliday, A. N. & Porcelli, D. (2005). In search of live 247Cm in the early solar system. *Geochimica et Cosmochimica Acta* **69**, 1059-1071.

Stirling, C. H., Halliday, A. N., Potter, E.-K., Andersen, M. B. & Zanda, B. (2006). A low initial abundance of 247Cm in the early solar system and implications for r-process nucleosynthesis. *Earth and Planetary Science Letters* **251**, 386-397.

Stratford, W. R. & Stern, T. A. (2004). Strong seismic reflections and melts in the mantle of a continental back-arc basin. *Geophysical Research Letters* **31**.

Straub, S. M., Goldstein, S. L., Class, C., Schmidt, A. & Gomez-Tuena, A. (2010). Slab and Mantle Controls on the Sr–Nd–Pb–Hf Isotope Evolution of the Post 42 Ma Izu–Bonin Volcanic Arc. *Journal of Petrology* **51**, 993-1026.

Straub, S. M., Gómez-Tuena, A., Bindeman, I. N., Bolge, L. L., Brandl, P. A., Espinasa-Perena, R., Solari, L., Stuart, F. M., Vannucchi, P. & Zellmer, G. F. (2015). Crustal recycling by subduction erosion in the central Mexican Volcanic Belt. *Geochimica et Cosmochimica Acta* **166**, 29-52.

Straub, S. M., Gomez-Tuena, A., Stuart, F. M., Zellmer, G. F., Espinasa-Perena, R., Cai, Y. & Iizuka, Y. (2011). Formation of hybrid arc andesites beneath thick continental crust. *Earth and Planetary Science Letters* **303**, 337-347.

Straub, S. M., Gómez-Tuena, A. & Vannucchi, P. (2020). Subduction erosion and arc volcanism. *Nature Reviews Earth & Environment* **1**, 574-589.

Straub, S. M., LaGatta, A. B., Martin-Del Pozzo, A. L. & Langmuir, C. H. (2008). Evidence from high-Ni olivines for a hybridized peridotite/pyroxenite source for orogenic andesites from the central Mexican Volcanic Belt. *Geochemistry, Geophysics, Geosystems* **9**.

Sun, S.-s. & McDonough, W. F. (1989). Chemical and isotopic systematics of oceanic basalts: implications for mantle composition and processes. *Geological Society, London, Special Publications* **42**, 313-345.

Sun, Y., Teng, F.-Z., Hu, Y., Chen, X.-Y. & Pang, K.-N. (2020). Tracing subducted oceanic slabs in the mantle by using potassium isotopes. *Geochimica et Cosmochimica Acta* **278**, 353-360.

Sutton, A. N., Blake, S. & Wilson, C. J. N. (1995). An outline geochemistry of rhyolite eruptives from Taupo volcanic centre, New Zealand. *Journal of Volcanology and Geothermal Research* **68**, 153-175.

Svoboda, C., Rooney, T. O., Girard, G. & Deering, C. (2021). Transcrustal magmatic systems: evidence from andesites of the southern Taupo Volcanic Zone. *Journal of the Geological Society* **179**, jgs2020-2204.

Tanaka, H., Turner, G. M., Houghton, B. F., Tachibana, T., Kono, M. & McWilliams, M. O. (1996). Palaeomagnetism and chronology of the central Taupo Volcanic Zone, New Zealand. *Geophysical Journal International* **124**, 919-934.

Tanaka, T., Togashi, S., Kamioka, H., Amakawa, H., Kagami, H., Hamamoto, T., Yuhara, M., Orihashi, Y., Yoneda, S., Shimizu, H., Kunimaru, T., Takahashi, K., Yanagi, T.,

Nakano, T., Fujimaki, H., Shinjo, R., Asahara, Y., Tanimizu, M. & Dragusanu, C. (2000). JNdi-1: a neodymium isotopic reference in consistency with LaJolla neodymium. *Chemical Geology* **168**, 279-281.

Tatsumi, Y. (2001). Geochemical modeling of partial melting of subducting sediments and subsequent melt-mantle interaction: Generation of high-Mg andesites in the Setouchi volcanic belt, southwest Japan. *Geology* **29**, 323-326.

Tatsumi, Y. & Hanyu, T. (2003). Geochemical modeling of dehydration and partial melting of subducting lithosphere: Toward a comprehensive understanding of high-Mg andesite formation in the Setouchi volcanic belt, SW Japan. *Geochemistry, Geophysics, Geosystems* **4**.

Taylor, B. (2006). The single largest oceanic plateau: Ontong Java–Manihiki–Hikurangi. *Earth and Planetary Science Letters* **241**, 372-380.

Taylor, R. J. M., Harley, S. L., Hinton, R. W., Elphick, S., Clark, C. & Kelly, N. M. (2015). Experimental determination of REE partition coefficients between zircon, garnet and melt: a key to understanding high-T crustal processes. *Journal of Metamorphic Geology* **33**, 231-248.

Taylor, S. R. (1967). The origin and growth of continents. *Tectonophysics* **4**, 17-34.

Taylor, S. R. & McLennan, S. M. (1985). *The continental crust: Its composition and evolution*. United States: Blackwell Scientific Pub.,Palo Alto, CA.

Thompson, B. N. (1964). Quaternary Volcanism of the Central Volcanic Region. *New Zealand Journal of Geology and Geophysics* **7**, 45-66.

Tiepolo, M., Oberti, R., Zanetti, A., Vannucci, R. & Foley, S. F. (2007). Trace-Element Partitioning Between Amphibole and Silicate Melt. *Reviews in Mineralogy and Geochemistry* **67**, 417-452.

Timm, C., Bassett, D., Graham, I. J., Leybourne, M. I., de Ronde, C. E. J., Woodhead, J., Layton-Matthews, D. & Watts, A. B. (2013). Louisville seamount subduction and its implication on mantle flow beneath the central Tonga–Kermadec arc. *Nature Communications* **4**, 1720.

Timm, C., Davy, B., Haase, K., Hoernle, K. A., Graham, I. J., de Ronde, C. E. J., Woodhead, J., Bassett, D., Hauff, F., Mortimer, N., Seebeck, H. C., Wysoczanski, R. J., Caratori-Tontini, F. & Gamble, J. A. (2014). Subduction of the oceanic Hikurangi Plateau and its impact on the Kermadec arc. *Nature Communications* **5**, 4923.

Todd, E., Gill, J.B., Wysoczanski, R.J., Handler, M.R., Wright, I.C., Gamble, J.A., 2010. Sources of constructional cross-chain volcanism in the southern Havre Trough: New insights from HFSE and REE concentration and isotope systematics. Geochem. Geophys. Geosyst. 11(4). doi.org/https://doi.org/10.1029/2009GC002888.

Todd, E., Gill, J. B., Wysoczanski, R. J., Hergt, J., Wright, I. C., Leybourne, M. I. & Mortimer, N. (2011). Hf isotopic evidence for small-scale heterogeneity in the mode of mantle wedge enrichment: Southern Havre Trough and South Fiji Basin back arcs. *Geochemistry, Geophysics, Geosystems* **12**.

Tollstrup, D. L. & Gill, J. B. (2005). Hafnium systematics of the Mariana arc: Evidence for sediment melt and residual phases. *Geology* **33**, 737-740.

Turner, S., Hawkesworth, C., Rogers, N., Bartlett, J., Worthington, T., Hergt, J., Pearce, J. & Smith, I. (1997). 238U-230Th disequilibria, magma petrogenesis, and flux rates beneath the depleted Tonga-Kermadec island arc. *Geochimica et Cosmochimica Acta* **61**, 4855-4884.

Turner, S. J. & Langmuir, C. H. (2015a). The global chemical systematics of arc front stratovolcanoes: Evaluating the role of crustal processes. *Earth and Planetary Science Letters* **422**, 182-193.

Turner, S. J. & Langmuir, C. H. (2015b). What processes control the chemical compositions of arc front stratovolcanoes? *Geochemistry, Geophysics, Geosystems* **16**, 1865-1893.

Turner, S. J. & Langmuir, C. H. (2022). Sediment and ocean crust both melt at subduction zones. *Earth and Planetary Science Letters* **584**, 117424.

Ulfbeck, D., Baker, J., Waight, T. & Krogstad, E. (2003). Rapid sample digestion by fusion and chemical separation of Hf for isotopic analysis by MC-ICPMS. *Talanta* **59**, 365-373.

Vervoort, J. D. & Blichert-Toft, J. (1999). Evolution of the depleted mantle: Hf isotope evidence from juvenile rocks through time. *Geochimica et Cosmochimica Acta* **63**, 533-556.

Vervoort, J. D., Patchett, P. J., Blichert-Toft, J. & Albarède, F. (1999). Relationships between Lu–Hf and Sm–Nd isotopic systems in the global sedimentary system. *Earth and Planetary Science Letters* **168**, 79-99.

Villamor, P. & Berryman, K. (2001). A late Quaternary extension rate in the Taupo Volcanic Zone, New Zealand, derived from fault slip data. *New Zealand Journal of Geology and Geophysics* **44**, 243-269.

Villamor, P. & Berryman, K. R. (2006). Evolution of the southern termination of the Taupo Rift, New Zealand. *New Zealand Journal of Geology and Geophysics* **49**, 23-37.

Villamor, P., Berryman, K. R., Ellis, S. M., Schreurs, G., Wallace, L. M., Leonard, G. S., Langridge, R. M. & Ries, W. F. (2017). Rapid Evolution of Subduction-Related Continental Intraarc Rifts: The Taupo Rift, New Zealand. *Tectonics* **36**, 2250-2272.

von Huene, R., Ranero, C. s. R. & Vannucchi, P. (2004). Generic model of subduction erosion. *Geology* **32**, 913-916.

von Huene, R. & Scholl, D. W. (1991). Observations at convergent margins concerning sediment subduction, subduction erosion, and the growth of continental crust. *Reviews of Geophysics* **29**, 279-316.

von Huene, R. & Scholl, D. W. (1993). The return of sialic material to the mantle indicated by terrigeneous material subducted at convergent margins. *Tectonophysics* **219**, 163-175.

Waight, T. E., Troll, V. R., Gamble, J. A., Price, R. C. & Chadwick, J. P. (2017). Hf isotope evidence for variable slab input and crustal addition in basalts and andesites of the Taupo Volcanic Zone, New Zealand. *Lithos* **284-285**, 222-236.

Walker, G. P. L., Self, S. & Wilson, L. (1984). Tarawera 1886, New Zealand — A basaltic plinian fissure eruption. *Journal of Volcanology and Geothermal Research* **21**, 61-78.

Wallace, L. M., Saffer, D. M., Barnes, P. M., Pecher, I. A., Petronotis, K. E., LeVay, L. J. & Scientists, a. t. E. (2019). Hikurangi Subduction Margin Coring, Logging, and Observatories. *Proceedings of the International Ocean Discovery Program, College Station, TX (International Ocean Discovery Program* **372B/375**.

Weaver, B. L. (1991). The origin of ocean island basalt end-member compositions: trace element and isotopic constraints. *Earth and Planetary Science Letters* **104**, 381-397.

Weis, D., Kieffer, B., Maerschalk, C., Barling, J., de Jong, J., Williams, G. A., Hanano, D., Pretorius, W., Mattielli, N., Scoates, J. S., Goolaerts, A., Friedman, R. M. & Mahoney, J. B. (2006). High-precision isotopic characterization of USGS reference materials by TIMS and MC-ICP-MS. *Geochemistry, Geophysics, Geosystems* **7**.

White, W. M. & Dupré, B. (1986). Sediment subduction and magma genesis in the Lesser Antilles: Isotopic and trace element constraints. *Journal of Geophysical Research: Solid Earth* **91**, 5927-5941.

White, W. M. & Patchett, J. (1984). HfNdSr isotopes and incompatible element abundances in island arcs: implications for magma origins and crust-mantle evolution. *Earth and Planetary Science Letters* **67**, 167-185.

Wilson, C. J. N. (2001). The 26.5ka Oruanui eruption, New Zealand: an introduction and overview. *Journal of Volcanology and Geothermal Research* **112**, 133-174.

Wilson, C. J. N., Houghton, B. F., McWilliams, M. O., Lanphere, M. A., Weaver, S. D. & Briggs, R. M. (1995). Volcanic and structural evolution of Taupo Volcanic Zone, New Zealand: a review. *Journal of Volcanology and Geothermal Research* **68**, 1-28.

Wilson, C. J. N., Rogan, A. M., Smith, I. E. M., Northey, D. J., Nairn, I. A. & Houghton, B. F. (1984). Caldera volcanoes of the Taupo Volcanic Zone, New Zealand. *Journal of Geophysical Research: Solid Earth* **89**, 8463-8484.

Wilson, C. J. N. & Smith, I. E. M. (1985). A basaltic phreatomagmatic eruptive centre at Acacia Bay, Taupo Volcanic Centre. *Journal of the Royal Society of New Zealand* **15**, 329-337.

Woodhead, J. (2002). A simple method for obtaining highly accurate Pb isotope data by MC-ICP-MS. *Journal of Analytical Atomic Spectrometry* **17**, 1381-1385.

Worthington, T. J., Hekinian, R., Stoffers, P., Kuhn, T. & Hauff, F. (2006). Osbourn Trough: Structure, geochemistry and implications of a mid-Cretaceous paleospreading ridge in the South Pacific. *Earth and Planetary Science Letters* **245**, 685-701.

Wu, X., Tian, L., Wang, X.-C., Chu, F., Yan, Q., Sun, F., Li, X., Wang, W., Yu, L., Li, Z. & Chen, L. (2020). Tracing mantle sources in the northern Lau back-arc basin by independent component analysis of basalt isotopic compositions. *International Geology Review* **62**, 938-954.

Xu, Y.-G., Ma, J.-L., Huang, X.-L., Iizuka, Y., Chung, S.-L., Wang, Y.-B. & Wu, X.-Y. (2004). Early Cretaceous gabbroic complex from Yinan, Shandong Province: petrogenesis and mantle domains beneath the North China Craton. *International Journal of Earth Sciences* **93**, 1025-1041.

Xu, Y. (2002). Evidence for crustal components in the mantle and constraints on crustal recycling mechanisms: pyroxenite xenoliths from Hannuoba, North China. *Chemical Geology* **182**, 301-322.

Yogodzinski, G. M., Kay, R. W., Volynets, O. N., Koloskov, A. V. & Kay, S. M. (1995). Magnesian andesite in the western Aleutian Komandorsky region: Implications for slab melting and processes in the mantle wedge. *GSA Bulletin* **107**, 505-519.

Yuan, H., Yuan, W., Cheng, C., Liang, P., Liu, X., Dai, M., Bao, Z., Zong, C., Chen, K. & Lai, S. (2016). Evaluation of lead isotope compositions of NIST NBS 981 measured by thermal ionization mass spectrometer and multiple-collector inductively coupled plasma mass spectrometer. *Solid Earth Sciences* **1**, 74-78.

Zellmer, G. F., Kimura, J.-I., Stirling, C. H., Lube, G., Shane, P. A. & Iizuka, Y. (2020). Genesis of Recent Mafic Magmatism in the Taupo Volcanic Zone, New Zealand: Insights into the Birth and Death of Very Large Volume Rhyolitic Systems? *Journal of Petrology*.

Appendix A

Analytical results of total procedure replicates, and reference materials for major oxide compositions using WD-XRF, trace element concentrations using ICP-MS and Sr-Pb-Nd-Hf isotope ratios using MC-ICP-MS, re-normalisation of the previously reported Pb data. Provided as electronic supplement.

Appendix B

Files of the input and output data used in the Magma Chamber Simulator for each of the individual steps of each model, having the starting composition, starting pressure and step in the name of each file. Provided as electronic supplement.

Appendix C

DRC-16 forms for each chapter intended for or already submitted for publication.

MASSEY UNIVERSITY
TE KUNENGA KI PŪREHUROA
UNIVERSITY OF NEW ZEALAND

GRADUATE RESEARCH SCHOOL

STATEMENT OF CONTRIBUTION
DOCTORATE WITH PUBLICATIONS/MANUSCRIPTS

We, the candidate and the candidate's Primary Supervisor, certify that all co-authors have consented to their work being included in the thesis and they have accepted the candidate's contribution as indicated below in the *Statement of Originality*.

Name of candidate:	Carlos Rodolfo Corella Santa Cruz
Name/title of Primary Supervisor:	Georg Florian Zellmer
In which chapter is the manuscript /published work:	Chapter 4

Please select one of the following three options:

(●) The manuscript/published work is published or in press

- Please provide the full reference of the Research Output:

Corella Santa Cruz, C.R., Zellmer, G.F., Stirling, C.H., Straub, S.M., Brenna, M., Reid, M.R., Németh, K., Barr, D., 2023. Transcrustal and source processes affecting the chemical characteristics of magmas in a hyperactive volcanic zone. Geochim. Cosmochim. Acta 352, 86-106. doi.org/https://doi.org/10.1016/j.gca.2023.05.003.

( ) The manuscript is currently under review for publication – please indicate:

- The name of the journal:

- The percentage of the manuscript/published work that was contributed by the candidate:

- Describe the contribution that the candidate has made to the manuscript/published work:

( ) It is intended that the manuscript will be published, but it has not yet been submitted to a journal

Candidate's Signature:	Carlos Rodolfo Corella Santa Cruz — Digitally signed by Carlos Rodolfo Corella Santa Cruz DN: cn=Carlos Rodolfo Corella Santa Cruz, c=NZ, o=Massey University, ou=Agriculture and Enviroment, email=c.santacruz@massey.ac.nz Date: 2023.08.08 14:05:40 +12'00'
Date:	08-Aug-2023
Primary Supervisor's Signature:	Georg F. Zellmer — Digitally signed by Georg F. Zellmer DN: cn=Georg F. Zellmer, c=NZ, o=Massey University, ou=School of Agriculture and Environment, email=g.f.zellmer@massey.ac.nz Date: 2023.08.08 14:27:16 +12'00'
Date:	8-Aug-2023

This form should appear at the end of each thesis chapter/section/appendix submitted as a manuscript/ publication or collected as an appendix at the end of the thesis.

MASSEY UNIVERSITY
TE KUNENGA KI PŪREHUROA
UNIVERSITY OF NEW ZEALAND

GRADUATE RESEARCH SCHOOL

STATEMENT OF CONTRIBUTION
DOCTORATE WITH PUBLICATIONS/MANUSCRIPTS

We, the candidate and the candidate's Primary Supervisor, certify that all co-authors have consented to their work being included in the thesis and they have accepted the candidate's contribution as indicated below in the *Statement of Originality*.

Name of candidate:	Carlos Rodolfo Corella Santa Cruz
Name/title of Primary Supervisor:	Georg Florian Zellmer
In which chapter is the manuscript /published work:	Chapter 5

Please select one of the following three options:

○ The manuscript/published work is published or in press

- Please provide the full reference of the Research Output:

◉ The manuscript is currently under review for publication – please indicate:

- The name of the journal:

New Zealand Journal of Geology and Geophysics

- The percentage of the manuscript/published work that was contributed by the candidate: 85.00
- Describe the contribution that the candidate has made to the manuscript/published work:

Sample selection, preparation and analytical procedures. Writing manuscript alongside supervisors. Figure development.

○ It is intended that the manuscript will be published, but it has not yet been submitted to a journal

Candidate's Signature:	Carlos Rodolfo Corella Santa Cruz Digitally signed by Carlos Rodolfo Corella Santa Cruz DN: cn=Carlos Rodolfo Corella Santa Cruz, c=NZ, o=Massey University, ou=Agriculture and Enviroment, email=c.santacruz@massey.ac.nz Date: 2023.08.08 14:07:37 +12'00'
Date:	08-Aug-2023
Primary Supervisor's Signature:	Georg F. Zellmer Digitally signed by Georg F. Zellmer DN: cn=Georg F. Zellmer, c=NZ, o=Massey University, ou=School of Agriculture and Environment, email=g.f.zellmer@massey.ac.nz Date: 2023.08.08 14:26:55 +12'00'
Date:	8-Aug-2023

This form should appear at the end of each thesis chapter/section/appendix submitted as a manuscript/ publication or collected as an appendix at the end of the thesis.

MASSEY UNIVERSITY
TE KUNENGA KI PŪREHUROA
UNIVERSITY OF NEW ZEALAND

GRADUATE RESEARCH SCHOOL

STATEMENT OF CONTRIBUTION
DOCTORATE WITH PUBLICATIONS/MANUSCRIPTS

We, the candidate and the candidate's Primary Supervisor, certify that all co-authors have consented to their work being included in the thesis and they have accepted the candidate's contribution as indicated below in the *Statement of Originality*.

Name of candidate:	Carlos Rodolfo Corella Santa Cruz
Name/title of Primary Supervisor:	Georg Florian Zellmer
In which chapter is the manuscript /published work:	Chapter 6

Please select one of the following three options:

○ The manuscript/published work is published or in press

- Please provide the full reference of the Research Output:

○ The manuscript is currently under review for publication – please indicate:

- The name of the journal:

- The percentage of the manuscript/published work that was contributed by the candidate:

- Describe the contribution that the candidate has made to the manuscript/published work:

◉ It is intended that the manuscript will be published, but it has not yet been submitted to a journal

Candidate's Signature:	Carlos Rodolfo Corella Santa Cruz Digitally signed by Carlos Rodolfo Corella Santa Cruz DN: cn=Carlos Rodolfo Corella Santa Cruz, c=NZ, o=Massey University, ou=Agriculture and Enviroment, email=c.santacruz@massey.ac.nz Date: 2023.03.21 16:23:50 +13'00'
Date:	21-Mar-2023
Primary Supervisor's Signature:	Georg F. Zellmer Digitally signed by Georg F. Zellmer DN: cn=Georg F. Zellmer, c=NZ, o=Massey University, ou=School of Agriculture and Environment, email=g.f.zellmer@massey.ac.nz Date: 2023.03.21 16:30:16 +13'00'
Date:	21-Mar-2023

This form should appear at the end of each thesis chapter/section/appendix submitted as a manuscript/ publication or collected as an appendix at the end of the thesis.